Understanding the Mechanical Behavior of Polymer Composites Across Stress States, Length and Time Scales Via Size Effect, Multi-axial Testing and Computational Modeling

Yao Qiao

A dissertation
submitted in partial fulfillment of the
requirements for the degree of

Doctor of Philosophy

University of Washington

2021

Reading Committee:

Marco Salviato, Chair

Jinkyu Yang

Richard Wiebe

Program Authorized to Offer Degree:
Aeronautics and Astronautics

University of Washington

Abstract

Understanding the Mechanical Behavior of Polymer Composites Across Stress States, Length and Time Scales Via Size Effect, Multi-axial Testing and Computational Modeling

Yao Qiao

Chair of the Supervisory Committee:
Professor Marco Salviato
Department of Aeronautics and Astronautics

Advanced composite materials have been developed for several decades whereas the current rising demand for lightweight and high-performance materials across many engineering fields is still boosting the global market of these composite materials. A quintessential condition for the efficient, safe, and durable applications of composite materials is the attainment of high-fidelity computational models that can capture all the possible effects such as curing process, manufacturing defects, stacking sequence, structural geometries and sizes, nanomodification, statistical behavior, multi-axiality ratio, loading type, etc. However, many aspects are still poorly understood in the community of composite materials in spite of tremendous efforts into these subjects thus weakening the full exploration of these materials. Towards this direction, the entire work here is expected to make contributions to the proper understanding of these aspects and the further development of composite materials.

The initial investigation focused on the effects of local stress state and size scaling on the plastic deformation and fracturing behavior of thermoset polymers and related fiber-reinforced composites. It was concluded that the entire local tensorial stress components and the multi-scale behavior of the materials must be considered into the computational micro-mechanics otherwise the determination of the damage initiation and the morphologies of the damage evolution in these materials cannot be computationally reproduced. The latter

aspect further leads to the inspiration of leveraging micro-scale behavior of the materials to improve the structural capacity via engineered porosity. This approach was shown to make thermoset polymers as tough as conventional metals.

Further attention was moved to explore the fracturing behavior and size scaling of polymer nanocomposites. It was found that the investigated graphene nanocomposites and most of generic nanocomposites in the literature exhibit significant quasi-brittleness both in quasi-static and fatigue loading conditions due to the non-negligible Fracture Process Zone (FPZ) in the materials and this important feature cannot be described through the Linear Elastic Fracture Mechanics (LEFM) which was extensively used in the current literature. The correct analysis on the polymer composites must leverage quasi-brittle mechanics and high-fidelity computational models otherwise the characterization of the materials and related structures by means of LEFM can lead to unacceptable errors.

In addition to the forgoing studies, the mechanical behavior of fiber-reinforced composites due to the effects of stress multi-axiality ratio, loading type, stacking sequence, and the structural geometry were also investigated and the detailed damage mechanisms triggering the foregoing behavior were also clarified. It was most interestingly found that the loading multi-axiality ratio can significantly affect the fracturing behavior and morphology of fiber-reinforced composites whereas the loading type can lead to a remarkable difference in the damage progression of fiber-reinforced composites. These studies are utmost of importance for the calibration and validation of high-fidelity computational models which enable the description of all the foregoing aspects with respect to the structural size.

TABLE OF CONTENTS

LIST OF FIGURES

LIST OF TABLES

ACKNOWLEDGMENTS

I would like to thank Professor Marco Salviato for his illuminating guidance and mentorship during my doctoral study. He always has rigorous attitude towards research and creative ideas for the exploration of brand-new knowledge which have deeply influenced my professional and personal growth. It is my great honor and privilege to pursue my doctorate under his advisorship.

I would also like to thank Prof. Jinkyu Yang, Prof. Dana Dabiri, Prof. Richard Wiebe and Prof. Dwayne D. Arola for serving as my doctoral committee members and providing generous guidelines and suggestions. In addition, I also have many thanks for the following colleagues and friends who discussed with me on various topics in Solid Mechanics and spent great moments with me during this arduous journey: Mr. Sean Ensuik Phenisee, Mr. Antonio Alessandro Deleo, Mr. Seunghyun Ko, Dr. Han-Gyu Kim, Mr. Drew Byungkyu Kang, Ms. Corry Hage Mefford, Mr. Abishek Das, Ms. Siqi Chen, Mr. Qiwei Zhang, Mr. Kuotian Liao, Mr. Kevin Guo, Mr. Brian Walker, Mr. Minh Nguyen, Mr. Weihong Li, Mr. Shiva Goutham Kumar, Mr. Troy Nakagawa, Mr. Kenta Suzuki, Mr. Rohith Jayaram, Mr. Abhiram Aithal, Mr. Pablo Trefftz Posada, Dr. Gustavo Eidji Camarinha Fujiwara, Mr. Xiaotian Shi, Dr. Hiromi Yasuda, Dr. Rajesh Chaunsali, Mr. Shiyao Lin. Mr. Minh Hoang Nguyen, Mr. Avinkrishnan Vijayachandran, Mr. Chun-Wei Chen, Mr. James O'Neil, Mr. ZT Yang, Dr. Sang Wu, Mr. Dawei Lu, Dr. Luke Richard, Dr. Francesco Deleo, etc.

Let me extend my thanks to other people at my department and other departments for their warm encouragement and support: Prof. Kuen-Yuan Lin, Mr. Ed Connery, Ms. Danyel Hacker, Ms. Winnie Lin, Ms. Nancy-Lou Polk, Mr. George Eliot, Ms. Spencer Fiona, Mr. Dzung Tran, Ms. Michelle Hickner, Mr. Bill Kuykendall, Mr. Sean Yeung, etc.

DEDICATION

to my parents, Baozhu Gu and Shunmin Qiao
and to my wife and son, Wenwen Ou and Evan Qiao for their unconditional love, encouragement, and support. My gratitude for them is beyond words.

Chapter 1
INTRODUCTION AND MOTIVATION

The last few decades have seen a tremendous increase in the use of composite materials in aerospace [1, 2], automotive [3, 4], and civil [5–9] applications as well as wind energy production [10, 11]. While, fostered by the need for lightweight and durable structures, the market of composites will continuously expand in future years, the widespread use of these materials is exposing the demand for safe and reliable design rules under the guidance of high-fidelity computational models that can capture all the possible effects from the manufacturing to the service. Tremendous efforts on this tough task were dedicated in the past to guarantee the structural integrity and functional performance of composite structures whereas many important aspects (e.g. multi-scale analysis, nanomodification, complex loading condition, etc.) are still elusive in the community of composite materials and the solutions of these aspects can definitely improve the current design rules for composite structures.

This dissertation aims to make contributions to solving these challenges through size effect, multi-axial testing and computational modeling on polymer composites and the results facilitate the proper understanding and the further development of composite materials.

1.1 Multi-scale analysis of composite structures

As illustrated in Figure 1.1, the damage progression of composite structures typically span multiple scales. The length scale can be in the order of few nano-meters for the cavitation of molecular structure to millimeter or centimeter for the fracture of multi-directional laminate and eventually moving to the catastrophic failure of full-scale composite structure with few meters. On the other hand, the time scale can be lower than millisecond for severe damage evolution due to high-speed impact loading to slow damage accumulation due to high-cycle

fatigue at least few days. To achieve an accurate description of these aspects, a multi-scale strategy for the modeling of composites is required but it is still a challenging task in the composite materials since it was attempted in the past with the undesirable characterization [12–16] for both micro- and macro-scale mechanical performance of the material. This is mainly due to the lack of proper understanding on the mechanical behavior of the material across multiple scales and stress states.

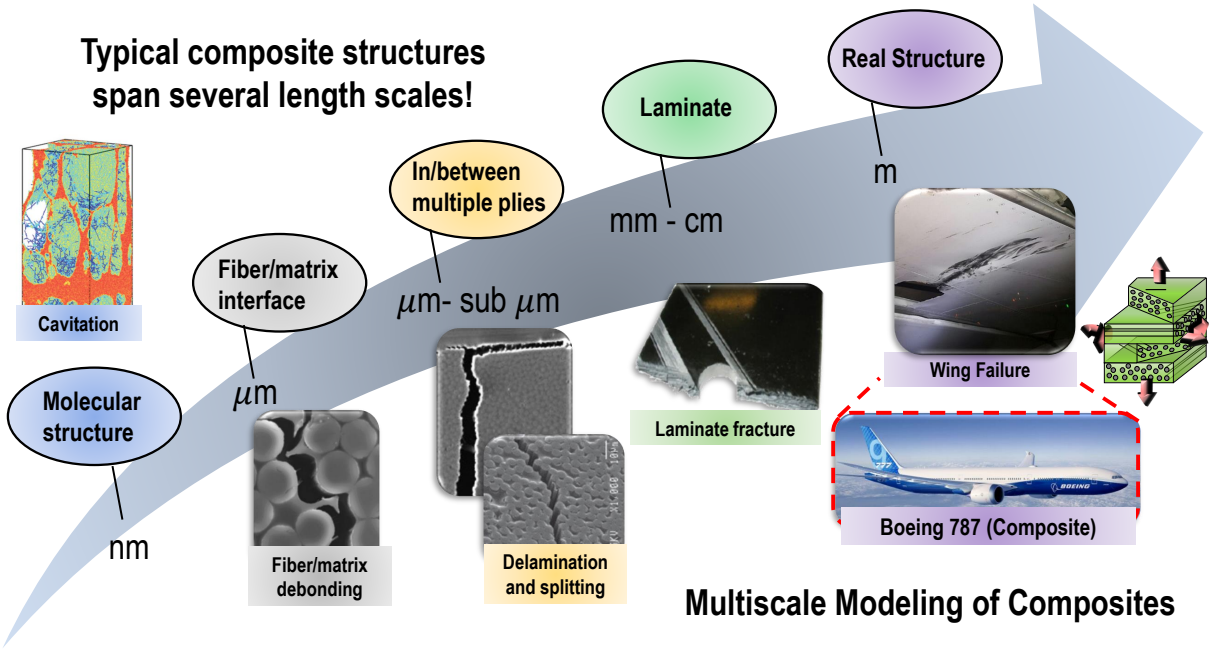

Figure 1.1: Damage progression at multiple length scales for composite structures. These multi-scale features must be characterized through multi-scale modeling of composites.

In recent years, several studies focusing on the investigation of thermoset polymer at various length scales especially for the micro-scale behavior were conducted. One of the interesting results was provided by Hobbiebrunken *et al.* [17] who measured the material strength from sub-micron specimens. It was shown that the material strength of thermoset polymer at that scale can be several times higher than the macro-scale strength. In addition, Kaneko *et al.* [18] conducted fracture tests on the micro-scale specimens showing that the fracture energy corresponding to the investigated scale is one order of magnitude lower that

the macro-scale fracture energy. On the other hand, the importance of local stress state for the inelastic and fracturing behavior of thermoset polymer and their fiber-reinforced composites was also emphasized in the literature [19–24] but mostly overlooked in the community of composite materials. These outstanding results are extremely insightful for further understanding the mechanical behavior of polymer matrix composites and indicate the fact that the multi-scale modeling of composites must also include the multi-scale material behavior.

However, this important step requires time-consuming procedures for the material preparation and advanced testing techniques to determine the multi-scale material properties through multi-scale mechanical tests. More importantly, an accurate fracture energy at the micro-scale cannot be determined although the material strength and Young's modulus at that scale can be obtained [17]. This is due to the fact that the fracture energy must be determined based on the entire area under a complete load-displacement curve which not only includes the pre-peak part but also the post-peak behavior. Unfortunately, the micro-scale specimen only exhibits a dynamic failure after the peak load due to the snap-back instability [18]. On the other hand, the material behavior at the micro-scale under fatigue loading condition was even rarely investigated in the open literature and this aspect can be even challenging with the foregoing considerations. To the best of authors' knowledge, few studies [25, 26] were conducted on the nano-scale fatigue behavior of polymers by leveraging molecular dynamics simulations with a significantly high strain rate at least in the order of about 10^8 per second. As a consequence, the simulation results were lack of confidence due to the fact that the mechanical behavior of polymers can be strongly affected by the high strain rate. An alternative solution for these challenges can be the physical-based scaling methods obtained from quasi-brittle mechanics and computational modeling and this important approach must be properly studied with tremendous efforts.

1.2 Composite structures under complex loading conditions

On the other hand, the engineering design of composite structures must also account for other possible effects such as curing process, manufacturing defects, stacking sequence, structural

geometries, statistical behavior, multi-axiality ratio, loading type, etc. However, some important aspects particularly for the complex loading conditions (e.g. stress multi-axiality, fatigue, impact, etc.) on the mechanical behavior of composite materials were rarely investigated in the past decades due to the complexity of the problems and the slow progress in this topic [27]. The former reason is partially derived from the insufficient understanding of composite materials even in the simple loading conditions thus leading to the weak foundation for solving this complex situation. The latter one is mainly attributed to the lack of appropriate experimental methods and efficient multi-scale computational techniques thus leading to the limited studies and hindering the interest in this complicated research direction. In addition, the main damage mechanisms in the complex loading conditions as illustrated in Figure 1.2 were also less explored but significantly important since these damage mechanisms strongly affect the mechanical behavior of composites and lead to important size effects that must be carefully considered in structural design as emphasized in the previous paragraphs.

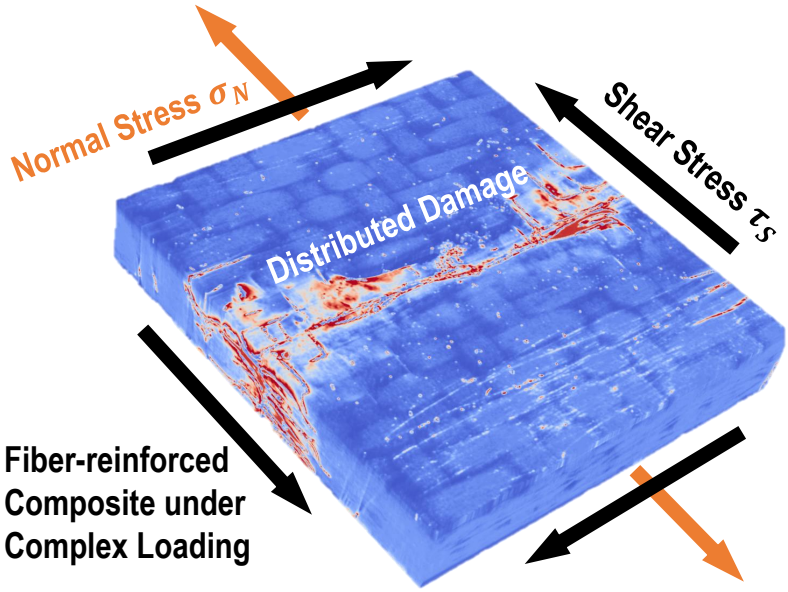

Figure 1.2: Fiber-reinforced composite under complex multi-axial stress state.

In the past decades, limited efforts were dedicated to the investigation on the mechanical

behavior and damage morphologies of fiber-reinforced composites under multi-axial cyclic loading [28–52] which was considered as one of the complex loading conditions and the existence of the real engineering scenario. In spite of plentiful experimental studies, it was still difficult to draw a solid conclusion due to the facts of different geometries, materials and incomplete loading conditions. This is also one of the reasons for the less contributions [53] to the development of excellent models for the complex loading conditions. The current results are still far away from the better understanding of fiber-reinforced composites under complex loading conditions. The possible solutions of these challenges must leverage tremendous efforts in providing the comprehensive experimental results for composite materials under various complex loading conditions (e.g. multi-axial loading, different stress ratios and frequencies in fatigue, low or high velocity impact, environment degradation, etc.) and analyzing these scenarios by leveraging multi-scale computational strategy through both continuum and discrete approaches.

1.3 Effects of modification through nanoparticles

Except for the foregoing challenges, tremendous efforts were also dedicated to the exploration of methods for improving the mechanical behavior of polymers. One of the promising candidates is the nanomodification through nanoparticles as shown in Figure 1.3 due to the remarkable physical properties of these materials [54]. This research direction has been attracting attention in the past decade which paved the way for their broad applications across many engineering fields. While a large bulk of data on the mechanical properties of polymer nanocomposites is available already, an aspect often overlooked in the community of nanocomposites is still the effects of aforementioned size scaling on the fracturing behavior of these materials. The importance of this aspect was extensively shown in other quasi-brittle materials (e.g. concrete, ceramics, bone, wood, sea ice, bio-inspired materials, etc.) [55–60] but not for the materials with the modification of nanoparticles. The consequence of neglecting this important factor can lead to significant errors for the characterization of mechanical behavior of nanoparticle-reinforced materials. Understanding the size scaling effects is the

key step for the development of these materials since this aspect can possibly solve the argument on the applicability of nanoparticles into advanced materials. This argument already existed in the research community of nanoparticle-reinforced materials for a decade and partially reduced the research interest toward this promising topic.

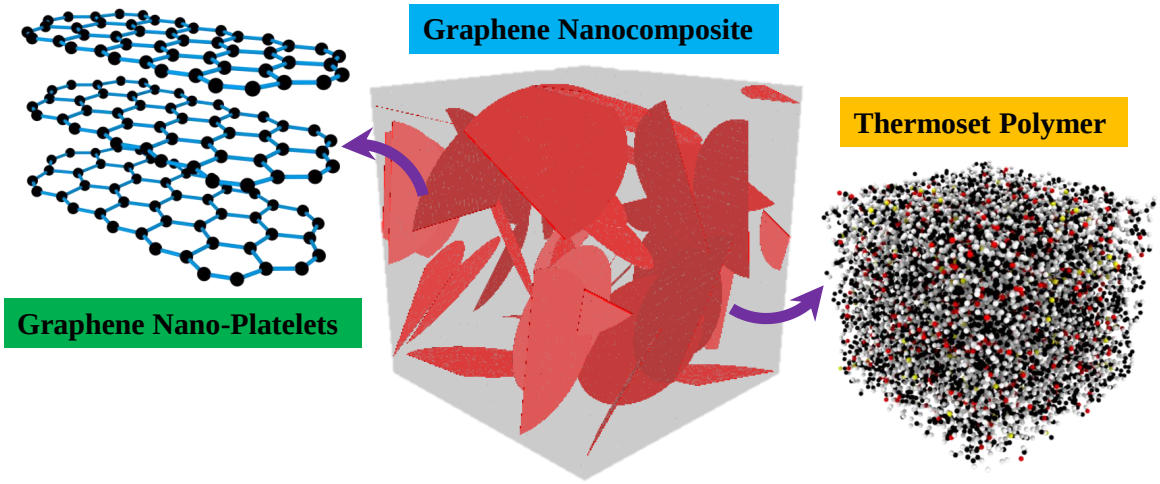

Figure 1.3: Polymer composites with the nano-modification of graphene platelets.

On the other hand, the failure behavior and size scaling of nanoparticle-reinforced materials under complex loading conditions (e.g. fatigue, impact, environment-related conditions, etc) were less investigated in the literature. This situation also leads to the less exploration on the associated morphological features and toughening mechanisms of these materials in the complex scenario despite the fact that enormous morphological studies were well documented in the literature for polymer nanocomposites under quasi-static loading condition. Understanding these aspects must leverage multi-scale strategy for computational models since the global fracturing behavior and the important size effects can be characterized through large-scale and homogenized models whereas the local morphological features and toughening mechanisms can be described through small-scale models with multiple phases.

Chapter 2

EFFECTS OF *IN-SITU* STRESS STATE ON THE MECHANICAL BEHAVIOR OF THERMOSET POLYMER

In this chapter, the effects of *in-situ* stress state on the plastic deformation, fracture, size scaling, and statistical behavior of thermoset polymer was comprehensively investigated by leveraging uni-axial tensile, three-point bending, Mode I, and Mode II mechanical tests. These cases were further computationally modeled by using the Drucker-Prager (DP) plasticity and Crack Band models. The successful characterization of the experimental results showed that the deformation of polymeric materials can exhibit either brittleness or ductility depending on the local stress state whereas the fracturing behavior of the materials can be better described with a bi-linear cohesive law instead of a conventional linear cohesive law.

2.1 Material preparation

The thermoset polymer used in this work was made of an EPIKOTE™ Resin MGS™ and an EPICURE™ Curing Agent MGS™ RIMH 137 combined in a 100:32 ratio by weight [61]. The manufacturing process started from manually mixing the epoxy and hardener for 10 minutes and followed by degassing the mixture for 20 minutes in a vacuum trap using a mobile vacuum system [62] in order to remove any air bubbles. The consistent geometry of the specimens was achieved by pouring the mixture into the silicone mould made of RTV silicone from TAP Plastics [63]. After the foregoing procedures, the specimens were cured at room temperature for approximately 48 hours and post-cured in an oven for additional 4 hours at 60°C. With the completion of the cross-linking process, the surface of the specimen was painted white and then speckled with black paint to allow for Digital Image Correlation (DIC) analysis. Thanks to DIC, no mechanical device was attached to the specimens during

the experimental tests by using a closed-loop and electro-actuated 5585H Instron machine.

2.2 Specimen preparation and testing methods

2.2.1 Uni-axial tensile and three-point bending tests

Dogbone specimens were used for uni-axial tensile tests and designed following ASTM D638-02a [64]. As illustrated in Figure 2.1a, the cross section of the specimen has a smooth transition in the area from the tab to the gauge section for the purpose of avoiding significant stress concentration leading to the failure close to the tab area. On the other hand, geometrically-scaled rectangular specimens were prepared for three-point bending tests as illustrated in Figure 2.1b to provide a significantly different loading condition compared to the foregoing case. It is worth mentioning here that the thickness of the rectangular specimen does not participate in the geometrical scaling.

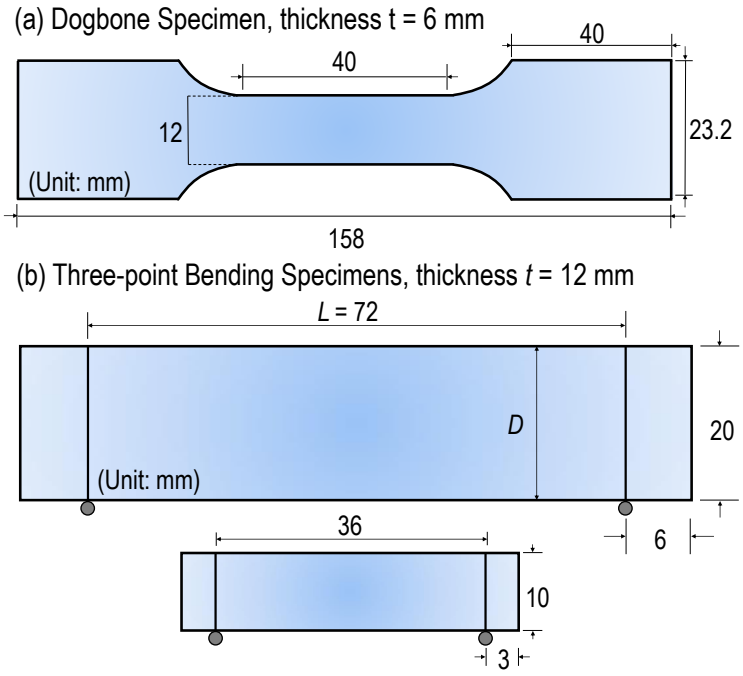

Figure 2.1: (a) Dogbone specimen for uni-axial tensile tests; (b) Geometrically-scaled rectangular specimens for three-point bending tests.

2.2.2 Mode I fracture test

In addition to the foregoing tests, geometrically-scaled Single Edge Notch Bending (SENB) specimens were designed based on ASTM D5045-99 [65] and used for Mode I fracture tests as illustrated in Figure 2.2a-b. The dimensions, scaled as 1:2:4, are 10×36mm, 20×72mm, and 40×144mm, respectively. The thickness of the specimen was not scaled and kept about 12 mm for all the investigated sizes. Both pre-cracked and pre-notched specimens were investigated in this study to clarify the effects of the notch type and provide different local stress states. The manufacturing of pre-notched specimens was proceeded by means of a 0.3mm wide diamond-coated saw leading to a 0.4mm wide notch whereas pre-cracked specimens were created following a two-stage procedure. The first step consisted in creating a notch about one quarter of the specimen width leveraging the foregoing saw and followed by using a sharp razor blade to tap the last portion of the crack. The length of the initial notch was about $0.5D$ where D is the width of the specimen but the length of the initial crack was scaled with the range approximately from $0.35D$ to $0.55D$ due to the difficulties in tapping the consistent crack length.

2.2.3 Mode II fracture test

To further explore the mechanical behavior of thermoset polymers at various stress states and length scales, mode II fracture tests were conducted on the geometrically-scales End Notch Flexure (ENF) specimens featuring both crack and notch as illustrated in Figure 2.2c-d. The manufacturing of the crack and notch followed the same procedures as described for the foregoing SENB specimens. The length of the initial crack was defined as the portion between two supports and scaled with the range approximately from $0.35L$ to $0.39L$ where L is the span between two supports. On the other hand, the length of the initial notch has the same definition with the crack and was kept about $0.36L$ for all the investigated sizes. The thickness of the specimen was also not scaled and the dimensions were kept the same as described in the previous section for Mode I fracture tests.

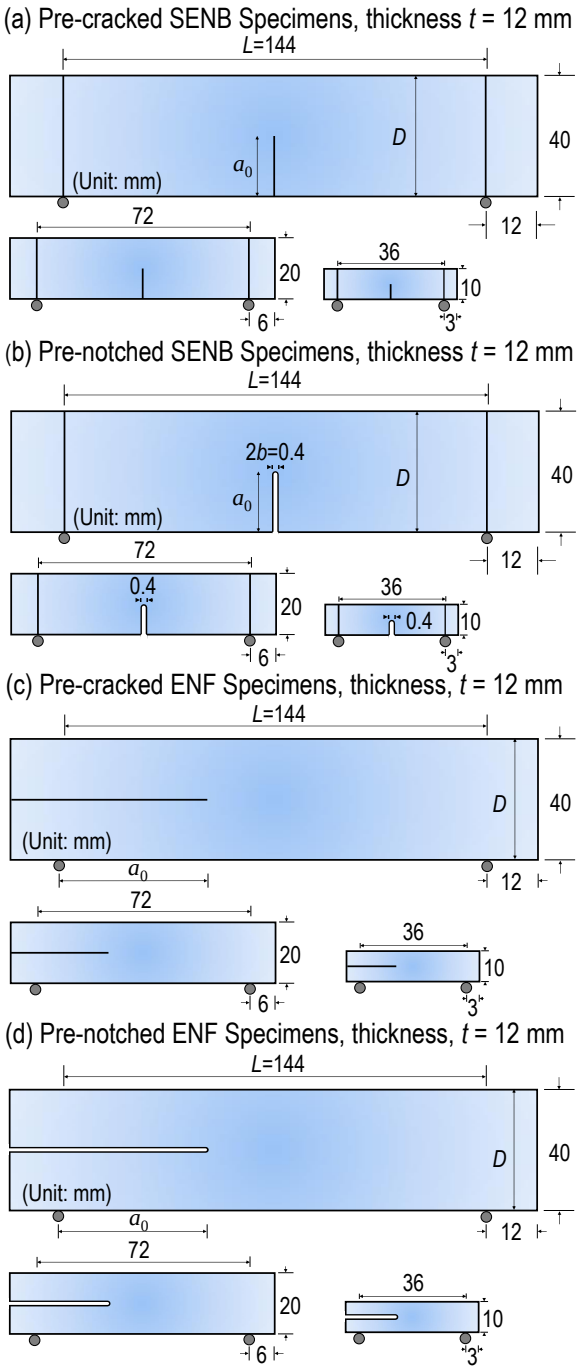

Figure 2.2: Geometrically-scaled specimens for Mode I and Mode II fracture tests: (a) SENB specimens featuring cracks; (b) SENB specimens featuring notches; (c) ENF specimens featuring cracks; (d) ENF specimens featuring notches.

2.3 Experimental results and analysis

2.3.1 Uni-axial tensile and bending behavior

The load-displacement curves obtained from uni-axial tensile tests are plotted in Figure 2.3a. As can be noted from the figure, these curves exhibit a significant non-linearity and start to deviate from the linear part after about 25% of the total quasi-static life. On the other hand, an even remarkable ductility in terms of load-displacement curves was observed from three-point bending specimens featuring different sizes as illustrated in Figure 2.3b. In this scenario, the load remains a pronounced plateau for about 40% of the entire quasi-static life after reaching the peak value.

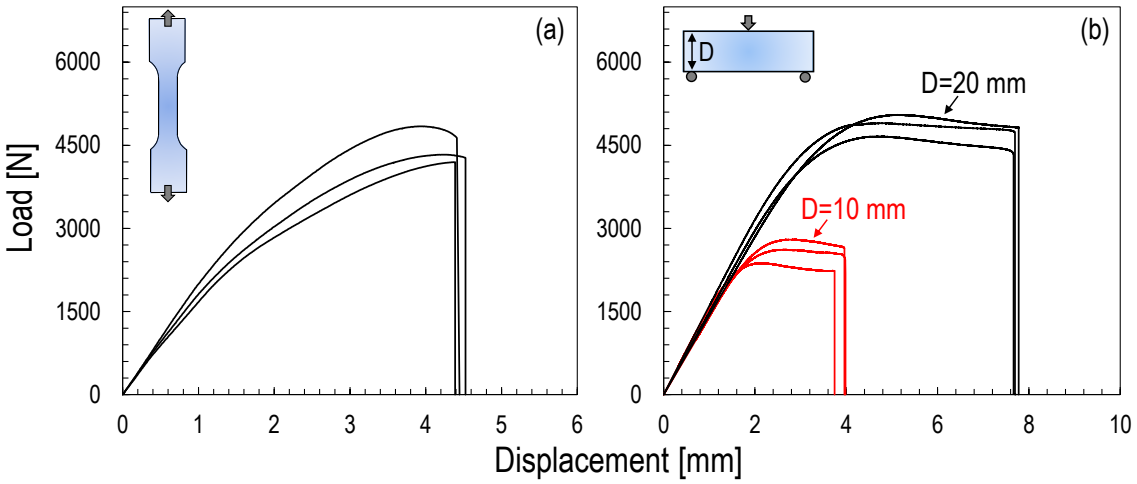

Figure 2.3: Experimental load-displacement curves obtained from (a) uni-axial tensile tests on dogbone specimens and (b) three-point bending tests on rectangular specimens with different sizes.

The foregoing ductility is mainly due to the significant plastic deformation occurring at the bottom of the specimen which differs from the uni-axial tensile case. This indicates that the evolution of the plasticity can be sensitively dependent on the global loading condition. It is worth mentioning here that the average Young's modulus E and uni-axial tensile strength σ_t obtained from dogbone specimens and the nominal tensile strength σ_{Nc} measured from

three-point bending specimens featuring different sizes are tabulated in Table 2.1. The nominal tensile strength is defined as $\sigma_{Nc} = 3P_cL/2tD^2$ where P_c is the critical load, t is the thickness of the specimen, L is the span between two supports and D is the width of the specimen.

Testing Configuration	Testing Number	Material Properties
Uni-axial tension	30	$\overline{E} = 2263$, $\overline{\sigma}_t = 60$ MPa
Three-point bending ($D = 10$ mm)	40	$\overline{\sigma}_{Nc} = 108$ MPa
Three-point bending ($D = 20$ mm)	40	$\overline{\sigma}_{Nc} = 103$ MPa

Table 2.1: Average mechanical properties of dogbone specimens and rectangular specimens featuring different sizes under uni-axial tensile and three-point bending tests respectively.

2.3.2 Statistical behavior and failure probability

The statistical behavior of uni-axial tensile and three-point bending tests was further analyzed and presented in this section. The probability distribution of the nominal strength is plotted in the Weibull scale and the failure probability was calculated based on the following method. The strength values are ranked in an ascending order $p = 1, 2, ..., n_s$ where p is the rank and n_s is the total number of testing specimens. By leveraging the midpoint position method [66], the strength cumulative density function (cdf) can be calculated as:

$$Prob\left(\sigma_{Nc} \leq \sigma_p\right) = \frac{p - 0.5}{n_s} \tag{2.1}$$

where the nominal strength of the dogbone specimen is defined as $\sigma_{Nc} = \sigma_t = P_c/tD$ whereas the one of the rectangular specimen has the same definition as described in the previous section 2.3.1. As illustrated in Figure 2.4, the failure probability of the forgoing specimen geometries follows the classical two-parameter Weibull distribution. The low Weibull modulus $m \approx 20$ leads to the uni-axial tensile strength of dogbone specimen in the range of 50 MPa to 70 MPa whereas the nominal strength of rectangular specimen is approximately

about 90 MPa to 117 MPa. More importantly, the nominal strength of rectangular specimen exhibits a size effect showing a higher average value for the smaller specimen and vice versa. Although the foregoing size effect is weak and only exhibits the difference in the magnitude of the nominal strength, the size effect can be significantly magnified at the micro-scale showing a different failure probability distribution which will be discussed in the next chapter.

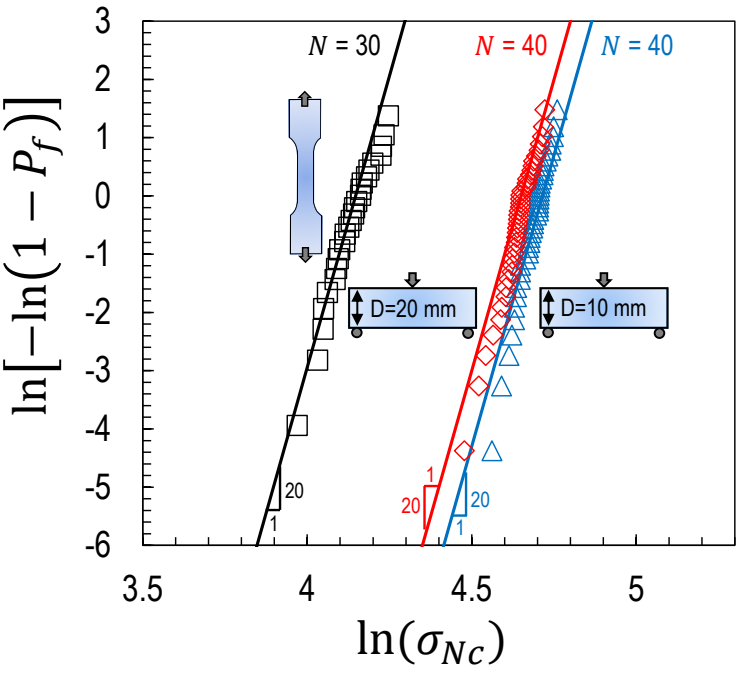

Figure 2.4: Probability distribution measured from dogbone and rectangular specimens. Note that N represents number of tests.

2.3.3 Mode I fracturing behavior

In contrast to the previous cases, the load-displacement curves for both pre-cracked and pre-notched SENB specimens are linear up to the peak load and followed by unstable crack propagation as illustrated in Figure 2.5a-b. The linear pre-peak response is an indication of pronounced brittle behavior for all the investigated sizes and notch types whereas the unstable crack propagation after reaching the peak load is due to the snap-back instability

which leads to the dynamic failure of the specimen. The foregoing brittleness is associated to the dramatically reduced plastic deformation occurring in front of notch or crack tip for the specimen under Mode I loading condition compared to the cases described in section 2.3.1. This interesting aspect further implies the importance of considering all the local stress components for the successful micro-scale modeling of sub-critical damage and their evolution in polymer matrix composites since the stress state at the micro scale varies with the evolution of the sub-critical damage and affects the failure behavior of the polymer.

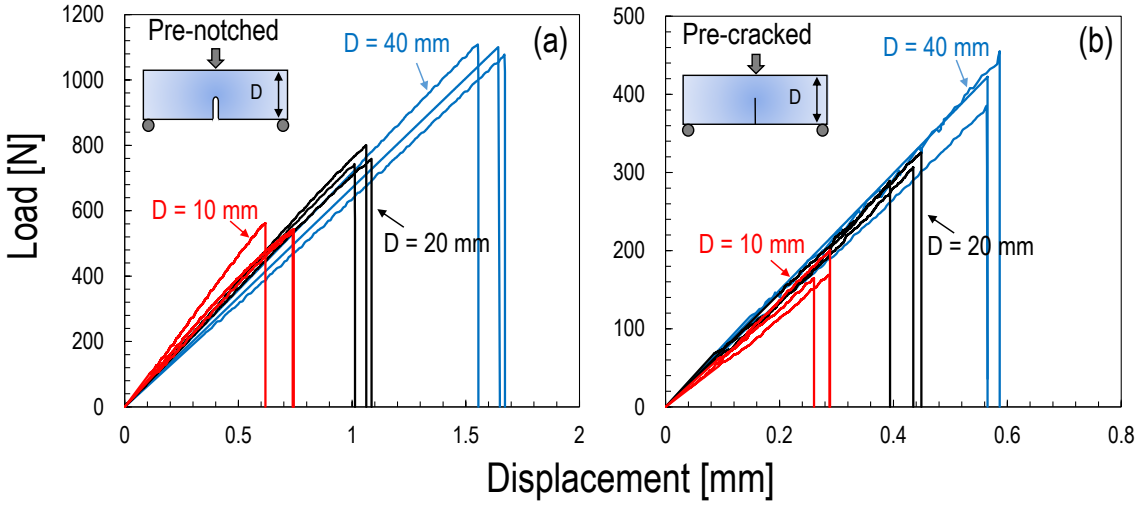

Figure 2.5: Experimental load-displacement curves obtained from Mode I fracture tests on geometrically-scaled pre-cracked and pre-notched SENB specimens.

On the other hand, it is clearly shown in Figure 2.5 that the notch type has a remarkable effect on the failure behavior of the polymer under Mode I loading condition. The critical load of pre-notched specimens is significantly distinct from the one of pre-cracked specimens with the difference reaching up to 300% for all the investigated sizes. This difference can further inherently lead to a completely mismatch in the calculation of Mode I fracture energy for pre-cracked and pre-notched specimens. To shed more light on this aspect, the Linear Elastic Fracture Mechanics (LEFM) was adopted for the foregoing calculation by using the

following expression:

$$G_f(\alpha_0) = \frac{\sigma_{Nc}^2 D}{E^*} g(\alpha_0) \tag{2.2}$$

where $\alpha_0 = a_0/D$ = normalized initial crack length, $E^* = E$ for plane stress and $E^* = E/(1-\nu^2)$ for plane strain, ν is the Poisson's ratio, σ_{Nc} has the same definition as described in section 2.3.1, and $g(\alpha_0)$ = dimensionless energy release rate. The function $g(\alpha)$ was obtained through the Finite Element Analyses (FEA) in ABAQUS Implicit 2017. 8-node biquadratic plain strain quadrilateral elements (CPS8) were adopted while the quarter element technique [67] was used at the crack tip to provide accurate results. The smallest element size at the tip was about $a_0 \cdot 10^{-5}$ leading to roughly 11000 elements for the whole model. A linear elastic isotropic constitutive model was used for the simulations and the J-integral approach [68] was adopted to estimate the energy release rate in the presence of a concentrated load centered on the top of the SENB specimen. Once the J-integral was calculated from ABAQUS, the value of $g(\alpha)$ with respect to the crack length can be obtained through the polynomial fitting in the following expression:

$$g(\alpha) = 1155.4\alpha^5 - 1896.7\alpha^4 + 1238.2\alpha^3 - 383.04\alpha^2 + 58.55\alpha - 3.0796 \tag{2.3}$$

As can be noted from Figure 2.6, the calculated Mode I fracture energies are not affected by the specimen size but the notch type. This consistence in the fracture energy regardless of the investigated specimen sizes indicates that not only the plastic deformation in the Plastic Zone (PZ) but also the non-linear damage in the Fracture Fracture Zone (FPZ) has a negligible effect on the structural behavior in this case. Thanks to this, the estimation through the LEFM can provide a first approximation and the average Mode I fracture energy estimated from pre-cracked specimens is about 0.8 N/mm. However, the higher apparent fracture energy obtained from pre-notched specimens is not the real Mode I fracture energy which can be roughly 10 times higher than the one from pre-cracked specimens. This interesting phenomenon will be explained in the next chapter which is related to the exploration of the micro-scale mechanical behavior of the polymer.

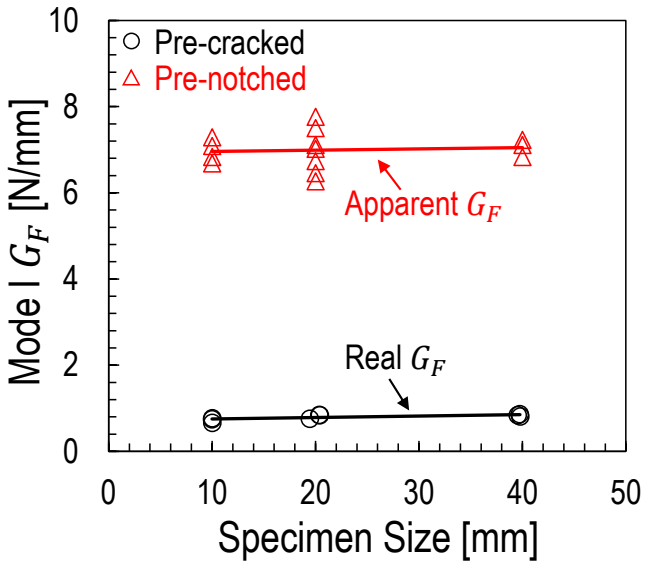

Figure 2.6: Mode I Fracture energy estimated from Linear Elastic Fracture Mechanics (LEFM) for geometrically-scaled pre-cracked and pre-notched SENB specimens. Note that only the value obtained from pre-cracked case is the real fracture energy whereas the one for pre-notched case is apparent fracture energy.

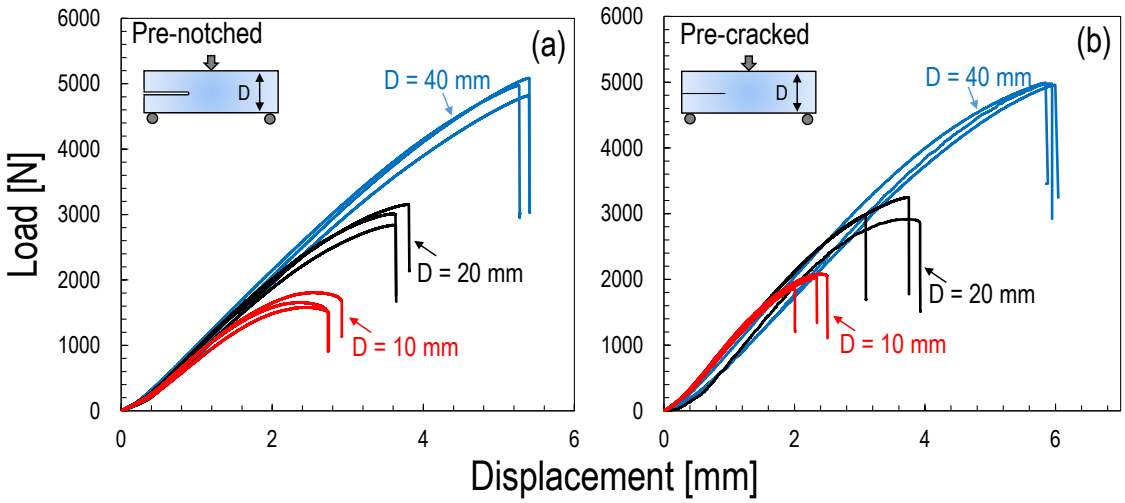

Figure 2.7: Experimental load-displacement curves obtained from Mode II fracture tests on geometrically-scaled pre-cracked and pre-notched ENF specimens.

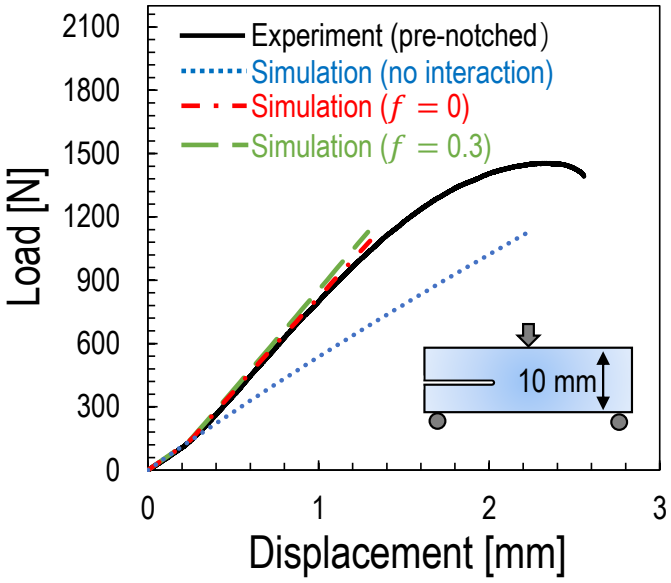

Figure 2.8: Comparison between experimental results and linear elastic simulations for the load-displacement curve of pre-notched ENF specimen featuring 10 mm in width. Note that the foregoing simulations were conducted with and without the interaction between upper and lower arms of the specimen and f in the legend represents the friction coefficient.

2.3.4 Global Mode II fracturing behavior

In contrast to the Mode I case, the notch type has negligible effects on the mechanical behavior of the material under Mode II loading condition. As can be noted from Figure 2.7a-b, both pre-cracked and pre-notched specimens exhibit similar load-displacement curves for all the investigated sizes. In comparison with the previous case for Mode I loading scenario, smaller specimens exhibit significant non-linearity before reaching the peak load whereas less pronounced non-linear behavior characterizes the largest specimen investigated in this work. This is mainly due to the significant plastic deformation occurring at the notch tip and the bottom of the smaller specimens as it will be shown in the following section leveraging the analyses of the Digital Imaging Correlation (DIC) and Transmission Optical Microscopy (TOM). The noticeable plasticity in the former location leads to the fact that the crack is blunted thus behaving equivalent to the notch. This mechanism does not happen in the

previous Mode I loading condition due to the different local stress state thus further showing the importance of the stress state on the failure behavior of the polymer.

On the other hand, the slopes of the load-displacement curves for all the investigated specimens exhibit a noticeable increase at the early stage of the quasi-static loading as illustrated in Figure 2.7a-b. This can be explained due to the contact between upper and lower arms of the specimen instead of the effects of the friction as can be noted from Figure 2.8. In this figure, the friction has a negligible effect on the material stiffness based on the linear elastic simulation whereas the interaction is the key to capture the mechanical behavior of the material at the early stage. It is worth mentioning here that all the specimens are characterized by a catastrophic failure after peak load due to the snap-back instability similar to the mode I fracturing behavior as previously described in section 2.3.3.

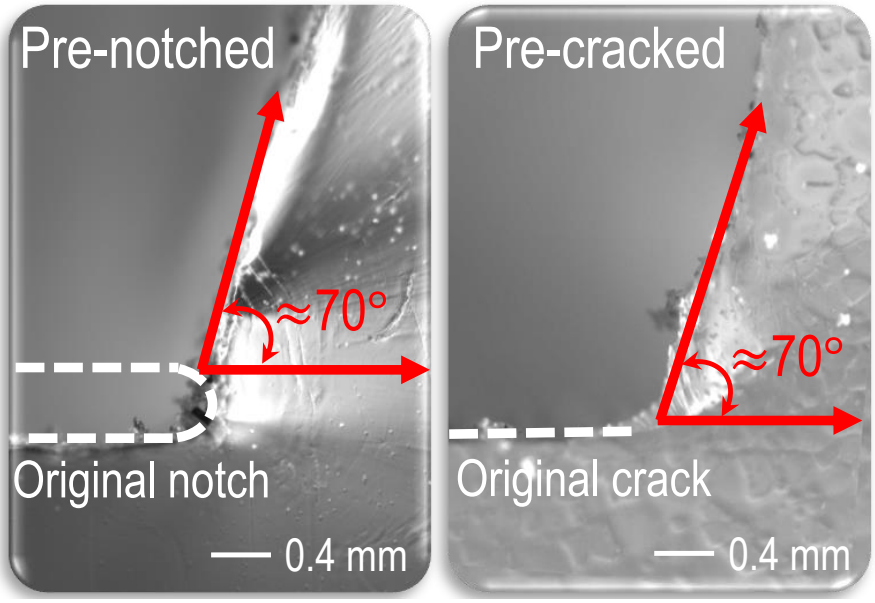

Figure 2.9: Fracture surfaces for pre-cracked and pre-notched ENF specimens under global Mode II loading condition. Both cases fractured around 70° respect to the direction of initial crack or notch.

2.3.4.1 Morphological characteristics

Regarding to the fracturing morphology of the material under Mode II loading condition, both pre-notched and pre-cracked specimens fracture at an angle of roughly 70° with respect to the direction of the initial notch or crack as illustrated in Figure 2.9. This implies that, in the scenario of global mode II loading condition, thermoset polymers only fracture locally under mode I loading condition since maximum principle stress happens at the foregoing angle for the material under Mode II loading condition. This is utmost of importance for the micro-scale modeling of the sub-critical damage in polymer matrix composites since only Mode I fracture criterion needs to be included instead of mixed-mode fracture criterion.

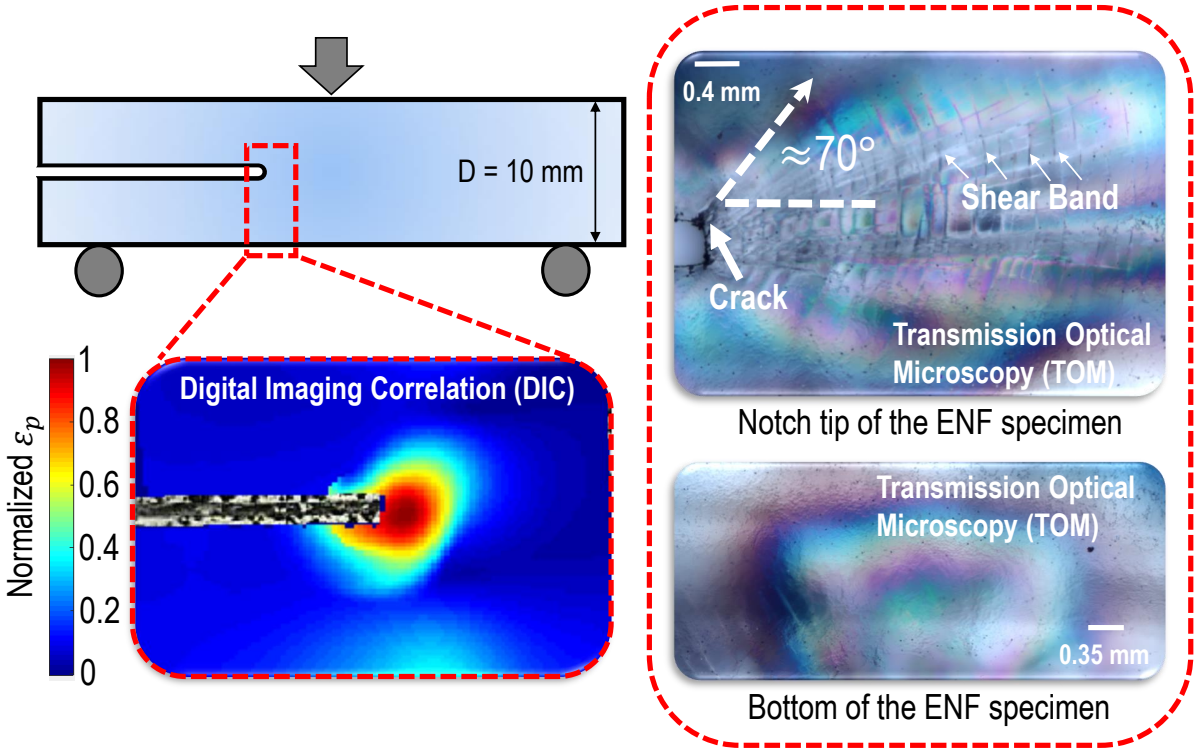

Figure 2.10: Digital Imaging Correlation (DIC) and Transmission Optical Microscopy (TOM) analyses on the pre-notched ENF specimen at roughly 95% of the critical quasi-static load. Note that ε_p means the maximum principle strain obtained from DIC.

In addition to this, Transmission Optical Microscopy (TOM) was used to visualize the local morphology of the ENF specimen under Mode II loading condition. As illustrated in Figure 2.10 for the case that the load level approaches about 95% of the critical quasi-static load, a remarkable plastic zone in the order of at least few millimeters was observed at the notch tip and bottom of the smallest pre-notched specimen investigated in this work. This observation is consistent with the DIC results showing the large deformation at the corresponding locations. It is interesting to notice that the foregoing plastic zone is mainly formed by the significant shear bands as shown in Figure 2.10 which are the most important features needed to be captured through the computational modeling as it will be shown in the next section.

2.3.4.2 Calculation of apparent local Mode I fracture energy

The foregoing non-negligible plastic deformation strongly overestimates the calculation of the real local Mode I fracture energy based on the Linear Elastic Fracture Mechanics (LEFM). As can be noted from Figure 2.11, the local Mode I fracture energy for all the investigated ENF specimens is significantly higher than the one previously calculated from pre-cracked SENB specimens. In addition to this, the local Mode I fracture energy is severely affected by the specimen size showing the evolution of the plastic deformation with increasing the specimen size. It is worth mentioning here that the foregoing fracture energy was calculated by using Eq.(2.2) and the value of $g(\alpha)$ was obtained through the same method as discussed in the previous section 2.3.3.

In this scenario, the size scaling on the Mode II failure behavior of the polymer cannot be predicted either from Quasi-Brittle or Elastic-Plastic Fracture Mechanics without considering the growing plastic zone corresponding to the specimen size. This leads to the requirement of a computational modeling to understand the foregoing behavior of the polymer with various sizes which will be described in the next section. On the other hand, it is worth mentioning here that the foregoing local Mode I or global Mode II fracture energy can also be close to the one obtained from pre-cracked SENB specimens depending on the brittleness of the

polymer which was reported by several authors in the literature [69–73].

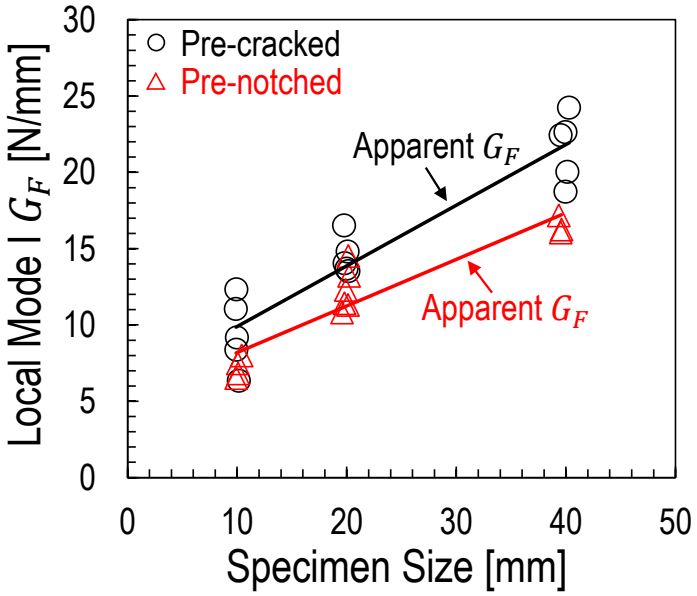

Figure 2.11: Local Mode I fracture energy estimated from LEFM for pre-cracked and pre-notched ENF specimens with different sizes. Note that all the values obtained from ENF specimen are not real but apparent fracture energies.

2.4 Computational modeling of thermoset polymer

2.4.1 Computational description

To have a further understanding of the sensitive plastic and fracture behavior of thermoset polymer due to the size scaling and stress state, a computational analysis within the framework of Drucker-Prager (DP) plasticity was conducted for all the investigated specimens. The choice of the Drucker-Prager model is due to the fact that the hydrostatic stress plays a pivotal role in the failure behavior of polymer matrix composites [19–21] which is not considered in other plasticity models (e.g. Von-Mises, Hill, etc). In addition to this, the validation of the Drucker-Prager model for describing the mechanical behavior of all the investigated cases can lead to a further decision if a brand-new model for polymeric materials needs to

be developed or not. According to the Drucker-Prager plasticity, the yielding criterion can be written in the following expression and illustrated in Figure 2.12 :

$$t - p \times tan(\beta) - d = 0 \tag{2.4}$$

where β is the friction angle and $d = [1/k + tan(\beta)/3]\,\sigma_t$ is the cohesion for uni-axial tensile case corresponding to the slope and intersection of the yielding surface in $t - p$ coordinate respectively, $p = -(\sigma_1 + \sigma_2 + \sigma_3)/3$ is the equivalent pressure stress and $t = 0.5q\,[1 + 1/k - (1 - 1/k)(r/q)^3]$ is related to equivalent Von-Mises stress. In these parameters, $k = \sigma_{tri,t}/\sigma_{tri,c}$ is the flow stress ratio of yielding stress in tri-axial tension to the one in tri-axial compression, $q = [(\sigma_1 - \sigma_2)^2 + (\sigma_2 - \sigma_3)^2 + (\sigma_3 - \sigma_1)^2]^{0.5}$ is the equivalent Von-Mises stress, and r is the third invariant of deviatoric stress.

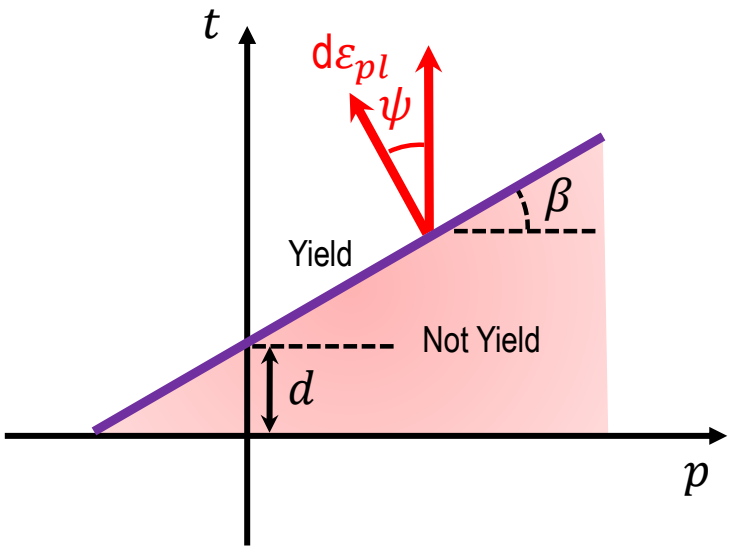

Figure 2.12: Schematic illustration for the Drucker-Prager model in $t - p$ plane.

In addition to the yielding criterion, plastic flow potential G is defined in the following:

$$G = t - p \times tan\psi \tag{2.5}$$

where ψ is the dilation angle which describes the direction of the plastic strain increment with respect to the t axis in $t - p$ plane. In the case of $\psi \neq \beta$, the plastic flow of the

material is recognized as non-associated flow which turned out to be the case of investigated thermoset polymer as it will be presented in the following sections. It is worth mentioning here that, while the foregoing Drucker-Prager plasticity was used for the characterization of pre-peak behavior of thermoset polymer, the critical strain corresponding to the damage initiation is not included in the Drucker-Prager model. Considering the significant differences in plasticity as experimentally shown for the foregoing investigated cases, it is not surprising that an unique value of the critical strain is impossibly able to capture all the loading scenarios and this aspect was computationally confirmed in the next section.

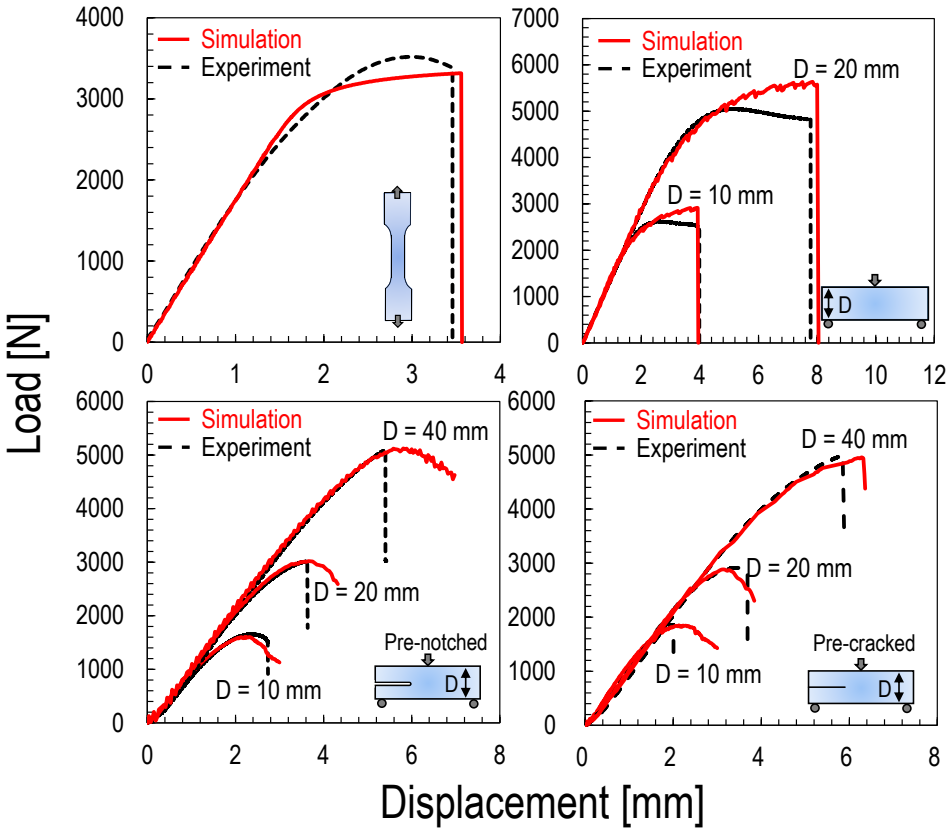

Figure 2.13: Simulation results vs. experimental data for all the different geometries, specimen sizes, and loading conditions. This figure does not include the specimen under Mode I loading condition and rectangular specimen with engineered holes under three-point bending condition. Note that different critical strains were used in the simulations for these cases to trigger the damage evolution.

2.4.2 Computational results

2.4.2.1 Plastic behavior of thermoset polymer

By leveraging the foregoing model, an excellent agreement with the experimental load-displacement curves was achieved for all the different geometries, specimen sizes, and loading conditions as illustrated in Figure 2.13. This figure does not include the successful characterization of the specimen under Mode I loading condition which will be discussed in the next section and chapter. In addition to this, the morphological characteristics in the simulation were also consistent with the experimental observation as shown in Figure 2.14 by taking the most representative example for pre-notched specimen under mode II loading condition. In this figure, a huge plastic zone was generated at the notch tip with remarkable shear bands due to the deviatoric stresses. It is worth mentioning here that the simulation for the Mode II case also predicted the fracturing angle about 70° with respect to the direction of the initial notch thus further confirming the local mode I fracture for the specimen under global Mode II loading condition.

Testing Configurations	Uni-axial Tensile Strength	Critical Cumulative Plastic Strain	Other Properties
Dogbone	55 MPa	0.04	$\beta = 40°$ $\psi = 20°$ $k = 1.0$ $G_F = 0.8$ N/mm
3PB	60.7 MPa	0.24	
3PB (holes)	64.7 MPa	0.8	
ENF (notch)	64.3 MPa	0.7	
ENF (crack)	64.3 MPa	0.7	
SENB (notch)	220 to 300 MPa	0.01 to 0.1	
SENB (crack)*	55 to 300 MPa	0 to 0.01	

Table 2.2: Material parameters used in the simulations with Drucker-Prager plasticity for all the investigated cases. Same parameters were used for geometrically scaled specimens. Note that the detailed material parameters used for the simulations of pre-cracked and pre-notched SENB specimens can be referred to Figure 3.12.

These successful results can only be obtained through the simulations with the same material parameters in the DP plasticity as summarized in Table 2.2 but different critical

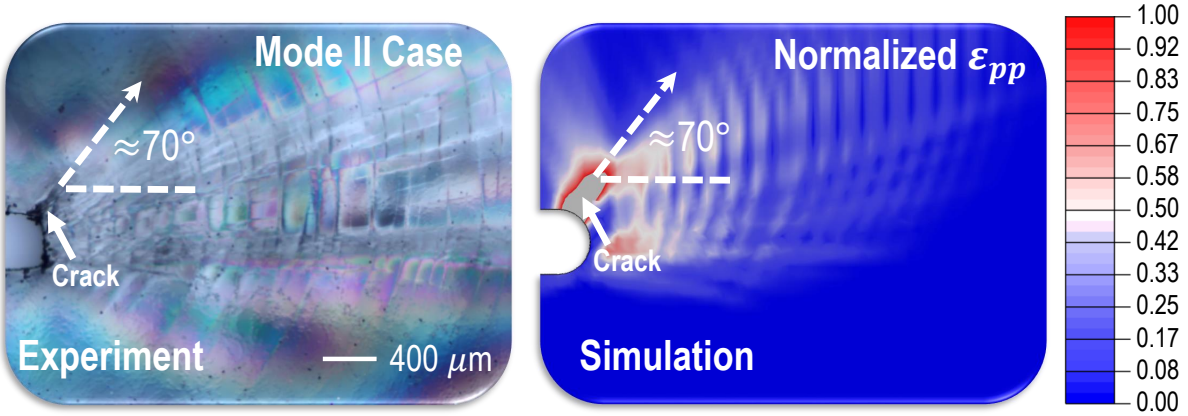

Figure 2.14: Experimental morphology vs. simulation result for Mode II case. Note that the experimental images were obtained through the Transmission Optical Microscopy (TOM) under polarized light and ε_{pp} denotes the maximum principle plastic strain.

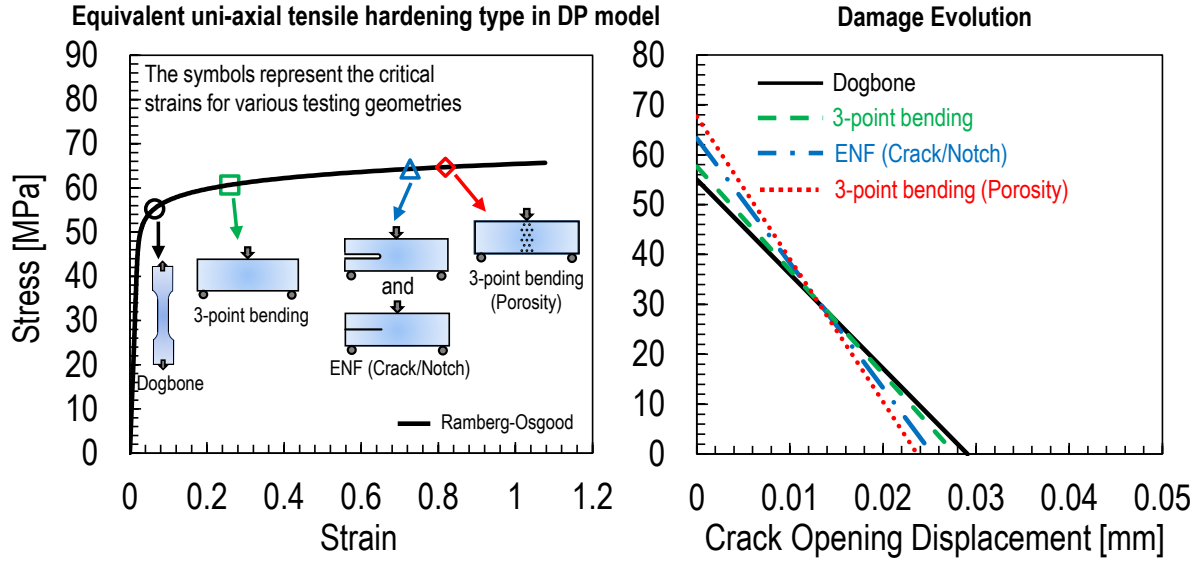

Figure 2.15: Equivalent uni-axial tensile hardening behavior and damage evolution used in the simulations for all the investigated cases excluding Mode I scenario. Note that the simulation results for these cases were less affected by the damage evolution part thus the use of a bi-linear softening law with the same fracture energy as it will be presented in the next section leading to the similar results.

equivalent plastic strains in the equivalent uni-axial tensile hardening type as plotted in Figure 2.15. In this figure, the cumulative (equivalent) plastic strain is defined as $\int_0^t \sqrt{\frac{2}{3}\dot{\boldsymbol{\varepsilon}}^{pl} : \dot{\boldsymbol{\varepsilon}}^{pl}}dt$ where $\dot{\boldsymbol{\varepsilon}}^{pl}$ is the plastic strain increment tensor. It is interesting to notice from the foregoing figure that the stress-strain behavior actually follows the classical Ramberg-Osgood relation as written in the following expression:

$$\varepsilon/\varepsilon_0 = \sigma/\sigma_0 + \gamma\,(\sigma/\sigma_0)^n \tag{2.6}$$

where $\sigma_0 = 40$ MPa is the yielding stress, $\varepsilon_0 = \sigma_0/E$ is the elastic strain, and $\gamma = 0.005$ and $n = 19$ are the material constants describing the calibrated hardening curve as plotted in Figure 2.15. It is worth mentioning here that the calibrated mechanical behavior includes the results for rectangular specimen with engineered holes under three-point bending condition which will be discussed in chapter 4 whereas the case for the specimen under Mode I loading condition is not included here but it will be presented in the next section and chapter.

The remarkable difference in the critical strain to trigger the damage evolution is definitely not the statistical behavior. In fact, this is attributed to the variety of the local stress states affecting the mechanical behavior of the foregoing testing configurations. By taking the most representative example of pre-notched ENF specimen under Mode II loading condition, the material at the notch tip experiences significant deviatoric stresses thus activating the ductility of the material with the critical strain for damage initiation about 0.7. However, this is not the case for dogbone specimen showing the critical strain being one order of magnitude lower than the aforementioned case since the material is mainly subjected to the uni-axial normal stress parallel to the global loading direction with negligible shear stresses. This interesting phenomenon is similar to the experimental and computational studies in the literature showing the significant effects of the deviatoric stresses on the ductile behavior of thermoset polymers [74, 75]. On the other hand, the brittle behavior of the material can be awoken depending on the level of hydrostatic stresses. In the case for pre-cracked SENB specimen under Mode I loading condition, the material at the crack tip experiences highly tri-axial stress state without shear stresses acting on it. As a consequence, the material at

the crack tip exhibits pronounced brittle behavior compared to other investigated cases. This aspect was also extensively reported in the literature showing the brittleness of the material due to the constraint of tri-axial stress components [19–21].

The foregoing description clearly shows the fact that deviatoric and hydrostatic stresses are the major factors governing the mechanical behavior of thermoset polymers exhibiting either brittleness or ductility. However, to the best of author's knowledge, no unified model in the literature can automatically provide an accurate prediction on the critical strain for damage initiation due to the local stress state and the significant size effect as it will be discussed in the next chapter. This is considered as the future work aiming to propose a physical-based model accounting for all the foregoing aspects.

2.4.2.2 Bi-linear cohesive behavior of thermoset polymer

On the other hand, the simulation results with the hardening behavior as shown in Figure 2.13 were less affected by using different fracture energies indicating the fact that, while the pre-peak behavior of the polymer can be characterized through the foregoing tests, the features of the cohesive behavior must be uniquely determined by leveraging the Mode I fracture tests. To this end, the characteristics of the cohesive behavior for pre-cracked and geometrically-scaled SENB specimens made of thermoset polymer were studied. Both linear and bi-linear cohesive laws with the same fracture energy are used to match the load-displacement curves obtained from experimental fracture tests. As illustrated in Figure 2.16, a linear cohesive law can be described through two parameters: (a) tensile strength, f_t and (b) fracture energy, G_f, which represents the area under the linear cohesive law. On the other hand, a bi-linear cohesive law requires four parameters: (a) tensile strength f_t, (b) initial fracture energy, G_f, which represents the area under the initial segment of the bi-linear cohesive law; (c) total fracture energy, G_F, which is the total area under the bi-linear cohesive law; (d) change-of-slope stress, σ_k, which is the value of stress at the intersection of the initial and tail segments. It is worth mentioning here that, for the bi-linear cohesive law, different intersection points were investigated in order to match the experimental load-displacement curves.

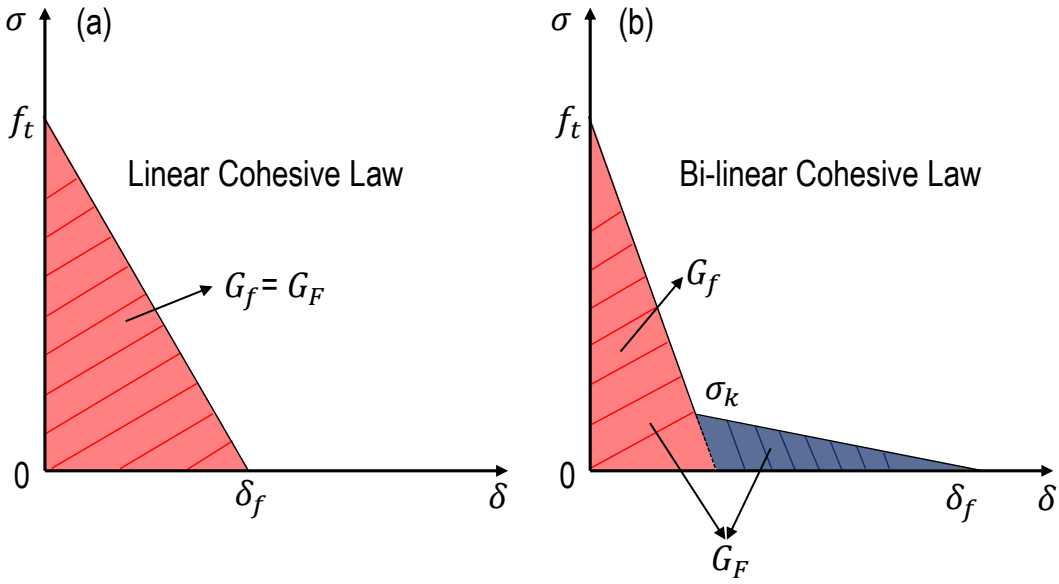

Figure 2.16: Cohesive laws used in this study: (a) Linear Cohesive Law (LCL); (b) Bi-linear Cohesive Law (BCL).

Figure 2.17 shows a comparison between the experimental load-displacement curves and simulation through a Cohesive Zone Model (CZM) featuring a linear and bi-linear cohesive law respectively. It can be noted that, while the bi-linear cohesive law successfully matches experimental curves of specimens with different sizes, this is not the case for the linear cohesive law, with a significant overestimation of the experimental curves. This result suggests that a bi-linear cohesive law may be better suited for the description of the cohesive fracture behavior of thermoset polymer, although a linear cohesive law may still provide reasonable results and can be used for a preliminary, course, approximation. A comparison between the calibrated linear and bi-linear cohesive laws for pre-cracked SENB specimens made of thermoset polymer is shown in Figures 2.17.

However, notwithstanding the excellent agreement with the data on pre-cracked specimens, it is impossible to match the experimental results on the pre-notched specimens by means of the foregoing cohesive law. A relatively good agreement cannot be even achieved

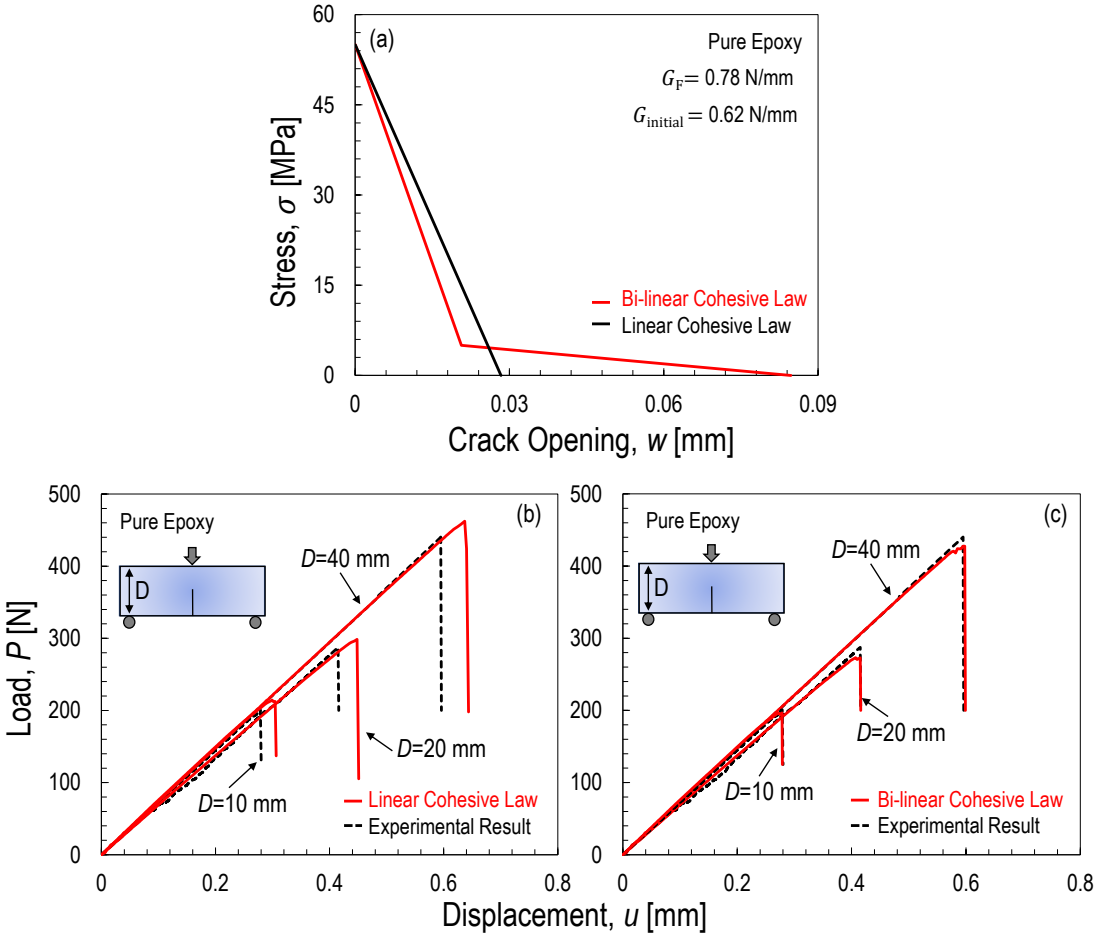

Figure 2.17: (a) Calibrated bi-linear cohesive law vs. linear cohesive law with the same total fracture energy. (b,c) Load-displacement curves vs. cohesive zone model featuring a linear or bi-linear cohesive Law for different specimen sizes.

with the consideration of the plastic pre-peak behavior which will be shown in the next chapter. One of the possibilities for a decent agreement can be made by increasing the total fracture energy to $G_F = 7.2$ N/mm, the value corresponding to the energy estimated by LEFM. However, this value would lead to a significant over-prediction of the structural strength of the pre-cracked specimens. Considering that the cohesive law should be a material property, the discrepancy between the results for pre-cracked and pre-notched specimens must be explained using the same cohesive law. A possible solution is presented in the next

chapter related to the exploration of the micro-scale behavior of the polymer.

2.5 Conclusions

1. The investigated thermoset polymer exhibits pronounced brittle behavior in Mode I fracture tests and relatively less plasticity for uni-axial tension whereas a remarkable ductility characterizes the material under three-point bending and Mode II loading conditions;

2. The foregoing phenomenon is related to the variety of local stress states in the investigated specimens and can be explained due to the fact that the deviatoric stresses can activate the ductile behavior of the material whereas the brittleness of the material can be awoken leveraging a high level of hydrostatic stresses (e.g. the material at the crack tip under Mode I loading condition);

3. The global load-displacement curves and local morphological features for all the different geometries, specimen sizes, and loading conditions can only be computationally characterized by leveraging the Drucker-Prager plasticity model with the same flow stress ratio $k = 1.0$, dilation angle $\psi = 20^\circ$ and friction angle $\beta = 40^\circ$ but completely different critical strain in the equivalent uni-axial tensile hardening type for damage initiation due to various local stress states;

4. The foregoing calibrated equivalent uni-axial hardening type in the DP plasticity model can be described by the classical Ramberg-Osgood stress-strain relationship with the yielding stress σ_0 about 40 MPa and material constants $\gamma = 0.005$ and $n = 19$;

5. The inequality for the calibrated dilation and friction angles indicates that the local plastic behavior of the investigated thermoset polymer can be better described by a non-associated plastic flow rule which was consistent with the extensive studies for thermoset polymers in the literature;

6. The meaningless and higher local Mode I apparent fracture energy of ENF specimens

in Mode II scenario is due to the significant plastic deformation occurring at crack or notch tip. The blunted crack or notch tip for the ENF specimen in global Mode II scenario eventually leads to the catastrophic failure happening at an angle of roughly 70° with respect to the initial crack or notch direction. This angle indicates the fact that the polymer locally fractures in Mode I scenario under global Mode II loading condition which simplifies the failure criteria for the micro-scale modeling of polymer matrix composites under complex multi-axial stress states;

7. The foregoing successful simulations for all the investigated cases excluding Mode I scenario were less sensitive to the damage evolution part (i.e. the shape and area of the softening law) thus strongly suggesting the fact that the accurate features of the softening law can only be determined through Mode I fracture tests instead of other investigated cases only for a better description of pre-peak behavior;

8. By conducting a cohesive zone modeling for the pre-cracked specimens with all the sizes under Mode I loading condition, it is concluded that, in general, a bi-linear cohesive law provides a very accurate description of fracture tests with errors on the structural strength less than 7%. A reasonable agreement is also found leveraging a linear cohesive law, with errors on structural strength no larger than 30%.

Chapter 3

MICRO-SCALE STRENGTH AND COHESIVE BEHAVIOR OF THERMOSET POLYMER

In this chapter, an interesting study for investigating the effects of size scaling on the fracturing behavior of the same thermoset polymer was presented and discussed in the following sections. By leveraging the comprehensive experimental and computational analyses on both pre-cracked and pre-notched SENB specimens with various sizes, it was concluded that the material strength and the fracture energy of the investigated thermoset polymer at the micro-scale can be remarkably different from the conventional behavior usually measured from the macro-scale laboratory tests. In fact, the material strength of the investigated thermoset polymer at the micro-scale can be four to six times higher than the macro-scale value whereas the fracture energy at the micro-scale can be as least forty times lower. This was further computationally confirmed through the excellent match with the experimental results obtained from the micro-scale fracture tests.

3.1 Past and current work on the micro-scale behavior

Over the past decade, it was shown that materials exhibit higher strength as structure size decreases due to the energetic-statistical size effect of the materials [76–80]. Although this phenomenon was discovered in many engineering materials (e.g. concrete, ceramics, sandstone, metal, etc.), it was rarely studied for the thermoset polymer which is the key component of polymer matrix composites. To the best of author's knowledge, a direct *in-situ* measurement of the micro-scale polymer strength and fracture energy has rarely been accomplished and reported in the open literature. This is mainly due to the evident challenges deriving from the micro- or nano-scale experimental tests.

However, some researchers attempted to estimate the material strength through various methods. In 2007, Hobbiebrunken *et al.* [17] proposed an experimental approach for the investigation of the micro-scale strength in epoxy polymers. With the inherent assumption that the source of size effect on the strength is mainly statistical-energetic (Type I), they manufactured epoxy fibers featuring diameters from 22 to 50 micron and various gauge volumes and then tested them under uni-axial tension. Their results showed a significant size effect, the tensile strength reaching 166 MPa for a gauge volume of $1.5\text{x}10^{-3}$ mm^3 compared to a strength of 92 MPa estimated from tensile tests on traditional dogbone specimens (gauge volume about 66 mm^3). Although the gauge volume for the micro-scale tests was still not small enough, the authors concluded from the reported size effect that the inherent strength of epoxy at the micro-scale can be close to its theoretical value, estimated as 275 MPa in their work. Although the thermoset system investigated in Hobbiebrunken *et al.* [17] is not the same as the one characterized in this work, it clearly showed the scaling effects on the material strength of thermoset polymers.

Another indirect approach was proposed in 2016 by Zike *et al.* [81] who investigated the strain deformation close to the tip of a blunt notch in Double Cantilever Beam (DCB) specimens made of epoxy. The 2 mm-deep specimens had a length of approximately 70 mm, a width of 10 mm and featured a 0.7 mm wide notch. The specimens were speckled for Digital Image Correlation (DIC) and tested in an Environmental Scanning Electron Microscope (ESEM). Leveraging the strain field measured from DIC and the load captured by the load-cell, the authors were able to estimate the non-linear stress-strain response of the polymer by estimating the J-integral from DIC for different sub-critical load levels. They concluded that the strength of the polymer they investigated must be within 220 to 300 MPa. Although it can be argued that the specimens were not micro-metric, it should be noted that the estimate of the constitutive behavior was conducted using *in-situ* strains. This work also implied the possibility of a significantly higher strength of thermoset polymers at the micro-scale.

In a recent publication [82], Di Luzio and Cusatis investigated the Mode I fracturing behavior of quasi-brittle materials featuring blunt notches and characterized by materials

exhibiting a linear cohesive law. In their numerical study, they found that when the notch tip radius is approximately equal to the Irwin's characteristic length $l_{ch} = E^* G_f / f_t^2$ the failure occurs when the maximum stress at the notch approximately reaches the material strength, i.e. $\sigma_{Nc} = f_t / k$ with k = stress concentration factor. On the other hand, for sufficiently sharp notches, the fracture is driven by the formation of a Fracture Process Zone (FPZ) in front of the notch which ultimately propagates and leads to the final failure.

Based on the foregoing considerations, the micro-scale strength of thermoset polymer can be indirectly explored by leveraging the Mode I fracture tests on the SENB specimens in presence of blunt notches which will be presented in the following sections. It is worth mentioning here that this method can only be used to investigate the micro-scale strength corresponding to a specific micro-scale size but this size must be determined through a comprehensive study on the statistical behavior of pre-notched specimens with various notch sizes which will be partially discussed later.

3.2 Experimental results and analysis

The manufacturing of the thermoset polymer in this work followed the same procedure as presented in the previous chapter. Geometrically scaled pre-notched specimens of four different sizes were prepared and the dimensions, scaled as $1 : 2 : 4 : 8$, were 10×36 mm, 20×72 mm, 40×144 mm and 80×288 mm as similarly illustrated in Figure 2.2. It is worth mentioning that the width of the notch was kept the same for all the investigated sizes. Accordingly, the ratio between the depth and the radius of the notch, a_0/b, was 25, 50, 100, and 200 respectively. The notch length was always half of the width of the specimen and a magnification of the notch tip by means of Scanning Electron Microscopy (SEM) was shown in Figure 3.1.

As can be noted from Figure 2.5 in the previous chapter, the stiffness of the specimens is not affected by the sharpness of the notch which is not surprising given the significantly large aspect ratios. In contrast, the peak load of pre-notched specimens is approximately 3 times higher that the one of pre-cracked specimens as shown in the previous chapter for

all the investigated sizes. This difference agrees with the previous investigations [83–87] which will be discussed later. The crack or notch length, peak load, and nominal strength $\sigma_{Nc} = 3P_cL/2tD^2$ for all the geometrically scaled, pre-notched specimens tested in this work are tabulated in Table 3.1.

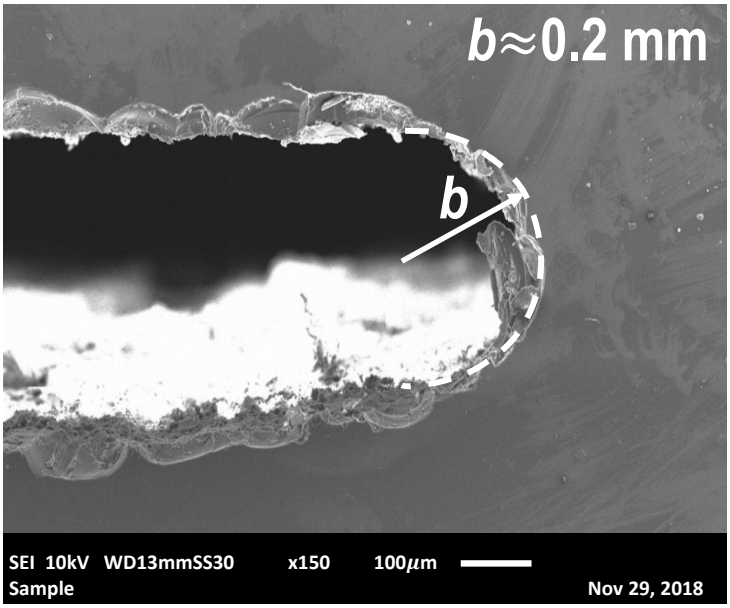

Figure 3.1: Notch tip geometry from Scanning Electron Microscopy (SEM).

On the other hand, several investigations [88–93] showed that, when the notch radius is sufficiently smaller than the Irwin's characteristic length, the notch has the same effects on the ultimate failure load as a crack of the same length. In this study, the notch radius b = 0.2 mm is significantly smaller than the Irwin's characteristic length $l_{ch} = E^*G_F/f_t^2 \approx$ 0.75 mm. In this context, pre-notched specimens were analyzed by means of LEFM which provided a very accurate description of the fracturing scaling in epoxy for previous pre-cracked specimens. As can be noted from Figure 2.6 in the previous chapter regarding to the calculation of the Mode I fracture energy for different specimen sizes and notch types, the results showed a very significant effect of the notch type, the fracture energy of pre-notched specimens being approximately 10 times higher than the one of pre-cracked specimens. This

result, abundantly confirmed in the literature [83–87], cannot be explained by LEFM since, according to this theory, the notched specimens investigated in this work should fail at the same load as the cracked ones and the fracture energy should be a material property not affected by any geometrical feature.

Specimen type	Specimen width (mm)	Crack or notch length (mm)	Max load (N)	Nominal strength (MPa)
Pre-notched	D=10	5.00	647.01	28.12
Pre-notched	D=10	5.00	543.07	23.60
Pre-notched	D=10	5.00	613.01	26.65
Pre-notched	D=10	5.00	654.10	28.40
Pre-notched	D=10	5.00	561.12	24.39
Pre-notched	D=10	5.00	537.22	23.34
Pre-notched	D=10	5.00	553.40	24.03
Pre-notched	D=10	5.00	630.18	27.38
Pre-notched	D=20	10.00	800.66	17.49
Pre-notched	D=20	10.00	758.70	16.57
Pre-notched	D=20	10.00	742.83	16.22
Pre-notched	D=20	10.00	779.50	17.02
Pre-notched	D=20	10.00	693.15	15.14
Pre-notched	D=20	10.00	731.95	15.99
Pre-notched	D=20	10.00	814.50	17.79
Pre-notched	D=20	10.00	774.82	16.92
Pre-notched	D=40	20.00	1100.05	12.04
Pre-notched	D=40	20.00	1077.89	11.80
Pre-notched	D=40	20.00	1108.72	12.14
Pre-notched	D=80	40.00	1580.11	8.66
Pre-notched	D=80	40.00	1542.20	8.45
Pre-notched	D=80	40.00	1653.11	9.06
Pre-notched	D=80	40.00	1532.03	8.40
Pre-notched	D=80	40.00	1455.30	7.97
Pre-notched	D=80	40.00	1755.01	9.62

Table 3.1: Max load and nominal strength of pre-notched specimens at different sizes.

It was proposed that residual plastic stresses induced by the manufacturing of the notch may lead to very high values of apparent fracture toughness of the polymer. However, a direct validation of this statement was never provided. The following section focuses on this particular aspect and shows that these hypothetical residual stresses should not be the solution since it must be unrealistically high to justify the difference in the fracture energy reported in the present work and in the literature.

3.3 Disproof of hypothetical residual stresses

To check the possibility that the higher apparent fracture energy of pre-notched specimens is related to the presence of residual stresses as generally accepted in the literature, a simple analysis can be conducted within the framework of the Linear Elastic Fracture Mechanics (LEFM). Taking advantage the superposition principle, the total mode I Stress Intensity Factor (SIF) can be calculated summing the effects of the applied load P and the residual stress distribution ahead of the crack tip:

$$K_{I(1)} + K_{I(2)} = K_{I,total} \tag{3.1}$$

where, as illustrated in Figure 3.2, $K_{I(1)}$ refers to the SIF associated to the concentrated load on the middle top of the specimen without the effect of residual stresses while $K_{I(2)}$ refers only to compressive stresses acting on the equivalent Fracture Process Zone of length c_f [88, 94–103],. The length c_f is proportional to the Irwin's characteristic length l_{ch} and it is defined as an additional equivalent crack length required to capture the nonlinear effects of the FPZ.

The stress intensity factor $K_{I(1)}$ can be expressed as $\sqrt{E^*G}$ for a plane strain condition whereas $K_{I(2)}$ has the following expression [104]:

$$K_{I(2)} = -\int_{a_0}^{a_0+c_f} \frac{2\sigma_\theta(x)}{\sqrt{\pi a_0}} \frac{f(\frac{x}{a_0}, \frac{a_0}{D})}{(1-\frac{a_0}{D})^{3/2}[1-(\frac{x}{a_0})^2]^{1/2}} \mathrm{d}x \tag{3.2}$$

where $\sigma_\theta(x)$ is the magnitude of the compressive stresses applied on the equivalent FPZ, $f(\frac{x}{a_0}, \frac{a_0}{D}) = g_1(\frac{a_0}{D}) + \frac{x}{a_0} g_2(\frac{a_0}{D}) - (\frac{x}{a_0})^2 g_3 \frac{a_0}{D} + (\frac{x}{a_0})^3 g_4(\frac{a_0}{D})$ is a dimensionless geometry function,

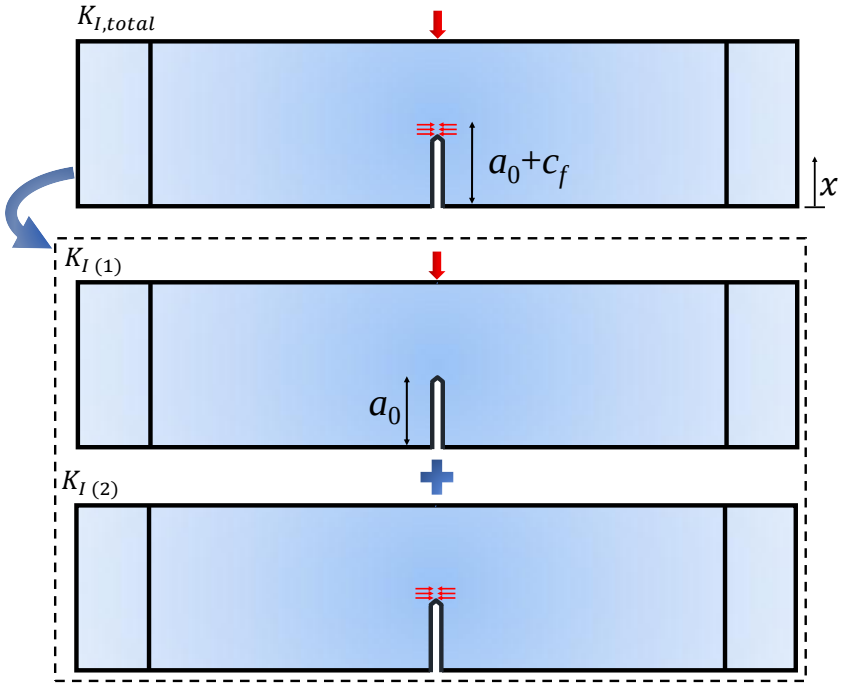

Figure 3.2: Schematic description of the boundary conditions used for the estimation of the residual stresses by the superposition principle.

and x is the distance from the bottom surface of the SENB specimen as shown in Figure 3.2. The value of the constants g_i with $i = 1...4$ can be found in [104]. At incipient crack onset, the stress intensity factor $K_{I,total}$ is ought to be equal to the fracture toughness of the pre-cracked specimens measured from the experiments. Accordingly, with the assumption that $a_0/D \approx 0.5$, $c_f \approx 0.5 l_{ch} \approx 0.4$ mm [88, 100], and the residual stresses are uniformly distributed, the magnitude can be estimated. As illustrated in Figure 3.3, the residual stress for the pre-notched specimens investigated in this work is higher than 100 MPa which seems unrealistically high to be created by sawing during the pre-notching process. It is worth mentioning that Eq.(3.2) is obtained by superimposing the Stress Intensity Factors (SIFs) induced by a uniform distribution of infinitesimal forces, $dP = \sigma_\theta dx$, acting on the equivalent crack faces, $x \in [a_0, a_0 + c_f]$.

The choice of the equivalent crack length cf $\approx 0.5\ l_{ch}$ is based on the assumption that,

in first approximation, the traction-separation law can be considered as a linear function. As it was discussed in the previous chapter, this hypothesis was validated by the previous size effect tests on cracked Single Edge Notch Bending Specimens (SENB) made of the same thermoset polymer investigated in this work to provide a course approximation of the fracturing behavior. Once it is agreed that the cohesive law can be approximated by a linear function, a parametric study on the relation between the Irwin's characteristic length and the effective FPZ size is not necessary. In fact, it should be noted that the effective FPZ size (c_f) is always equal to 0.44 l_{ch} provided that the cohesive law is linear, regardless of the mechanical properties of the material or the geometry of the specimen. This was proven via an extensive computational study by Cusatis and Schauffert [88].

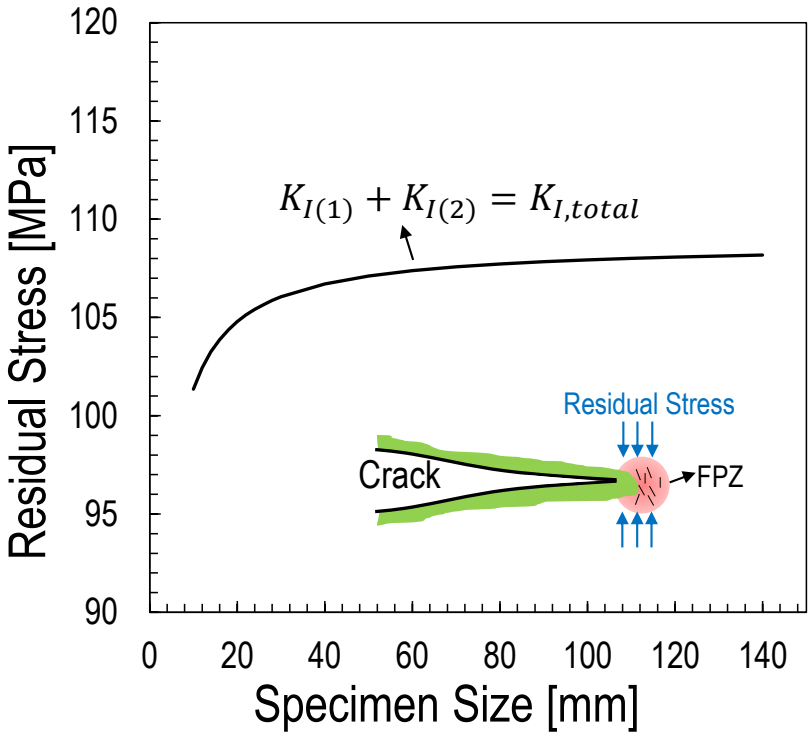

Figure 3.3: The residual stress estimated from equivalent linear elastic fracture mechanics as shown in Eq.(3.1).

In the foregoing analysis, the Fracture Process Zone (FPZ) at the notch tip was assumed

to be fully developed and the residual stresses were considered to act on the effective crack length. Although it is very unlikely that due to the sawing process the FPZ propagates sub-critically to form a longer crack, an additional computational study was conducted to investigate the effects of the size of the FPZ on the magnitude of the residual stresses required to match the experiments. For the analysis, a finite element model of the SENB specimen of width $D = 20$ mm was constructed. The mesh was created using 4-node iso-parametric quadrilateral elements for a total number of degrees of freedom of 35452. Thanks to the fine mesh, more than 100 elements were located along the FPZ. The crack was simulated via the cohesive interaction algorithm available in ABAQUS/Implicit with a linear traction-separation law featuring a strength of 55 MPa and a fracture energy of 0.8 N/mm. These values were obtained from previous tests on cracked specimens. An uniform pressure representing the residual stresses was applied on the left and right faces with cohesive interaction, from the initial crack tip to a distance l from the tip. A schematic of the geometry of the problem and related boundary conditions is provided in Figure 3.4. For every length l, the residual stresses were adjusted so that the peak load applied to the specimen matched the experimental value from the tests. This way, a more thorough analysis of the effects of the residual stresses on the development of the cohesive zone ahead of the notch was possible. Figure 3.4 shows the evolution of the residual stresses as a function of the extent of the plastic stress region normalized by the Irwin's characteristic length l_{ch}. As can be noted, the relation is highly nonlinear, the residual stresses increasing significantly with decreasing values of l. It is remarkable that, for a plastic stress region close to 0.4 l_{ch}, the residual stresses required to match the experiments are in the order of 500 MPa. On the other hand, for plastic regions exceeding a length of 0.5 l_{ch} the stresses decrease at a very low rate, reaching about 90 MPa for a plastic region as large as the Irwin's characteristic length. For the residual stresses to be within a realistic range, the plastic zone size should be more than 30% larger than Irwin's characteristic length. This is considered by the authors as a very unlikely event.

To shed more light on the possible effects of residual stresses on the fracturing behavior, additional tests on pre-notched specimens were conducted. However, this time, a sharp razor

blade was pre-inserted into the specimens during the manufacturing process and eventually removed after the curing of the epoxy resin to create the notch. Thanks to this procedure, notch tip radii similar to the ones of the sawed specimens were obtained without the possible emergence of plastic residual stresses. Figure 3.5 compares the load displacement curves for specimens with pre-cracks made by tapping, with pre-notches made by sawing, and with pre-notches made by pre-inserting a razor blade. As can be noted, all the notched specimens exhibit a significantly larger peak load compared to cracked specimens. More importantly, the mechanical behavior of specimens with notches made by pre-inserting a razor blade is basically identical to the one reported for the case of sawed notches. Considering that the former cannot feature any residual stress, it is concluded that plastic residual stresses are not likely the dominant reason of the higher apparent fracture energy of pre-notched specimens.

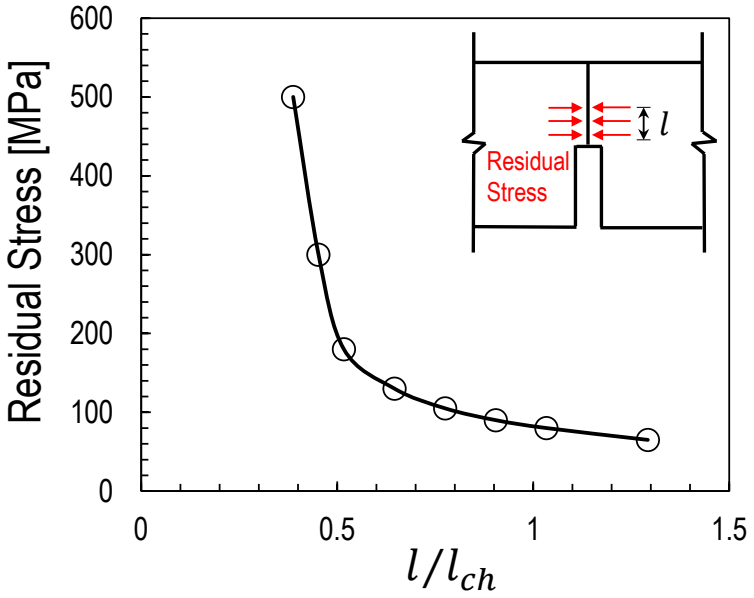

Figure 3.4: The evolution of residual stresses with the extent of the plastic region, l, through cohesive zone modeling ($D = 20$ mm).

To further prove this statement, we took advantage of the transparency of epoxy and investigated the region close to the notch tip via Transmission Optical Microscopy (TOM)

with cross-polarized light. In this technology, cross-polarized light is transmitted through the specimen enabling the visualization of permanent deformation by the analysis of the fringe patterns. This is now an established approach to visualize crazing and plastic deformation at the crack tip in thermoset polymers (see, among others, [105–107]). Figures 3.6a-c summarize the results of the analysis for cracked and notched specimens. These Figures show three cases: (a) a pre-cracked specimen before applying any load, (b) a pre-notched specimen before applying any load, and (c) a pre-notched specimen after applying a load equal to 80% of the failure load and unloading. Micrographs taken using bright field and cross-polarized light are shown for comparison. As can be noted from Figure 3.6d, the pre-cracked specimens exhibited a damage zone prior the application of any mechanical load. This damage took the form of micro-crazing as the typical fringes in the insert show. A similar morphology was reported for other thermoset systems in [105–107].

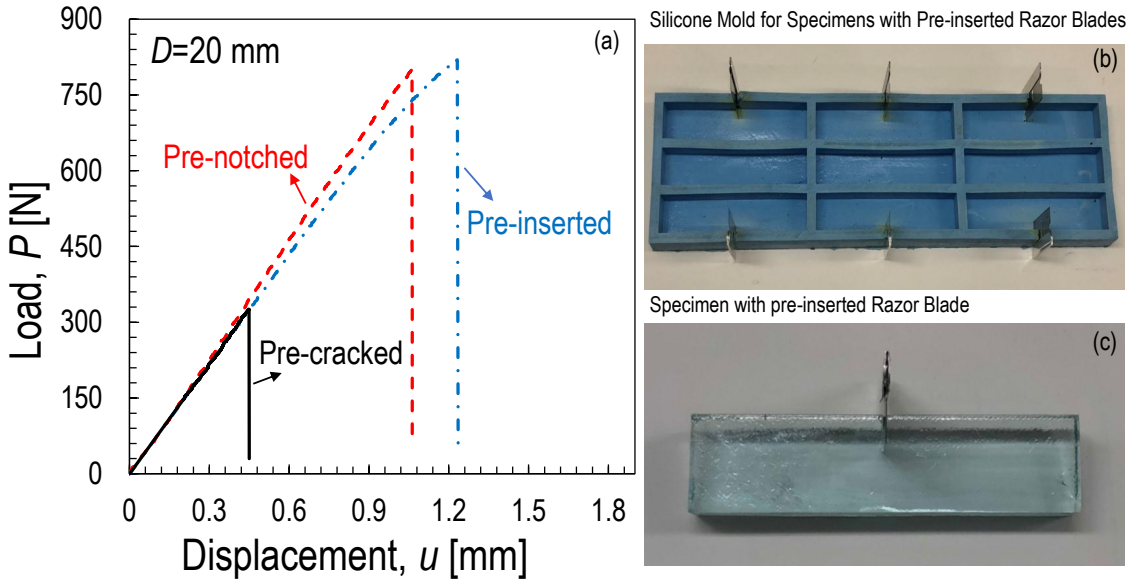

Figure 3.5: (a) Experimental load-displacement curves for pre-cracked and pre-notched specimens, and specimens with the notch made by a pre-inserted razor blade; (b) silicone molds for the manufacturing of the specimens with the pre-inserted razor blade; (c) typical specimens with the pre-inserted razor blade right after curing. Note that the blade was removed before the tests.

Not surprisingly, the micrographs on the pre-crack tip confirmed that tapping indeed leads to the formation of an FPZ before the application of any mechanical load. What was unexpected is that, as clearly shown in Figure 3.6e, the notch tip of the pre-notched specimens did not exhibit significant permanent deformations. To further corroborate this observation, the specimens were loaded up to 80% of the failure load and unloaded. Then, TOM pictures of the notch tip were taken for comparison. As can be noted from Figure 3.6f, in this case the stress concentration at the notch indeed led to plasticity as confirmed by the very visible fringes ahead of the tip. This provides further evidence that if a region of pre-existing plastic residual stresses exists, either it is significantly smaller than the notch width or the residual stresses are almost negligible. In this context, it is not surprising that the specimens featuring notches made by pre-inserting a razor blade exhibited the same failure loads as the one made by sawing. In both cases the plastic residual stresses were negligible. A possible explanation of the true cause is presented next leveraging cohesive fracture mechanics.

3.4 Two-scale cohesive behavior of thermoset polymer

In this section a two-scale cohesive zone model [108] is proposed to capture the fracturing behavior of both pre-cracked and pre-notched specimens seamlessly. The main observations that led to the development of the model are described next along with the comparison with the experimental data. Based on the foregoing considerations, a cohesive zone model should be able to capture the behavior of notched and cracked specimens seamlessly provided that some particular features are added to the cohesive law. In this work, it is assumed that the cohesive behavior can be described by a two-scale cohesive law as represented in Figure 3.7a. As shown in the figure, f_t^{μ} represents the initial strength whereas G_f^{μ} is the initial fracture energy or, in other words, the area under the first linear branch of the curve. The rest of the curve is identical to the cohesive law identified by fracture tests on geometrically-scaled SENB specimens as discussed in the previous chapter and is characterized by f_t = macroscopic strength, σ_k = stress at the third change of slope, G_f = initial macroscopic

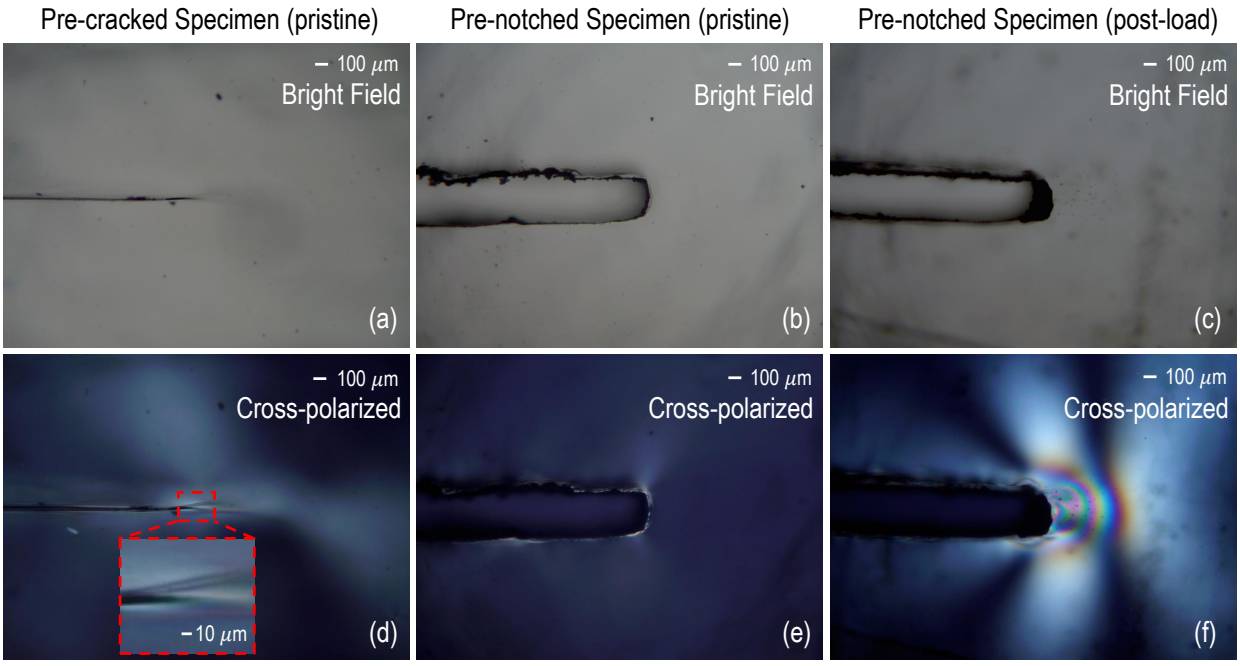

Figure 3.6: Transmission Optical Microscopy (TOM) micrographs of specimens under: (a-c) bright field and (d-f) cross-polarized light. Note that figures (a-e) are the specimens before applying any load whereas figures (c and f) are the specimens after applying a load equal to 80% of the failure load and unloading.

fracture energy (area AOBDE), and the total fracture energy G_F (area AOBCDE).

The proposed cohesive law must differ from the linear one investigated in [82] to capture the peculiar cohesive behavior of thermoset polymers. Until the crack opening displacements are in the sub-micron regime, the resulting cohesive stresses are equivalent to the ones predicted by a linear cohesive law of strength f_t^{μ} and total energy G_f^{μ}. For larger opening displacements, the cohesive law becomes equivalent to the bi-linear law that provided an excellent agreement with the experimental data on pre-cracked specimens. Since the first portion of the cohesive law describes the cohesive stresses at the microscale while the rest of the cohesive curve captures the behavior for larger displacements, the proposed cohesive law is characterized by two very distinct length scales. For this reason, in this and in future contributions the model will be referred to as a *two-scale cohesive model*.

In this work, it is assumed that for sub-micron crack opening displacements the cohesive strength f_t^μ is about 300 MPa and the cohesive stresses decrease linearly and very steeply with increasing crack openings. This captures the fact that, due to statistical size effect, the microscopic strength of the polymer can be several times higher than the one measured from macroscopic tests [17, 81, 109]. At the same time, the steep initial part of the cohesive curve, leading to an initial fracture energy of only about 2.5% of the total one, captures the lower energy dissipation occurring at the sub-micron scale.

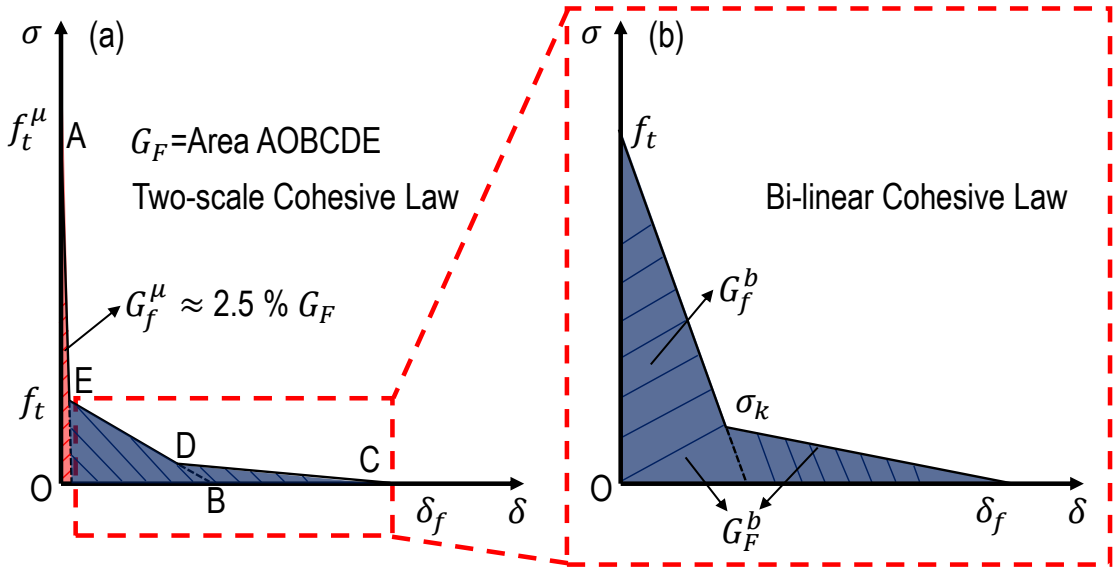

Figure 3.7: (a) Schematic of the two-scale cohesive law proposed in this study describing the cohesive stresses associated to micro to macro crack opening displacements; (b) Bi-linear portion describing the fracturing for large crack opening displacements.

The value of about 300 MPa is estimated from the failure loads of the pre-notched specimens. In fact, since the initial fracture energy G_f^μ is only a fraction of the total energy dissipated and the initial strength f_t^μ is significantly larger than in macroscopic tests, the Irwin's characteristic length $l_{ch}^\mu = E^* G_f^\mu / \left(f_t^\mu\right)^2$ related to the initial formation of the FPZ is significantly smaller than the width of the notches investigated in this work. Accordingly, following [82] the fracturing behavior of the notched specimens must depart from the one of

the cracked specimens and the nominal stress at failure is determined by the elastic limit condition $\sigma_{Nc} = f_t^{\mu}/k$. It is worth mentioning here that, thanks to the foregoing considerations, the initial strength can be determined very precisely. Small variations on the value proposed in this work would lead to significant changes on the predicted structural strength.

Having clarified the reason for the very high strength at the micro-scale, another question needs to be answered: why do the cohesive stresses of the initial portion of the cohesive curve decrease so steeply? The reason is that, if the initial slope of the cohesive curve were milder, it would not be possible to capture the size effect data on pre-cracked specimens. In the presence of a crack or a sufficiently sharp notch, the stress intensity at the tip at incipient failure would always lead to elastic stresses that are greater than the micro-scale strength. Accordingly, since the cohesive stresses decrease very quickly in the initial part of the cohesive curve, a cohesive FPZ can emerge and develop up to the second portion of the two-scale cohesive curve. The cohesive law becomes equivalent to the bi-linear law of strength f_t and total fracture energy G_F^b since the initial energy G_f^{μ} is only about 2.5% of G_F or, in other words, $G_F \approx G_F^b \approx 0.80$ N/mm. Thanks to the foregoing considerations it is possible to estimate the initial slope of the two-scale cohesive model very precisely by testing notched specimens of various notch tip radii and matching the experimental data by means of the two-scale cohesive model. Such a comprehensive experimental campaign is beyond the scope of the present work and will be the subject of future contributions. In this study, the initial fracture energy was calibrated against one notch tip radius only, leading to the initial fracture energy G_f^{μ} =0.02 N/mm.

Finally, one last question remains: why was not the foregoing cohesive behavior found before from tests on pre-cracked specimens? The answer lies in the particular shape of the cohesive curve. Since the initial fracture energy is only a negligible portion of the total fracture energy and, in laboratory-scale cracked specimens the cohesive stresses always overcome the initial portion of the cohesive law, it is not possible to characterize f_t^{μ} and G_f^{μ} unless micro-metric specimens are tested. In fact, any tests on large specimens would provide an estimate of G_F which takes approximately the same value as G_F^b. It is worth

mentioning here that micro-tests are very challenging and are generally affected by significant uncertainties. However, based on the results of this work, a valid alternative is to test both cracked and pre-notched specimens and use the results on the latter configuration to characterize f_t^{μ}.

To verify the foregoing assumptions, both pre-cracked and pre-notched specimens were simulated in ABAQUS/Explicit 2017. The models combined 4-node bi-linear plain strain quadrilateral elements (CPE4R) with a linear elastic isotropic behavior and 4-node two-dimensional cohesive elements (COH2D4) with the traction-separation law shown in Figure 3.8 to model the crack. To guarantee an accurate characterization of the cohesive behavior, 20 elements were assigned in the micro-scale FPZ leading to 600 elements for the total FPZ. The width of the cohesive band was 0.1 μm and the stable time increment was about 10^{-9} s. The parameters of the two-scale cohesive model that provided the best matching with the experimental data are given in Table 3.2.

Figure 3.8 shows a comparison between the experimental load-displacement curves and simulations by the two-scale cohesive model. As can be noted the model successfully matches the experimental curves of both the pre-notched and pre-cracked specimens of different sizes. The most remarkable aspect related to these results is that the excellent matching was possible leveraging the *same cohesive law* which can now be treated as a material property.

It is interesting to plot the structural strength σ_{Nc} as a function of the structure size D in double-logarithmic scale. As can be noted from Figure 3.9a, the computational model is in excellent agreement with the experimental data for all the sizes and types of notch. In case of cracked specimens the radius at the crack tip is extremely small, approximately zero. For sufficiently large specimens, the FPZ size is negligible compared to the structure size and, as predicted by LEFM, the structural strength scales with $D^{-1/2}$. For decreasing sizes, the fraction of the structure occupied by the nonlinear FPZ becomes larger and larger thus affecting the fracturing behavior. The structural strength departs from the values predicted by the LEFM which is a linear theory and, inherently, ignores the cohesive stresses in the FPZ. For sufficiently small geometrically-scaled structures the nominal strength tends to the

plastic limit.

For the cases shown in Figure 3.9a for pre-notched specimens, all the geometrical features of the structure are geometrically-scaled except for the thickness and notch tip radius, b. Accordingly, the aspect ratio of the notch a_0/b increases along with the structure size, D. As can be noted, for sufficiently large specimens with the investigated aspect ratios, the structural strength coincides with the elastic limit. For decreasing sizes with the same aspect ratios, the specimens tend to be similar to the cracked specimens and eventually converge to the performance of cracked specimens when the specimen size is sufficiently small. It is worth mentioning here that the elastic limit can also be obtained without using any cohesive models. As shown in Figure 3.9b, the smooth curve represents the elastic limit calculated numerically in ABAQUS/Implicit for various specimen sizes whereas the diamond symbols represent the elastic limit for all the investigated specimen sizes obtained from the experiments. The computational model featured 8-node bi-quadratic plane strain quadrilateral elements (CPS8) with a linear elastic isotropic behavior. The smallest mesh size at the notch tip was about 0.1 μm leading to 20 elements in the microscopic FPZ and 600 elements for the total FPZ. In the expression of elastic limit $\psi(b, D) = f_t^{\mu}/k(b, D)$, the stress concentration factor is a function of D since the notch tip radius is not geometrically scaled. As can be noted in Figure 3.9b, the function $\psi(b, D)$ agrees very well with the experimental data. This confirms that, for the notched specimens investigated in this work, all the failures happened by approximately reaching the elastic limit of the structure.

Cohesive Law	G_F (N/mm)	G_F^b (N/mm)	G_F^l (N/mm)	G_f (N/mm)	G_f^b (N/mm)	f_t (MPa)	f_t^{μ} (MPa)	σ_k (MPa)
Two-scale	0.8	/	/	0.645	/	55	300	5
Bi-linear	/	0.78	/	/	0.625	55	/	5
Linear	/	/	0.78	/	/	55	/	/

Table 3.2: Calibrated cohesive parameters for linear, bi-linear and two-scale cohesive laws.

On the other hand, it is also interesting to have a comparison between the simulations by the two-scale cohesive model and the generalized cohesive crack size effect curves proposed

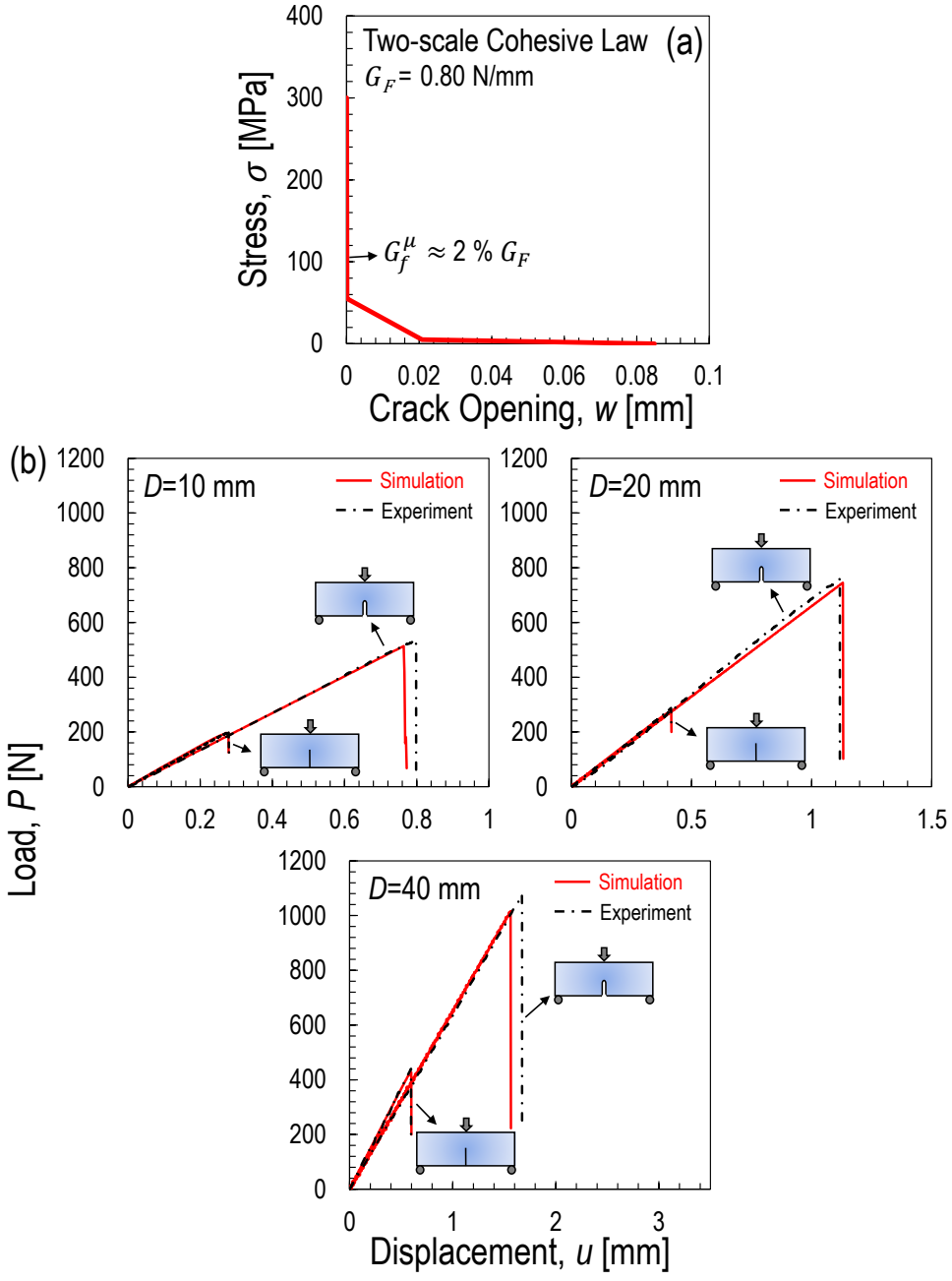

Figure 3.8: Cohesive zone modeling results: (a) calibrated cohesive law; (b) load-displacement curves vs. two-scale Cohesive Zone Model (CZM) simulations for both pre-cracked and pre-notched specimens of different sizes.

by [82]. As shown in Figure 3.9b, the generalized CCSECs are plotted by using the initial fracture energy for pre-notched specimens while both initial and total fracture energy are used for pre-cracked specimens. As can be noted, for the smallest aspect ratio investigated ($a_0/b = 25$), the simulation results exactly follow the generalized CCSEC. This indicates that, for decreasing the specimen size, the cohesive stress only develops into the first portion of the two-scale cohesive law since the generalized CCSEC is based on the assumption of a linear cohesive law and the initial fracture energy is used for these curves. However, for increasing the aspect ratio, the simulation results start to depart from the generalized CCSEC. This is not surprising since the cohesive stress in these cases develops into the remaining portion of the two-scale cohesive law. For the sufficiently large aspect ratio ($a_0/b = \infty$), the simulation results are located between the two asymptotes, the generalized CCSEC by using initial fracture energy and total fracture energy. These two asymptotes successfully capture the simulation results for sufficiently small and large specimens. This indicates that the cohesive stress completely develops for sufficiently large specimens thus the shape of the cohesive law does not affect the results. However, for decreasing the specimen size, the cohesive stress only partially develops thus the shape of the cohesive law plays an important role as shown in the figure.

Finally, it is interesting to compare the cohesive stresses at the condition of incipient failure for the case of the specimens weakened by cracks and notches of equal depth considered in this work. As shown in Figures 3.10a,b, the cohesive stresses in these two cases differ significantly, in accordance with the observations that motivated the proposed two-scale cohesive model. For notches, the FPZ is developed only partially, with the minimum cohesive stress being significantly larger than f_t. This means that, in agreement with the theory, only the initial part of the two-scale cohesive model governs the behavior of the notched structures investigated in this work. In contrast, in case of pre-cracked specimens, the FPZ is far more developed and the minimum cohesive stress at the tip is generally much lower than f_t. This means that the second part of the cohesive law is entered and the cohesive behavior is equivalent to a bi-linear cohesive law of total fracture energy $G_F^b \approx G_F$. All the foregoing

observations confirm firmly the validity of the two-scale cohesive model and the following information provides a significant insight on the main damage mechanisms associated with the two-scale cohesive model.

In a recent publication, Yang and Qu [110] used a course grained molecular dynamics model to investigate the tensile behavior of thermoset polymers. In contrast to other MD simulations, their approach enabled the analysis of one of the largest volumes ever simulated by MD (85 x 85 x 85 nm). Thanks to this, it was possible to capture phenomena such as void formation and coalescence which occur at a length scale that is typically one or two orders of magnitude larger than the length of a polymer chain. The result of the simulation is shown in Figures 3.11a-e which were re-adapted from [110] and show the typical deformation occurring during a tensile test. In the figures, the volumes colored in yellow represent regions of high-densely packed polymer chains. In grey are the volumes of low density featuring voids and particles with very low coordination numbers. According to [110] the material reaches its yield strength of 298 MPa at about 7% strain. As reported by [110], this happens by micro-crazing and stretching of the densely packed regions with cavity nucleation and coalescence in the remaining portion of the domain (note that a similar mechanism was observed experimentally in [105–107]). The opening displacement required to stretch and re-align the short polymer chains in the densely packed regions are low, in the order of several nanometers. After that, cavity nucleation and coalescence as shown in Figures 3.11b-e leads to a sudden drop of the tensile stress. As shown in Figures 3.11b-e, cavities grow both longitudinally and laterally. The scenario presented by the foregoing MD analysis is in perfect agreement with the two-scale cohesive law proposed in this study. In fact, the first steep decrease of the cohesive stresses in the proposed traction-separation law captures the sudden drop of the stress due to the cavity initiation and coalescence occurring at sub-micron opening displacements. The second branch of the cohesive curve captures the later stages of the fracturing process occurring at significantly lower stresses by re-alignment of the polymer chains in the less densely packed regions. This happens with a very mild decrease of the cohesive stresses.

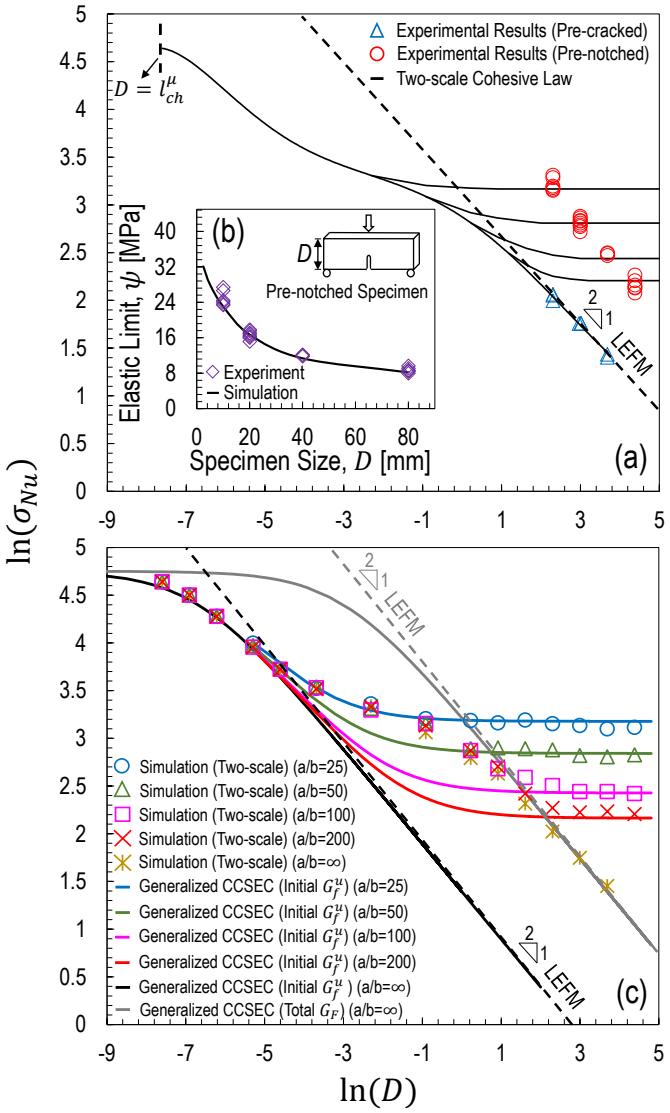

Figure 3.9: Size effect on the notched and cracked specimens investigated in this work: (a) nominal strength predicted by the two-scale cohesive model as a function of the specimen size. Note the excellent agreement with the experimental data for both cracked and notched specimens; (b) comparison on the elastic limit between simulations without any cohesive model and experimental data for notched specimens; (c) comparison between the two-scale cohesive model and the Generalized Cohesive Crack Size Effect Curves using the initial and total fracture energy.

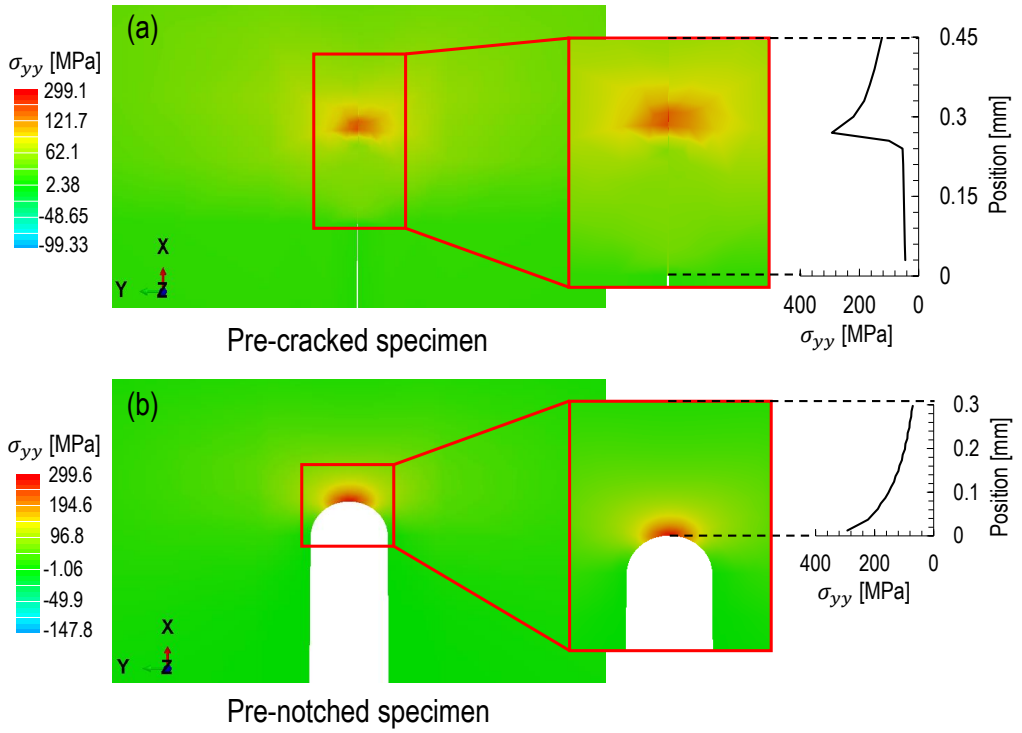

Figure 3.10: FE models and cohesive stresses at the condition of incipient failure for (a) pre-cracked specimen and (b) pre-notched specimen.

Furthermore, based on the two-scale model proposed in this work, some considerations on the applicability of LEFM for a course estimate of the failure load can be made. In case of pre-cracked specimens, LEFM can only be applied when the FPZ size is negligible compared to the structure size. If this condition is met for micro-metric structures, then the fracture energy to be used in the calculations is G_f^{μ}. This means that to predict e.g. the onset of a microcrack in a polymer matrix composite by LEFM, one has to first verify that the micro Irwin's characteristic length l_{ch}^{μ} is significantly smaller than the smallest geometrical features (e.g. fiber diameter, inter-fiber distance, etc.). On the other hand, if the condition of negligible FPZ size is met for structures of size $D \gg l_{ch} = E^* G_F / f_t^2$, the total fracture energy G_F should be used in the calculations. In case of pre-notched specimens, LEFM can only be applied when the notch tip radius is extremely small, smaller than the micro Irwin's

characteristic length. If this condition is met, then the same observations on the applicability of LEFM to pre-cracked structures hold.

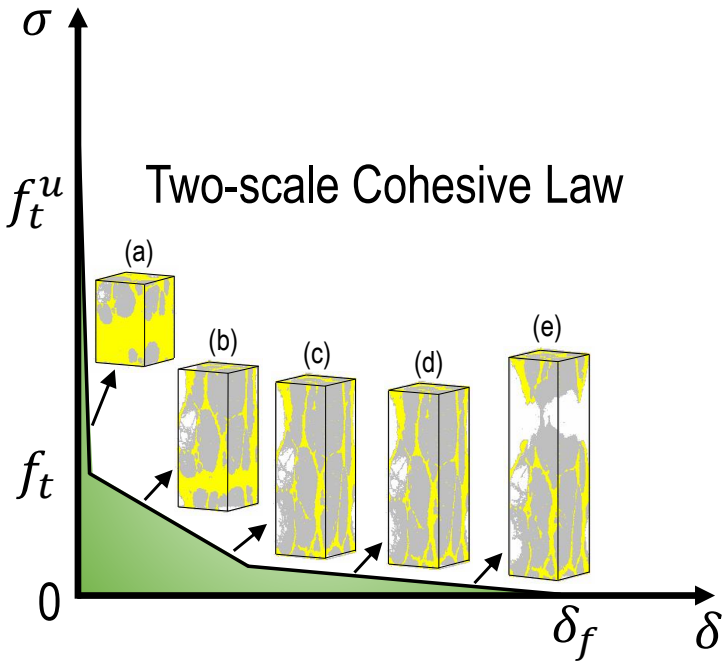

Figure 3.11: Two-scale cohesive law with related main damage mechanisms. The pictures are the MD simulation results of the deformation of a thermoset polymer. Pictures reproduced from Yang and Qu 2014 [110].

It is worth mentioning that thermosets are inherently less viscous compared to other polymers such as e.g. thermoplastics thanks to the very short polymer chains and strong covalent bonds between particles. Yet, as shown for concrete and other quasi-brittle materials [111, 112], thermosets do exhibit strain rate dependence and increase of brittleness as the loading rate becomes slower. To reduce the foregoing effects on the size effect data, the applied displacement was scaled with the specimen size so to keep the same nominal strain rate as mentioned in the previous chapter. While this approach limited strain-rate-dependent shifts of the size effect curve, it could not prevent the fact that the two-scale cohesive model we are proposing holds for the given strain-rate applied during the tests. Although the

authors think that the traction-separation law would change significantly only for extremely large rates, a study on the rate effect would be needed to validate this statement. This is beyond the scope of this work and will be subject of future investigations.

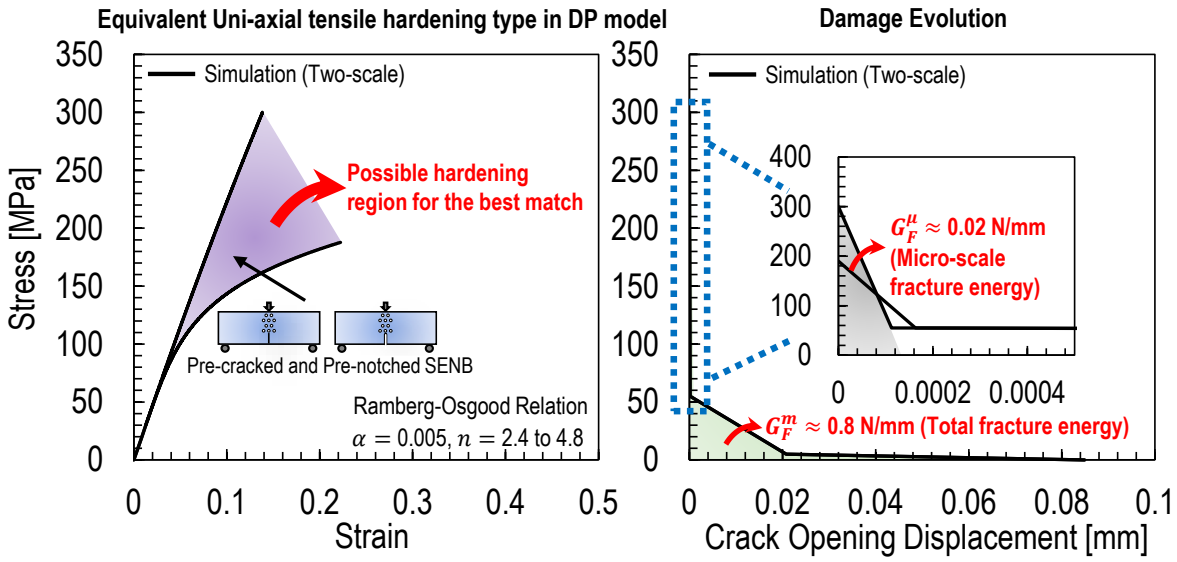

Figure 3.12: Two-scale equivalent uni-axial tensile hardening behavior and damage evolution used in the simulations for Mode I scenario. Note that any possible pre-peak behaviors in the hardening region highlighted in purple were used for the modeling of both pre-cracked and pre-notched SENB specimens with various sizes.

3.4.1 Consideration of plasticity in the non-linear pre-peak behavior

The foregoing cohesive simulations only consider a linear elastic pre-peak behavior. However, due to the fact that a small area of plastic deformation occurring in front of the notch was observed by using TOM under polarized light, the hardening behavior of the material was further considered to better capture the morphological feature as illustrated in Figure 3.6f. In this direction, as plotted in Figure 3.12, the proposed pre-peak behavior can have a possible hardening region which is characterized by a small non-linearity before reaching the high strength ($f_t^{\mu} \approx 200$ to 300 MPa) and followed by a steep softening initially ($G_F^{\mu} \approx 0.02$

N/mm) and a mild softening ($G_F^m \approx 0.78$ N/mm) accordingly. The foregoing micro-scale pre-peak behavior also follows the classical Ramberg-Osgood relation with the same parameter $\gamma = 0.005$ but a different exponent n in the range from 2.4 to 4.8. It is worth pointing out here that this is actually similar to the previous two-scale cohesive law except for the hardening region. In the case of a negligible hardening part, it noticeably becomes equivalent to the previous two-scale cohesive law. Thanks to this non-linear pre-peak behavior in the DP plasticity model, an excellent match with the micro-scale morphology and the load-displacement curves for both pre-cracked and pre-notched specimens with various sizes was also successfully achieved as illustrated in Figure 3.13. It is worth mentioning here that the parameters (i.e. friction angle, dilation angle, and flow stress ratio) in the DP plasticity model were kept the same as the ones presented in the previous chapter.

To support the foregoing statement, the equivalent uni-axial tensile hardening behavior calibrated from dogbone specimen was used for the modeling of pre-notched specimens with different sizes under Mode I loading condition. As can be noted from Figure 3.14a, an unacceptable mismatch on the critical load between simulation and experiment was observed for all the investigated sizes. In addition to this fact, the computational load-displacement curves exhibit small non-linearity close to the critical load due to the slow crack propagation and this aspect further contradicts the experimental results showing almost linear load-displacement response and fast crack propagation at the failure.

On the other hand, an acceptable agreement between simulation and experiment cannot be achieved by increasing the critical strain for damage initiation since this can lead to more pronounced non-linearity for the computational load-displacement curves thus noticeably deviating from the experimental results as shown in Figure 3.14b. The situation can be even worse by considering even larger critical strain for damage initiation in the same model. Thanks to this investigation, the foregoing mismatch confirms the fact that the mechanical behavior of pre-notched specimen in Mode I case cannot be successfully captured with the macro-scale constitute law featuring low strength and mild softening or the consideration of large plastic strain. It is worth mentioning here that the same fracture energy was adopted

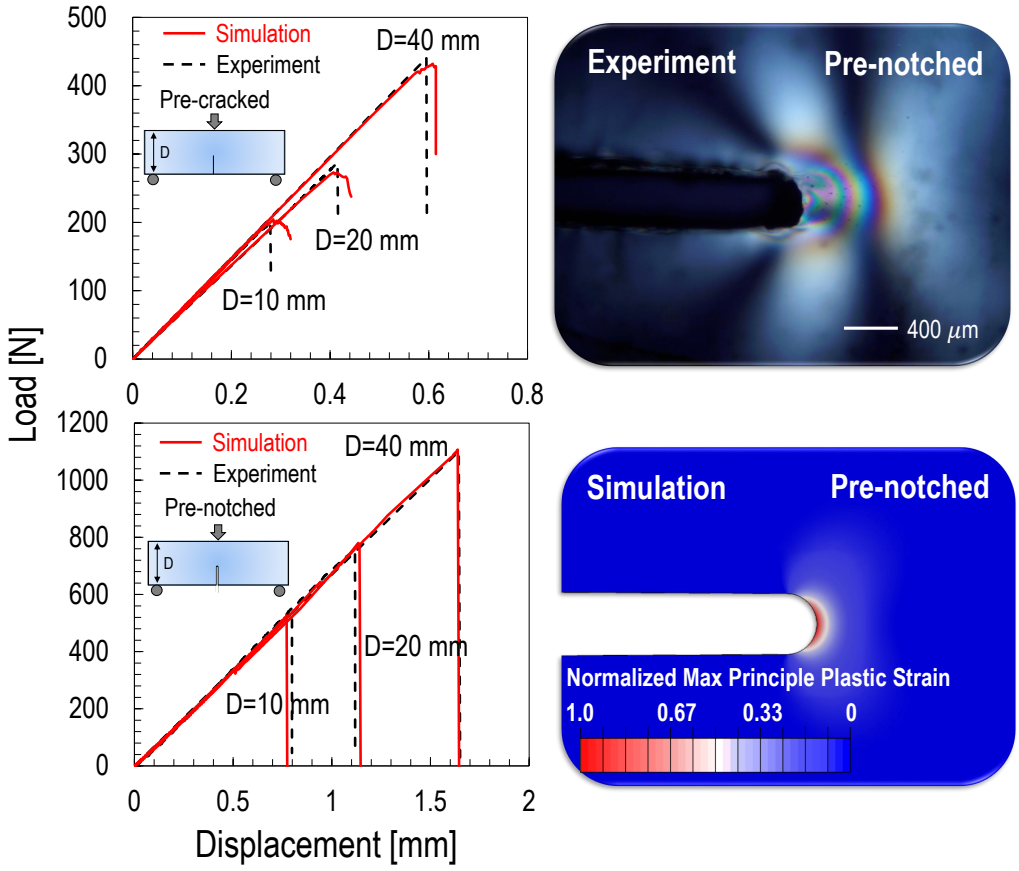

Figure 3.13: Experimental and numerical load-displacement curves for both pre-cracked and pre-notched SENB specimens with various sizes. This figure also compares experimental morphology vs. simulation result for pre-notched specimen in Mode I case.

in this simulation and the foregoing one considering the micro-scale material properties.

3.4.2 Validation for micro-scale thermoset polymer specimen

The outstanding micro-scale cohesive behavior was further computationally validated through the Mode I fracture tests on the micro-scale Single Edge Notch Tension (SENT) specimen made of thermoset polymer provided by Kaneko *et al.* [18]. Thanks to the Focused Ion Beam (FIB) milling technique and the outstanding pre-cracking method, the micro-scale specimen was manufactured with the dimension of about 5.7 × 5.2 × 2 μm and the sharp

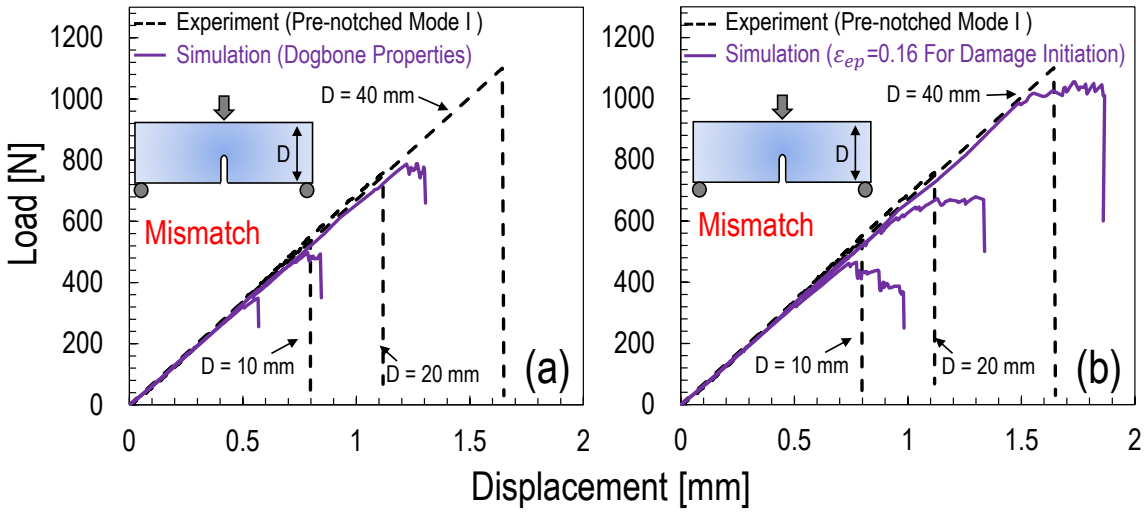

Figure 3.14: Mismatch between experiment and simulation for load-displacement curves of pre-notched SENB specimens with different sizes. The material properties used in the simulations including: (a) calibrated dogbone specimens; (b) equivalent plastic strain $\varepsilon_{ep} = 0.16$ for damage initiation.

crack featuring about 2.7 μm in length was created by pre-applying the moment on the specimen before conducting the fracture tests as illustrated in Figure 3.15. By utilizing the foregoing two-scale softening law to predict the load-displacement curve of the micro-scale SENT specimen, as illustrated in Figure 3.16, simulation result has an excellent agreement with the experimental data but this is not the case for the simulation with lower material strength and mild softening showing a remarkable mismatch.

The recipe for the foregoing success mainly lies on the initial segment of the two-scale softening law instead of the microscale strength since the strong stress intensity at the tip would always lead to elastic stresses greater than the microscale strength. This initial segment of the two-scale softening law corresponds to the initial fracture energy ($G_f^{\mu} \approx 0.02$ N/mm) which is almost equivalent to the one ($G_f^{\mu} \approx 0.012$ N/m) experimentally estimated from the micro-scale Mode I fracture tests. This difference is mainly due to the fact that the reported micro-scale fracture energy was calculated by LEFM which neglects the effects of

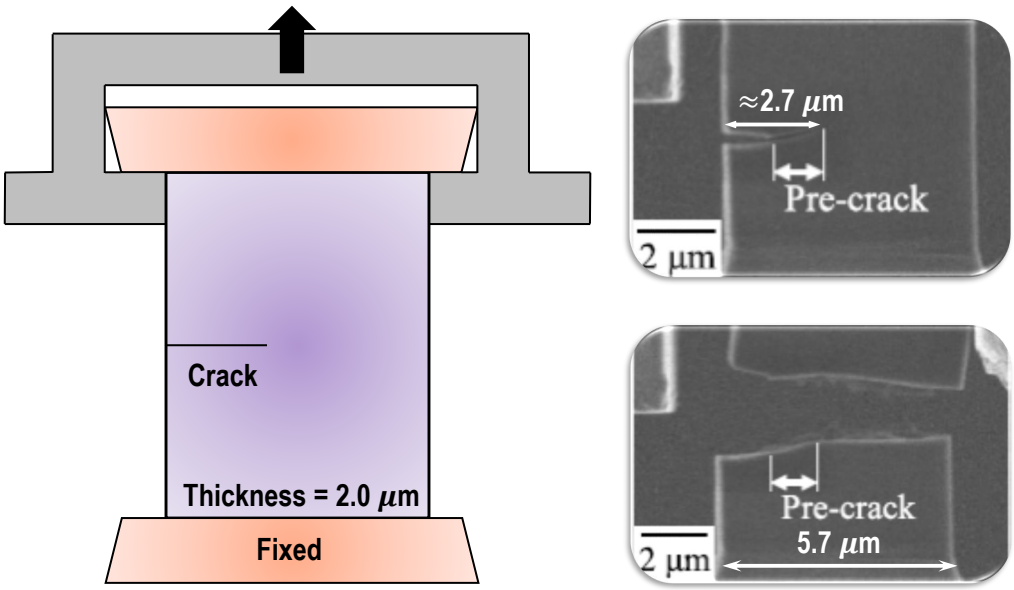

Figure 3.15: Dimensions and mechanical test set-up for micro-scale SENT specimen. Note that these images were obtained from [18]

the FPZ thus leading to the underestimation. The importance of the non-linear FPZ size on the structural behavior and the calculation of the fracture energy will be discussed in the following chapters. This example clearly shows the consequence to characterize the fracturing behavior of micro-scale specimen using inappropriate material properties from conventional laboratory tests and provides a solid confirmation for the extremely different mechanical behavior of thermoset polymer at the micro scale compared to the one at the large scale.

3.5 Statistical behavior of thermoset polymer at the micro-scale

A statistical study on pre-notched SENB specimens was conducted and presented in this section since it was shown in the previous sections that the micro-scale strength can be measured by leveraging this method. The purpose of this investigation is due to fact that the statistical behavior of thermoset polymer at the micro-scale possibly plays a role in better modeling of transverse matrix cracks in fiber-reinforced polymer composites. In fact, it has been shown that the crack propagation after the damage initiation at the fiber/matrix

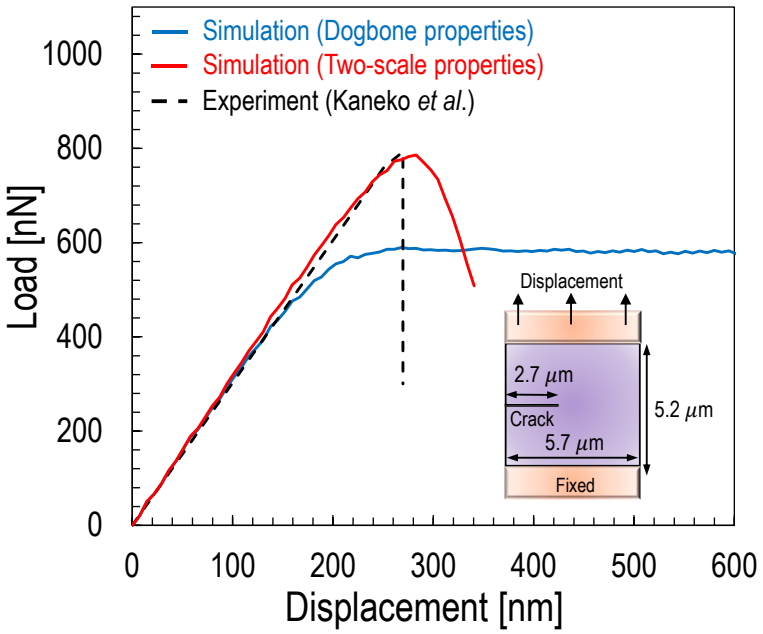

Figure 3.16: Simulation results vs. experimental data for Mode I fracture tests on micro-scale SENT specimen obtained from the outstanding work by kaneko *et al.* [18]. Note that the same total fracture energy was adopted for the foregoing simulations with and without considering micro-scale properties.

interface can be governed by the lower material strength rather than the mean value [13].

As illustrated in Figure 3.17, the probability distribution of the micro-scale strength is plotted in the Weibull scale and the failure probability was calculated based on the method as described in the previous chapter. It is interesting to notice from the figure that, while the probability distribution of macroscopic strength obtained from uni-axial tensile tests follows Weibull distribution, this is no the case for the micro-scale strength since its histogram is composed of two segments separated by a kink point. The lower portion follows Weibull distribution (i.e. straight line) whereas the upper part is curved following Gaussian distribution. The foregoing phenomenon indicates that the probability transits from Weibull to Gaussian-Weibull distribution as specimen size decreases. This is consistent with the observations for many quasi-brittle materials [113–117].

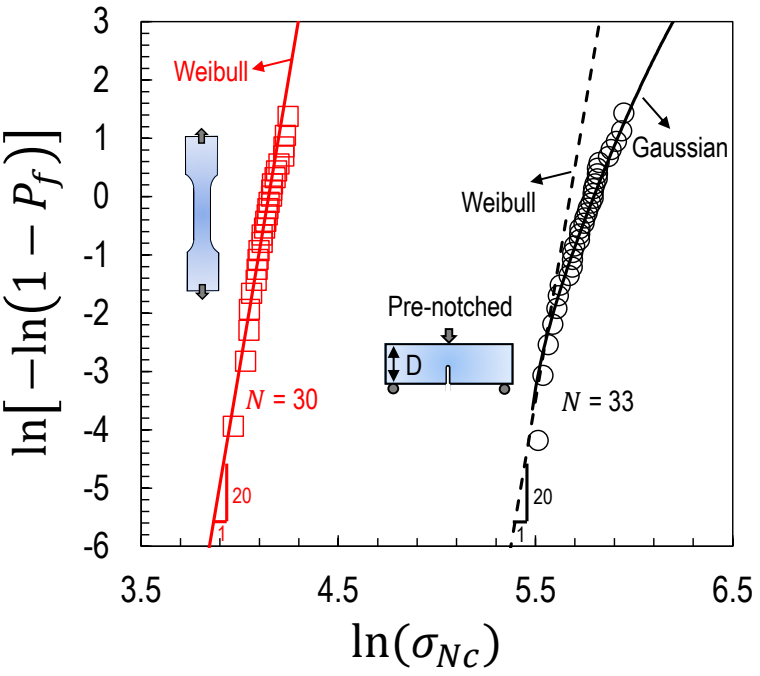

Figure 3.17: Probability distribution measured from dogbone and pre-notched SENB specimens. Note that N represents number of tests.

With knowing the micro-scale strength histogram, a finite weakest link model can be used to determine the equivalent RVE size since the structure can be modeled as a chain of finite RVEs. According to the joint probability theorem, the failure probability of the structure P_f can be calculated as:

$$1 - P_f(\sigma) = \prod_{i=1}^{N} [1 - P_1(\sigma)] \tag{3.3}$$

where P_1 = failure probability of one RVE and N = number of RVEs in the structure. It was shown recently that the strength cdf of one RVE can be approximately expressed as Gaussian core grafted with Weibull tail [118]:

$$P_1(\sigma) = 1 - e^{(\sigma/s_0)^m} \approx (\sigma/s_0)^m \qquad (\sigma \le \sigma_{gr}) \tag{3.4}$$

$$P_1(\sigma) = P_{gr} + \frac{r_f}{\delta_G \sqrt{2\pi}} \int_{\sigma_{gr}}^{\sigma} e^{-(\sigma - \mu_G^2)/2\delta_G^2} d\sigma \qquad (\sigma > \sigma_{gr}) \tag{3.5}$$

where m = Weibull modulus, s_0 = scaling parameter of the Weibull tail, δ_G and μ_G are the standard deviation and mean of the Gaussian core, σ_{gr} = grafting stress, and r_f is the scaling parameter required to normalize the grafted cdf such that $P_1(\infty) = 1$. In these parameters, s_0 can be obtained from the macro-scale strength histogram for un-axial tensile tests and m approximately equals to 20 based on the results as show in Figure 3.17. By fitting the micro-scale strength histogram leveraging Eqs. (3.3) to (3.5), it was found that the maximum RVE length is about 1.6 μm and the length can be smaller than this value. It is worth mentioning here that the micro-scale strength histogram was obtained assuming negligible plasticity of the material and three-dimensional scaling. The more accurate results about the RVE length can be determined by testing pre-notched SENB specimens featuring different notch radii and considering the material plasticity. The foregoing determination of one RVE length of the material is extremely important since this is the key information for a stochastic modeling of progressive damage and its scaling of thermoset polymer.

3.6 Conclusions

1. The fracturing behavior of thermoset polymer structures featuring cracks is distinctively different than the one of structures weakened by U-notches. Although this result is not surprising for blunt notches with large tip radii, it was not expected for the notches investigated in this work which featured a tip radius significantly smaller than the Irwin's characteristic length of the material;

2. In contrast to what has been proposed in the literature, plastic residual stresses induced by the manufacturing of the notch cannot be the dominant cause of such a high apparent fracture toughness. In fact, the residual stresses that would be required to justify such a high toughness are larger than 100 MPa and it seems unlikely that they can be generated by the sawing procedure. This statement is supported by additional tests on specimens with notches created by pre-inserting a sharp razor blade. Even if in such case plastic stresses cannot be induced, the failure loads were similar to those

of the other notched specimens. A further confirmation for this statement is provided by the results from Transmission Optical Microscopy (TOM) with cross-polarized light showing almost negligible residual stresses due to the pre-notching process;

3. To capture the behavior of both the cracked and notched specimens, a *two-scale cohesive model* is proposed. For sub-micron crack opening displacements, the cohesive strength is about 300 MPa and the cohesive stresses decrease linearly and very steeply with increasing crack openings. When the cohesive stresses reach the strength estimated from typical laboratory-scale specimens (about 55 MPa) and the opening displacements are beyond the sub-micron range, the slope of the cohesive law becomes milder. Finally, the cohesive law ends with another linear branch starting when the stresses reach 5 MPa. This last part of the cohesive law is characterized by a very slow decay of the cohesive stresses;

4. The proposed two-scale cohesive model captures the fact that, due to energetic-statistical size effect [76–80], the microscopic strength of the polymer can be several times higher than the one measured from macroscopic tests [17, 81, 110]. At the same time, the steep initial part of the cohesive curve, leading to an initial fracture energy of only about 2.5% of the total one, captures the lower energy dissipation occurring at the sub-micron scale;

5. Thanks to the foregoing model the different behavior of polymer structures featuring cracks and sharp U-notches can be easily explained. Since the initial fracture energy G_f^μ is only a fraction of the total energy dissipated and the initial strength f_t^μ is significantly larger than in macroscopic tests, the Irwin's characteristic length $l_{ch}^\mu = E^* G_f^\mu / \left(f_t^\mu\right)^2 = 0.54\ \mu m$ related to the initial formation of the FPZ is significantly smaller than the width of the notches investigated in this work. Accordingly, the fracturing behavior of the notched specimens must depart from the one of cracked specimens and the nominal stress at failure is determined by the elastic limit condition, i.e. $\sigma_{Nc} = f_t^\mu / k$

with k = stress concentration factor. On the other hand, in laboratory-scaled cracked specimens the cohesive stresses in the FPZ at incipient failure always reach the second portion of the cohesive curve. In such a case, the Irwin's characteristic length l_{ch} describing the FPZ is significantly larger since it depends on the total fracture energy $G_F \approx 40 G_f^{\mu}$ and a significantly lower strength $f_t \approx f_t^{\mu}/6$. Accordingly, the failure behavior of macroscopic cracked specimens depends only on the total fracture energy and macroscopic strength;

6. The higher fracture energy of pre-notched specimens has not meaning since the investigated specimens fail at the elastic limit. This indicates that LEFM cannot be applied to the calculation of the fracture energy for pre-notched specimens in general, unless the width is sufficiently lower than the Irwin's characteristic length associated to the initial part of the traction-separation law;

7. Since the initial fracture energy is only a negligible portion of the total fracture energy and, in laboratory-scale cracked specimens the cohesive stresses always overcome the initial portion of the cohesive law, it is not possible to characterize f_t^{μ} and G_f^{μ} unless micro-metric specimens are tested. These tests are very challenging and are generally affected by significant uncertainties. Based on the results of this work, a valid alternative is to test both cracked and pre-notched specimens and use the results on the latter configuration to characterize f_t^{μ};

8. The foregoing considerations are further supported by the excellent agreement between the numerical predictions through the plasticity and crack band models and the experimental data on geometrically-scaled Single Edge Notch Bending (SENB) and micro-scale Single Edge Notch Tension (SENB) specimens. By considering the hardening behavior of the material in the Drucker-Prager (DP) plasticity model, the proposed two-scale constitute model is similar to the previous two-scale cohesive zone model without including plasticity and able to capture not only the macro-scale load-

displacement curves but also the micro-scale morphological features;

9. The foregoing results are of utmost importance for the design of microelectronic devices or polymer matrix composites. In fact, in these systems, the main damage mechanisms belong to the sub-micron scale and the fracturing behavior is dominated by the initial portion of the cohesive law since the opening displacements are not large enough to reach the second portion of the curve. The two-scale model proposed in this work and the related testing protocol, represent a first step towards the accurate yet simple simulation of thermoset polymers at the micro-scale;.

Chapter 4

MAKING THERMOSET POLYMER AS TOUGH AS METAL VIA ENGINEERED POROSITY DUE TO THE ACTIVATION OF MICRO-SCALE BEHAVIOR

The previous chapters described the strategies to characterize the superior plastic deformation and micro-scale behavior of thermoset polymer. Thanks to the inspiration from these excellent studies, this chapter focused on improving the structural performance of thermoset polymer through engineered porosity which successfully utilized the micro-scale strength of the material. It was concluded that the presence of engineered porosity can effectively impede the fast propagation of the cracks in the material thus leading to the apparent fracture energy comparable to the ones of conventional metals. Moreover, the residual behavior of the polymeric structure in presence of pre-defects can also be significantly improved after cyclic load by leveraging the porosity. The foregoing improvements were further computationally confirmed by considering the micro-scale behavior of thermoset polymer in the simulations.

4.1 Specimen preparation and testing description

The investigated thermoset polymer and the corresponding manufacturing procedures in this work were exactly the same as described in the foregoing chapters. To study the feasibility of leveraging porosity to improve the structural performance of polymeric materials, various testing geometries featuring cylindrical holes were prepared as illustrated in Figure 4.1. The effects of hole arrangements were also considered in this work by investigating both square and triangular patterns of cylindrical holes manufactured by using a tungsten carbide drill bit. On the other hand, the effects of loading conditions were also considered by conducting the quasi-static tests on all the investigated geometries and the fatigue tests on only U- an

V-notched specimens. The quasi-static tests were performed under the displacement control with a displacement rate of 0.01 mm/s by leveraging electro-actuated Psylotech meso-scale machine coupled with a BXFM Olympus Microscope [119, 120] whereas fatigue tests were conducted under load control with a stress ratio of $R = 0.1$ and a low frequency of $f = 5$ Hz by using servo-hydraulic 8511 Instron machine. The detailed information for each testing geometry is described in the following sections.

4.1.1 SENB specimen with sharp crack and cylindrical holes

The effects of porosity on the crack propagation of the material were initially investigated as illustrated in Figure 4.1a by leveraging the Mode I fracture tests on the Single Edge Notch Bending (SENB) specimens featuring a sharp crack but different patterns of cylindrical holes in front of that crack. The crack length is about $0.35D$ where D is the width of the specimen. It is worth mentioning here that the sharp crack was manufactured by tapping using a razor blade after the initial sawing using a diamond-coated saw and the detailed procedures can be found in [94, 108]. On the other hand, the distance between the edges of cylindrical holes $S = 2$mm was kept the same whereas four different radii of cylindrical holes $R = 0$, 0.2, 0.5 and 1mm were considered in this work as illustrated in Figure 4.1a. As a consequence, the investigated specimens comprise different volume fractions of cylindrical holes $V_f = 0\%$, 2.2%, 8.7% and 19.6% for both square and triangular patterns since the volume fraction is defined as $V_f = V_h/V_t = \pi(S/R + 2)^{-2}$ where V_h is the volume of the cylindrical holes in the Representative Volume Element (RVE) and V_t is the total volume of the RVE as shown in Figure 4.1c. In the case of volume fraction $V_f = 0\%$, this situation corresponds to the reference material representing the specimen without cylindrical holes.

4.1.2 U- and V-notched specimens with cylindrical holes

Except for the fracture tests focusing on the sharp crack, different types of notches were also investigated as shown in Figure 4.1b for the specimens featuring triangular pattern of cylindrical holes ahead of V- and U-notches under three-point bending condition. In

addition, the residual structural performance of these materials was further evaluated by conducting the quasi-static bending tests on the specimens which already experienced cyclic load up to about 93% of total fatigue lifetime in average. The exactly same cyclic load was applied on the pre-notched specimens with and without cylindrical holes in order to provide a fair condition for the following measurement of the residual structural performance of the foregoing specimens. The maximum load in the applied cyclic load was about 350N for V-notched geometries and 275N for U-notched geometries which all corresponds to about 30% of the critical quasi-static load for the specimen in presence of cylindrical holes but about 26% of the one for the specimen without cylindrical holes.

On the other hand, while these notches have the same length as the crack one for the critical comparison, the notch geometries are significantly different from the sharp crack since the investigated V-notch features right triangle with 90° angle inward the specimen and U-notch has a width about 0.4mm leading to the radius of the notch tip about 0.2mm. It is worth mentioning here that the manufactured V-notch does not have an ideal sharp tip but features a finite radius of about 0.25mm. The purpose of this investigation is to have a comprehensive understanding for the effects of porosity on the mechanical behavior of polymeric structures in presence of various pre-defects. On the other hand, both V- and U-notched specimens without cylindrical holes were also tested for the reference materials and only one radius of the cylindrical hole (R = 0.5mm for V-notch and R = 1mm for U-notch) was selected for each notch type.

4.1.3 Rectangular specimen with cylindrical holes

Rectangular specimens only with cylindrical holes were further prepared for the three-point bending tests as illustrated in Figure 4.1c to study the effects of porosity on the possible structural degradation of intact polymeric materials. This investigation is definitely crucial for designing the optimized size range and pattern of porosity for the overall structural improvement of polymeric materials and the importance of this aspect will be shown throughout the following sections. As illustrated in Figure 4.1c, four different sets of hole arrangements

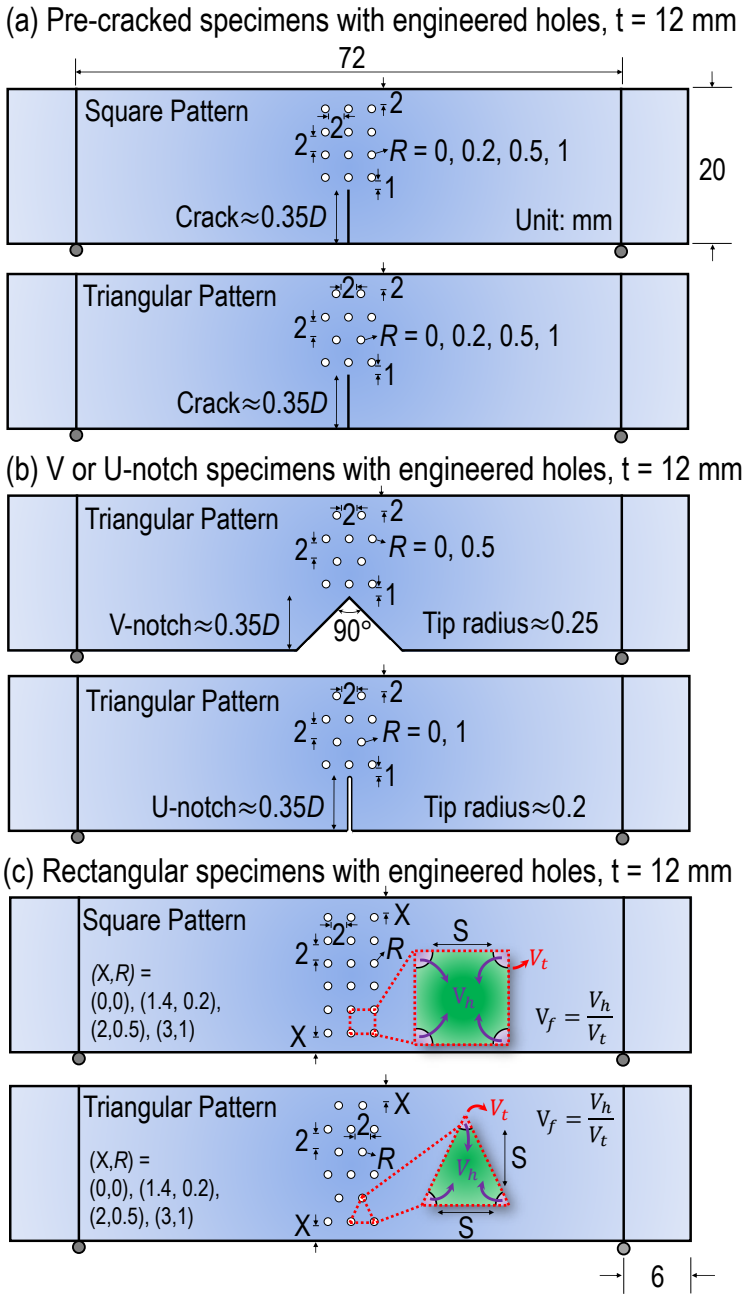

Figure 4.1: (a) Pre-cracked SENB specimens with different patterns and sizes of cylindrical holes for Mode I fracture tests; (b) V- and U-notched specimens with triangular pattern of cylindrical holes for Mode I fracture tests; (c) Rectangular specimens with different patterns and sizes of cylindrical holes for three-point bending tests.

(X, R) were selected in this work and they were $(0, 0)$, $(1.4, 0.2)$, $(2, 0.5)$ and $(3, 1)$ leading to different volume fractions for each investigated pattern exactly the same as the ones described in the foregoing Mode I fracture tests. It is worth mentioning here that the symbol X represents the edge distance as shown in Figure 4.1c and the set $(X = 0, R = 0)$ is the reference material representing the specimen without cylindrical holes.

4.2 Experimental results

4.2.1 Effects of porosity on the fracturing behavior of sharp crack

4.2.1.1 Global structural performance and damage characteristics

The load-displacement curves obtained from the Mode I fracture tests on pre-cracked SENB specimens with different sizes and patterns of cylindrical holes are plotted in Figure 4.2. As can be noted from the highlighted regions in the figure, the existence of cylindrical holes can successfully hinder the crack propagation in the material since the load on the specimen exhibits a sudden drop due to the initial crack propagation but does not further decrease leading to the catastrophic failure of the specimen. Thanks to this crack pinning process, the structure can be further loaded and the critical load can be improved up to about 300% for both investigated patterns with the volume fraction $V_f = 2.2\%$ compared to the one of the reference material without cylindrical holes.

On the other hand, it is also interesting to notice from the figure that, while the mechanical behavior for most investigated specimens is almost linear up to the critical load exhibiting pronounced brittle behavior, a remarkable pre-peak non-linearity and stable post-peak softening was observed with increasing the volume fraction up to $V_f = 19.63\%$ for the one with triangular pattern of cylindrical holes. This can be partially explained that the crack propagation is not always hindered by the center of the cylindrical hole due to the manufacturing misalignment as shown in Figure 4.3a. As a consequence, the following damage was formed by the crack deflection between adjacent holes and the further crack propagation features tortuous path between cylindrical holes as illustrated in Figure 4.3b.

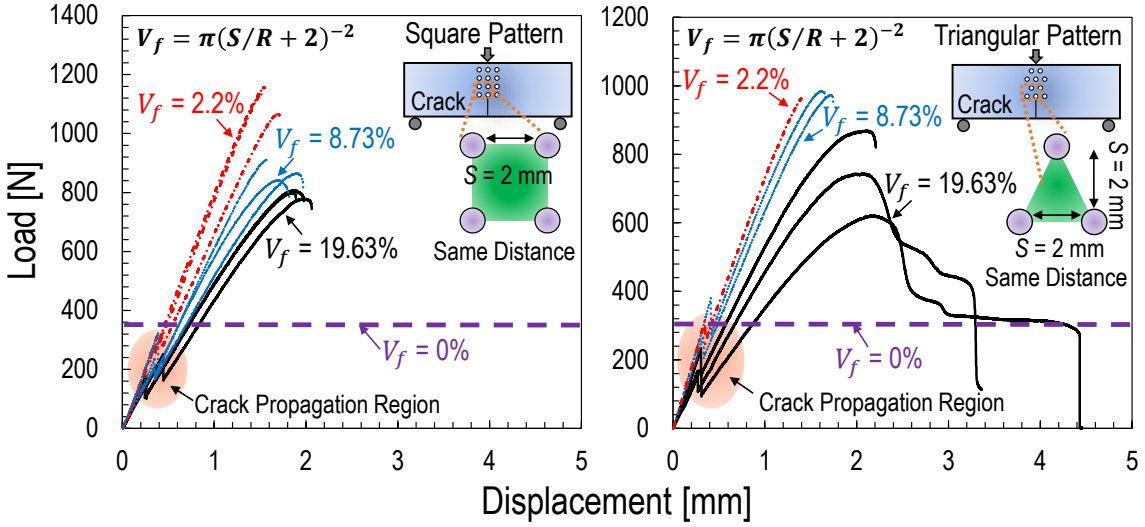

Figure 4.2: Experimental load-displacement curves for pre-cracked SENB specimens featuring different volume fractions of cylindrical holes for both square and triangular patterns. Note that the highlighted region in the plot represents the situation that the crack propagates and stops by the cylindrical hole.

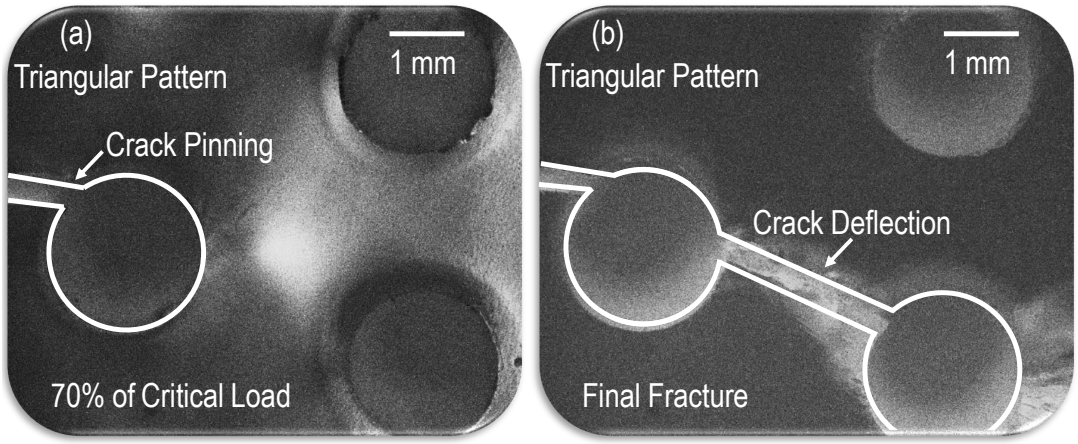

Figure 4.3: Representative fracture sequences for pre-cracked SENB specimen with triangular pattern of cylindrical holes (R = 1mm) under Mode I loading condition: (a) crack pinning due to the nearest cylindrical hole; (b) crack deflection between cylindrical holes. Note that these images were taken at 70% of the critical load and the final fracture respectively.

These damage characteristics lead to larger fracture region in the material thus dissipating more energy which contributes to the forgoing non-linearity in the load-displacement curves and this aspect is completely different from the case with lower volume fraction of cylindrical holes which shows rapid crack propagation separating the entire specimen after the initial crack pinning stage.

4.2.1.2 Apparent fracture energy: polymers with porosity vs. conventional metals

To shed more light on the previous structural improvement by means of porosity, the apparent Mode I fracture energy estimated from the final peak load of the specimen was used to have a critical comparison with the one obtained from the conventional SENB specimen without cylindrical holes. The calculation of the fracture energy was based on the Linear Elastic Fracture Mechanics (LEFM) which was expressed in the previous chapters and $g(\alpha_0) =$ dimensionless energy release rate which must be calculated for each pattern and volume fraction of cylindrical holes as illustrated in Figure 4.4b.

It is worth pointing out here that the calculated fracture energy for the specimen only featuring a sharp crack represents the real Mode I fracture energy of the material which cannot be appropriately estimated by using the initial peak load of the specimen with larger volume fraction of cylindrical holes. This aspect can be clearly seen from Figure 4.4a that, while the estimated fracture energy corresponding to the lower volume fraction (2.2%) of cylindrical holes has acceptable difference compared to the one of the conventional SENB specimen without cylindrical holes, the larger volume fraction (19.63%) of counterparts can lead to more than 50% underestimation of the real Mode I fracture energy. The consistent results are regardless of hole arrangements and can be explained due to fact that the stress field at the crack tip is significantly affected by the existence of larger cylindrical holes thus violating the application of LEFM for the calculation of the fracture energy.

Moving back to the discussion on the aforementioned comparison, the fracture energy required for the catastrophic failure of the structure can be significantly increased by leveraging cylindrical holes compared to the one obtained from the conventional SENB specimen

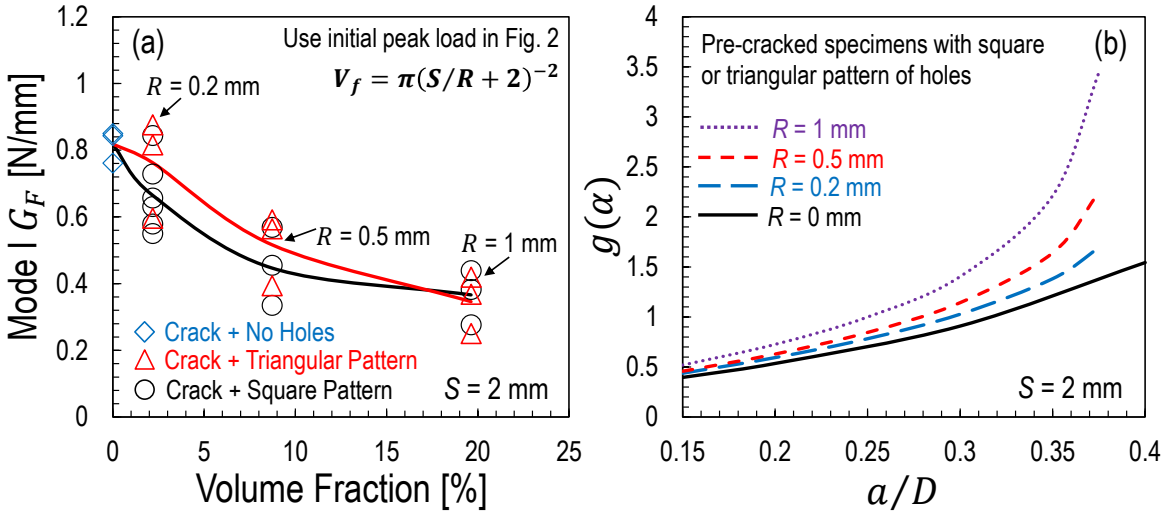

Figure 4.4: (a) Mode I fracture energy estimated from the initial peak load of experimental load-displacement curves for pre-cracked SENB specimens with different patterns and sizes of cylindrical holes; (b) Dimensionless energy release rate with respect to normalized crack length for all the investigated patterns and sizes of cylindrical holes.

for all the investigated hole arrangements as illustrated in Figure 4.5. In this figure, it is interesting to notice that the possible quantity of improved fracture energy is characterized by three different regions depending on the volume fraction of cylindrical holes. In region one as highlighted in green in the figure, the initial crack propagation may not be successfully hindered by the small size of the front cylindrical hole due to the possible misaligned locations between hole and crack. As the size of the cylindrical hole increases, the fracturing behavior of the structure enters region two as highlighted in red in the figure. In this region, the initial crack propagation can be hindered by the cylindrical hole at the second row even if the front cylindrical hole fails to impede the foregoing crack propagation. The last region as highlighted in blue in the figure represents the case for the largest investigated size of the cylindrical hole which always successfully stops the initial crack propagation. It is worth mentioning here that the crack propagation is supposed to be ideally hindered by the smallest investigated size of the nearest cylindrical hole if the crack is located at the center of the cylindrical hole. But this is not always the truth for the real engineering applications

since the initiation location of the sharp crack in the material under complex service load can be randomly emerged.

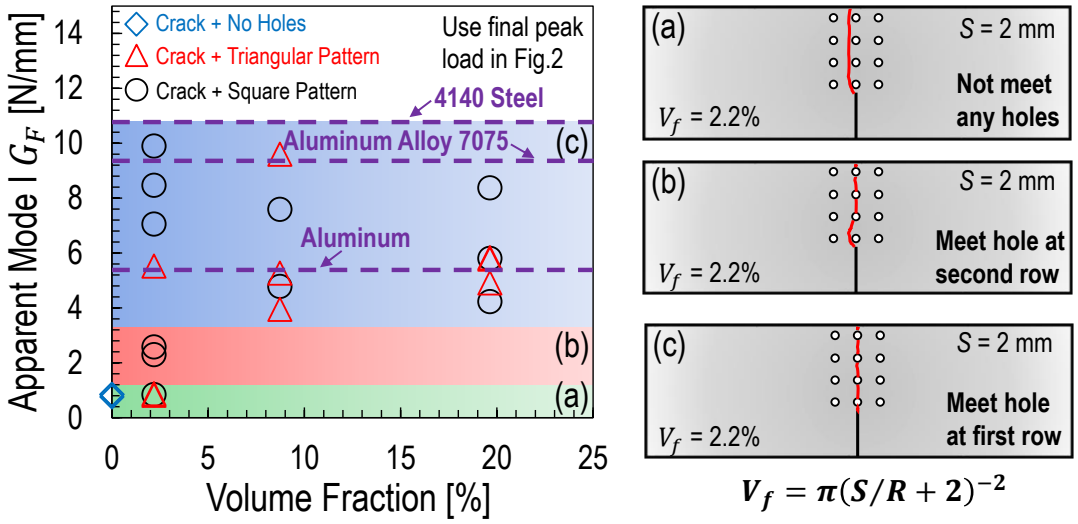

Figure 4.5: Mode I fracture energy estimated from the final peak load of experimental load-displacement curves for pre-cracked SENB specimens with different patterns and sizes of cylindrical holes. Note that the initial crack length was used for the estimation of the foregoing fracture energy.

It is surprising that the most improvement on the fracture energy can reach up to 1000% compared to the one obtained from the reference material. This superior improvement with one order of magnitude was never reported in the literature and can further leads to the high apparent fracture energy about 10 N/mm which is equivalent or even higher than the conventional metals (e.g. aluminum, steel, etc) as illustrated in Figure 4.5. Despite the fact that some similar toughening methods were reported in the literature showing great structural improvement but less than this work, the most important toughening mechanism was not properly understood or different from other metallic materials and this aspect will be well explained in the later sections which was inspired from the previous chapter regarding to the micro-scale behavior of thermoset polymers.

4.2.2 Effects of porosity on the fracturing behavior of V- and U-notches

4.2.2.1 Quasi-static structural performance

The load-displacement curves obtained from the Mode I fracture tests on V- and U-notched specimens with the investigated sizes of cylindrical holes arranged in triangular pattern are plotted in Figure 4.6. In contrast to the previous mechanical behavior of the specimen featuring sharp crack and cylindrical holes, the load-displacement curves in this case are almost linear up to the peak value without exhibiting further structural improvement since the ultimate failure of V- or U-notched specimen with cylindrical holes is only triggered by the catastrophic fracture at the notch tip and the front cylindrical hole does not contribute to the hindering of crack propagation from the notch tip. This phenomenon is mainly attributed to the finite radius of V- or U-notch tip for the pre-activation of the toughening mechanism before leveraging the cylindrical holes ahead of these notch types which is substantially different from the situation for the specimen with the sharp crack and cylindrical holes. This aforementioned toughening mechanism is also related to the micro-scale strength of thermoset polymers and the detailed explanation will be discussed in the later sections.

The results obtained from these tests clearly indicate the importance of the overall design for the structural improvement through the optimized geometries of engineered porosity which must find the best compromise among all the possible scenarios otherwise the expected improvement may not be achieved through the engineered porosity but the structural strength and stiffness of the original material can be degraded as exemplified in Figure 4.6. On the other hand, it is worth mentioning here that the engineered porosity does not always have negative effects on the structural performance of polymeric materials in presence of blunt notches under other loading conditions (e.g. fatigue, quasi-static after fatigue, etc) and this aspect further leads to the following study by investigating the effects of porosity on the residual structural performance of U- or V-notched polymeric materials which already experienced cyclic load. In this scenario, the residual structural behavior may be improved in the consideration of the possible crack initiation at the notch tip and the interesting results

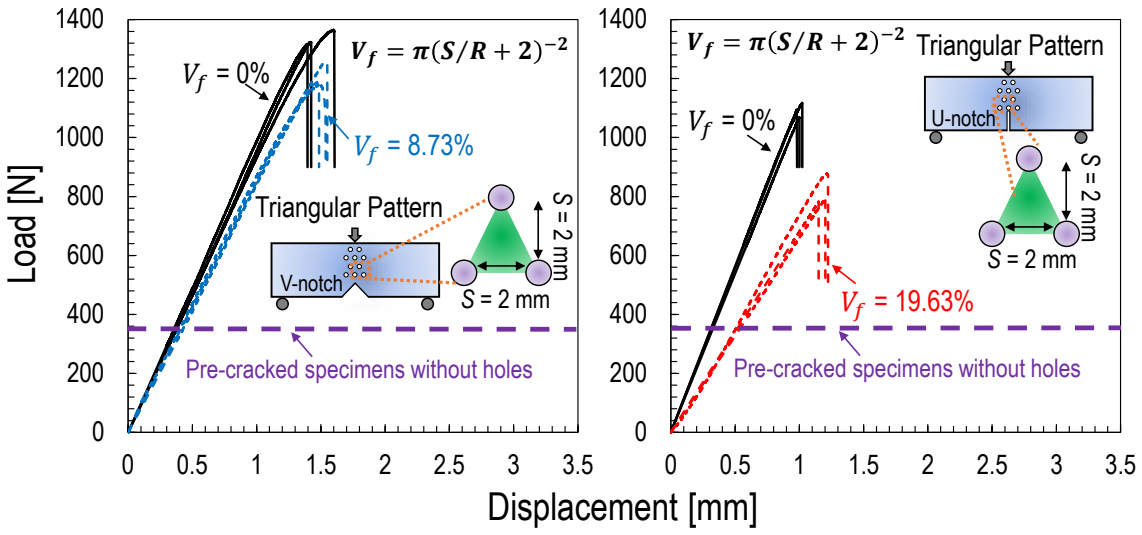

Figure 4.6: Experimental load-displacement curves for U- and V-notched specimens featuring the investigated volume fractions of cylindrical holes arranged in triangular pattern.

are presented in the next section.

4.2.2.2 Residual structural performance after cyclic load

The residual structural performance of V- and U-notched polymeric materials with the investigated cylindrical holes was further evaluated as just mentioned in the previous section and the corresponding results in terms of load-displacement curves are plotted in Figures 4.7 and 4.8. As can be noted from the figures for both pre-notched specimens without cylindrical holes, the global residual stiffness of the materials generally does not deteriorate after about 93% of total fatigue lifetime whereas the residual loading capacity exhibits a dramatic degradation more than 50% of the value measured from the original quasi-static tests. Surprisingly, this does not happen for both pre-notched specimens with the investigated cylindrical holes under a similar loading history as illustrated in Figures 4.7b and 4.8b since only the residual critical load of the material features a less degradation with about 20% decrease in maximum compared to the measurement from the original quasi-static tests. On the other hand, it was

observed that some of the pre-notched specimens with the investigated cylindrical holes have stable post-peak stage in the quasi-static tests after cyclic load as shown in Figures 4.7b and 4.8b and this aspect is also due to the tortuous crack propagation between cylindrical holes in the materials as similarly described in the previous section for the specimen featuring the sharp crack and cylindrical holes.

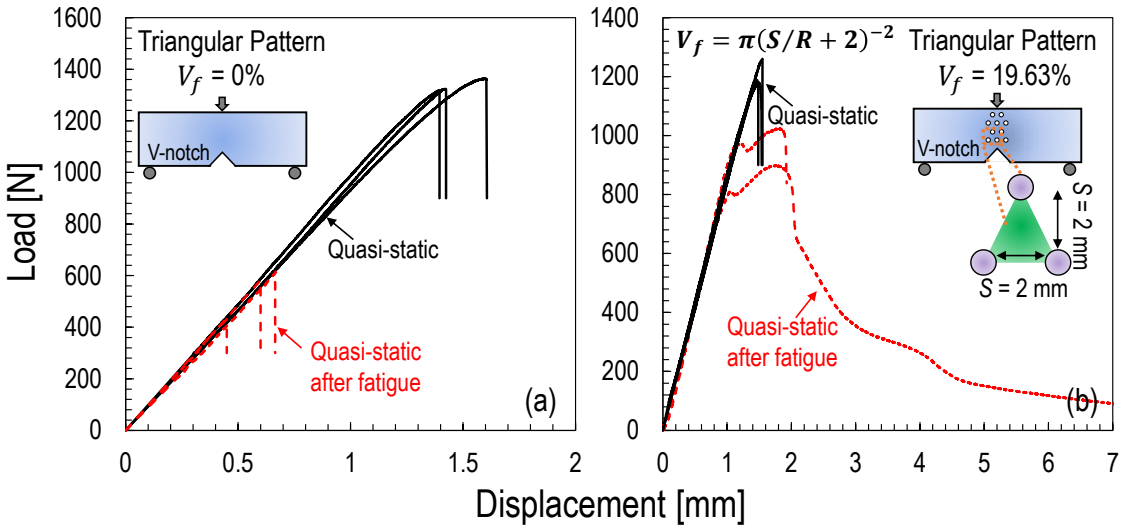

Figure 4.7: Experimental load-displacement curves for V-notched specimens (a) without cylindrical holes and (b) with triangular pattern of cylindrical holes. These plots compare the results for quasi-static load only and quasi-static load after cyclic load up to 90% of the total fatigue lifetime.

The foregoing results provide a positive example for leveraging the porosity to improve the structural performance of polymeric materials which must contain notches for certain engineering purpose under complex loading scenario and further emphansize the importance of the optimized design for this method. However, the possible reasons for the foregoing observation can be more complicated and associated to the local evolution of the stress and stiffness around the notch tip of the material under cyclic load and the boundary of the fatigue cohesive law. This aspect is undergoing and will not be covered here since the investigation is beyond the scope of this study and will be conducted in the future.

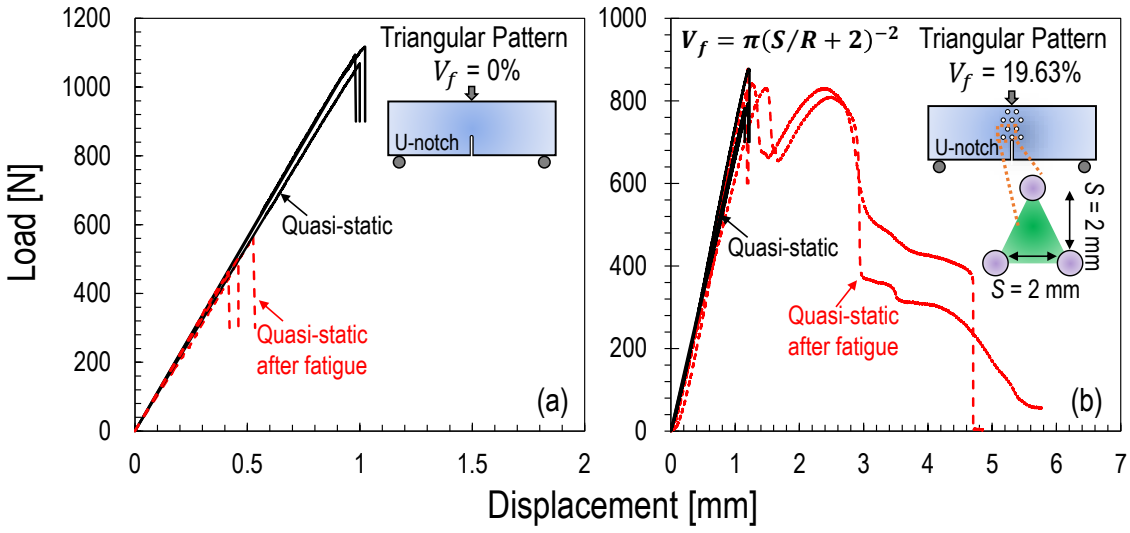

Figure 4.8: Experimental load-displacement curves for U-notched specimens (a) without cylindrical holes and (b) with triangular pattern of cylindrical holes. These plots compare the results for quasi-static load only and quasi-static load after cyclic load up to 90% of the total fatigue lifetime.

4.2.3 Effects of porosity on the structural performance of intact materials

It is convinced from the foregoing results that the porosity can be used through the proper design for the retardation of crack propagation thus guaranteeing the application of this method for the structural improvement of polymeric materials with pre-defects for certain engineering purpose. However, the negative aspect of using this method was also shown in the previous section for the structural degradation of pre-notched polymeric materials under quasi-static loading condition and this aspect can also be the truth for the polymeric structures without featuring defects or potentially having defects in the future. In this consideration, the effects of porosity on the structural performance of intact polymeric materials must also be investigated to provide the useful information for the reliable design of porous polymeric structures.

As can be noted from Figure 4.9, the specimens with the investigated volume fractions of cylindrical holes exhibit negligible reduction on the structural stiffness but features a re-

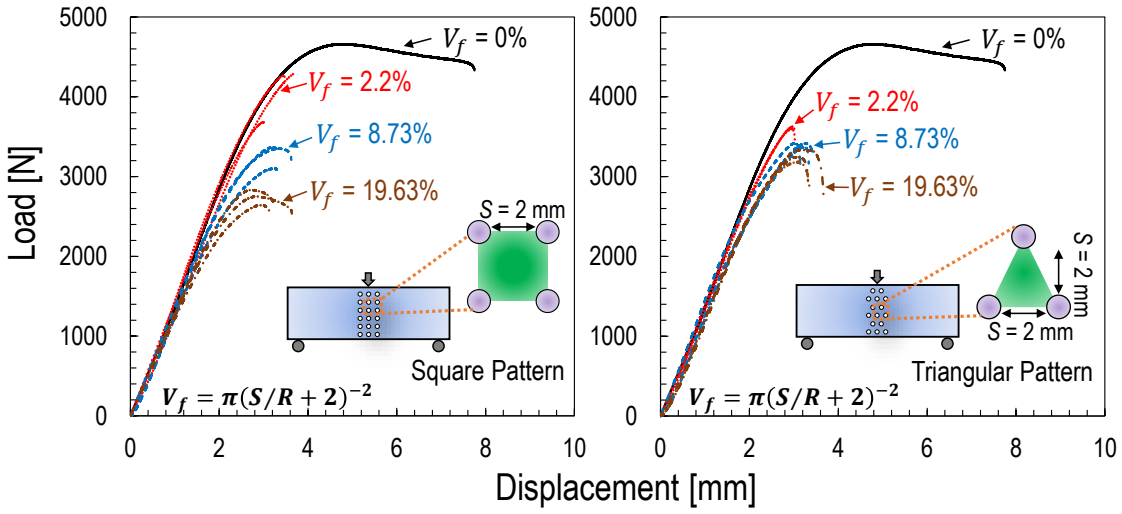

Figure 4.9: Experimental load-displacement curves for rectangular specimens with different volume fractions of cylindrical holes. Both square and triangular patterns were investigated in this work.

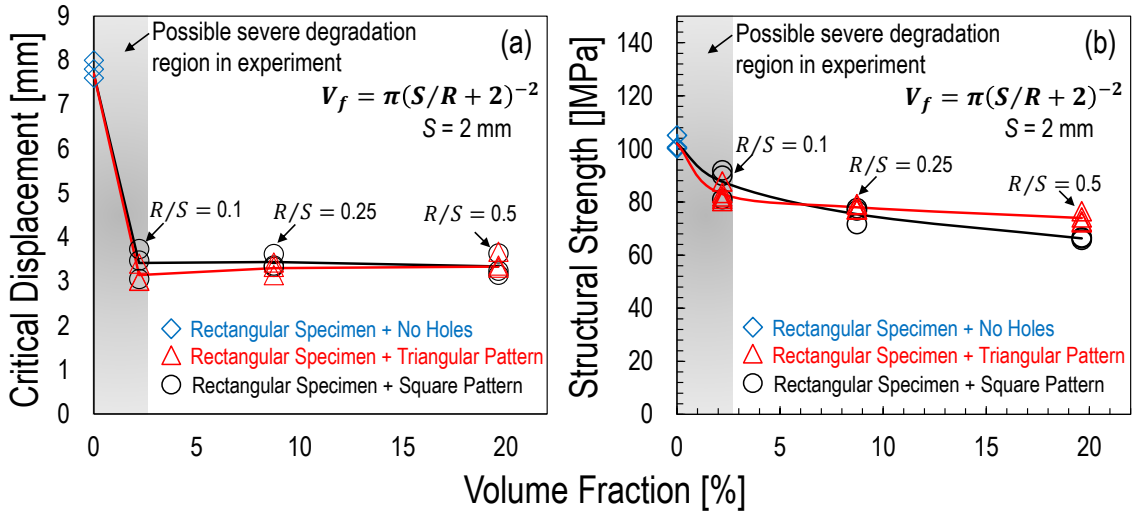

Figure 4.10: Experimental results obtained from three-point bending tests for: (a) critical displacement vs. volume fraction of cylindrical holes; (b) structural strength vs. volume fraction of cylindrical holes. Both square and triangular patterns were investigated in this work.

markable reduction of the structural toughness more than about 70% for both investigated patterns compared to the reference one almost featuring a pronounced plateau after reaching the critical load. Such a noticeable degradation reflects in both critical displacement and structural strength and features different rates with respect to the volume fraction as illustrated in Figure 4.10. The definition of the structural strength in this case has the same expression as written in section 2.3.1. As can be noted from the figure that, while the rapid degradation on both critical displacement and structural strength happens approximately lower than only 2.2% volume fraction of cylindrical holes for both investigated patterns in the experiment, a mild degradation on these aspects was observed up to the maximum investigated volume fraction of cylindrical holes. The foregoing volume fraction is actually only related to the ratio of the cylindrical hole radius R to the edge distance between adjacent cylindrical holes S as shown in Figure 4.10. By knowing the evolution of the structural strength with this ratio R/S is quintessential since it is possible to leverage the small size of porosity to not only prevent the further crack propagation in polymeric materials thus enhancing the structural capability but also have less structural degradation of polymeric materials. This interesting aspect is associated to the optimized design of porosity for the structural performance of polymeric materials which is beyond the purpose of this work.

4.3 Computational Analysis and Discussion

4.3.1 Computational modeling strategy

To have a computational characterization for the plastic deformation and fracture behavior of all the investigated polymeric geometries in this study, the Drucker-Prager (DP) plasticity model was used in the simulations to account the pressure-dependent plastic behavior of thermoset polymers [121–124] whereas the following damage evolution was modeled in the framework of Crack Band model to include all the stress components in the material which was shown to play a significant role in the prediction of the fracture initiation for various materials [22,125,126]. This computational strategy is exactly the same as the one described

in chapter 2 which leads to an excellent agreement with the experimental results of thermoset polymers under various loading conditions.

4.3.2 Toughening mechanisms and characteristics of porosity for crack pinning

By leveraging the foregoing computational strategy, it is curious to initially study why can the porosity impede the crack propagation in the polymeric materials? To answer this question, the conventional material properties of thermoset polymers obtained from the experimental mechanical tests and related computational validations as reported in the literature [22, 94, 108] were used in the simulations as a first attempt to capture the experimental results of pre-cracked specimens featuring different patterns of sub-micron cylindrical holes. Before moving to the insightful discussion on the simulation results, it is worth clarifying what are the conventional material properties of thermoset polymers? By taking a representative example as shown in Figure 4.12a for the dogbone specimen under uni-axial tension, the conventional material strength can be about 55MPa at the critical strain of roughly 7% and the corresponding pre-peak behavior can be described by the same macro-scale Ramberg-Osgood relation as mentioned in chapter 2. On the other hand, the conventional fracture energy of the investigated thermoset polymer can be directly measured from the rectangular specimen only features a sharp edge crack which leads to about 0.8 N/mm as reported in the previous studies [22,94,108] whereas the conventional fracturing evolution can follow either a linear softening behavior for an approximation or a bi-linear one for a better description [96] as highlighted in black curves in Figure 4.12b.

However, the foregoing simulations lead to a miserable underestimation with the experimental results as exemplified in Figure 4.11 for the pre-cracked specimens with 2.2% volume fraction of cylindrical holes arranged in both square and triangular patterns. In other words, the simulations with the conventional material properties of thermoset polymers can only capture the sudden drop of the load due to the initial crack propagation as clearly shown in this figure but fail to further reproduce the crack pinning process induced by the sub-micron cylindrical holes ahead of that initial crack. This unacceptable mismatch clearly shows the

inadequate ability of using conventional material properties of thermoset polymers to characterize the mechanical behavior of the material at the edge tip of the foregoing sub-micron cylindrical holes and further implies a different material behavior at that location which can possibly be the micro-scale behavior of thermoset polymers as recently reported in the literature [17, 22, 81, 108].

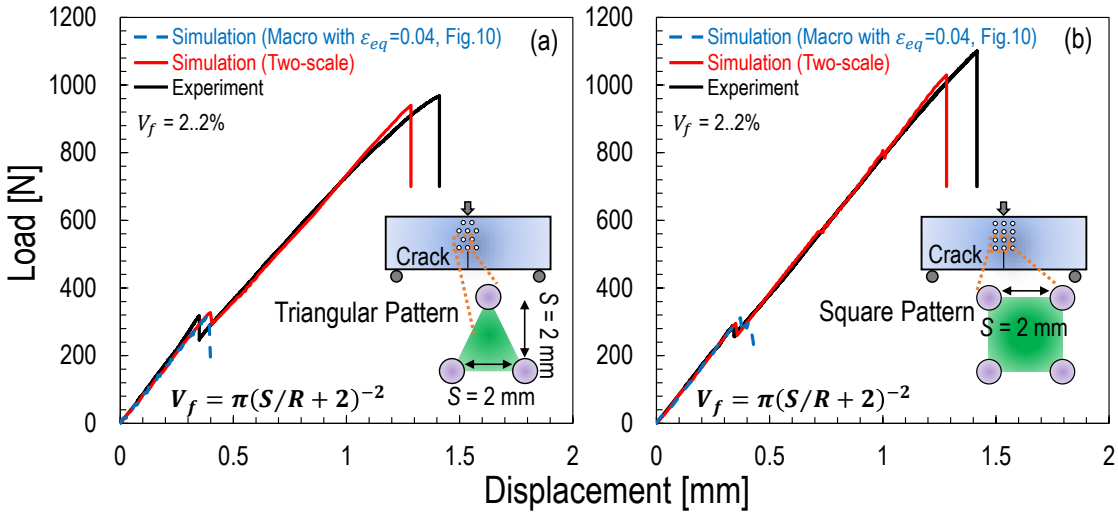

Figure 4.11: Critical comparison between simulation and experiment for the load-displacement curves of pre-cracked specimens featuring both square and triangular patterns of cylindrical holes. Note that two different material behaviors were used in the simulations to illustrate the fact that the experimental results cannot be characterized by using the conventional material properties as typically reported in the literature showing miserable underestimation but an excellent agreement for both cases can be achieved by considering the micro-scale behavior of the material.

Following this direction, the simulations with the same parameters in the DP model (i.e. $k = 1.0$, $\psi = 20^\circ$ and $\beta = 40^\circ$) but a different constitutive law were conducted on the specimens featuring a sharp crack and cylindrical holes. As can be noted from Figure 4.11, the simulation results can have an excellent agreement with the experimental load-displacement curves for both investigated hole arrangements and such a great success is indeed due to the consideration for the micro-scale behavior of thermoset polymers into the constitutive law

in the simulations as plotted in Figure 4.12. In this figure, the non-linear pre-peak behavior can have a possible region for the best match with the experimental results which leads to the micro-scale material strength in the range from about 200 to 300 MPa. This is followed by a steep initial softening with the micro-scale fracture energy about 0.02 N/mm and a mild softening featuring the foregoing conventional material strength and fracture energy. This peculiar behavior is considered as a two-scale constitutive law since the high strength and low fracture energy describe the micro-scale material behavior whereas the low strength and high fracture energy captures the behavior for larger crack opening displacements. It is worth mentioning here that the micro-scale pre-peak behavior of the investigated thermoset polymer also follows the classical Ramberg-Osgood relation with the same parameter $\gamma = 0.005$ but a different exponent n in the range from 2.4 to 4.8.

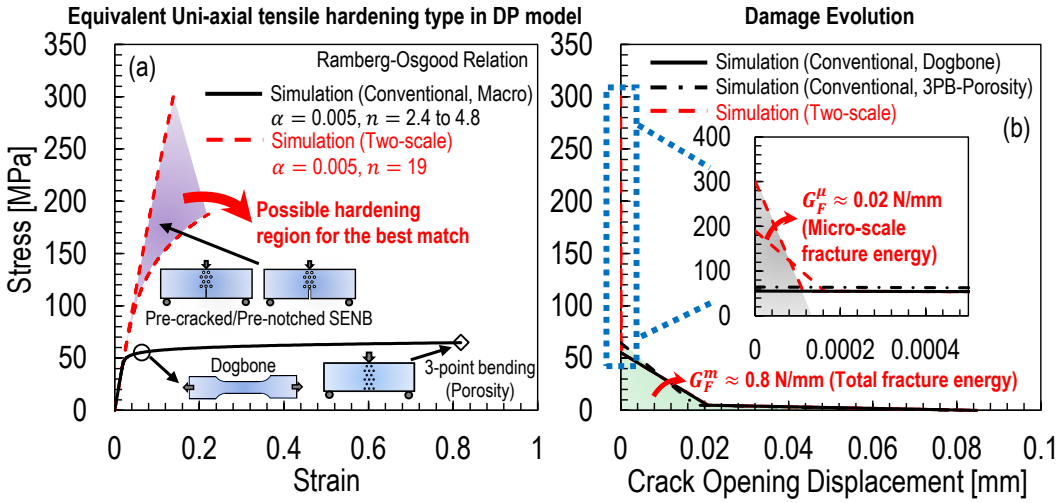

Figure 4.12: Comparison between two-scale and macro-scale (conventional) equivalent uni-axial tensile hardening behavior and damage evolution used in the simulations. Note that both pre-cracked and pre-notched specimens with the sub-micron size of cylindrical holes can only be captured by using two-scale behavior whereas the dogbone specimens and the porous rectangular specimens can only be characterized by using macro-scale (conventional) behavior.

Having illustrated the capability of using the proposed two-scale constitutive law in the

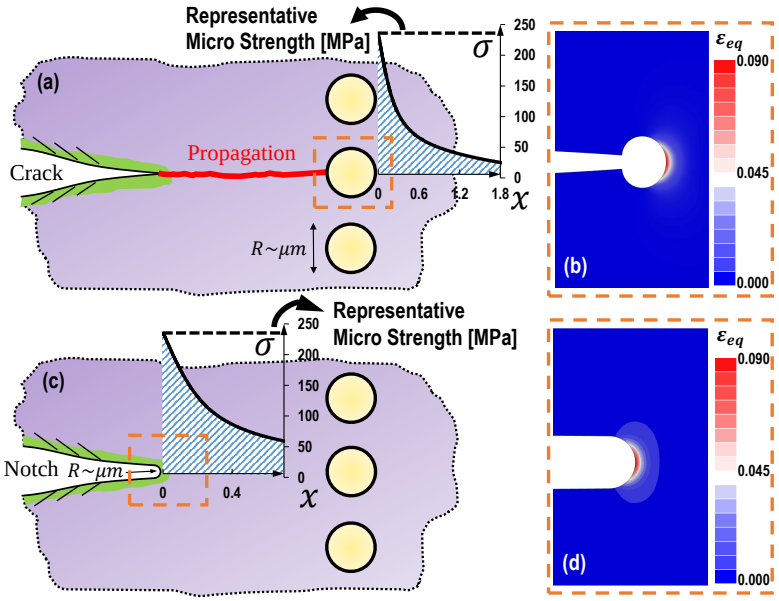

Figure 4.13: Illustration of dominant toughening mechanism of sub-micron porosity for the material with (a-b) sharp crack or (c-d) blunt notch. This mechanism is mainly associated with the activation of micro-scale behavior of thermoset polymers featuring higher material strength. Note that the symbol ε_{eq} represents the equivalent plastic strain.

simulations to mimic the entire fracturing evolution including both initial crack propagation and the following crack arresting due to the sub-micron cylindrical holes, the dominant mechanisms behind this toughening phenomenon can be further clarified as schematically shown in Figures 4.13a-b. In the case of the porous polymeric structure featuring a sharp crack under the Mode I loading condition, the material at the crack tip enters the softening region rapidly due to strong stress intensity at that location thus triggering the fast initial crack propagation as highlighted in red in Figure 4.13a. This propagating crack is immediately hindered by the nearest cylindrical hole mainly due to the activation of the forging micro-scale material strength (200 to 300 MPa) at the edge tip of that hole as illustrated in Figure 4.13a otherwise the crack must penetrate this cylindrical hole since the stress concentration can always lead to the local stress near the edge tip of that hole higher than the conventional material strength of thermoset polymers (50 to 70 MPa) thus leading to the

catastrophic failure of the entire polymeric structure as shown in Figure 4.11. In addition to the contribution of the micro-scale material strength for the crack pinning process, the plasticity of the investigated thermoset polymer also plays a role in arresting the foregoing initial crack propagation as illustrated in Figure 4.13b showing the representative equivalent plastic strain accumulated at the edge tip of the cylindrical hole right before the dramatic failure of the structure. It is definitely worth pointing out here that the plasticity is commonly considered as the main contribution to the crack blunting in the literature for the studies focusing on the polymer toughening [89, 127–129]. However, all the foregoing results show that the higher material strength of thermoset polymers at the micro-scale is the leading factor for hindering the crack propagation through the sub-micron porosity. It is worth mentioning here that the toughening mechanism can be switched to mainly reply on the plasticity of the material if the porosity radius is sufficiently large and this aspect can be considered in the future studies.

Finally, the even smaller sizes of porosity for the crack pinning process can be alternatively investigated through the simulations with the foregoing two-scale constitutive law considering the experimental difficulties in the manufacturing of the cylindrical holes with that sizes. As illustrated in Figure 4.14, the complete evolution of the normalized structural behavior of pre-cracked specimens with the geometries of cylindrical holes (R/S) was plotted through the results from both experiment and simulation. In this figure, the predicted normalized structural stiffness for the porosity with smaller sizes is not noticeably reduced but the normalized structural strength for these cases show a great improvement up to 300% compared to the original pre-cracked specimen without cylindrical holes. This predicted part basically represents the transition from energy-driven to stress-driven failure for the material at the edge tip of the cylindrical hole as reported in the previous work [108] showing the effects of the aspect ratio a_0/R on the fracturing behavior of pre-notched specimens. It is worth mentioning here that all the foregoing predictions are based on the assumption that the material at the edge tip of the cylindrical hole with even smaller sizes has a similar micro-scale behavior. However, the different material behavior at that location of the poros-

ity with different radii can also be possible considering the statistical-energetic size effect of the material and this aspect can also play a role in the foregoing predictions for the smaller sizes of the porosity. But this possibility is definitely positive in the consideration of the higher material strength at lower length scale thus leading to the scenario that the normalized structural strength can be even higher than the computational predictions as plotted in Figure 4.14 for the extremely small sizes of the porosity.

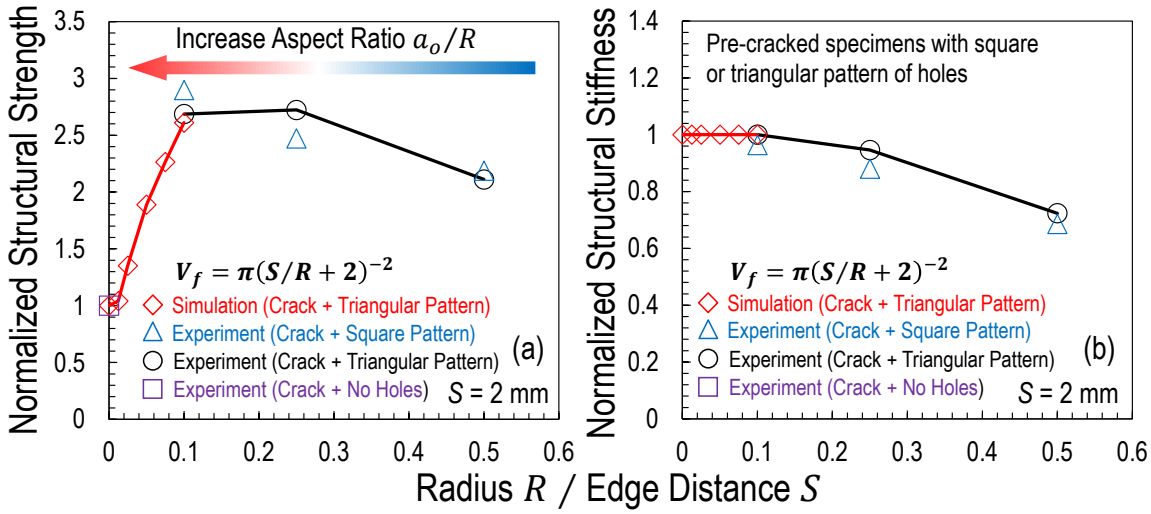

Figure 4.14: Evolution of the following normalized structural behavior for pre-cracked specimens with cylindrical holes constructed by both experimental and computational results: (a) structural strength and (b) structural stiffness. Note that the symbol a_o stands for the initial crack length.

4.3.3 Geometries of cylindrical holes for pre-notched materials

Having computationally shown the impossibility of leveraging conventional material behavior of thermoset polymers to explain the toughening phenomenon of sub-micron porosity for hindering the crack propagation as discussed in section 4.3.2, similar concept can also be used to clarify the failure behavior of polymeric structures in presence of blunt notches with sub-micron radius of curvature investigated in this work. As illustrated in Figure 4.15, the

experimental results of both V- and U-notched specimens with and without cylindrical holes can only be computationally characterized by considering the micro-scale behavior of the material since the use of the macro-scale material behavior as plotted in Figure 4.12 in the simulations can lead to a significant overestimation for pre-notched specimens without cylindrical holes in spite of the excellent agreement with the experimental results for the same geometry but featuring 19.64% volume fraction of cylindrical holes arranged in triangular pattern. This comparison confirms the previous discussion in section 4.2.2.1 that the micro-scale behavior of the material was pre-activated at the sub-micron notch tip before leveraging the following cylindrical holes as schematically shown in Figure 4.13c.

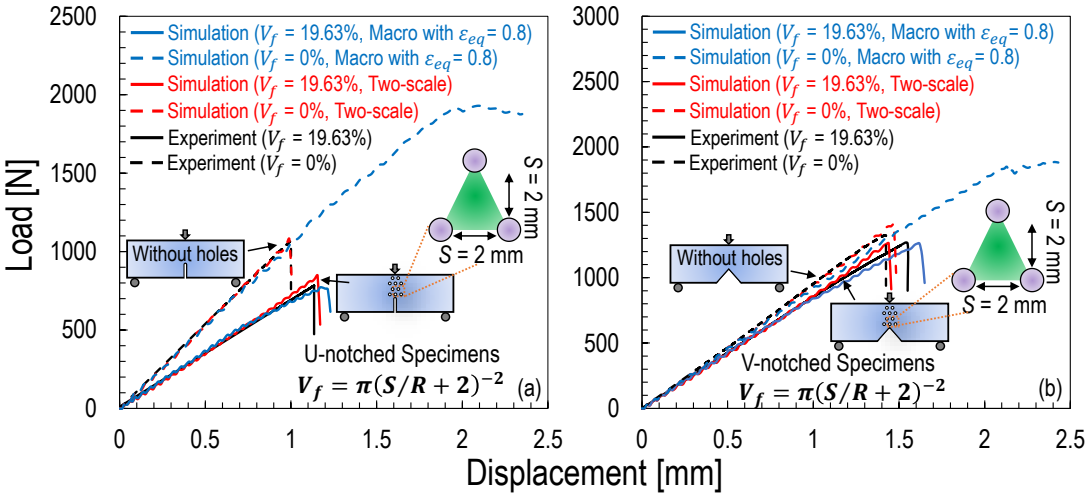

Figure 4.15: Critical comparison between simulation and experiment for the load-displacement curves of (a) U-notched specimens and (b) V-notched specimens. Note that two different material behaviors were used in the simulations to illustrate the fact that the material behavior in this scenario must be different from the previous one used for porous rectangular specimens as shown in Fig.4.12 in order to have an excellent agreement for both pre-notched specimens with and without cylindrical holes.

In the light of the successful characterization with the experimental results, the evolution of the normalized structural strength and stiffness of both V- and U-notched specimens with the geometries of cylindrical holes (R/S) can also be further computationally obtained

as plotted in Figure 4.16. In this figure, the structural strength and stiffness exhibit a gradual degradation for both notch types which differs from the forgoing results for the intact polymeric structures with cylindrical holes showing a severe degradation for the existence of the sub-micron porosity. This difference indicates that the structural performance of pre-notched specimens is mainly dependent on the volume of the material located at the notch tip as long as the radius of the porosity is not sufficiently large and this aspect corresponds to the micro-scale behavior of the material due to the sufficiently small volume of the material at the notch tip for the participation of the deformation.

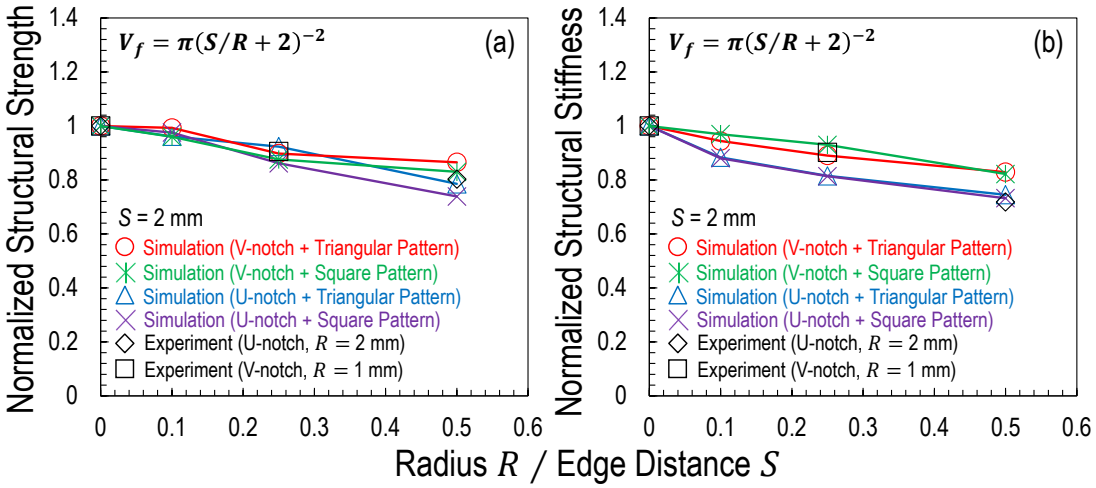

Figure 4.16: Simulation vs. experiment for the following normalized structural behavior of both V- and U-notched specimens with square and triangular patterns of cylindrical holes under three-point bending condition: (a) structural strength and (b) structural stiffness.

4.3.4 Characteristics of intact materials with cylindrical hole

The extremely small size of porosity for the less structural degradation of intact polymeric materials can also be alternatively investigated through the computational analysis. To reach this goal, the plastic deformation and fracture behavior of the material only with cylindrical holes under three-point bending condition must be initially calibrated from the

experimentally investigated specimens. As illustrated in Figure 4.17, the excellent agreement with the experimental load-displacement curves for all the investigated cases can be better achieved by leveraging the Drucker-Prager plasticity model with the same parameters (i.e. $k = 1.0$, $\psi = 20°$ and $\beta = 40°$) and the constitutive behavior of the material as shown in Figure 4.12 which differs from the foregoing micro-scale constitute behavior of the material. In this figure, the uni-axial pre-peak behavior of the material follows exactly the same macro-scale Ramberg-Osgood relation as mentioned in chapter 2 but the calibrated critical strain for damage initiation being one order of magnitude larger than the previous conventional value (7%) obtained form the uni-axial tensile tests on dogbone specimens.

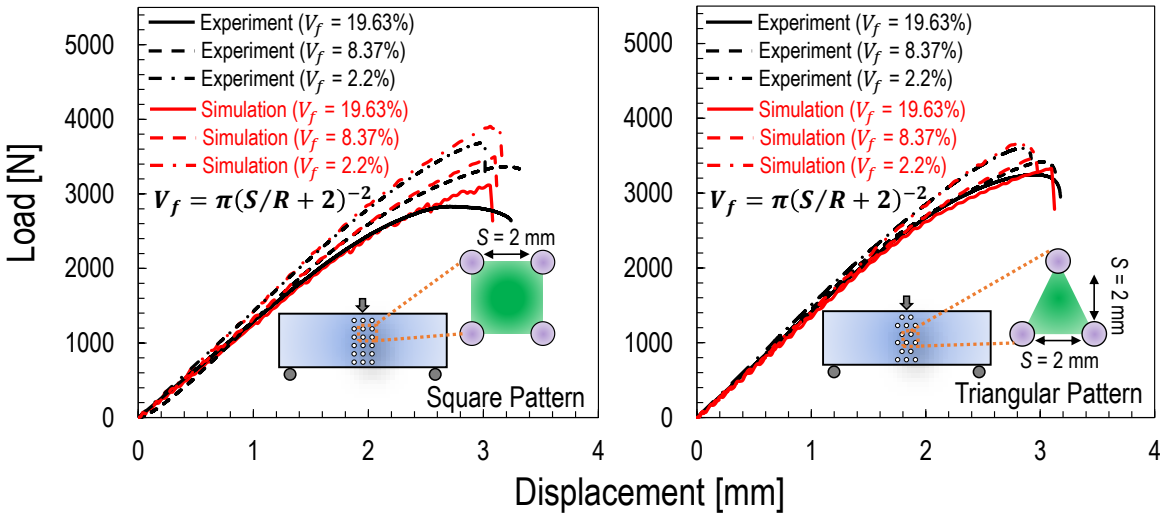

Figure 4.17: Simulation vs. experiment for the load-displacement curves of rectangular specimens with different patterns and volume fractions of cylindrical holes.

Such a remarkable difference mainly depends on the local stress state in the specimen which was reported for various materials in the literature [22, 125, 126, 130]. Thanks to the introduction of cylindrical holes in the material, the larger critical strain can be activated due to the local deviatoric stresses in the material and this aspect actually can be indicated from the critical comparison on the morphological features between experiment and simulation as

exemplified in Figure 4.18 showing a pronounced pattern of shear bands between cylindrical holes in the rectangular specimen under three-point bending condition. It is worth mentioning here that the simulation results for these cases were less affected by the damage evolution part as plotted in dashed black curves in Figure 4.12b thus the use of a linear softening law with the same fracture energy leading to the similar results.

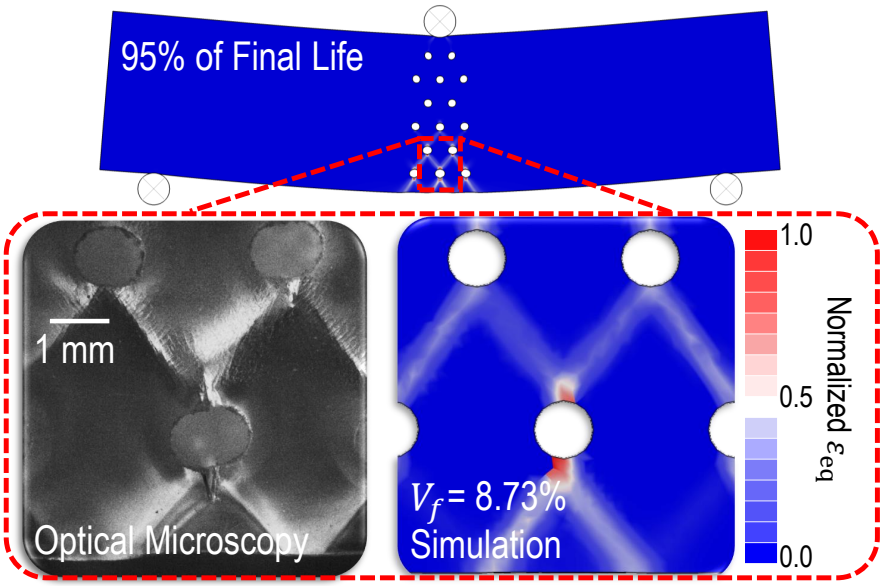

Figure 4.18: Experimental morphology vs. simulation result for the rectangular specimen with triangular pattern of 8.73% volume fraction of cylindrical holes under three point bending condition at 95% of total quasi-static life. Note that ε_{eq} represents the equivalent plastic strain.

By leveraging the foregoing model, the structural behavior of the same material with other geometries of cylindrical holes which was not experimentally investigated in this work can be further computationally predicted. Thanks to this aspect, the complete evolution of the normalized structural strength with the geometries of cylindrical holes (R/S) can be successfully achieved as illustrated in Figure 4.19a. It was observed from this figure that the severe degradation region for the structural strength of intact polymeric materials under three-point bending condition was further reduced to the ratio about $R/S = 0.025$ which

corresponds to 0.18% volume fraction of cylindrical holes. The foregoing results were further confirmed through the additional computational tests on the specimens with different radii and spacing of cylindrical holes as exemplified in Figure 4.19b which shows minor difference on the normalized structural strength of these cases as long as the same ratio of the hole radius R to the edge distance S between holes was considered.

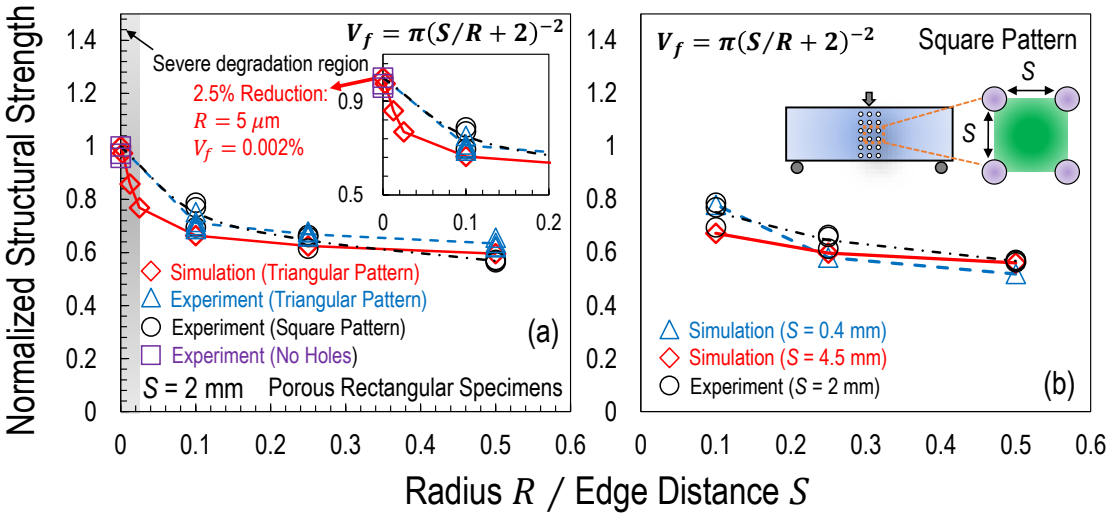

Figure 4.19: Simulation vs. experiment for the normalized structural strength of porous rectangular specimen under three-point bending condition. This figure compares and predicts the following cases: (a) different patterns and volume fractions of cylindrical holes but the same spacing $S = 2$mm between adjacent cylindrical holes ; (b) square pattern of cylindrical holes with different radii and spacing.

4.4 Conclusions

1. Crack propagation in the investigated thermoset polymer can be effectively hindered through the porosity and the extent of the corresponding structural improvement depends on the geometries of the porosity and the initial crack length;

2. By leveraging both experimental and numerical analyses, the best structural capacity (i.e. critical load of the structure) can be maximized up to three times through the

porosity leading to about ten times improvement on the apparent Mode I fracture energy ($G_f \approx 10$N/mm) which is comparable to the related value measured from conventional metals ($G_f \approx 5 \sim 15$N/mm);

3. The foregoing excellent toughening behavior cannot be computationally explained by using conventional material properties of thermoset polymers in the literature (material strength $f_t \approx 50 \sim 70$MPa and fracture energy $G_f \approx 0.1 \sim 1.0$N/mm) and the underlying reason is attributed to the distinct mechanical behavior of thermoset polymers at small length scale featuring higher material strength ($f_t^{\mu} \approx 200 \sim 300$MPa) and lower fracture energy ($G_f^{\mu} \approx 0.01 \sim 0.02$N/mm);

4. This interesting aspect, to the best of authors' knowledge, was never reported in the literature for studying the toughening mechanisms of polymers through various methods [122,127–129] since the plastic deformation of the material induced by the foregoing methods was always considered as the main mechanism for blunting the crack thus improving the structural behavior of polymeric materials;

5. On the other hand, the porosity cannot further improve but can reduce the critical load of polymeric structures without the initiation of the sharp crack and this unsatisfactory aspect can be seen from the results for both porous rectangular specimens with and without pre-existing notches under three-point bending condition;

6. The reasons for the worse performance of the foregoing cases are intrinsically different since the porous rectangular specimens with the investigated notches already activate the higher material strength at the small notch tip whereas a remarkable plasticity formed by shear bands at the bottom of the same specimens without any notches does not activate the foregoing exceptional behavior of the material;

7. Regarding the difference between square and triangular patterns of the porosity, the latter case can possibly deflect the path of the crack propagation depending on the geometries of the porosity and the orientation of the arrested crack as shown in the

results for the porous rectangular specimens featuring a sharp edge crack. In this consideration, the triangular pattern of the porosity can be a better candidate in the real engineering applications due to the random direction of the crack initiation in the polymeric structures under complex service load;

8. In order to achieve an even comprehensive and accurate design, the following aspects can be taken into further consideration: (a) the structural size of polymeric materials; (b) the initial crack length versus the radius of the porosity; (c) the possible different material strength and inelastic behavior evolving with the notch radius. These are considered as the future publications.

Chapter 5

THERMOSET POLYMER NANO-MODIFIED BY GRAPHENE NANOPLATELETS

In this chapter, the mechanical and thermal behavior of thermoset polymer with the addition of different contents of graphene nanoplatelets were further experimentally and computationally studied. It was shown that the graphene nanocomposites with the investigated sizes exhibit strong quasi-brittle fracturing behavior due to the complex damage mechanisms dissipating the energy which cannot be simply characterized by leveraging the Linear Elastic Fracture Mechanics showing significant errors. By further conducting the cohesive zone modeling analysis, it was confirmed that the foregoing non-linear fracturing behavior of graphene nanocomposites can also be better described with a bi-linear cohesive law rather than a traditional linear one. More importantly, the initial part of that cohesive law representing the initial fracture energy was shown almost no improvement with increasing the graphene content whereas the total area under the bi-linear cohesive law representing the total fracture energy was remarkably improved with the addition of graphene nanoplatelets.

5.1 Materials and preparation

Thermoset polymer used in this work was exactly the same as described in the foregoing chapters. The nanofiller was A-12 Graphene Nanoplatelet (Graphene Supermarket [131]) with an average flake thickness of greater than 3 nm (between 3-8 graphene monolayers) and lateral dimensions of approximately 2-8 microns.

For the preparation of the epoxy/graphene specimens, the desired amount of epoxy and graphene was mixed for 10 minutes and then high shear mixed at 1500 rpm for 20 minutes by means of an electrically activated high shear mixer with a 48 mm impeller (Mixer Direct

[132]). To promote platelet exfoliation, shear mixing was followed by sonication using a Hielscher UP200S sonicator [133] with a 7 mm sonotrode for 20 minutes at 70% amplitude and a duty cycle of 0.5 (it is worth noting here that a similar procedure was successfully adopted by the authors for the exfoliation of nanoclays in thermoset polymers [72,134,135]). The high shear mixing and sonication processes are shown in Figures 5.1a and 5.1b. After that, the following procedures are the same as the manufacturing of pure thermoset polymer as described in the previous chapters.

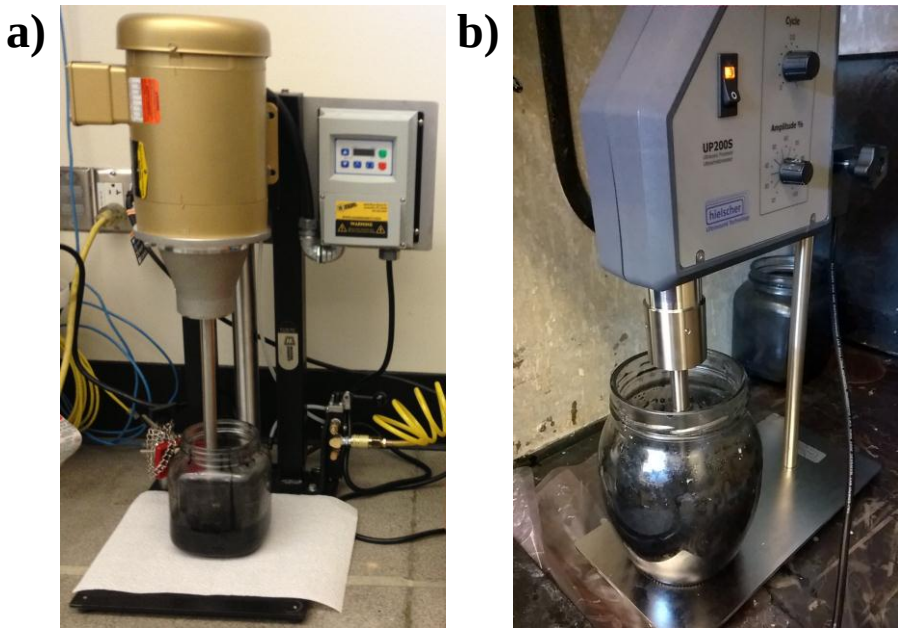

Figure 5.1: Graphene specimen preparation equipment: a) high shear mixer; b) sonicator.

5.2 Experimental results

To study the effect of graphene nanoplatelets on the mechanical behavior of thermoset polymer (e.g. Young's modulus, ultimate strength, ductility, etc.), four material configurations characterized by different graphene weight contents were prepared for uni-axial tensile tests, namely: pure epoxy, 0.3 wt%, 0.9 wt%, and 1.6 wt%. On the other hand, fracturing behavior

due to the addition of graphene nanoplatelets were studied by leveraging three-point bending tests on the SENB specimens with the same graphene weight contents as aforementioned for uni-axial tests. It was mentioning here that the dimensions for uni-axial tensile and fracture tests were exactly the same as the foregoing studies on the pure thermoset polymer.

5.2.1 Uni-axial tensile tests

The true stress and strain curves obtained from uni-axial tensile tests are plotted in Figure 5.2 for dogbone specimens of different graphene concentrations. As can be noted from the figure, all the tests were characterized by a significant non-linear behavior which becomes less and less significant with increasing graphene content.

This can be due to a higher presence of voids or defects with higher amounts of graphene which may lead to localization and failures during the non-linear deformation. On the other hand, the Young's modulus and ultimate tensile strength are plotted in Figure 5.3. As can be noted, the addition of graphene did not significantly affect the elastic behavior and strength of the investigated material.

5.2.2 Mode I fracture tests

The load-displacement curves of fracture tests are plotted in Figure 5.4 for different graphene concentrations. It is worth noting that, for the pure epoxy specimens, the mechanical behavior is linear up to the peak load which is followed by unstable crack propagation. With the addition of graphene, differences in the behavior of small specimens with respect to large specimens become visible, this effect being more pronounced for higher graphene contents.

In fact, while large specimens show a very linear response up to failure, a significant non-linear segment before the peak load characterizes the smaller sizes. This latter aspect indicates hardening inelastic behavior and reduced brittleness (or higher ductility) for the smallest specimen sizes. After reaching the peak load, the specimens exhibited snap-back instability for all the investigated sizes and graphene concentrations. As a consequence, the

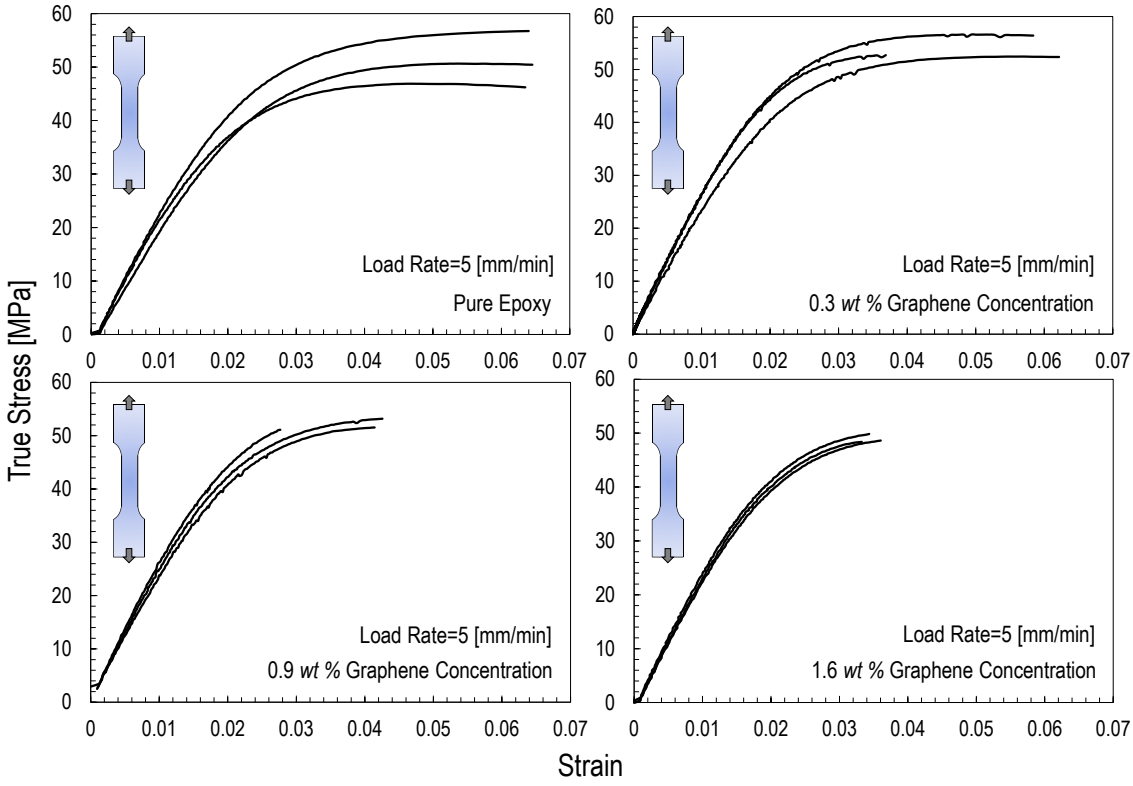

Figure 5.2: True stress vs strain measured from tensile tests on dogbone specimens with different graphene contents.

failures were catastrophic and occurred shortly after the peak load. The crack length, maximum load, and nominal strength for geometrically scaled specimens of different Graphene Concentrations (GC) are tabulated in Table 5.1.

5.2.3 Mode II fracture tests

The Mode II fracturing behavior of graphene nanocomposites was further studied in this section. The load-displacement curves of fracture tests on both pre-cracked and pre-notched ENF specimens with the addition of 1.6 wt% graphene nanoplatelets and different sizes are plotted in Figure 5.5. As can be noted from the figure, the mechanical behavior of the specimen is characterized by a significantly reduced non-linearity before reaching the critical

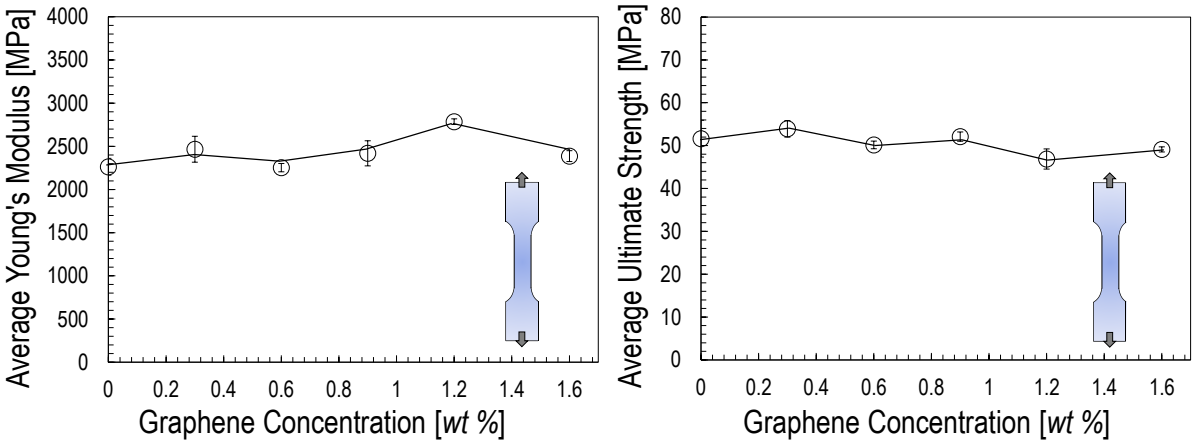

Figure 5.3: Young's modulus and ultimate strength as a function of graphene content.

load compared to the case of pure epoxy under the same loading condition as shown in Figure 2.7. This is mainly attributed to the effects of the graphene nanoplatelets on the reduction of the plastic deformation occurring in front of notch or crack tip and the bottom of the specimen. In addition to this, the critical load of pre-cracked ENF specimen nano-modified by 1.6 wt% graphene nanoplatelets exhibits relatively scattered behavior compared to the one of pure epoxy since the critical load of larger specimen is not always higher than the one of smaller specimen as illustrated in Figure 5.5.

This scattered behavior can also be observed in the calculation of apparent local Mode I fracture energy as illustrated in Figure 5.6. It is worth mentioning here that the fracture energy was calculated by using Eq.(2.2) and the value of $g(\alpha)$ was obtained through the same method as discussed in the previous section 2.3.3. As can be noted from the figure, the apparent local mode I fracture energy of pre-cracked 1.6 wt% graphene nanocomposite tends to exhibit significantly scatted behavior as the specimen size decreases. This is probably due to the fact that the global Mode II fracturing behavior of ENF specimen highly depends on the local dispersion of graphene nanoplatelets as decreasing the specimen size. On the other hand, a scatter of apparent local Mode I fracture energies is in the range from 2 N/mm to 12 N/mm depending on the specimen size. This scattered range is higher than the average Mode

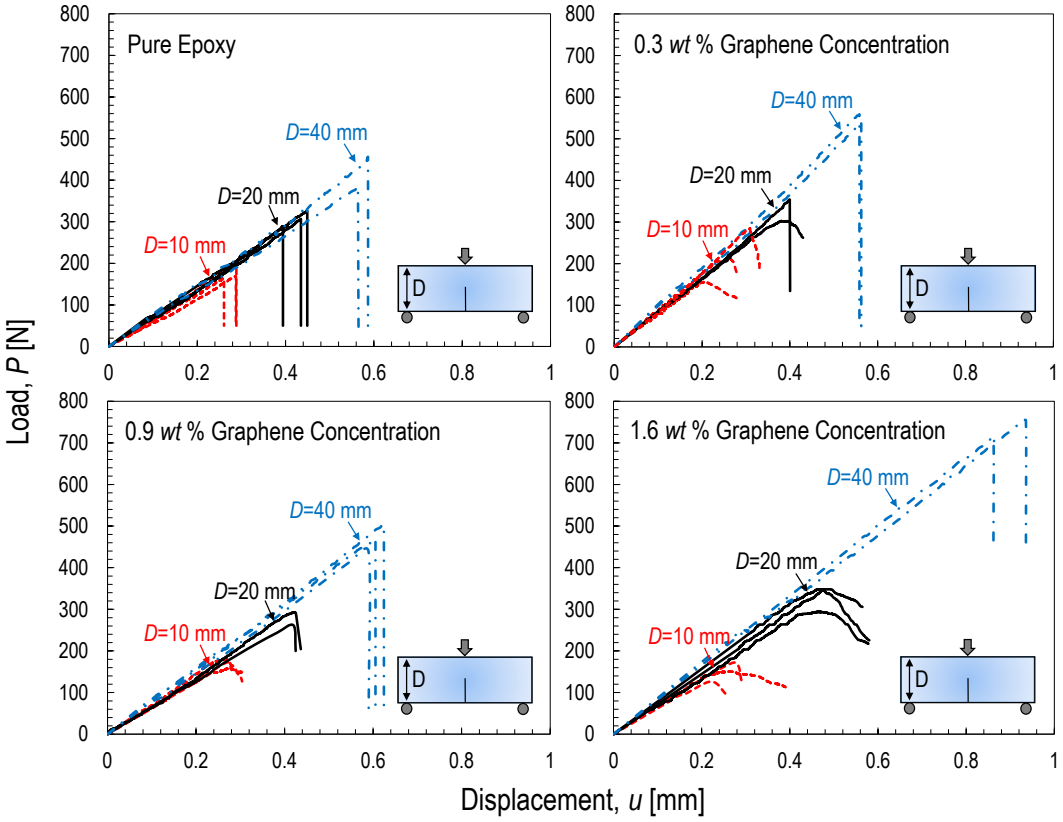

Figure 5.4: Load-displacement curves for different graphene concentrations and specimen sizes.

I fracture energy measured from the corresponding pre-cracked SENB specimen as it will be shown in the following sections. In this consideration, the estimated local Mode I fracture energy was considered as the apparent value, similar to the Mode II case of pure epoxy as described in chapter 2, despite the fact that less plasticity in the investigated graphene nanocomposite affects the calculation of local Mode I fracture energy through pre-cracked and pre-notched ENF specimens by leveraging LEFM.

It is interesting to investigate the fracturing morphology of the specimen with the addition of 1.6wt% graphene nanoplatelets under global Mode II loading condition. As illustrated in Figure 5.7, both pre-notched and pre-cracked specimens fracture at an angle of roughly 70° with respect to the direction of the initial notch or crack which is consistent with the

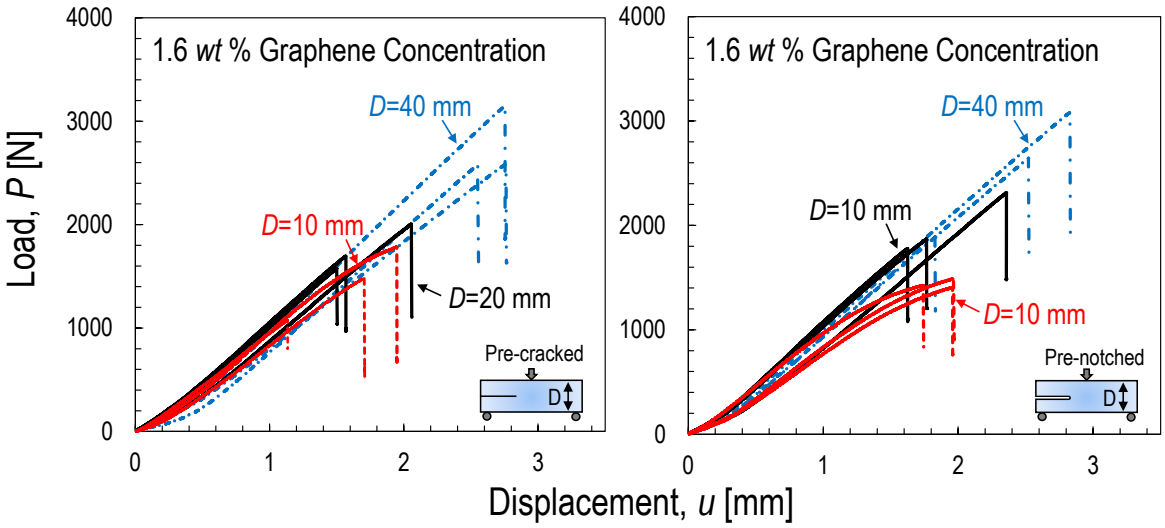

Figure 5.5: Load-displacement curves for pre-cracked and pre-notched ENF specimens with the addition of 1.6 wt% graphene nanoplatelets and different sizes.

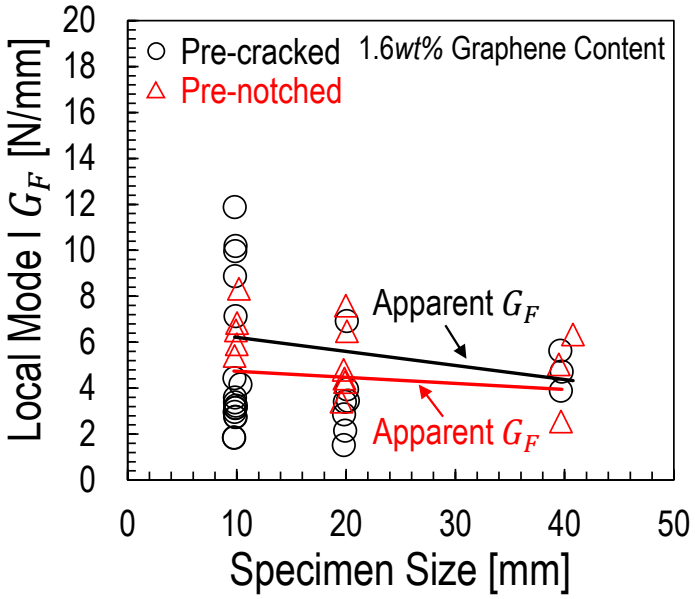

Figure 5.6: Local Mode I fracture energy estimated from LEFM for pre-cracked and pre-notched ENF specimens with the addition of 1.6wt% graphene nanoplatelets and different sizes. Note that all the estimated values are apparent fracture energies.

one for the pure epoxy under the same loading condition. This is another confirmation of the local Mode I fracturing behavior of the specimen under global Mode II loading condition. It is worth mentioning here that, for pre-cracked 1.6wt% graphene nanocomposite, the catastrophic failure does not always happen at the crack tip and may eventually happen at a distance away from the crack tip as shown in Figure 5.7.

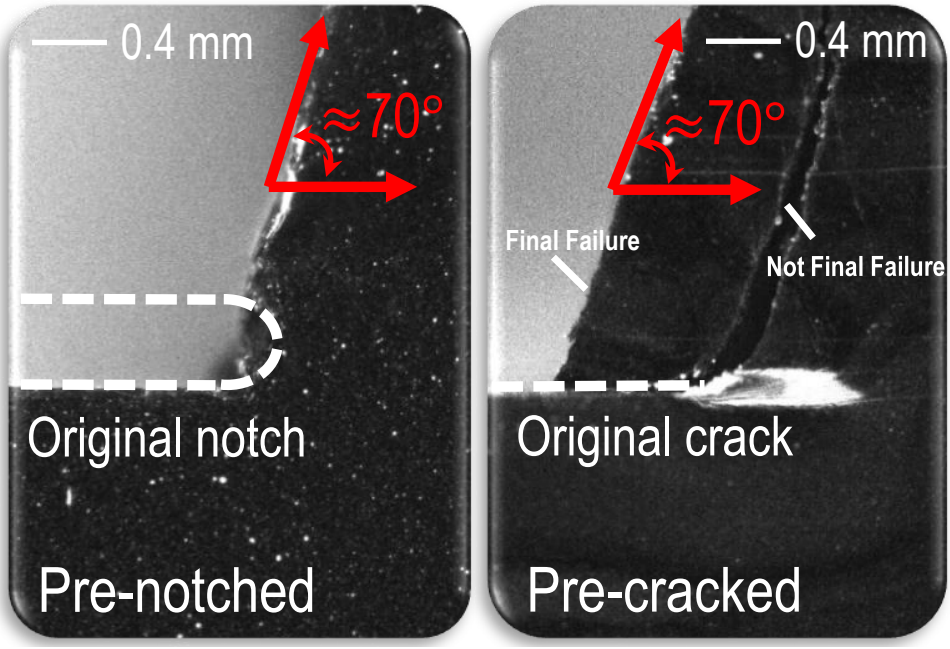

Figure 5.7: Fracture surfaces for pre-cracked and pre-notched ENF specimens with the addition of 1.6wt% graphene nanoplatelets under global Mode II loading condition. Both cases fractured around 70° respect to the direction of initial crack or notch.

5.2.4 SEM analysis

In order to investigate the main nanoscale mechanisms of damage that can lead to an increase in mode I fracture energy of graphene nanocomposites, the SENB specimens were cut and the fracture surfaces were gold-coated in order to be used for Scanning Electron Microscopy (SEM) by a JSM-6010PLUS/LA Electron Microscope [136]. The SEM images of some samples are showed in Figure 5.8 highlighting the differences between each graphene

concentration. As can be noted, the fracture surface of the pure epoxy specimen was very smooth (Figure 5.8a) whereas the surface becomes rougher in texture as the graphene concentration increases (Figure 5.8b-d).

GC (wt%)	Specimen width (mm)	Crack length (mm)	Max load (N)	Nominal strength (MPa)
0.3	D=10	5.01	155.00	7.35
0.3	D=10	4.04	212.84	10.38
0.3	D=10	3.39	284.40	13.45
0.3	D=20	7.03	353.95	9.04
0.3	D=20	4.88	538.00	12.48
0.3	D=20	7.67	302.23	7.78
0.3	D=40	13.84	539.04	6.61
0.3	D=40	13.13	558.68	7.12
0.9	D=10	4.62	179.58	8.39
0.9	D=10	5.19	157.52	6.87
0.9	D=10	5.21	172.87	7.36
0.9	D=20	8.46	292.67	7.10
0.9	D=20	9.86	261.56	5.94
0.9	D=40	15.86	503.51	6.04
0.9	D=40	16.93	469.50	5.52
0.9	D=40	17.68	457.80	5.15
1.6	D=10	5.69	150.36	6.51
1.6	D=10	5.54	171.04	7.49
1.6	D=10	6.02	126.40	5.61
1.6	D=20	9.27	348.10	7.76
1.6	D=20	9.04	348.27	7.92
1.6	D=20	10.35	294.07	6.56
1.6	D=40	13.80	717.68	8.41
1.6	D=40	13.53	769.07	8.73

Table 5.1: Max load and nominal strength of specimens at different graphene concentrations.

Higher magnification images in the propagation region are shown in Figures 5.9a-c for 0.9 wt% and 1.6 wt% graphene concentrations. Based on the pictures, the damage mechanisms are shown to be the following: a) microcrack deflection; b) microcrack pinning; and c)

separation between graphene layers. As Figure 5.9a shows, crack deflection occurs when the crack front meets the surface of the graphene sheets and the crack is deflected leading to crack propagation around the graphene sheet into another plane. On the other hand, Figure 5.9b shows that when the crack front meets the surface of the graphene sheets, it becomes pinned and splits into two cracks. Finally, as shown in Figure 5.9c, when the crack front meets the edge of the graphene sheets, the crack continues to propagate in between the layers, splitting the agglomerate in two.

These damage mechanisms, schematically illustrated in Figure 5.10, cause the crack to take a more torturous path thus requiring more energy to be released during the crack propagation. It is worth mentioning that similar damage mechanisms were reported by Chandrasekaran *et al.* [137, 138] for graphene nanocomposites and by Quaresimin *et al.* [134] and Zappalorto *et al.* [72, 135] for nanofillers of similar morphology.

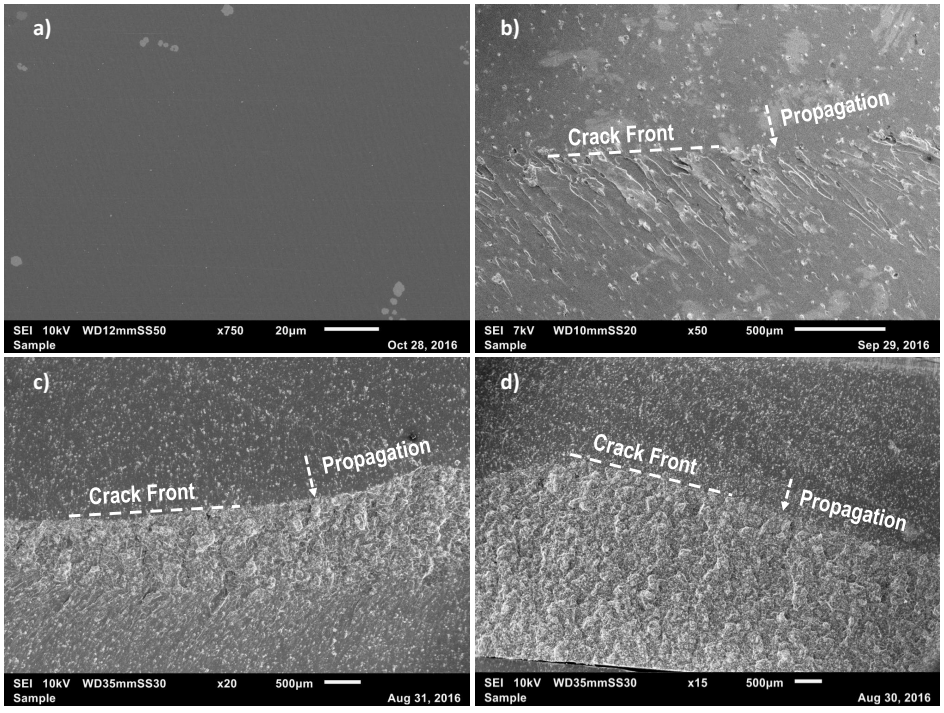

Figure 5.8: Fracture surfaces of specimens at different graphene concentrations: a) Pure epoxy; b) 0.3 wt%; c) 0.9 wt%; d) 1.6 wt%.

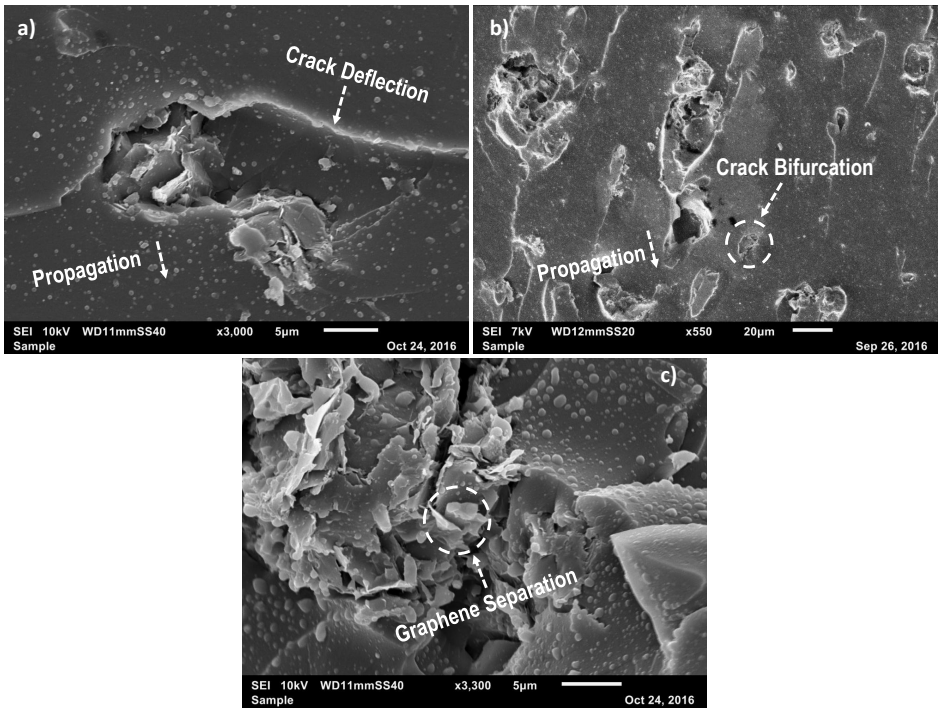

Figure 5.9: Damage mechanisms of graphene nanocomposites: a) crack deflection (1.6 wt% graphene concentration); b) crack pinning/bifurcation (0.9 wt% graphene concentration); c) separation between graphene layers (1.6 wt% graphene concentration).

5.3 Analysis and discussion

The size of the non-linear Fracture Process Zone (FPZ) occurring in the presence of a large stress-free crack is generally not negligible. The stress field along the FPZ is nonuniform and decreases with crack opening, due to discontinuous cracking, micro-crack deflection, micro-crack pinning and graphene layer separations [137, 138]. As a consequence, the fracturing behavior and, most importantly, the energetic size effect associated with the given structural geometry, cannot be described by means of classical Linear Elastic Fracture Mechanics (LEFM). To capture the effects of a finite, non-negligible FPZ, the introduction of a characteristic (finite) length scale related to the fracture energy and the strength of the material is necessary [101–103, 139, 140].

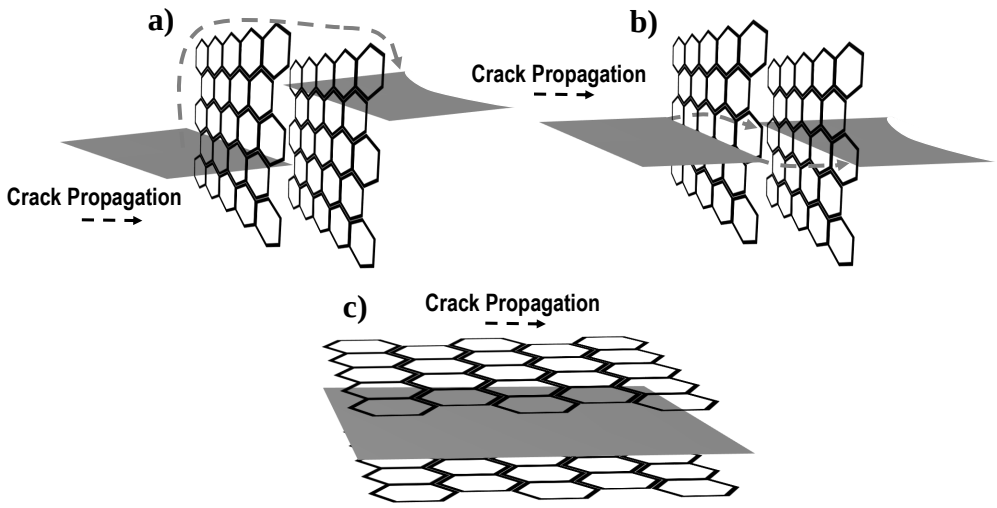

Figure 5.10: Schematic damage mechanisms of graphene nanocomposites: a) crack deflection; b) crack bifurcation/pinning; c) separation between graphene layers.

5.3.1 Analysis of Mode I fracture tests by Size Effect Law (SEL)

5.3.1.1 Size effect law for graphene nanocomposites

The fracture tests can be analyzed leveraging on an equivalent linear elastic fracture mechanics approach to account for the presence of a FPZ of finite size as shown in Figure 5.11. To this end, an effective crack length $a = a_0 + c_f$ with $a_0 =$ initial crack length and $c_f =$ effective FPZ length is considered. Following LEFM, the failure condition can now be written as

$$G\left(\alpha_0 + c_f/D\right) = \frac{\sigma_{Nc}^2 D}{E^*} g\left(\alpha_0 + c_f/D\right) = G_f \tag{5.1}$$

where G_f is the mode I fracture energy of the material and c_f is the effective FPZ length, both assumed to be material properties. It should be remarked that this equation characterizes the peak load conditions if $g'(\alpha) > 0$, i.e. only if the structure has positive geometry [102].

By approximating $g\left(\alpha\right)$ with its Taylor series expansion at α_0 and retaining only up to the linear term of the expansion, one obtains:

$$G_f = \frac{\sigma_{Nc}^2 D}{E^*} \left[g(\alpha_0) + \frac{c_f}{D} g'(\alpha_0) \right] \tag{5.2}$$

which can be rearranged as follows [102]:

$$\sigma_{Nc} = \sqrt{\frac{E^* G_f}{Dg(\alpha_0) + c_f g'(\alpha_0)}} \tag{5.3}$$

where $g'(\alpha_0) = \mathrm{d}g(\alpha_0)/\mathrm{d}\alpha$.

This equation relates the nominal strength of geometrically scaled structures to a characteristic size, D and it can be rewritten in the following form:

$$\sigma_{Nc} = \frac{\sigma_0}{\sqrt{1 + D/D_0}} \tag{5.4}$$

where $\sigma_0 = (E^* G_f / c_f g'(\alpha_0))^{0.5}$ and $D_0 = c_f g'(\alpha_0)/g(\alpha_0) =$ constant, depending on both FPZ size and specimen geometry. Contrary to classical LEFM, Eq. (5.4) is endowed with a characteristic length scale D_0. This is key to describe the transition from ductile to brittle behavior with increasing structure size reported in the fracture tests.

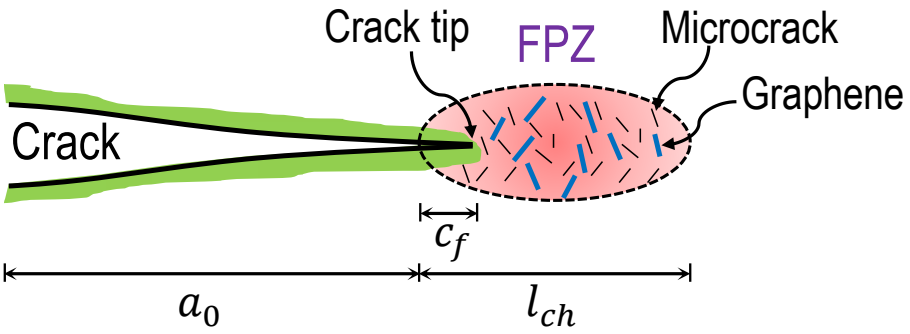

Figure 5.11: Fracture Process Zone (FPZ) for quasi-brittle materials.

5.3.1.2 Fitting of experimental data by SEL

The values of G_f and c_f can be determined by regression analysis of the experimental data. Assuming geometrically scaled structures, Bažant *et al.* [102] proposed to define the following:

$$X = D, \quad Y = \sigma_{Nc}^{-2} \tag{5.5}$$

$$\sigma_0 = C^{-1/2}, \quad D_0 = \frac{C}{A} = \frac{1}{A\,(\sigma_0)^2} \tag{5.6}$$

thanks to this, Eq. (5.4) can now be expressed in the following linear form:

$$Y = AX + C \tag{5.7}$$

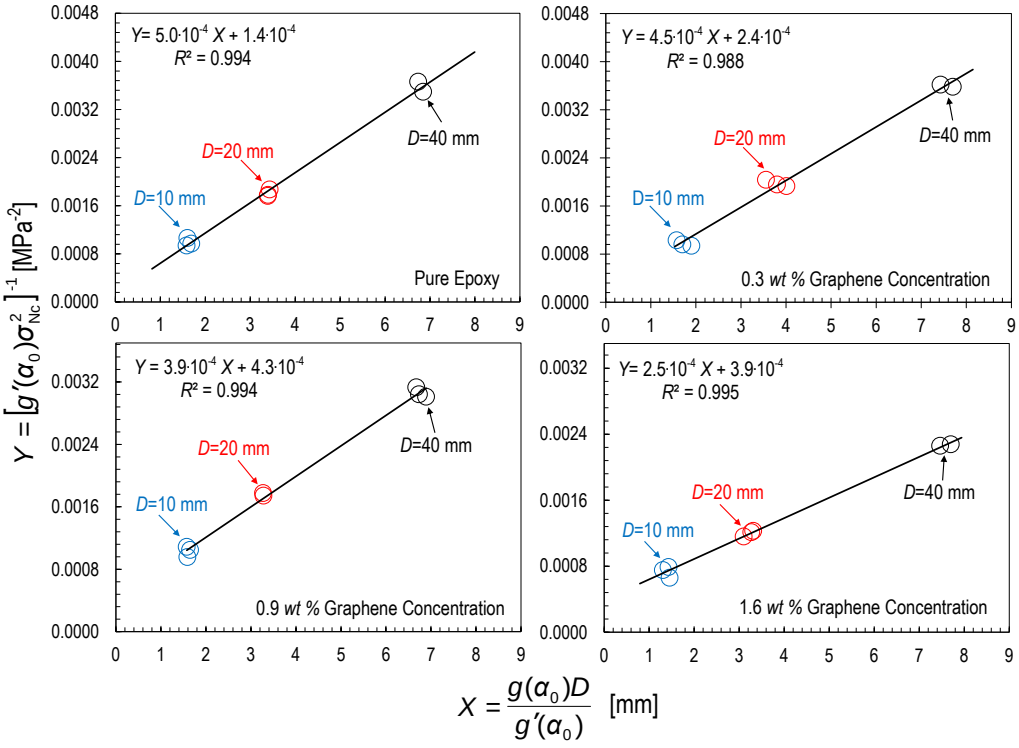

Figure 5.12: Estimation of fracture parameters G_f and c_f by fitting experimental data using Eq. (5.9).

Eq. (5.7) can be used to perform a linear regression analysis of the size effect data provided that all the specimens are scaled exactly (i.e. $g(\alpha_0)$ and $g'(\alpha_0)$ take the same values for all the tests). This implies that all the specimens of different sizes have the same normalized crack lengths. However, since the initial cracks for the nanocomposites were created by tapping, a perfect scaling could not be guaranteed. To overcome this issue, in this study, Eq. (5.7) was rearranged as follows:

$$\frac{1}{g'(\alpha_0)\sigma_{N_c}^2} = \frac{g(\alpha_0)}{g'(\alpha_0)E^*G_f}D + \frac{c_f}{E^*G_f} \tag{5.8}$$

$$Y = BX + M \tag{5.9}$$

where now $X = g(\alpha_0)D/g'(\alpha_0)$, $Y = (g'(\alpha_0)\sigma_{Nc}^2)^{-1}$, $B = (E^*G_f)^{-1}$, and $M = c_f/E^*G_f$. Following Eq. (5.9), a linear regression analysis was conducted for all the graphene concentrations as represented in Figure 5.12 and the parameters B and M, reported in Figures 5.12a-d, could be estimated for all the graphene concentrations.

It is interesting to note that the slope B of the regression curve decreases significantly with increasing concentrations of graphene whereas the intercept M shows an opposite trend. As can be noted from the expressions of B and M, a milder slope denotes a higher mode I fracture energy thus confirming a toughening effect of the graphene nanoplatelets. Conversely, for increasing fracture energies, a higher value of the intercept indicates an increasing size of the effective Fracture Process Zone (it is worth mentioning here that the case of a material with negligible FPZ, as assumed by LEFM, corresponds to regression lines passing through the origin). This suggests an increasing ductility of the material system with increasing graphene content.

5.3.2 Estimation of Mode I fracture properties by SEL

The parameters of the size effect law, B and M, can be directly related to the mode I fracture energy of the material, G_f and the effective FPZ size, c_f as follows:

$$G_f = \frac{1}{E^*B}, \quad c_f = \frac{M}{B} \tag{5.10}$$

provided that the functions $g(\alpha)$ and $g'(\alpha) = \mathrm{d}g(\alpha)/\mathrm{d}\alpha$ and the elastic modulus E^* are known. The function $g(\alpha)$ was obtained through the same method as described in the previous chapter and the expression is written in Eq. (2.3). To determine the function $g'(\alpha)$, various normalized crack lengths close to the selected value of α were considered in order to calculate the tangent slope of $g(\alpha)$ through linear interpolation. Based on the numerical analysis, the following polynomial fitting, plotted in Figure 5.13, was obtained:

$$g'(\alpha) = 18909\alpha^5 - 31733\alpha^4 + 20788\alpha^3 - 6461.5\alpha^2 + 955.06\alpha - 50.88 \tag{5.11}$$

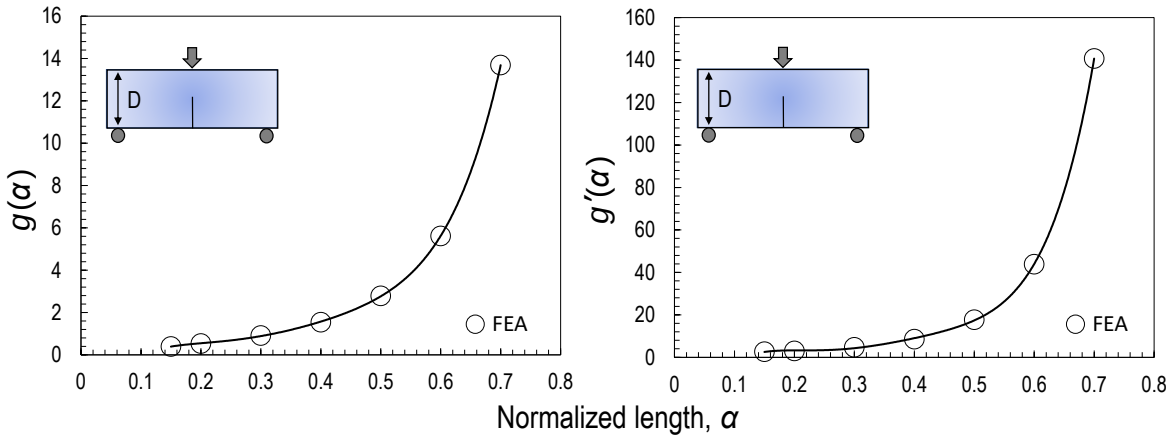

Figure 5.13: Dimensionless energy release rate $g(\alpha)$ and its first derivative $g'(\alpha)$ as a function of normalized crack length $\alpha = a/D$. The functions are calculated by means of FEA.

Graphene concentration (wt%)	Fracture energy G_f (N/mm)	c_f (mm)
0	0.880	0.283
0.3	0.911	0.546
0.9	1.059	1.096
1.6	1.693	1.587

Table 5.2: Experimental G_f and c_f values for different graphene concentrations.

The mode I fracture energy G_f and the effective FPZ length c_f estimated by means of Eq. (5.10) are tabulated in Table 5.2. It is worth noting here that, indeed, the addition of graphene led to an enhancement of the mode I fracture energy which increased from 0.880 N/mm for the pure epoxy case to 1.693 N/mm for the 1.6 wt% case, a 92.4% improvement. On the other hand, the addition of graphene caused a larger FPZ size which changed from 283 μm to 1587 μm. This latter aspect is of utmost importance: while the inherent assumption of LEFM of a negligible FPZ seems reasonable for the pure epoxy case, this is not true for graphene-modified specimens which show a FPZ about one order of magnitude larger and not negligible compared to e.g. the specimen width. This is in agreement with the

results obtained by Salviato *et al.* for other nanocomposite systems by means of multi-scale analytical models [141–149]. The importance of the finiteness of the FPZ for the estimation of nanocomposite fracture energy and its consequences on the structural scaling will be discussed in the following sections.

5.3.3 Size effect analysis

To investigate the scaling behavior of structural strength, it is interesting to analyze perfectly geometrically scaled specimens of different sizes. Now that the fracture properties of the various material systems are known, it is possible to estimate the structural strength for a given normalized crack length starting from the experimental data. In fact, let us consider a crack length of $0.5D$ for all the specimen sizes. One can relate the experimental results, calculated for crack lengths close to $0.5D$ but not exactly $0.5D$, to the desired case by imposing that the energy release rate at failure is G_f in both cases:

$$\frac{\sigma_{Nc,exp}^2 D}{E^*}\left[g(\alpha_{0,exp})+\frac{c_f}{D}g'(\alpha_{0,exp})\right]=\frac{\sigma_{Nc,desired}^2 D}{E^*}\left[g(0.5)+\frac{c_f}{D}g'(0.5)\right] \tag{5.12}$$

This leads to the following expression for the adjusted nominal strength:

$$\sigma_{Nc,desired}=\sigma_{Nc,exp}\sqrt{\frac{Dg(\alpha_{0,exp})+c_f g'(\alpha_{0,exp})}{Dg(0.5)+c_f g'(0.5)}} \tag{5.13}$$

The experimental data adjusted according to Eq. (5.13) and the fitting by SEL are shown in Figures 5.14a-d where the structural strength σ_{Nc} is plotted as a function of the structure size D in double logarithmic scale. In such a graph, the structural scaling predicted by LEFM is represented by a line of slope $-1/2$ whereas the case of no scaling, as predicted by stress-based failure criteria, is represented by a horizontal line. The intersection between the LEFM asymptote, typical of brittle behavior, and the plastic asymptote, typical of ductile behavior, corresponds to $D = D_0$, called the *transitional size* [102]. As can be noted from Figure 5.14a, the experimental data related to the pure epoxy system all lie very close to the LEFM asymptote showing that, for the range of sizes investigated in this work (or larger sizes), linear elastic fracture mechanics provides a very accurate description of

fracture scaling. This confirms that, for the pure epoxy and sufficiently large specimens, the FPZ size has a negligible effect and LEFM can be applied, as suggested by ASTM D5045-99. However, this is not the case for graphene nanocomposites which, as Figures 5.14b-d show, are characterized by a significant deviation from LEFM, the deviation being more pronounced for smaller sizes and higher graphene concentrations. In particular, the figures show a transition of the experimental data from stress-driven failure, characterized by the horizontal asymptote, to energy driven fracture characterized by the $-1/2$ asymptote.

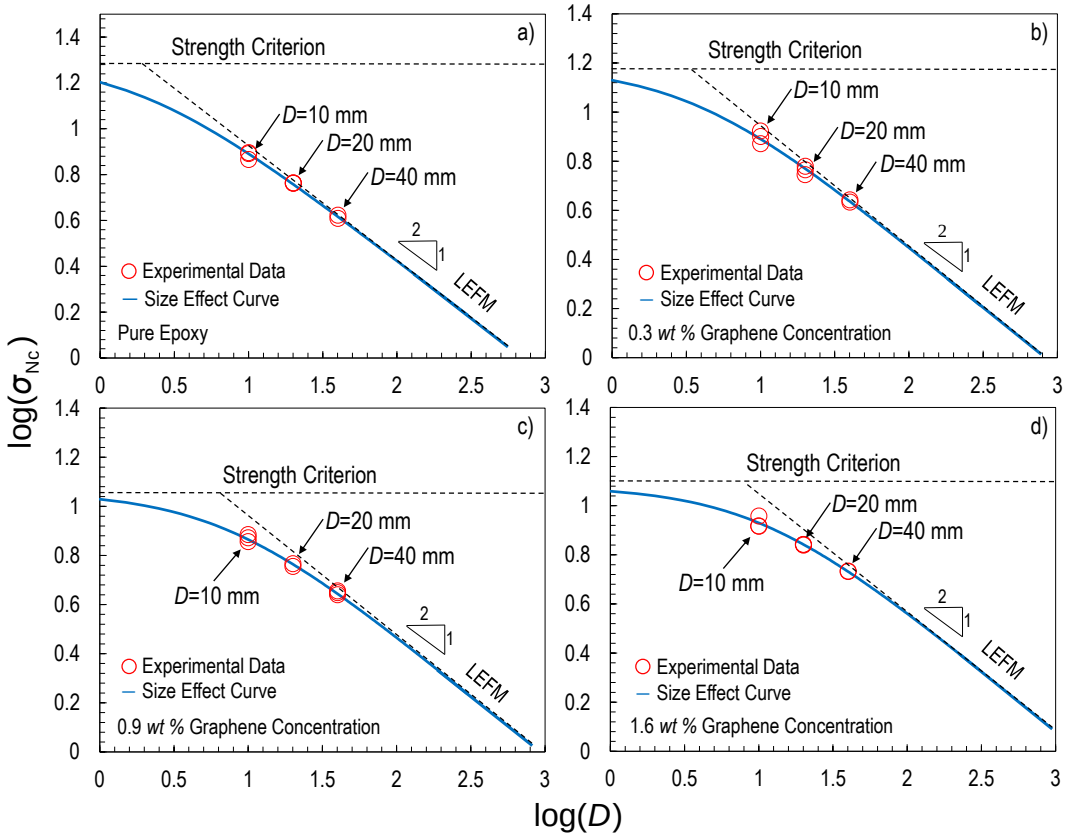

Figure 5.14: Size effect curves for different graphene concentrations.

This phenomenon can be ascribed to the increased size of the FPZ compared to the structure size which makes the non-linear effects caused by micro-damage in front of the crack tip not negligible. For sufficiently small specimens, the FPZ affects the structural

behavior and causes a significant deviation from the scaling predicted by LEFM with a much milder effect of the size on the structural strength. On the other hand, for increasing sizes, the effects of the FPZ become less and less significant thus leading to a stronger size effect closely captured by LEFM. Further, comparing the size effect plots of nanocomposites with different graphene concentrations, it can be noted a gradual shift towards the ductile region thus showing that not only the addition of graphene leads to a higher fracture toughness but also to a gradually more ductile structural behavior for a given size.

5.3.4 Estimation of Mode I fracture properties of nanocomposites : LEFM vs SEL

Having discussed the scaling of the fracturing behavior and having shown that, for graphene nanocomposites, the FPZ is not negligible for the range of specimen sizes investigated, it is interesting to check how the mode I fracture energy calculated through SEL compares to the estimation from LEFM for the various sizes and graphene contents.

The fracture energy can be calculated by means of LEFM which does not account for the FPZ length. Figures 5.15a-c show a comparison between the fracture energy estimated by SEL and by LEFM for different specimen sizes and graphene concentrations. As can be noted, for a given size, the difference between SEL and LEFM increases with the amount of graphene with LEFM underestimating G_f. The difference increases with the addition of graphene since, as shown in previous sections, the FPZ size increases monotonically and thus the cardinal assumption of LEFM becomes less and less accurate. The underestimation caused by LEFM can be very significant if one considers that the maximum difference, occurring at 1.6 wt% for all sizes, is 20.9%, 49.2% and even 113.3% for the large, medium and small sizes respectively. More importantly, a serious issue about using LEFM when the specimen sizes belong to the transitional region is that the estimate is not objective, i.e. it does depend on the size of the specimen tested. This can be noted from Figures 5.15a-c which show that, for a given graphene content, the fracture energy estimated by LEFM is size dependent, being lower for smaller sizes. It is interesting to note that, for example, the calculations based on LEFM for 1.6 wt% nanocomposites show basically no increment

in the fracture energy for the small size specimen while, for the large size, the increment is about 50%. Conversely, thanks to the characteristic length scale associated with the FPZ size, SEL provides the same estimate of the fracture energy for all the sizes. Of course, the size dependence of the fracture energy estimated by LEFM and its difference from SEL depends on the range of sizes investigated: for sufficiently large specimens, both the theories provide the same, size independent, fracture energy. This may explain why the range of fracture energy increments obtained by nanomodification reported in the literature is so large: neglecting the effects of the non-linear FPZ lead to fracture energy estimates which were size dependent and consistently underestimating, the underestimation being more significant for larger nanofiller concentrations and smaller specimen sizes.

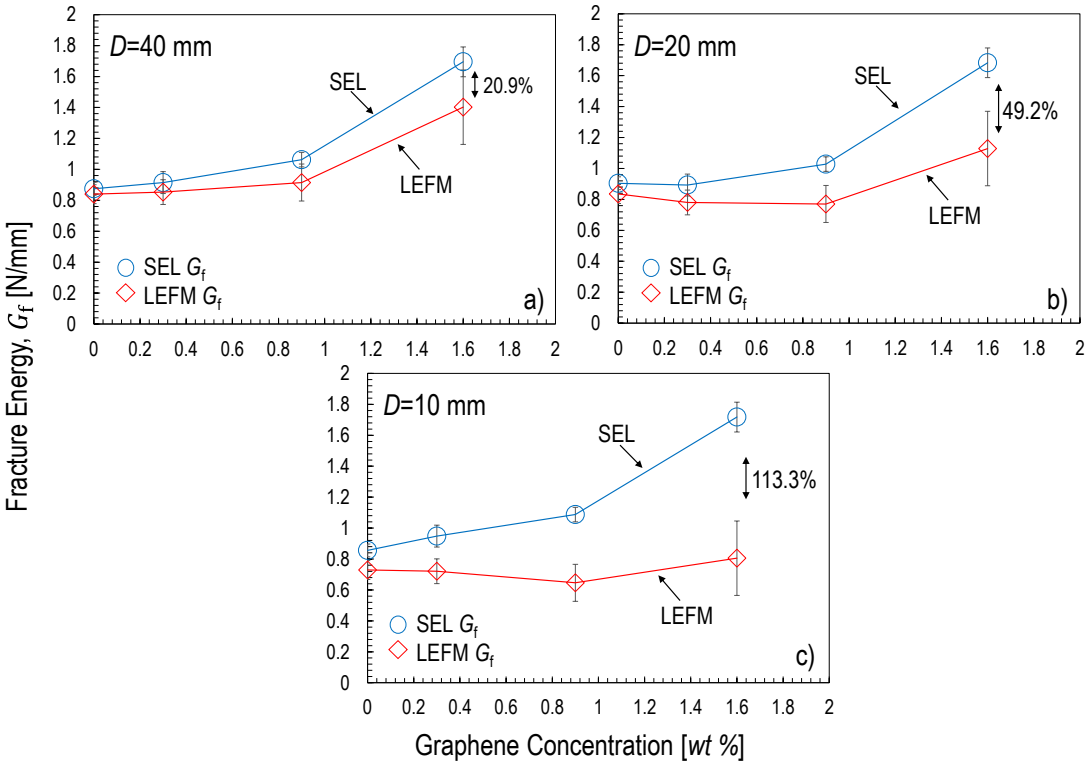

Figure 5.15: Fracture energy estimated from LEFM and SEL for several specimen sizes and graphene contents.

5.3.5 Study on the applicability of LEFM to polymer nanocomposites

The ASTM D5045-99 provides a lower limit for $(D-a)$ to guarantee a plane strain condition. According to the standard:

$$(D-a) \geq 2.5(K_{IC}/\sigma_y)^2 \tag{5.14}$$

where D is the specimen width, a is the crack length, K_{IC} is the fracture toughness, and σ_y is the yielding stress. Even if this limit is suggested for a different purpose, it is interesting to check if it would be enough to guarantee the use of LEFM to estimate the fracture energy of the material for the graphene nanocomposites investigated in this work. To this end, Eq. (5.14) is compared to the width D_{cr} which would be required to guarantee a difference between the nominal strength predicted by LEFM and SEL lower than 10%. Accordingly, the lower limit of D can be calculated as follows:

$$\sqrt{\frac{EG_f}{D_{cr}g(\alpha_0)+c_f g'(\alpha_0)}} = 0.9\sqrt{\frac{EG_f}{D_{cr}g(\alpha_0)}} \tag{5.15}$$

Finally, rearranging Eq. (5.15), the lower bound D_{cr} can be expressed in the following general form:

$$D_{cr} = 4.263\frac{g'(\alpha_0)}{g(\alpha_0)}c_f \tag{5.16}$$

A comparison between the standard ASTM D5045-99 and SEL for the case in which the crack length is half the width D of the specimen is reported in Table 5.3 by using an average Poisson's ratio of 0.4 for all the graphene concentrations.

Graphene concentration (wt%)	ASTM D5045-99 (mm)	Size effect curve (mm)
0	D > 4.45	D > 7.70
0.3	D > 4.60	D > 14.80
0.9	D > 5.62	D > 29.71
1.6	D > 9.97	D > 43.04

Table 5.3: ASTM D5045-99 and SEL for the limitations of size criteria on SENB specimens.

According to Table 5.3, the difference between ASTM D5045-99 and size effect curve can be significant depending on the graphene content. For the highest graphene content and the geometry investigated in this study, D_{cr} (the width providing a difference between LEFM and SEL of 10% only) would be in the order of 40 mm. This limit is significantly reduced for the pure epoxy, with LEFM being valid for widths larger than approximately 7 mm. For both cases, the value calculated from the standard is always lower with $D_{cr} = 9.97$ mm and 4.45 mm for the 1.6 wt% and pure epoxy specimens respectively.

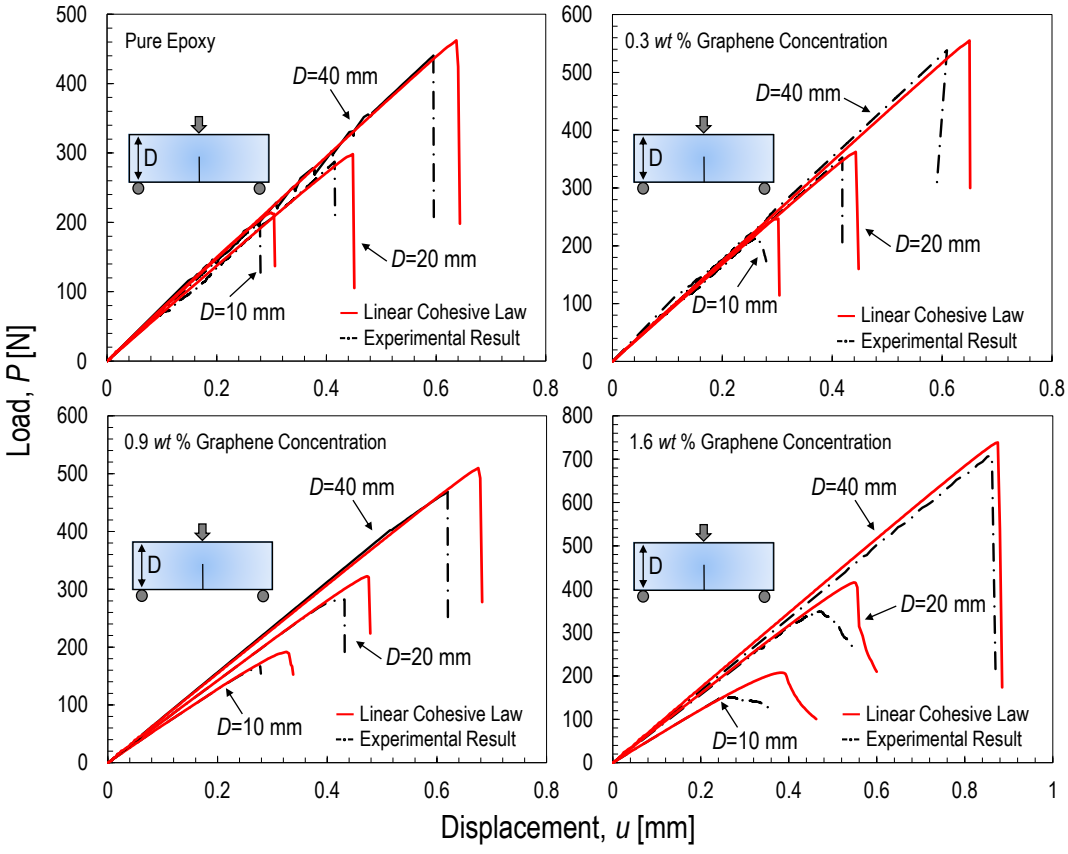

Figure 5.16: Load-displacement curves vs. cohesive zone model featuring a Linear Cohesive Law (LCL) for different graphene contents and specimen sizes. Experimental data taken from [94].

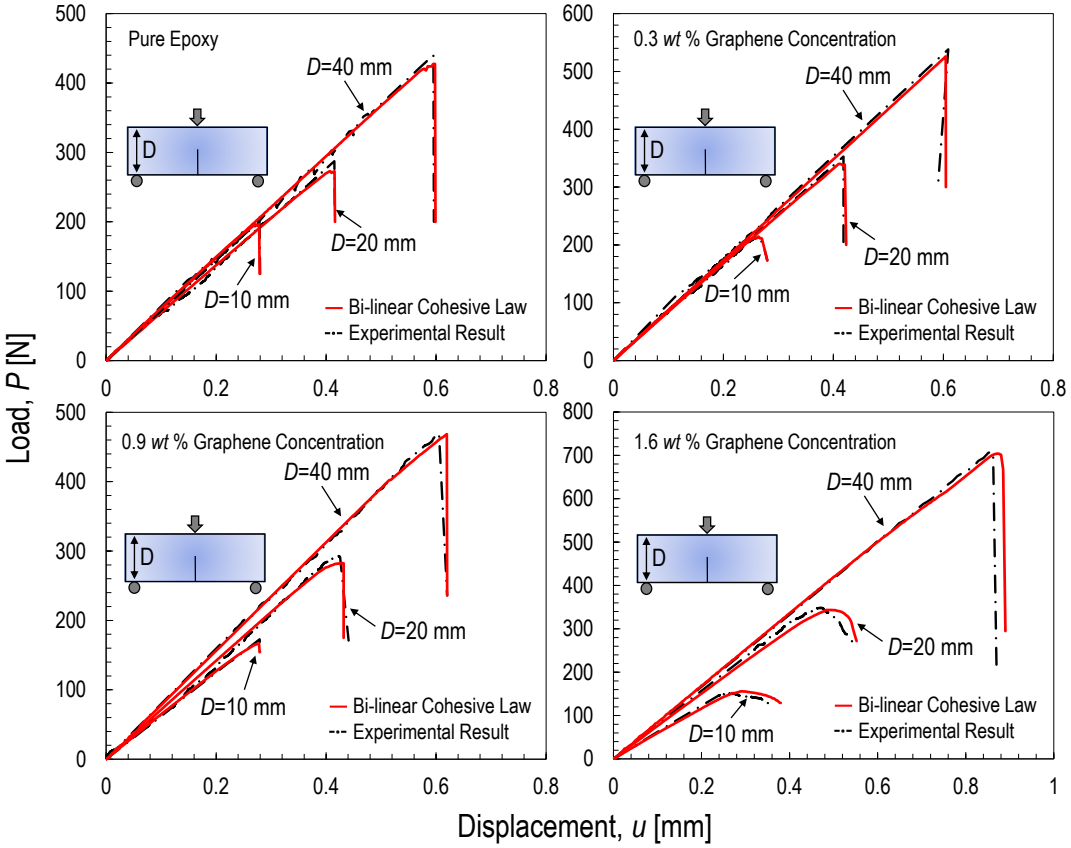

Figure 5.17: Load-displacement curves vs. cohesive zone model featuring a Bi-linear Cohesive Law (BCL) for different graphene contents and specimen sizes. Experimental data taken from [94].

5.4 Cohesive zone modeling: linear vs. bi-linear

Thanks to the comprehensive investigation on the size effect in graphene nanocomposites as discussed in the previous sections, the characteristics of the cohesive crack law can be studied. With knowing the fact that pure thermoset polymer is better described by a bi-linear cohesive law as shown in the previous chapter, it is interesting to check that this is also valid for graphene nanocomposites or not. To this end, both linear and bi-linear cohesive laws with the same fracture energy were used to match load-displacement curves obtained from experimental fracture tests on geometrically scaled Single Edge Notch Bending (SENB)

specimens with various contents of graphene. The description on the features of linear and bi-linear cohesive laws was presented in the previous chapter. It is worth mentioning here again that, for the bi-linear cohesive law, different intersection points were investigated in order to match experimental load-displacement curves.

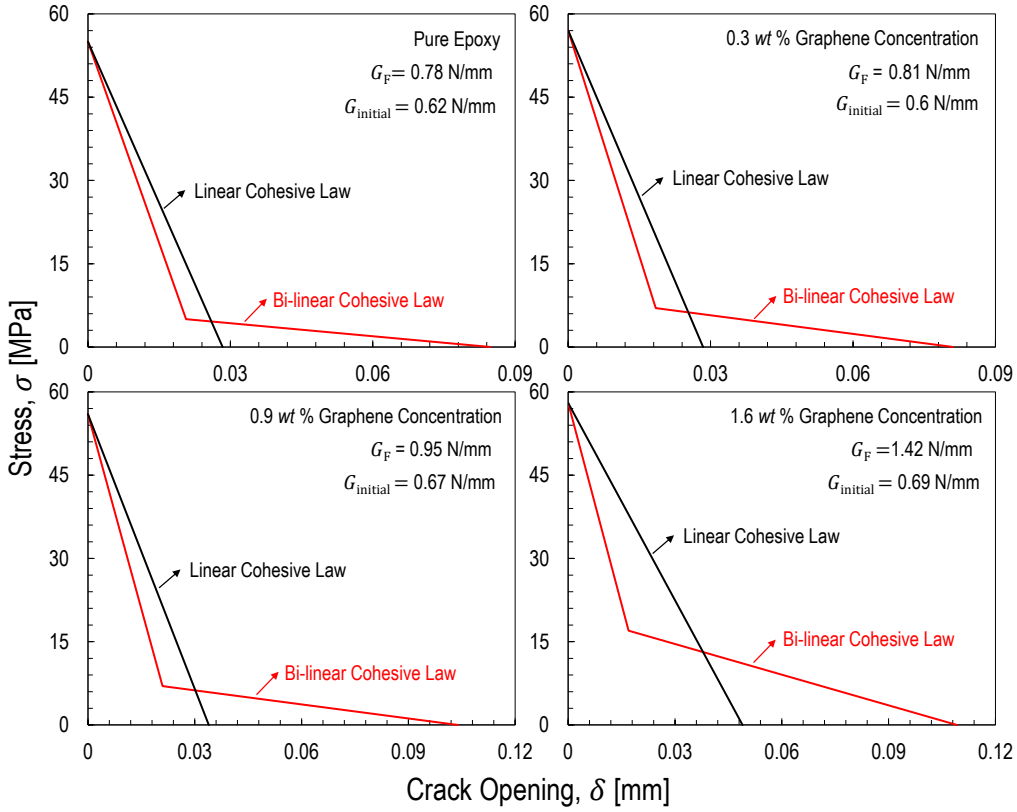

Figure 5.18: Calibrated bi-linear cohesive law vs. linear cohesive law with the same total fracture energy.

Figures 5.16-5.17 show a comparison between the experimental load defection curves and simulation through a Cohesive Zone Model (CZM) featuring a linear and bi-linear cohesive law respectively. It can be noted that specimens with different sizes and graphene concentrations are also better described by a bi-linear cohesive law instead of a linear cohesive law. In fact, the bi-linear cohesive law provides a very accurate description of the fracture tests with errors on the structural strength less than 7% whereas the linear cohesive law shows a

maximum deviation from the tests of 30%. A comparison between the calibrated linear and bi-linear cohesive laws for the various graphene contents is shown in Figures 5.18a-d.

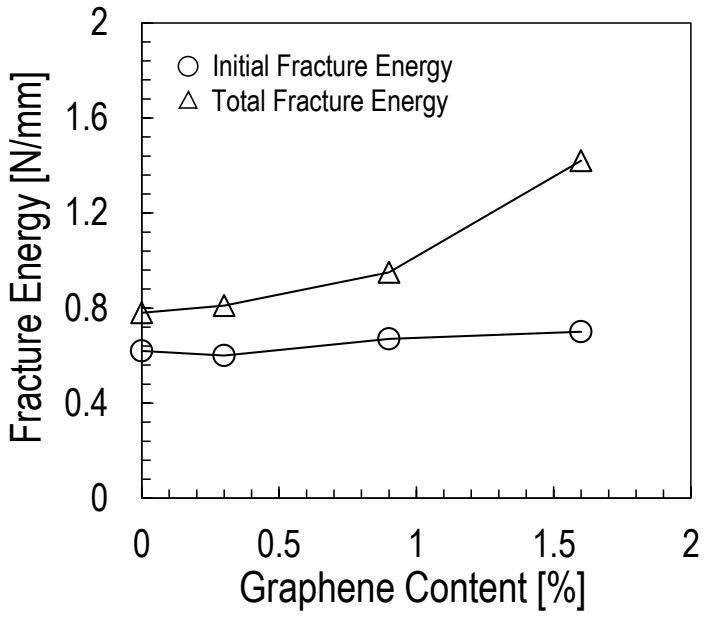

Figure 5.19: Evolution of the initial and total fracture energy of the calibrated bi-linear cohesive law as a function of the graphene content. As can be noted, the addition of graphene nanoplatelets increased the total fracture energy but did not improve the initial fracture energy.

Figure 5.19 shows the initial, G_f, and total, G_F, fracture energy as a function of graphene platelet content. It is interesting to note that the initial fracture energy does not increase significantly as a function of graphene content. The increasing total fracture energy for higher graphene contents can all be ascribed to the change in slope of the second part of the curve. This is the indication that, for crack opening displacements lower than about 20μm, which is e.g. the case of a crack propagating between micrometer fibers in a unidirectional composite (Figure 5.20), the effects of nanomodification may be negligible. In fact, as schematically explained in inserts (b) to (e) of Figure 5.20, in such a case only the initial part of the bi-linear cohesive law is developed and drives the fracturing behavior. This may explain why the use of nanomodification to improve the fracturing behavior of the polymer matrix in fiber

composites has met with changing fortunes. Even if increments of the total fracture energy by nanomodification can be observed from tests on laboratory-scale specimens, this does not guarantee that the initial portion of the cohesive curve, which drives the microcracking in composites, has improved. This latter aspect can be clarified only by size effect testing and cohesive zone modeling, as clearly shown in this work.

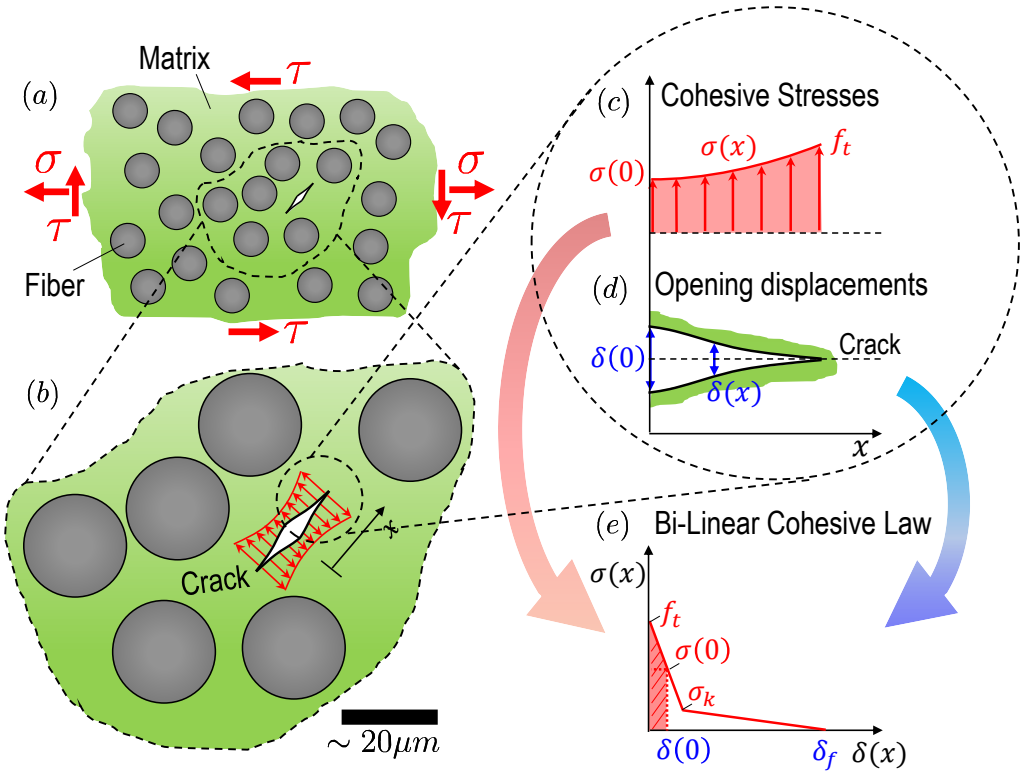

Figure 5.20: Schematic representation of a micro-crack propagating in a composite: (a) and (b) Cohesive crack formation; (c) cohesive stresses bridging the crack faces; (d) distribution of crack opening displacement and (e) corresponding stresses and displacements in the cohesive law. Note that, for a micro-crack, the cohesive stresses do not enter the second arm of the bi-linear cohesive law ($\sigma_{min} = \sigma(0) > \sigma_k$).

5.5 Experimental characterization of thermal properties

5.5.1 Materials and testing methods

5.5.1.1 Exothermic cross-linking process

Thermal behavior of the foregoing graphene nanocomposites was further characterized by leveraging the Differential Scanning Calorimetry (DSC) tests in order to computationally understand the coupled mechanical and thermal behavior of the material during the cross-linking process as it will be discussed in the future work. The effects of temperature and graphene nanoplatelets on the cross-linking process of polymers were initially investigated by conducting the thermal tests at three different isothermal conditions (80°C, 100°C and 120°C) using a Mettler Toledo DSC device [150]. The nano-modified specimen was placed in an aluminum crucible and the heat generation of the material was directly measured by the DSC sensor. To ensure that the material was mainly cured at the isothermal condition, the ramping temperature at the beginning of the thermal test was set up about 20°C/min in order to reach the investigated temperatures in few minutes.

5.5.1.2 Measurement of thermal conductivity

In addition to the studies of cross-linking process, the effects of graphene nanoplatelets on the thermal conductivity of polymers were further evaluated by using the simple DSC measurements. The detailed procedures were based on an interesting method proposed by Hakvoort and Van Regien [151]. As illustrated in Figure 5.21 for this study, an aluminum crucible with the Gallium was placed on the upper surface of the cylindrical specimen and the heat flowing into the specimen was measured after the melting point of the metal was reached. It is worth mentioning here that the melting temperature of the Gallium is about 30°C indicating that the measured thermal conductivity only corresponds to this investigated temperature. However, thermoset polymers can possibly exhibit different thermal conductive behavior at different temperatures and degrees of cross-linking process and this aspect can

be further studied in the future by leveraging a comprehensive set of thermal tests.

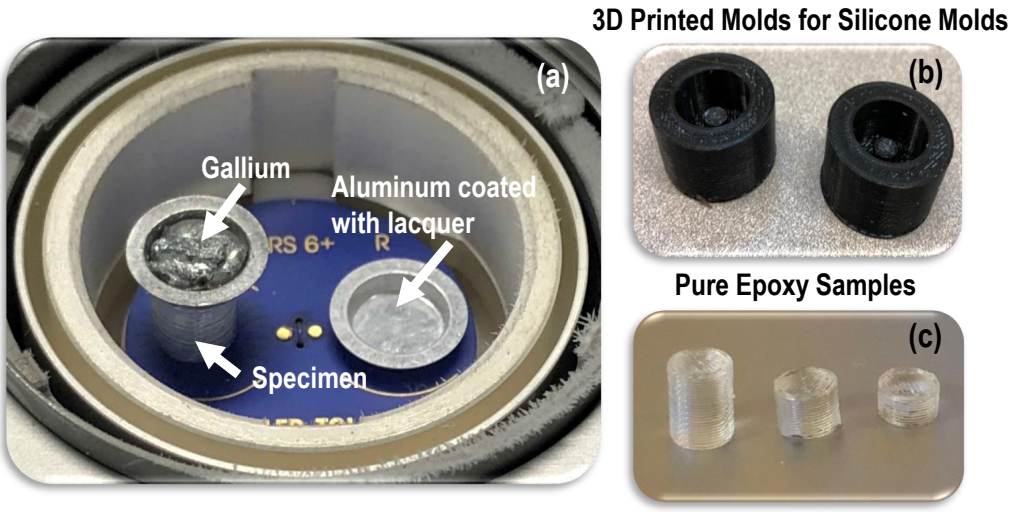

Figure 5.21: (a) Experimental setup for measuring the thermal conductivity of the material; (b) 3D printed plastic molds for the silicone molds; (c) Cylindrical pure epoxy specimens.

5.5.2 Experimental results and analysis

5.5.2.1 Degree of cross-linking process

To have a quantitative characterization on the cross-linking process, the heat generation due to the exothermic reaction of the material can be used to define the degree of curing as shown in the following expression:

$$\phi(t) = \frac{H(t)}{H_r} \tag{5.17}$$

where $\phi(t)$ is the degree of curing, $H(t)$ is the heat generated in the cross-linking process of the polymer at the time t and H_r is the total heat generation for the exothermic reaction. In this definition, the degree of curing equals to 0 representing the uncured polymer whereas the fully cross-linked polymer leads to the degree of curing equivalent to 1. It is interesting to plot how the degree of curing evolves with the curing time for all the investigated graphene nanocomposites at various isothermal conditions. As can be noted from Figure 5.22, the

rate of the cross-linking process strongly depends on the curing temperature for all the investigated graphene contents since the curing time is significantly faster for the material cross-linked at higher temperature.

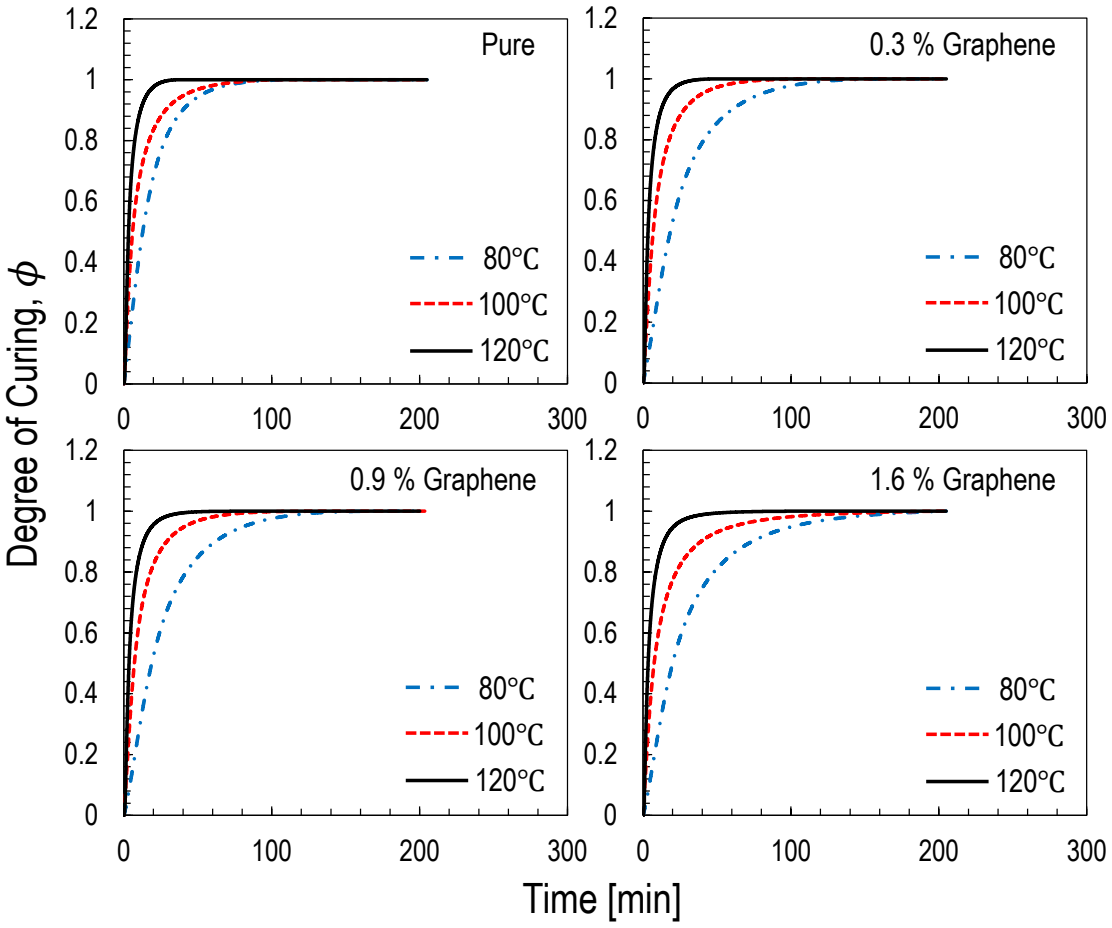

Figure 5.22: Comparison between degree of curing and time for all the investigated graphene nanocomposites cross-linked at various isothermal conditions.

However, the addition of graphene nanoplatelets does not significantly affect the cross-linking process for all the investigated materials exhibiting similar tendency for the degree of curing. This is mainly due to the small volume of the material in the crucible experimentally measured through the DSC tests. In fact, the kinetics of the cross-linking process for the polymer was subtly affected by the investigated contents of graphene nanoplatelets as it

will be shown in the next paragraph. It is worth mentioning here that larger volume of the specimen should be used to to investigate the effects of graphene content on the cross-linking process of the polymer by leveraging a coupled thermal and mechanical computational modeling in the future work.

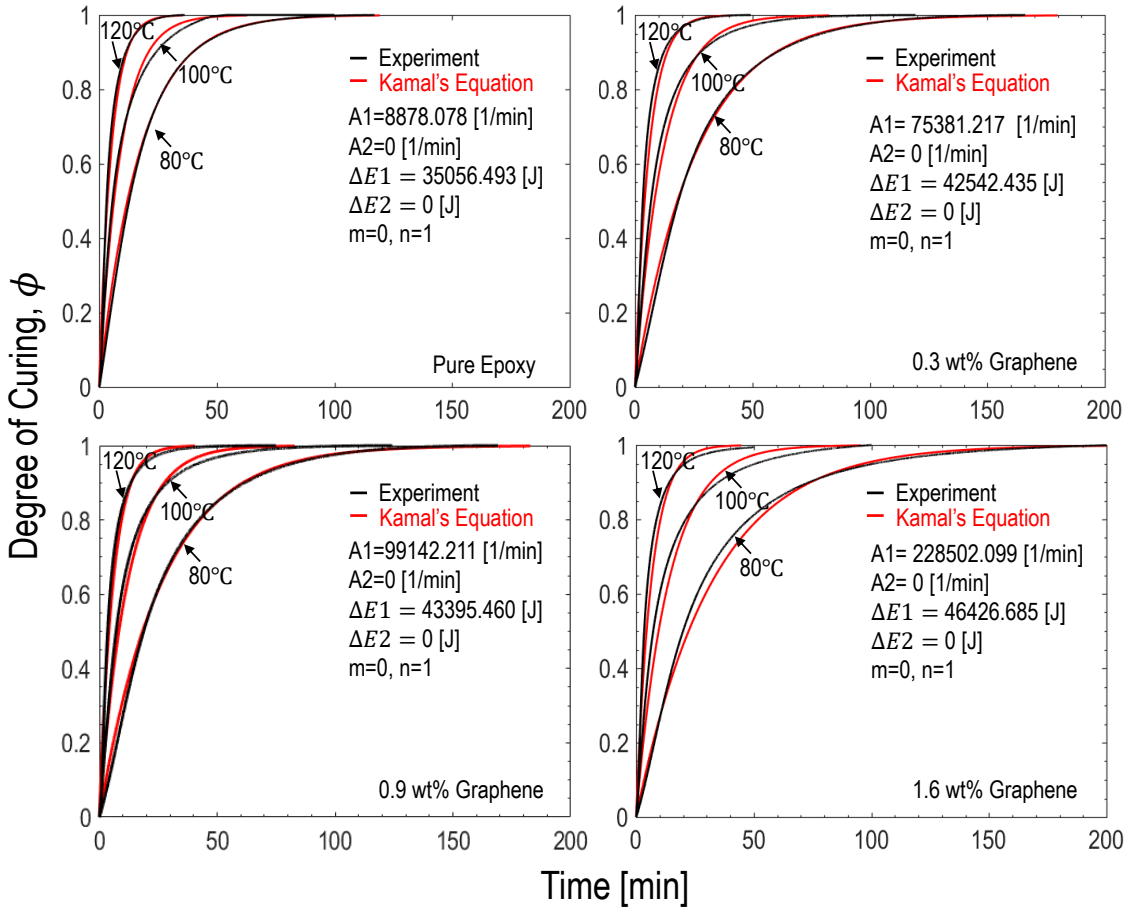

Figure 5.23: Best fitting of the experimental curves representing the degree of curing for all the investigated graphene contents at various curing temperatures by using Kamal's equation.

On the other hand, the heat generation of the material can be characterized by the following kinetic equation proposed by Kamal [152]:

$$\frac{d\phi}{dt} = f(T,\phi) = (k_1(T) + k_2(T)\phi^m)(1-\phi)^n \tag{5.18a}$$

$$k_1(T) = A_1 \cdot exp(-\frac{\Delta E_1}{TR}) \tag{5.18b}$$

$$k_2(T) = A_2 \cdot exp(-\frac{\Delta E_2}{TR}) \tag{5.18c}$$

where m and n are constants, $k_1(T)$ and $k_2(T)$ are the Arrhenius equations describing chemical reactions, A_1 and A_2 are the frequency-related constants, T is the temperature in Kelvin, R is the gas constant, and ΔE_1 and ΔE_2 are the activation energies. As illustrated in Figure 5.23, the experimental curves for the degree of curing with respect to the time can be successfully described by the foregoing kinetic equation based on the Levenberg–Marquardt algorithm for all the investigated graphene nanocomposites at various isothermal conditions.

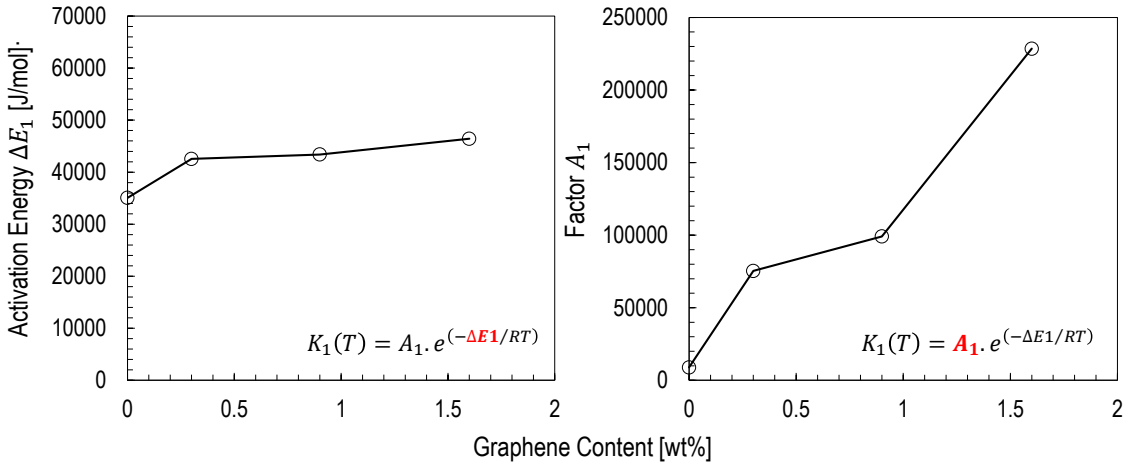

Figure 5.24: Calibrated parameters for Kamal's equation describing the kinetics of the cross-linking process for all the investigated graphene contents.

By leveraging this successful characterization, the effects of graphene content on the cross-linking process of the polymer can be indirectly investigated through the calibrated parameters in the foregoing kinetic equations. As illustrated in Figure 5.24, the activation

energy ΔE_1 does not significantly change with increasing the graphene content whereas the constant A_1 is remarkably affected exhibiting a soaring trend as increasing the graphene content. The weak effect on the increasing activation energy indicates that the investigated graphene nanoplatelets can increase the energy barrier for the cross-linking reaction of the polymer. However, the strong effect on the increasing factor A_1 implies that the cross-linking process of the polymer is intensified with the modification of graphene nanoplatelets thus leading to the higher heat generation as long as the chemical reaction is proceeded.

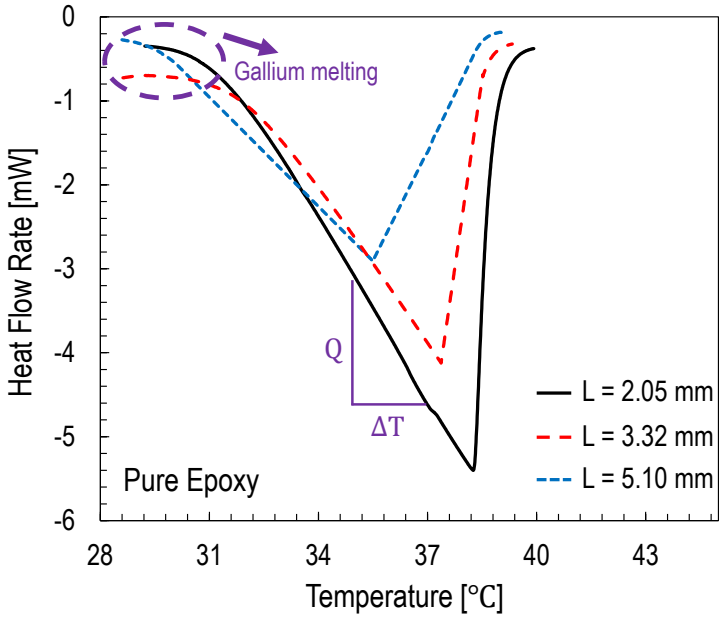

Figure 5.25: Heat flow rate vs. temperature obtained from the representative experimental tests for the purpose of measuring the thermal conductivity of the cylindrical pure epoxy with different heights.

5.5.2.2 Thermal conductive behavior

The thermal conductive behavior of the investigated graphene nanocomposites was further measured by leveraging the foregoing method as mentioned in the previous section 5.5.1.2 and the following description for the detailed analysis. The heat flow rate Q in a cylindrical

specimen can be expressed by $Q = A\lambda\triangle T/L$ where L and A are the length and cross-sectional area of the cylindrical specimen and λ is the thermal conductivity of the material. In this definition, the thermal resistance of the material can be further obtained in the expression $R = \triangle T/Q = L/(A\lambda)$. Thanks to this relation, the total thermal resistance of the system can be written in the following form:

$$\frac{\triangle T}{Q} = \frac{L}{\lambda A} + R_{s-s} + R_{s-m} \tag{5.19}$$

where R_{s-s} is the thermal resistance between specimen and sensor and R_{s-m} is the thermal resistance between specimen and metal.

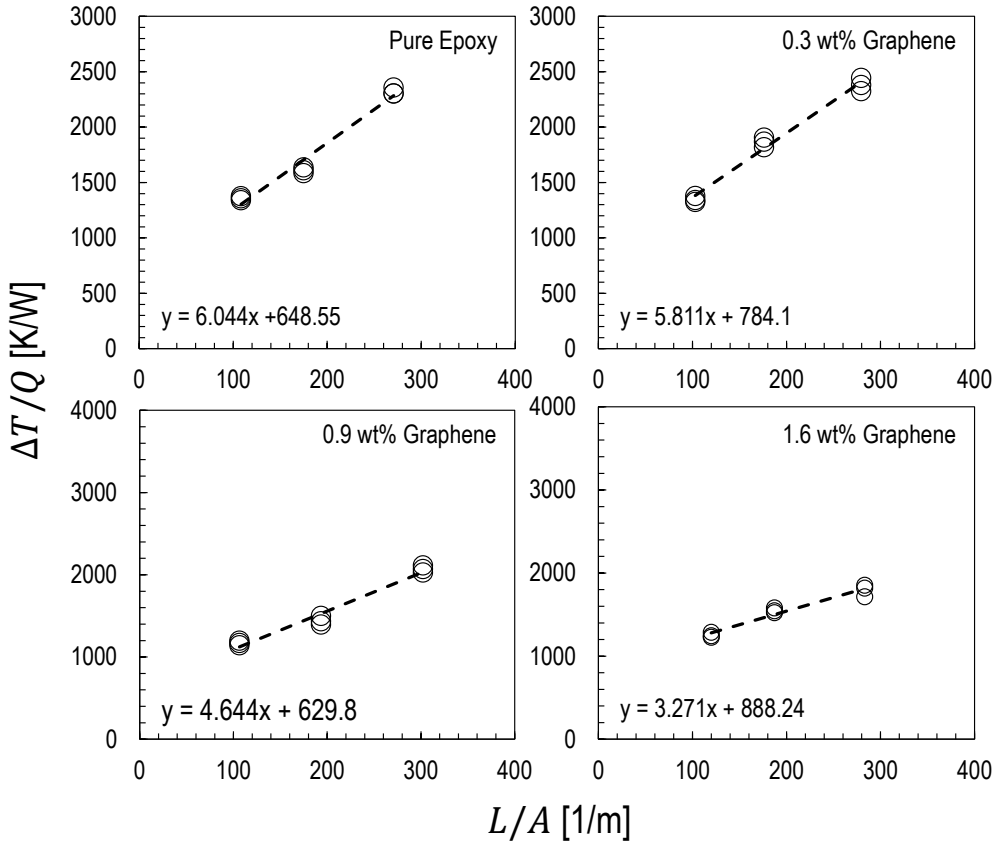

Figure 5.26: Linear regression fitting of the experimental tests for geometrically-scaled graphene nanocomposites. These figures plot the thermal resistance vs. the ratio of the length L to the cross-sectional area A.

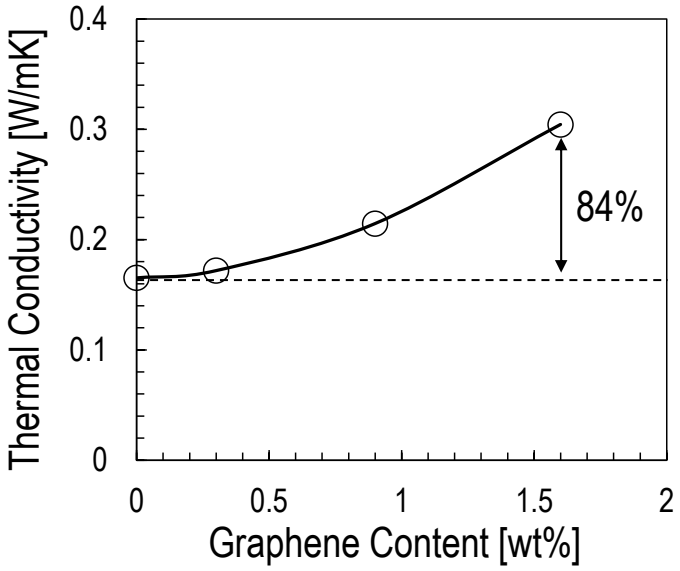

Figure 5.27: Evolution of the thermal conductivity with the investigated graphene content.

To obtain the thermal conductivity of the material by leveraging the foregoing expression, geometrically-scaled cylindrical specimens with the same cross-sectional area (17.5mm^2) but different heights (2.05 mm, 3.32mm and 5.1mm) are required for the thermal tests as illustrated in Figure 5.21c. On the other hand, the ratio of the temperature increment $\triangle T$ to the total heat flow rate can be measured from the experimental curves obtained from the DSC tests as shown in Figure 5.25. In this figure, the forgoing ratio can be directly estimated based on the slope of the curve after reaching the melting temperature of the Gallium. Thanks to this approach, the inverse of the thermal conductivity for the specimens with all the investigated graphene contents can be obtained by using a linear regression fitting as shown in Figure 5.26. As can be noted from the figure, the slope of the curve exhibits a decreasing trend as the graphene content increases. This clearly shows that the addition of graphene nanoplatelets improves the thermal conductive behavior of the polymer as illustrated in Figure 5.27 and the highest improvement can reach about 84% with the addition of 1.6% graphene nanoplatelets.

5.6 Conclusions

1. For all the investigated contents, the addition of graphene nanoplatelets to the resin did not provide a significant effect on the elastic properties and strength whereas an outstanding enhancement of mode I fracture energy was reported. A weight fraction of 1.6% of graphene resulted in an increase of the fracture energy of about 92.4% compared to the pure resin, this result making graphene-modified resins ideal candidates for the development of tougher and more ductile composite structures;

2. The fracture tests on geometrically-scaled SENB specimens confirmed a remarkable size effect. The analysis of the experimental data showed that the fracture scaling of the pure epoxy is captured accurately by Linear Elastic Fracture Mechanics (LEFM). However, this was not the case for graphene nanocomposites which exhibited a more complicated scaling. The double logarithmic plots of the nominal stress as a function of the characteristic size of the specimens showed that the fracturing behavior evolves from ductile to brittle with increasing sizes. For sufficiently large specimens, the data tend to the classical $-1/2$ asymptote predicted by LEFM. However, for smaller sizes, a significant deviation from LEFM was reported with data exhibiting a milder scaling, a behavior associated to a more pronounced ductility. This trend was more and more pronounced for increasing graphene contents;

3. The deviation from LEFM reported in the experiments is related to the size of the Fracture Process Zone (FPZ) for increasing contents of graphene. In the pure epoxy the damage/fracture zone close to the crack tip, characterized by significant non-linearity due to sub-critical damaging, was generally very small compared to the specimen sizes investigated. This was in agreement with the inherent assumption of LEFM of negligible non-linear effects during the fracturing process. However, the addition of graphene nanoplatelets with the various additional damage mechanisms that come with it (such as e.g. platelet/matrix delamination, nano-crack deflection and plastic yielding), re-

sulted in larger and larger FPZs. For sufficiently small specimens, the size of the highly non-linear FPZ was not negligible compared to the specimen characteristic size thus highly affecting the fracturing behavior, this resulting into a significant deviation from LEFM;

4. Capturing the correct scaling of the fracturing behavior is of utmost importance for structural design. Further, it is quintessential to correctly measure important material properties such as the fracture energy. The analysis of the results reported in this study shows that using LEFM to calculate the mode I fracture energy from the experiments leads to a size dependent G_f. Taking the specimens with 1.6% wt of graphene as an example, the fracture energy according to LEFM was 0.8 N/mm, 1.0 N/mm and 1.25 N/mm for the small, medium and large sizes respectively. The reason for this discrepancy is that LEFM lacks intrinsically of a characteristic length and thus cannot capture the effects of the FPZ size;

5. Following Bažant *et al.* [101,102], an Equivalent Fracture Mechanics approach was used to introduce a characteristic length, c_f, into the formulation. This length is related to the FPZ size and it is considered a material property as well as G_f. The resulting scaling equation, known as Bažant's Size Effect Law (SEL), depends not only on G_f but also on the FPZ size. An excellent agreement with experimental data is shown, with SEL capturing the transition from quasi-ductile to brittle behavior with increasing sizes. The fracture energy for the specimens with 1.6% wt of graphene, finally a material property independent of the specimen size, was 1.69 N/mm whereas $c_f = 1.59$ mm;

6. The difference between the fracture energy predicted by LEFM and SEL depends on the FPZ size compared to the specimen size, with LEFM underestimating G_f compared to SEL. For the specimens with 1.6% wt of graphene and the sizes considered in this work, LEFM predictions were about 113.3%, 49.2% and 20.9% lower compared to SEL for the small, medium and large sizes respectively. The difference decreases with

increasing specimen sizes and tends to zero for sufficiently large specimens as the FPZ becomes negligible compared to the specimen size;

7. The foregoing evidences show that particular care should be devoted to the understanding of the scaling of the fracture behavior of nanocomposites. In particular, the fracture tests carried out to characterize e.g. the fracture energy should guarantee objective results. Size effect testing on geometrically scaled specimens is a simple and effective approach to provide objective data. Alternatively, LEFM could be used provided that the specimen size is large enough. The size limit depends on the size of the FPZ and the geometry of the tested specimen. For the SENB specimens investigated, a difference lower than 10% between the nominal strength predicted by LEFM and SEL can be guaranteed if $D \geq 4.263 g'(\alpha_0) c_f / g(\alpha_0)$. This limit is generally higher than the one suggested by ASTM D5045-99 to guarantee a plane strain condition;

8. To get a deeper understanding on the foregoing results, fracture tests on thermosets reinforced by graphene nanoplatelets were re-analyzed via a cohesive modeling for all the sizes and graphene contents considered. It is concluded that, in general, a bi-linear cohesive law provides a very accurate description of fracture tests with errors on the structural strength less than 7%. A reasonable agreement is also found leveraging a linear cohesive law, with errors on structural strength no larger than 30%;

9. The analysis via the bi-linear cohesive law provided unprecedented insights on the influence of graphene nanoplatelets on the cohesive stresses. It is found that, for the size range investigated, the initial part of the cohesive law is unaffected by nanomodification. The increasing total fracture energy for higher graphene contents can all be ascribed to the change in slope of the second part of the cohesive law. Two main considerations can be made from this result: (a) the toughening by graphene nanoplatelets requires sufficiently large crack opening displacement (larger than about 20μm for the system investigated in this work), confirming that mechanisms such as crack deflection

and splitting are the main sources of energy dissipation; (b) for very small crack opening displacements, such as for the case of a crack propagating between micrometer fibers in a composite, the effect of nanomodification may be negligible, since no change in the cohesive behavior is induced by graphene nanoplatelets in that regime. Of course, different nanoparticles and manufacturing processes may affect the initial portion of the cohesive law differently. Future work will focus on understanding the physical relation between the characteristics of the cohesive law and the nano/microstructure of the material.

Chapter 6

QUASI-BRITTLE BEHAVIOR OF GENERIC POLYMER NANOCOMPOSITES

The previous chapter discussed the remarkable effects of the Fracture Process Zone (FPZ) on the fracturing and size scaling behavior of graphene nanocomposites. This chapter focuses on investigating the fracturing behavior of generic polymer nanocomposites inspired from the aforementioned interesting phenomenon. Towards this goal, a large bulk of data in the literature on the fracturing behavior of nanocomposites (nanomodification includes nanoclay, rubber and silica nanoparticles, carbon-based nano-fillers, etc) was critically re-analyzed by employing the expression derived from the Bažant Size Effect Law. The re-analyzed results show that most of generic nanocomposites are located in the quasi-brittle region which cannot be analyzed through the Linear Elastic Fracture Mechanics showing highest underestimation more than 150%. The correctness of the re-analyses was further confirmed through the computational studies by means of cohesive zone modeling with a linear softening law.

6.1 Fracture scaling of generic nanocomposites

To investigate the effects of the non-linear FPZ, the fracture tests on the thermoset polymer reinforced by nanoparticles in the literature were analyzed and discussed. Figure 6.1 shows the normalized structural strength σ_{Nc}/σ_0 of the literature data as a function of the normalized structure size D/D_0 in double logarithmic scale. The solid line represents the fitting by SEL. In such a graph, the structural scaling predicted by LEFM is represented by a dashed line of slope $-1/2$ whereas the case of no scaling, as predicted by stress-based failure criteria, is represented by a horizontal line. The intersection between the LEFM asymptote, typical of brittle behavior, and the pseudo-plastic asymptote, typical of ductile behavior, corresponds

to $D = D_0$, called the *transitional size* [102].

As can be noted from Figure 6.1, the experimental data are in excellent agreement with SEL, which inherently captures the transition from strength-dominated to toughness-dominated fracture. More importantly, the figure shows that although some fracture tests reported in the literature were conducted under LEFM conditions (assumed by ASTM D5045-99), most of the data are located in the transitional region.

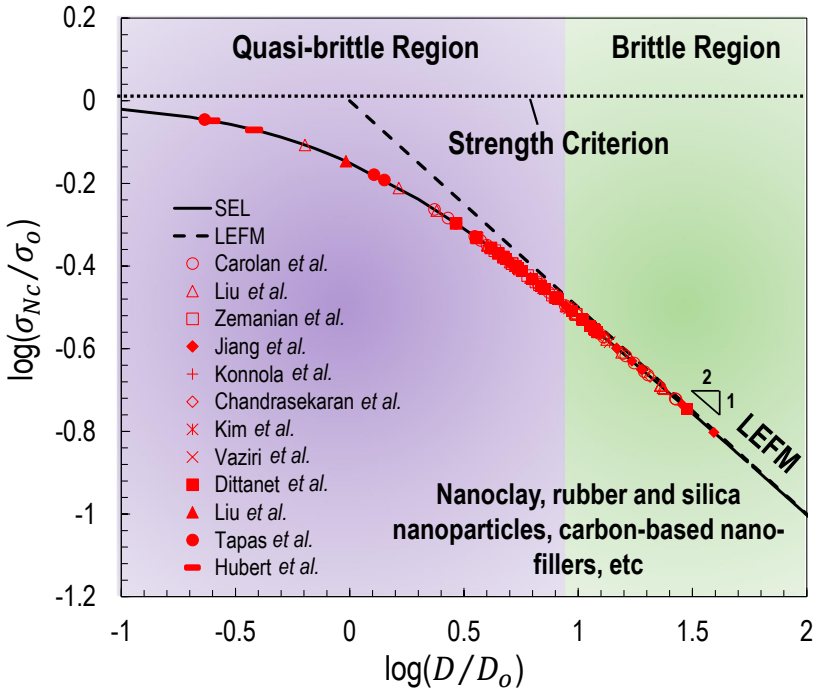

Figure 6.1: Size effect in polymer nanocomposites: data taken from the literature [138, 153–162].

Accordingly, the experimental data show that LEFM does not always provide an accurate method to extrapolate the structural strength of larger structures from lab tests on small-scale specimens, especially if the size of the specimens belonged to the transitional zone. In fact, the use of LEFM in such cases may lead to a significant underestimation of structural strength, thus hindering the full exploitation of graphene nanocomposite fracture properties. This is a severe limitation in several engineering applications such as e.g. aerospace or

aeronautics for which structural performance optimization is of utmost importance. On the other hand, LEFM always overestimates significantly the strength when used to predict the structural performance at smaller length-scales. This is a serious issue for the design of e.g. graphene-based MEMS and small electronic components or nano-modified carbon fiber composites in which the inter-fiber distance occupied by the resin is only a few micrometers and it is comparable to the FPZ size. In such cases, SEL or other material models characterized by a characteristic length scale ought to be used.

6.2 Effects of the FPZ on the calculation of the Mode I fracture energy

Notwithstanding the importance of understanding the scaling of the fracturing behavior, the tests conducted by Mefford *et al.* [94] as discussed in the previous chapter represent, to the best of the author's knowledge, the only comprehensive investigation on the size effect in nanocomposites available to date. All the fracture tests reported in the literature were conducted on one size and analyzed by means of LEFM. Considering the remarkable effects of the nonlinear FPZ on the fracturing behavior documented in the foregoing section, it is interesting to critically re-analyze the fracture tests available in the literature by means of SEL. This formulation is endowed with a characteristic length related to the FPZ size and, different from LEFM, it has been shown to accurately capture the transition from brittle to quasi-ductile behavior of nanocomposites.

6.2.1 Application of SEL to generic polymer nanocomposites

To understand if the quasi-brittle behavior reported in previous tests [94] is a salient feature of graphene nanocomposites only or if it characterizes other nanocomposites, a large bulk of literature data were re-analyzed by using Size Effet Law (SEL) in order to study the effects of the FPZ. In this analysis, in the absence of data on the effective FPZ length, c_f, from the literature, it is assumed that $c_f = 0.44 l_{ch}$ which, according to Cusatis *et al.* [82], corresponds to the assumption of a linear cohesive law. In this expression, $l_{ch} = E^* G_f / f_t^2$ is the Irwin's characteristic length which depends on the Young's modulus E^*, the mode I fracture energy

G_f and the ultimate strength of the material f_t. Substituting this expression into SEL and rearranging one gets the following expression which relates the fracture energy calculated according to SEL to the fracture energy calculated by LEFM:

$$G_{f,SEL} = \frac{G_{f,LEFM}}{1 - \frac{0.44E^* g'(\alpha_0) G_{f,LEFM}}{D f_t^2 g(\alpha_0)}} \tag{6.1}$$

where $G_{f,LEFM} = \sigma_{Nc}^2 D g(\alpha_0)/E^*$ represents the fracture energy which can be estimated by analyzing the fracture tests by LEFM.

It can be observed from Eq.(6.1) that the correct fracture energy in the literature can be calculated by knowing three key parameters in addition to $g(\alpha_0)$ and $g'(\alpha_0)$: (1) the fracture energy through the use of LEFM; (2) the Young's modulus of the specimens at different nanoparticle concentrations; and (3) the ultimate strength of the specimens at different nanoparticle concentrations. For the few cases in which those parameters were not provided by the authors, the ultimate strength, Young's modulus, and Poisson's ratio of nanocomposites were reasonably assumed to be 50 MPa, 3000 MPa, and 0.35 respectively.

The calculation of $g(\alpha)$ and $g'(\alpha)$ for SENB specimens can be done according to the procedure described in the previous chapter. In the case of CT specimens, the values for $g(\alpha)$ and $g'(\alpha)$ can be determined leveraging the equations provided by the ASTM D5045-99. Following the standard, the mode I Stress Intensity Factor (SIF), K_I, can be written as:

$$K_I = \frac{P}{t\sqrt{D}} f(\alpha) \tag{6.2}$$

where $\alpha = a/D$ and D is the distance between the center of the hole to the end of the specimen as defined in ASTM D5045-99. The nominal stress σ_N for CT specimens can be defined as:

$$\sigma_N = \frac{P}{tD} \tag{6.3}$$

The mode I Stress Intensity Factor can be rewritten as follows by combining Eq. (6.2) and Eq. (6.3):

$$K_I = \sqrt{D}\sigma_N f(\alpha) \tag{6.4}$$

By considering the relationship between energy release rate and stress intensity factor for a plane strain condition, the mode I energy release rate results into the following expression:

$$G_I = \frac{D\sigma_N^2}{E^*} g(\alpha) \tag{6.5}$$

where $g(\alpha) = f^2(\alpha)$, and $f(\alpha)$ is a dimensionless function accounting for geometrical effects and the finiteness of the structure. Once $g(\alpha)$ is derived, the expression of $g'(\alpha)$ can be obtained by differentiation leading to the following polynomial expressions for $g(\alpha)$ and $g'(\alpha)$ respectively:

$$g(\alpha) = 33325\alpha^5 - 52330\alpha^4 + 32016\alpha^3 - 9019.1\alpha^2 + 1230.1\alpha - 51.944 \tag{6.6}$$

$$g'(\alpha) = 555868\alpha^5 - 895197\alpha^4 + 554047\alpha^3 - 159153\alpha^2 + 21035\alpha - 917.3 \tag{6.7}$$

6.2.2 Mode I fracture energy of thermoset nanocomposites

Several types of nanofillers were investigated in this re-analysis including carbon-based nanofillers (such as carbon black, graphene oxide, graphene nanoplatelets, and multi-wall carbon nanotubes), rubber and silica nanoparticles, and nanoclay. The fracture energy estimated from LEFM compared to the calculation through SEL, Eq. (6.1), for nanomodified SENB and CT specimens are plotted in Figures 6.2-6.6 along with the highest difference.

Figure 6.2 shows the data elaborated from Carolan *et al.* [155] who conducted fracture tests on SENB specimens nano-modified by six different combinations of nanofillers. As can be noted, while for the pure polymer the difference between LEFM and SEL is negligible, this is not the case for the nanomodified polymers, the difference increasing with increasing nanofiller content. The difference varies based on the type of nanofiller used, with the greatest value being 42.6% for the addition of 8 wt% core shell rubber mixed with 25% diluent and 8% silica. This confirms that for the SENB specimens tested in [155] the nonlinear behavior of the FPZ is not negligible, leading to a more pseudo-ductile behavior compared to the pure polymer.

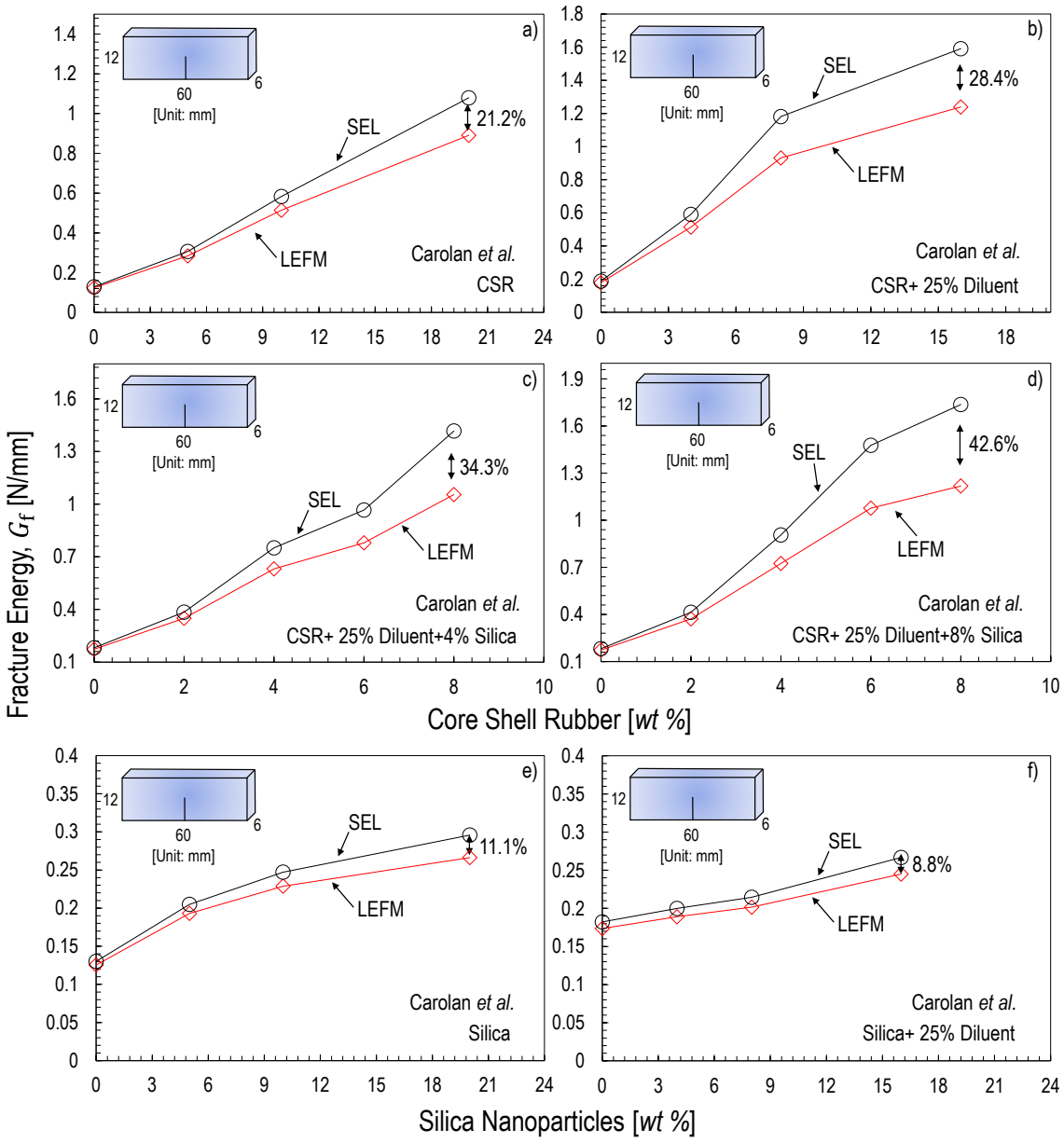

Figure 6.2: Mode I fracture energy estimated by Linear Elastic Fracture Mechanics (LEFM) and Size Effect Law (SEL), Eq. (6.1). The latter formulation accounts for the finite size of the nonlinear Fracture Process Zone (FPZ) in thermoset nanocomposites. Data re-analyzed from [155].

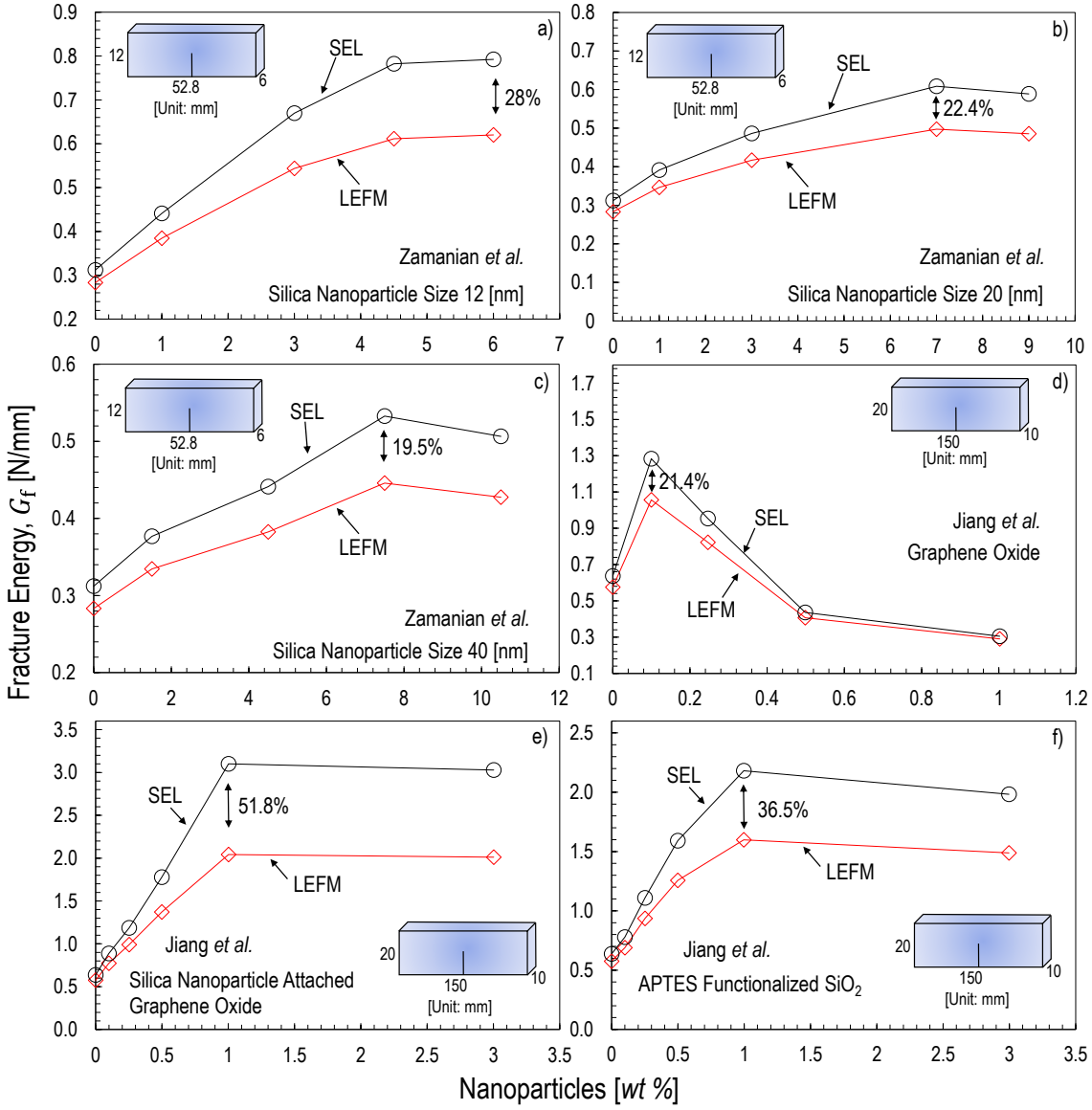

Figure 6.3: Mode I fracture energy estimated by Linear Elastic Fracture Mechanics (LEFM) and Size Effect Law (SEL), Eq. (6.1). The latter formulation accounts for the finite size of the nonlinear Fracture Process Zone (FPZ) in thermoset nanocomposites. Data re-analyzed from [153] and [156].

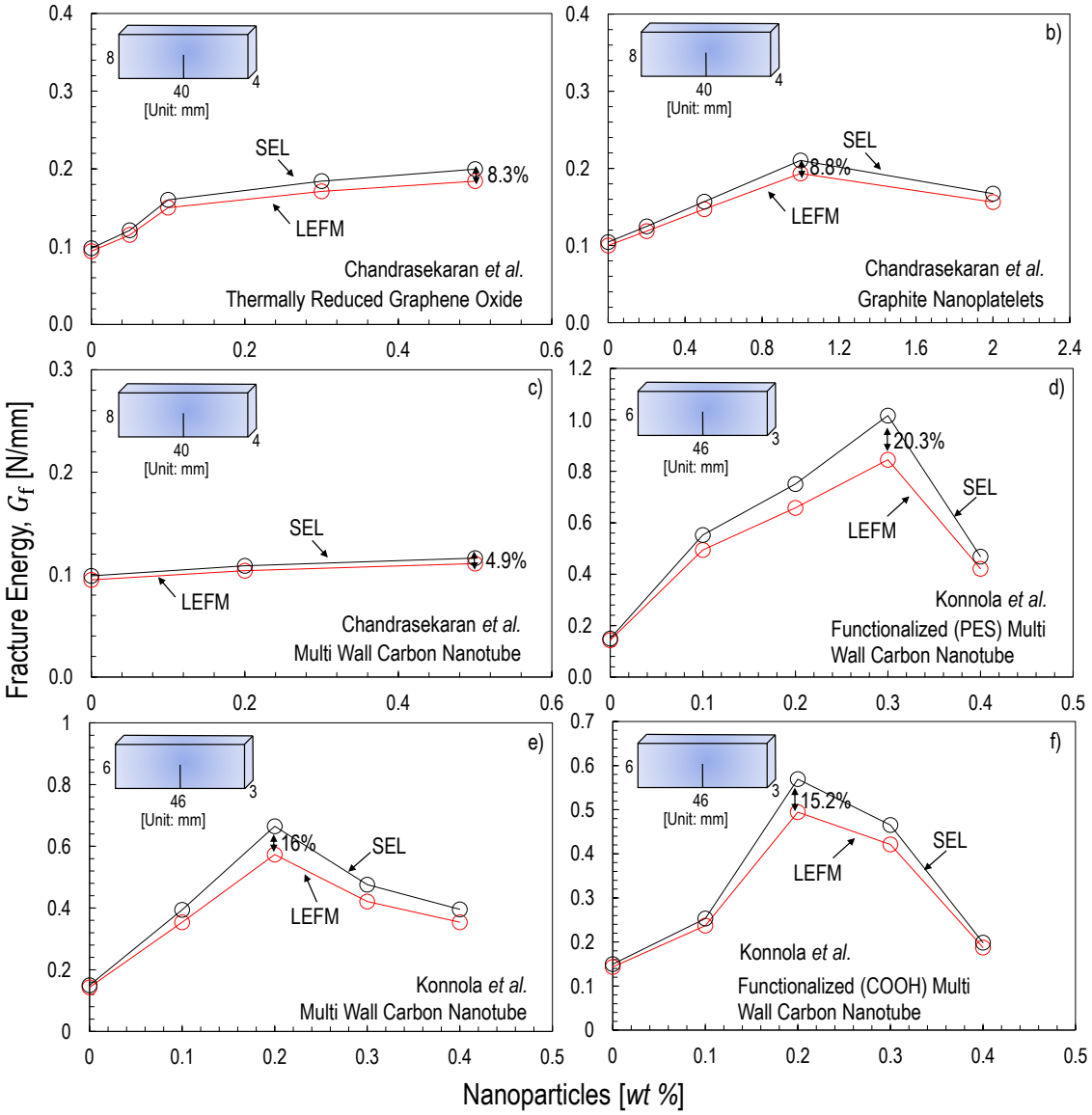

Figure 6.4: Mode I fracture energy estimated by Linear Elastic Fracture Mechanics (LEFM) and Size Effect Law (SEL), Eq. (6.1). The latter formulation accounts for the finite size of the nonlinear Fracture Process Zone (FPZ) in thermoset nanocomposites. Data re-analyzed from [138] and [154].

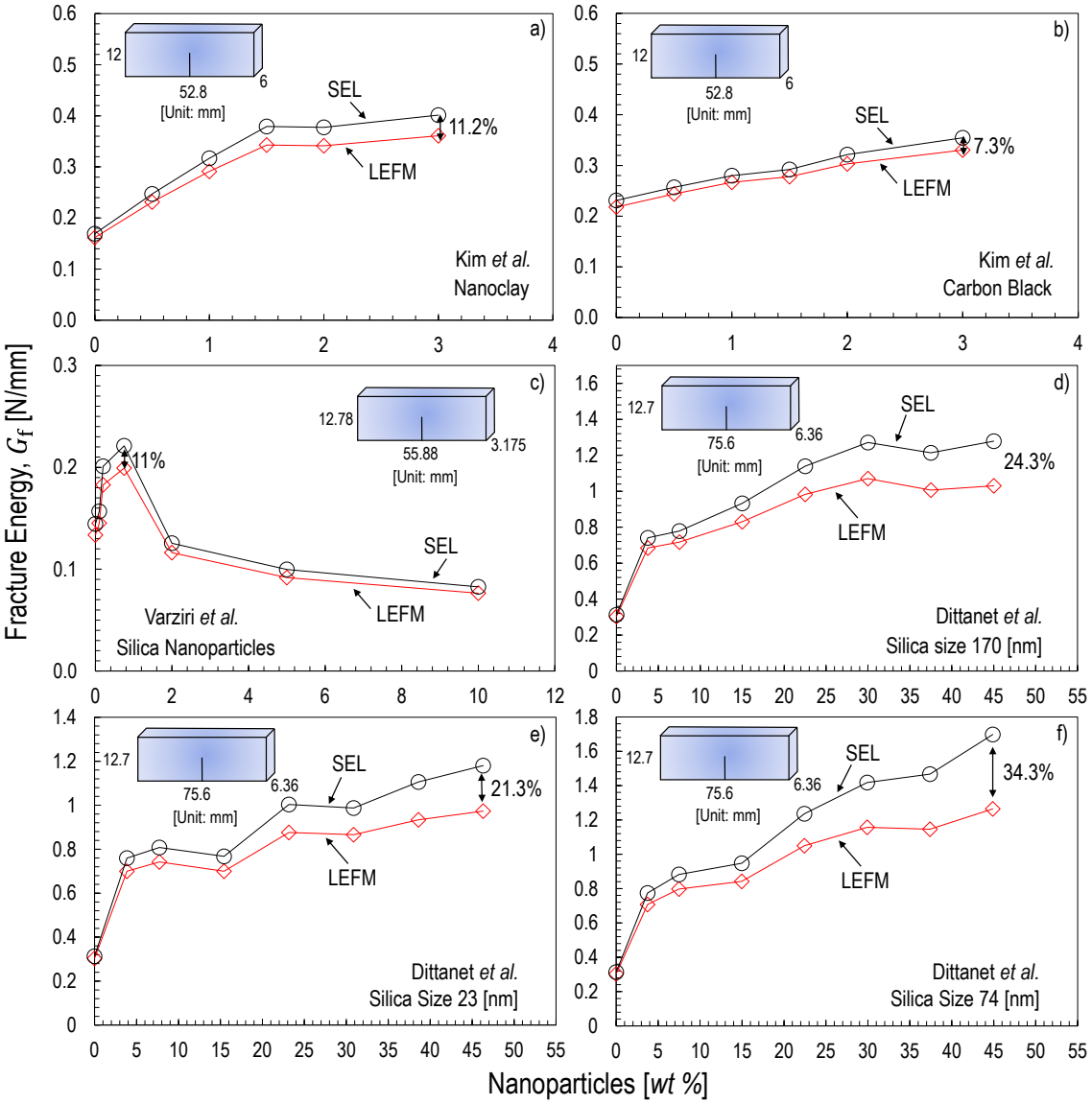

Figure 6.5: Mode I fracture energy estimated by Linear Elastic Fracture Mechanics (LEFM) and Size Effect Law (SEL), Eq. (6.1). The latter formulation accounts for the finite size of the nonlinear Fracture Process Zone (FPZ) in thermoset nanocomposites. Data re-analyzed from [157], [158] and [159].

Similar conclusions can be drawn based on Figures 6.3a-f which report the analysis of the fracture tests conducted by Zamanian *et al.* [156] and Jiang *et al.* [153] on polymers reinforced by silica nanoparticles and silica nanoparticle+graphene oxide respectively. For the data in [156], the greatest percent difference of the fracture energy between LEFM and SEL decreased as the size of silica nanoparticle increased, with the greatest difference being 28% for the addition of 6 wt% 12 nm silica nanoparticles. For all the systems investigated, the maximum deviation from LEFM is for the largest amount of nanofiller, confirming that nanomodification lead to larger FPZ sizes and more pronounced pseduo-ductility. On the other hand, the data by Jiang *et al.* [153] exhibit an even larger effect of the FPZ with the greatest difference in fracture energy between LEFM and SEL reaching up to 51.8% for silica nanoparticle attached to graphene oxide. A milder effect of the FPZ can be inferred from the data by Chandrasekaran *et al.* [138] who investigated three types of carbon-based nano-fillers (Figure 6.4): (1) thermally reduced graphene oxide; (2) graphene nanoplatelets; and (3) multi-wall carbon nanotubes. In these cases, the difference between SEL and LEFM ranges from 4.9% to 8.8%, the lowest difference among all the data analyzed in this study. For these systems, the specimen size compared to the size of the nonlinear FPZ is large enough to justify the use of LEFM which provided accurate and objective results. On the other hand, a more significant effect of the FPZ can be inferred from the data reported by Konnola *et al.* [154] who studied three different types of functionalized and nonfunctionalized nano-fillers. In this case, the greatest difference in fracture energy ranges between 15.2% to 20.3%.

SENB specimens nano-modified by nanoclay and carbon black respectively were tested by Kim *et al.* [157]. As Figure 6.5 shows, in this case, the specimen size is enough to justify the use of LEFM as confirmed by the low difference with SEL (11.2% for nanoclay and 7.3% for carbon black). Similar conclusions can be drawn on the silica nanoparticles investigated by Vaziri *et al.* [158]. However, for the three different sizes of silica nanoparticles investigated by Dittanet *et al.* [159], a significant difference between LEFM and SEL is observed, confirming that these specimens belonged to the transition zone between pseudo-ductile and brittle

behavior where the effects of the nonlinear FPZ cannot be neglected.

Figure 6.6 shows a re-analysis of the data reported by Liu *et al.* [160] who tested CT specimens nano-modified by four different combinations of silica nanoparticle and rubber. As can be noted, in this case, the FPZ indeed affects the fracturing behavior significantly. Adopting LEFM, which assumes the size of the FPZ to be negligible, for the estimation of G_f would lead to an underestimation of up to 156.8% for the case of polymer reinforced by 15 wt% rubber only. This tremendous difference, the largest found in the present study, gives a tangible idea of the importance of accounting for the nonlinear damage phenomena occurring in nanocomposites which can lead to a significant deviation from the typical brittle behavior of thermoset polymers.

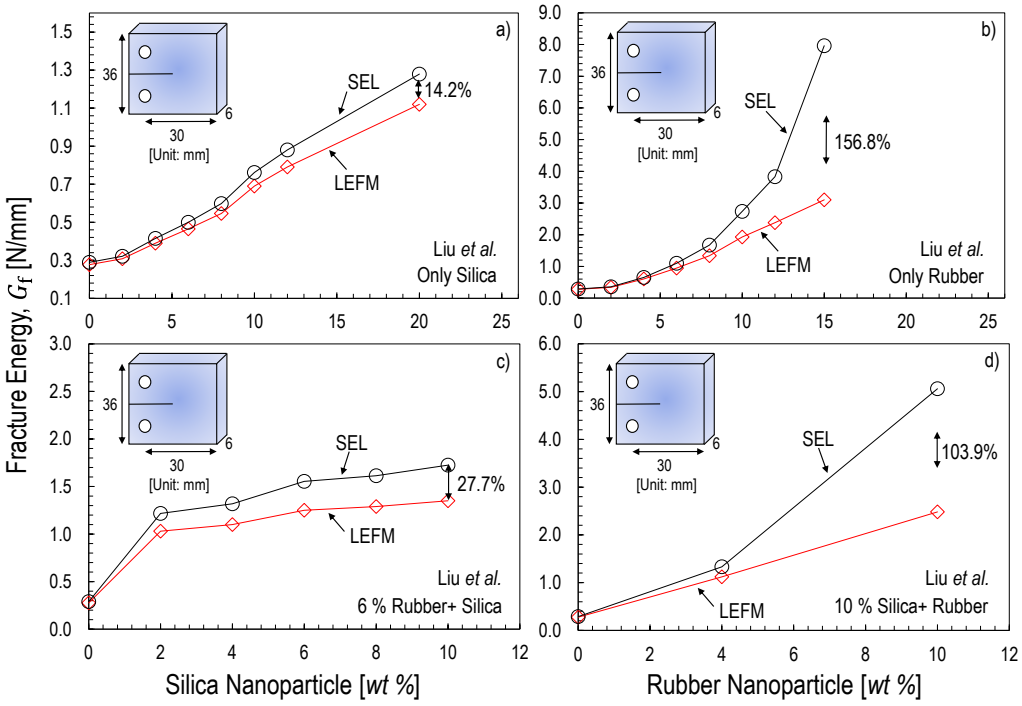

Figure 6.6: Mode I fracture energy estimated by Linear Elastic Fracture Mechanics (LEFM) and Size Effect Law (SEL), Eq. (6.1). The latter formulation accounts for the finite size of the nonlinear Fracture Process Zone (FPZ) in thermoset nanocomposites. Data re-analyzed from [160].

6.3 Cohesive zone modeling of thermoset polymer nanocomposites

To have a deeper understanding of the fracturing behavior of nanocomposites, a computational investigation is conducted leveraging a cohesive zone model featuring a Linear Cohesive Law (LCL) in ABAQUS Explicit 2017. To this end, a Single Edge Notch Bending (SENB) specimen is simulated by 4-node two-dimensional cohesive elements (COH2D4) with a traction-separation law to model the crack and 4-node bi-linear plain strain quadrilateral elements (CPE4R) with a linear elastic isotropic behavior to model the rest of the specimen.

To corroborate the results discussed in the forgoing sections, the analysis by means of a cohesive zone model is carried out using the fracture energy estimated via LEFM, G_f^{LEFM}, and the one calculated through Eq.(6.1), G_f^{SEL}. As can be noted from Figures 6.7-6.10, the cohesive zone model using G_f^{SEL} as input shows an excellent agreement with the experimental data in the literature. However, this is not the case if G_f by LEFM is used. In fact, this is a further confirmation that Size Effect Law (SEL) can be adapted to re-analyze the fracture tests available in the literature.

By leveraging a linear cohesive crack model with the corrected G_f, the fracturing behavior on the scaling of nanocomposites can be predicted without additional tests in the lab. As Figures 6.11-6.14 show, experimental data in the literature and simulation results using a linear cohesive crack law are plotted along with the analytical expression for Cohesive Size Effect Curves (CSEC) proposed by Cusatis *et al.* [88]. In these Figures, it can be noted that, for large specimen sizes, the prediction on the peak load of the investigated nanocomposites by using LEFM G_f leads to a significant underestimation. It is worth mentioning here that this analysis is on the assumption that the nanocomposites in the literature follow a linear cohesive law. The excellent agreement reported between simulations and experiments strongly supports this assumption.

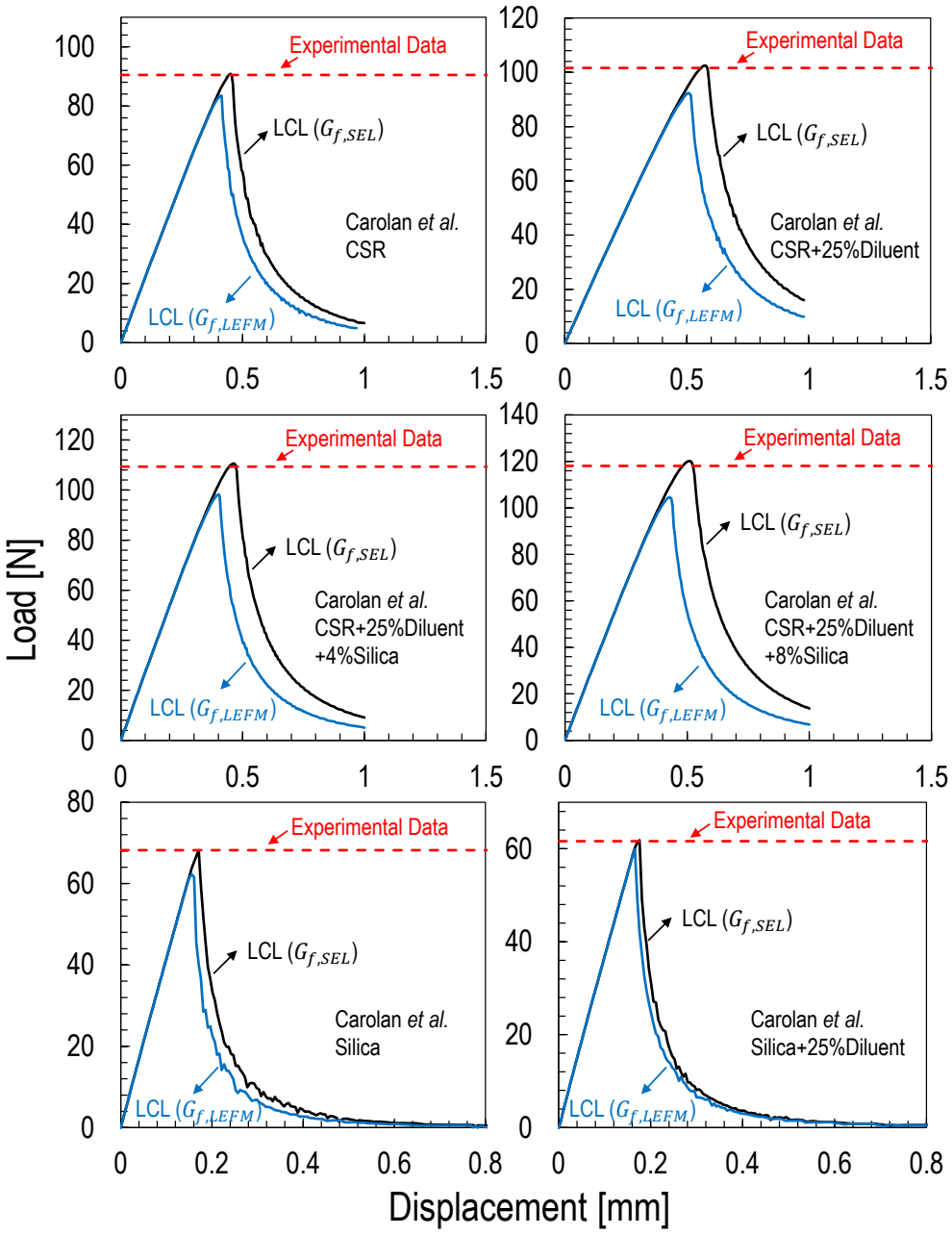

Figure 6.7: Load-displacement curves obtained by using a linear cohesive crack law with both LEFM and corrected G_f on the re-analysis of data from [155].

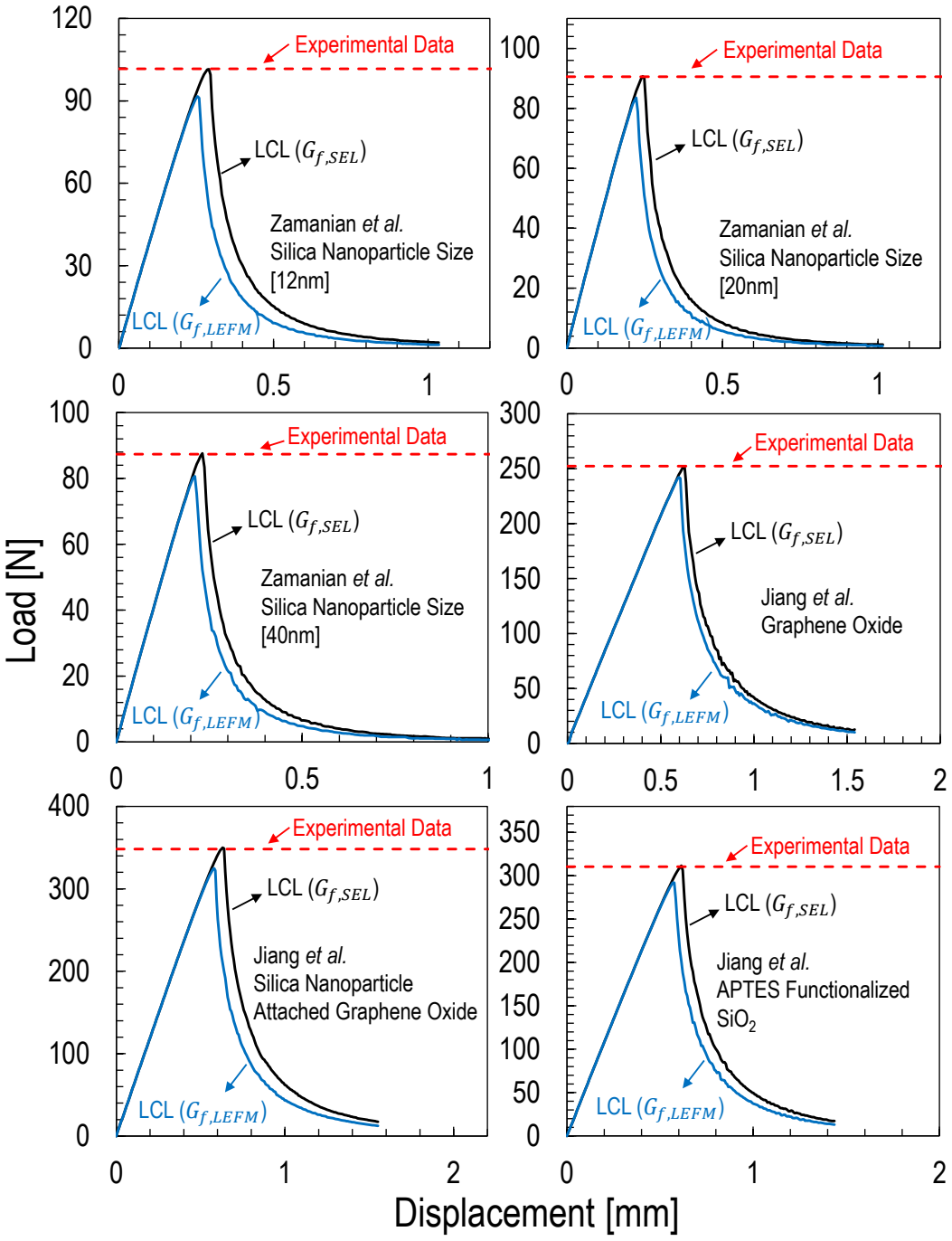

Figure 6.8: Load-displacement curves obtained by using a linear cohesive crack law with both LEFM and corrected G_f on the re-analysis of data from [153], [156].

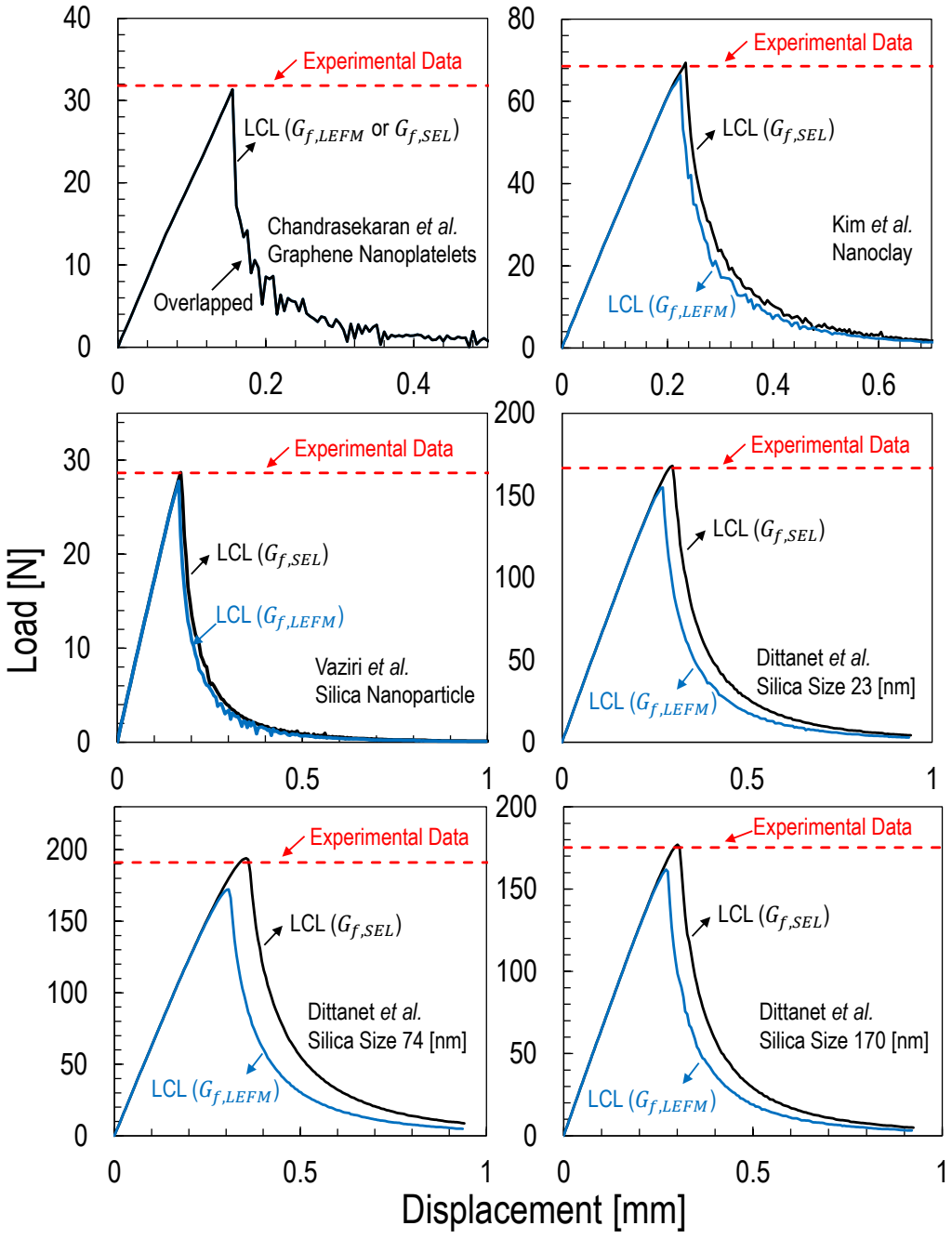

Figure 6.9: Load-displacement curves obtained by using a linear cohesive crack law with both LEFM and corrected G_f on the re-analysis of data from [138, 157–159].

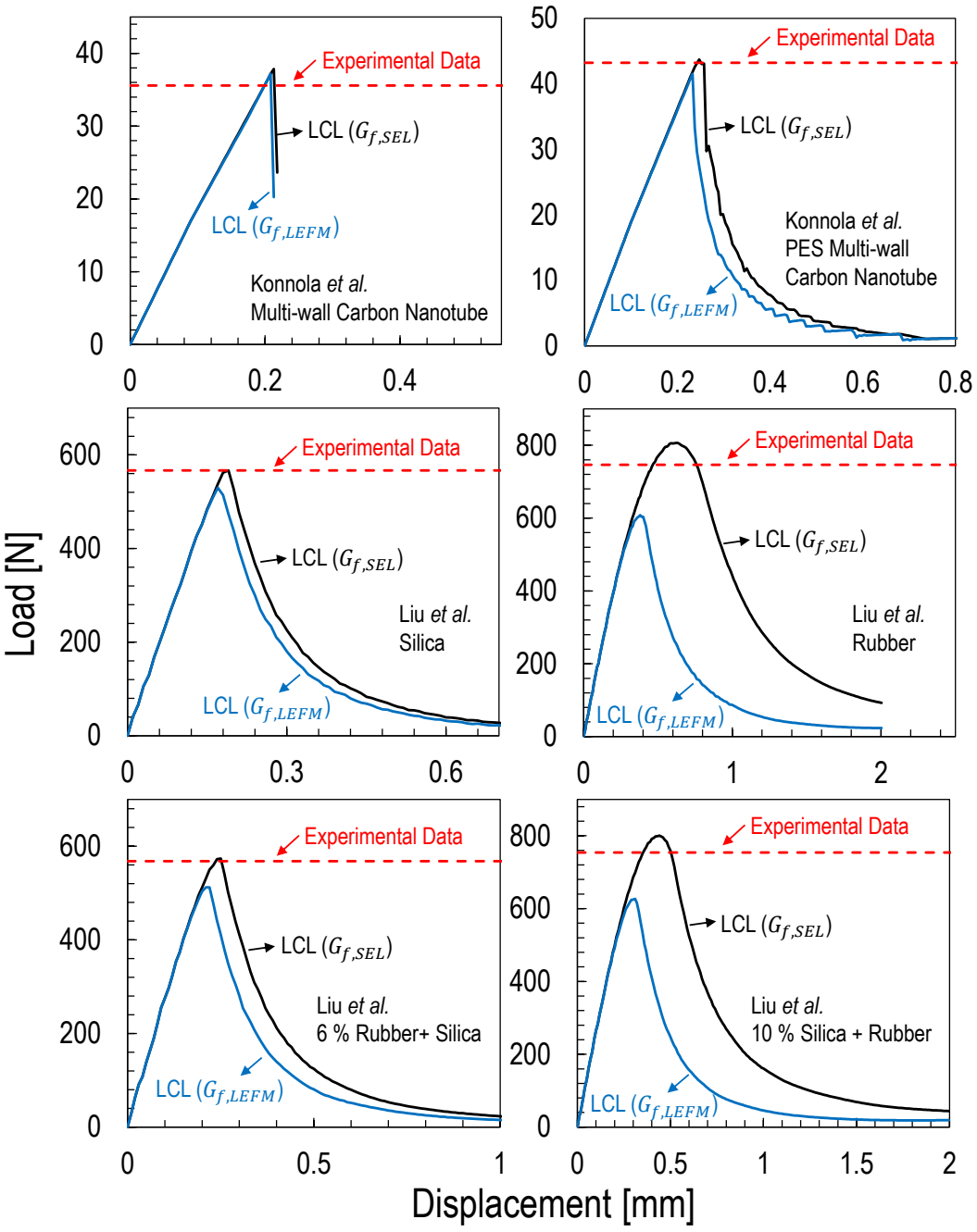

Figure 6.10: Load-displacement curves obtained by using a linear cohesive crack law with both LEFM and corrected G_f on the re-analysis of data from [154], [160].

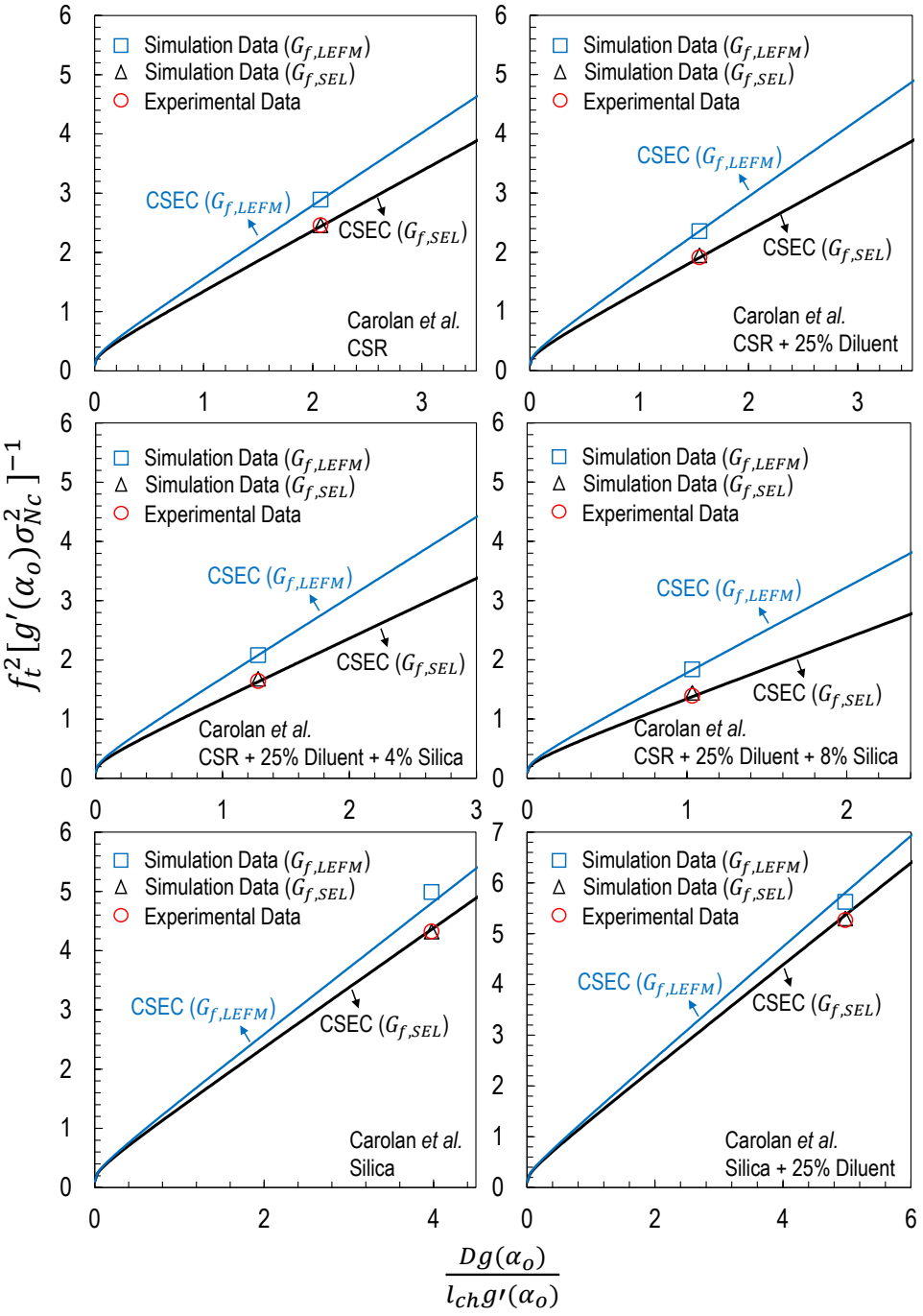

Figure 6.11: Comparison between LCL results and experimental data [155].

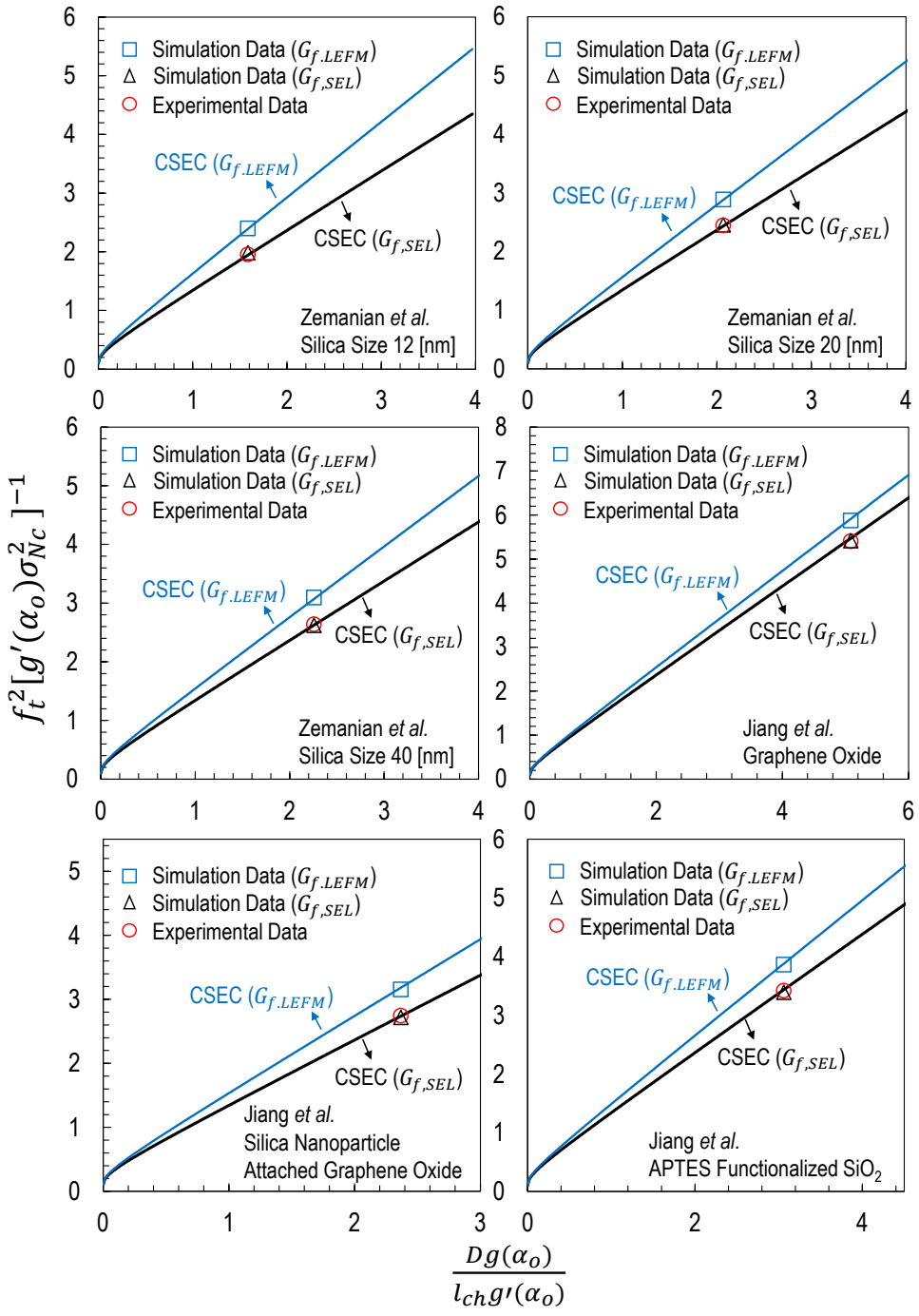

Figure 6.12: Comparison between LCL results and experimental data [153], [155], [156].

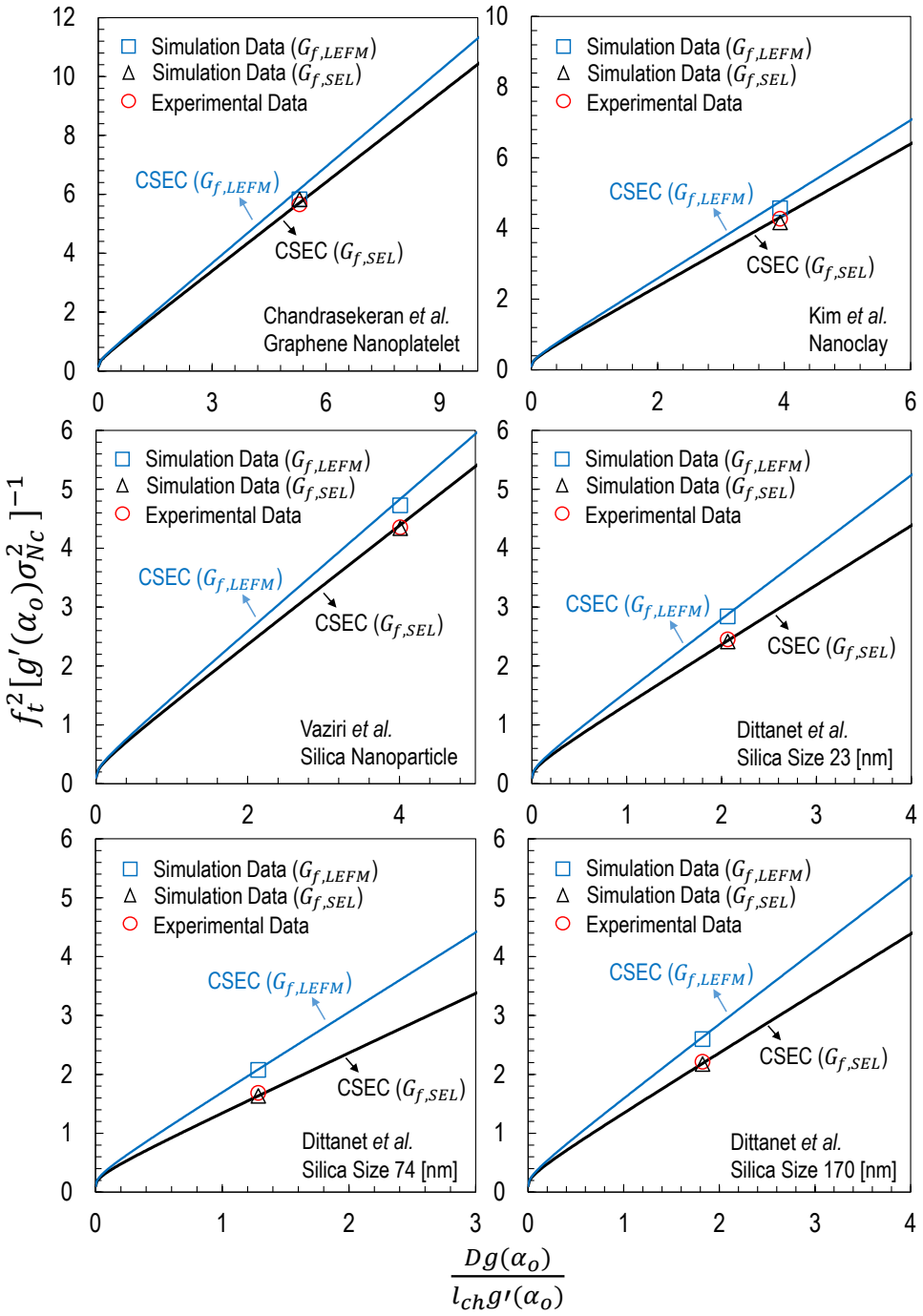

Figure 6.13: Comparison between LCL results and experimental data [138, 157–159].

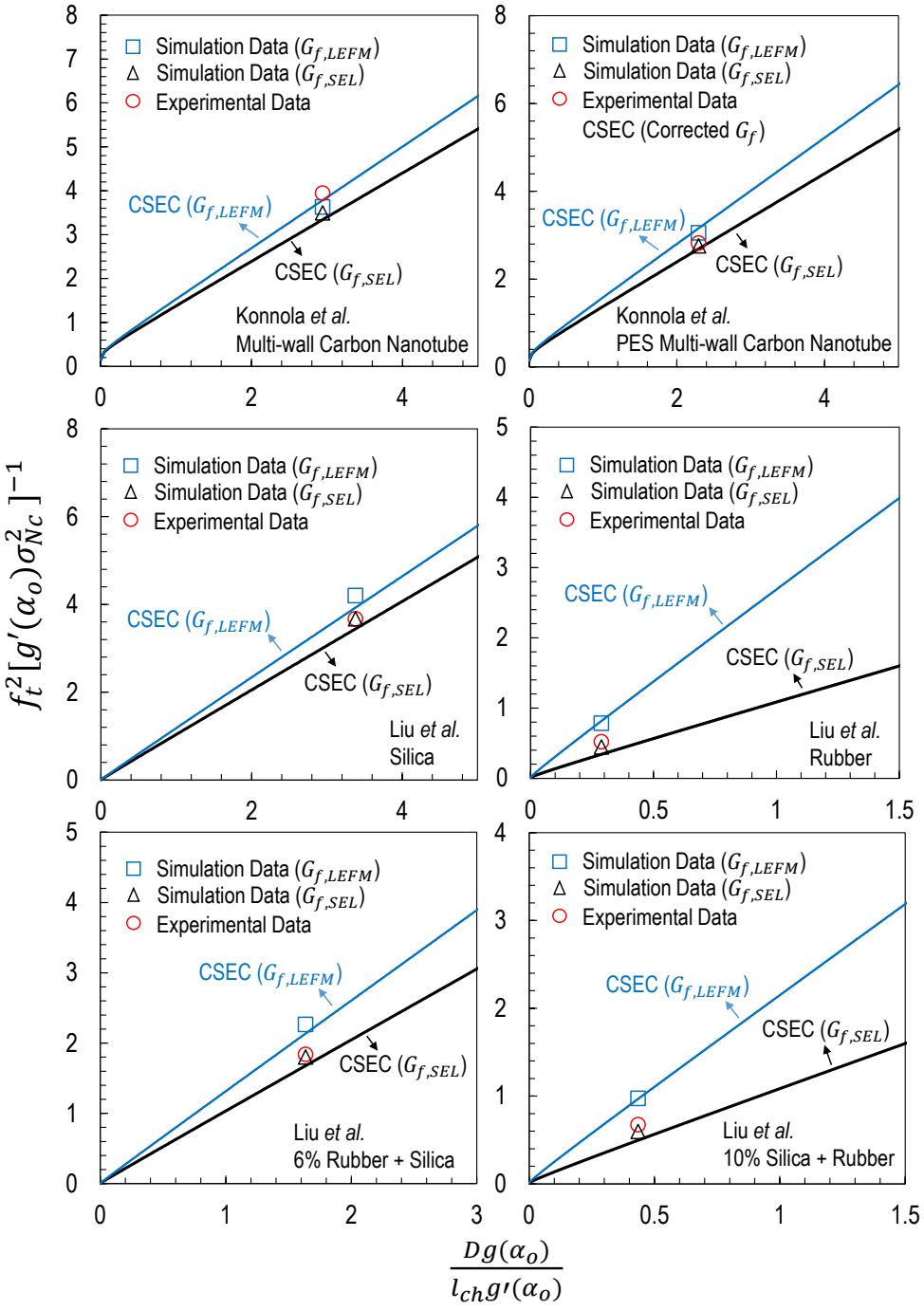

Figure 6.14: Comparison between LCL results and experimental data [154], [160].

6.4 Conclusions

1. The double logarithmic plots of the normalized structural strength as a function of the normalized characteristic size of geometrically-scaled SENB specimens show that the experimental data on generic nanocomposites available in the literature are in excellent agreement with Size Effect Law (SEL). Most of nanocomposites are located in the transitional range in which the fracturing behavior cannot be characterized by Linear Elastic Fracture Mechanics (LEFM);

2. Size Effect Law and Cohesive Zone Modeling show that for most of the fracture tests on generic polymer nanocomposites investigated in this work, the effects of the nonlinear FPZ are not negligible. As the data indicate, this aspect needs to be taken into serious consideration since the use of LEFM to estimate the mode I fracture energy can lead to an error as high as 156% depending on the specimen size and nanofiller content. This deviation is due to the larger formation of FPZ compared to the specimen characteristic size thus strongly affecting the fracturing behavior.

Chapter 7

SIZE EFFECT IN FATIGUE BEHAVIOR OF POLYMER-GRAPHENE NANOCOMPOSITES AND OTHER QUASI-BRITTLE MATERIALS

Having discussed the mechanical behavior of thermoset polymers and related nanomodification at various length scales and stress states under quasi-static loading condition. This chapter focuses on the fatigue failure behavior and size scaling of thermoset polymers and graphene nanocomposites. It was shown that the investigated nanocomposites exhibit great quasi-brittle fracturing behavior leading to even stronger size effects under fatigue loading condition compared to the previous investigation on the same materials under quasi-static scenario. This size scaling aspect cannot be simply described through the Linear Elastic Fracture Mechanics and even analyzed by leveraging the Quasi-brittle Fracture Mechanics due to the evolution of the damage zone. By conducting the computational analysis, it was found that the crack propagation in the fatigue scenario features two damage zones constituting the entire fatigue damage zone which is even complicated compared to the quasi-static scenario with the damage zone mainly driven by the energy. This study is extremely insightful for understanding the general fatigue behavior of other quasi-brittle materials.

7.1 Fatigue failure behavior of thermoset polymer

7.1.1 Direct measurement of fatigue crack growth

Geometrically-scaled SENB specimens made of thermoset polymer were manufactured and prepared following the same procedure as described in the previous chapters. Fatigue fracture tests on these specimens were performed on a servo-hydraulic 8511 Instron machine. The loading conditions are the followings: (1) a sinusoidal ramp load; (2) load ratio of $R = 0.1$;

(3) load frequencies were 5 Hz, 7.4 Hz and 11 Hz for D = 10 mm, 20 mm and 40 mm respectively in order to have the roughly same strain rate for specimens with different sizes.

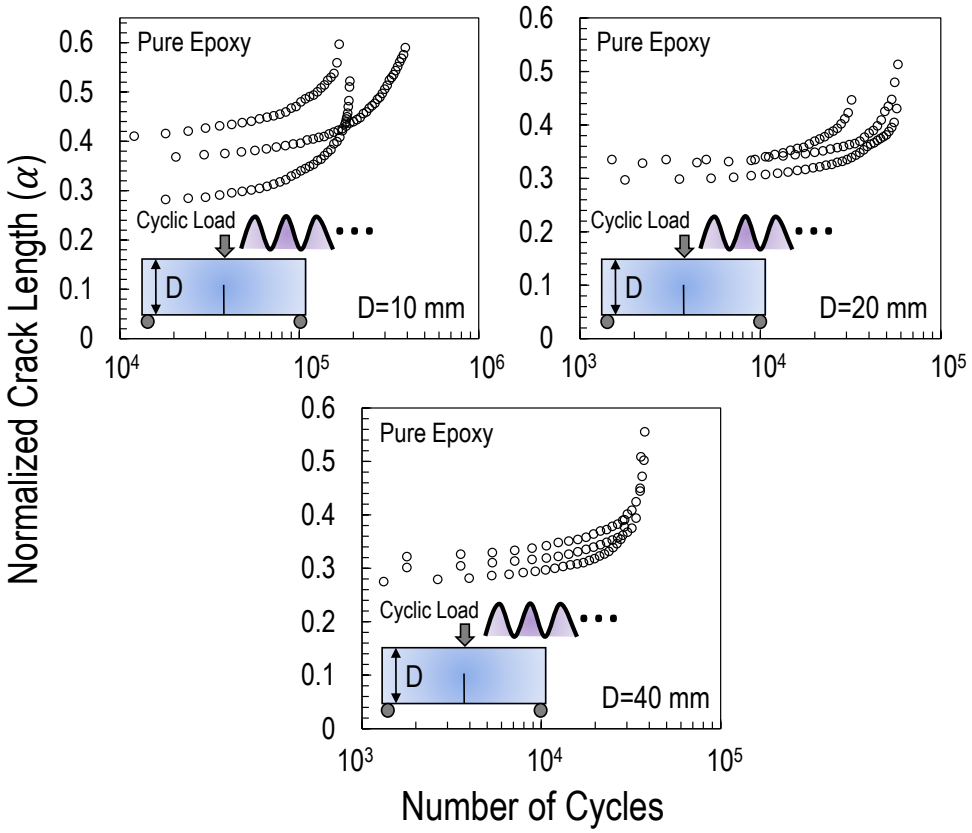

Figure 7.1: Direct measurement of crack length for pure epoxy: normalized crack length vs. fatigue life for pre-cracked SENB specimens.

Thanks to the transparency of pure epoxy, the evolution of crack growth of specimens during fatigue tests can be monitored by a digital microscope. Based on this direct measurement of crack length, the growth of normalized crack length with respect to number of cycles can be plotted in a semi-logarithmic coordinate as shown in Figure 7.1. The normalized crack length was defined as $\alpha = a/D$ where a is the crack length. As can be noted from the figure for different specimen sizes, crack grows slowly at the early stage of the fatigue life whereas it propagates rapidly as the structure approaches its catastrophic failure. In addition to this,

specimens featuring different sizes do not exhibit a similar fatigue life since it has significant reduction as structural size increases as illustrated in Figure 7.2. This phenomenon needs to be further studied by leveraging a computational model which will be discussed later.

It is worth mentioning here that the crack propagation of pure epoxy under fatigue loading condition has the following three stages: (1) uneven crack front due to the tapping propagates into an even crack front; (2) even crack front propagates into a parabolic shape of crack front; (3) stable propagation of the crack with almost the same parabolic shape. The chord length of the parabolic shape crack is about 0.8 mm, 0.9 mm and 1.1 mm for $D = 10$ mm, 20 mm and 40 mm respectively.

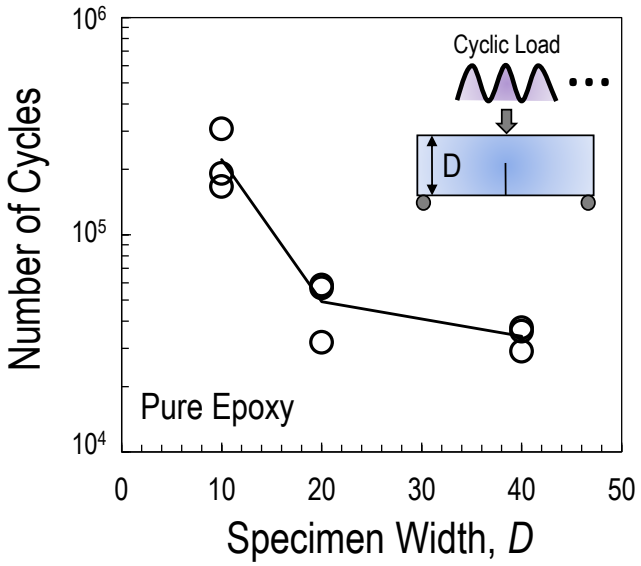

Figure 7.2: Fatigue life vs. specimen size for pre-cracked specimens of pure epoxy.

7.1.2 Paris-Erdogan curves: direct measurement of crack growth

Before analyzing the fatigue fracture tests by means of a well-known Paris-Erdogan law [163], the fatigue crack growth rate as a function of Stress Intensity Factor (SIF) amplitude, it is worth mentioning here that this law is based on the Linear Elastic Fracture Mechanics

(LEFM) which neglects the effects of the Fracture Process Zone (FPZ) and treats it to be a mathematical point. With knowing the fact that the effects of the FPZ on the quasi-static fracturing behavior of pure epoxy are negligible as shown in the previous chapters, it is interesting to confirm that this conclusion can be applied into the fatigue case or it has remarkable effects on the fatigue crack growth as reported by several authors on other qusi-brittle materials [164, 165] . This aspect is never confirmed for thermoset polymers in the literature and will be discussed throughout this chapter.

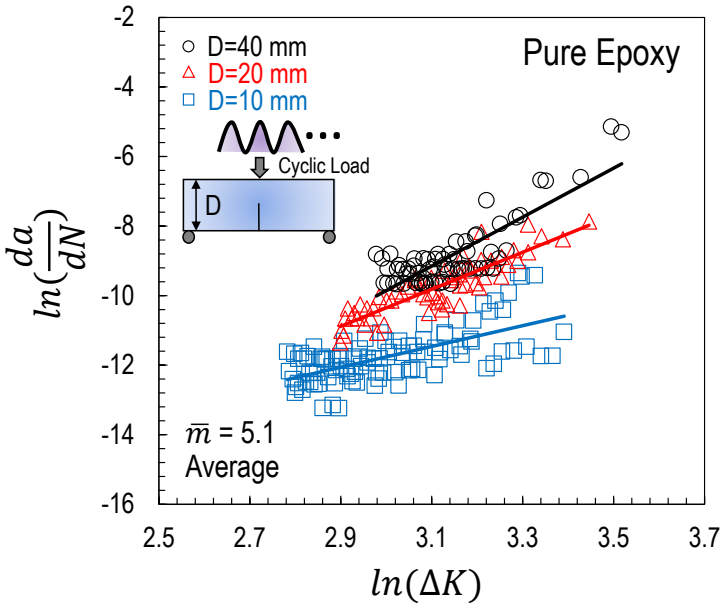

Figure 7.3: Direct measurement of crack length: crack growth rate vs. SIF amplitude.

Following the Linear Elastic Fracture Mechanics (LEFM), the Mode I Stress Intensity Factor K has the following form:

$$K = \sqrt{G(\alpha)E^*} \tag{7.1}$$

where the parameters have the same definitions as described in the previous chapters. With knowing the growth of the crack length, the relationship between crack growth rate (da/dN) and mode I Stress Intensity Factor (SIF) amplitude ($\Delta K = (1-R)K$) for all the investigated

specimen sizes can be plotted in a double logarithmic coordinate which is usually referred to the following well-known equation (Paris-Erdogan law):

$$da/dN = C(\Delta K)^m \tag{7.2}$$

In the case of the crack length obtained from a direct measurement as mentioned in the foregoing section, experimental results analyzed through Eq. (7.2) are plotted in Figure 7.3. As it can be noted from this figure that the investigated sizes of the specimens have remarkable effects on the aforementioned Paris-Erdogan curves showing pronounced differences mainly on the parameter C for different structural sizes. This is an indication of a larger FPZ in the fatigue condition thus affecting the fatigue failure behavior of the investigatd pure epoxy which is not the truth for the quasi-static condition.

7.1.3 Analysis and discussion

According to the previous studies on the scaling of fatigue crack growth in sandstone with a theoretical model describing the experimentally observed size effect in Paris-Erdogan curves [166, 167], it is considered that during each load cycle the energy dissipation associated with the growth of the macrocrack is equal to the sum of the energy dissipations associated with the propagation of all the active nano-scale cracks inside the cyclic FPZ. This can be written in the following:

$$U_{c,\infty} da/dN = \sum_{i=1}^{n_a} U_a da_i/dN \tag{7.3}$$

where $U_{c,\infty}$ = critical energy dissipation per unit growth of the macrocrack in an infinitely large specimen, U_a = critical energy dissipation associated with the breakage of one atomic bond. a_i = length of ith nano-scale crack and n_a = number of active nano-scale cracks in the cyclic FPZ.

By considering a well-established transition state theory from Kramers [168], the fatigue growth rate of a crack at the nano-scale can be obtained in the following:

$$da_i/dN = \upsilon_i e^{-Q_0/kT} \Delta K_{ai}^2 \tag{7.4}$$

where υ_i = constant determined by the geometry of the nano-scale element, Q_0 = dominant free activation energy barrier, k = Boltzmann constant, T = absolute temperature and ΔK_{ai} is the SIF amplitude of the nano-scale element.

With the assumption on the average energy dissipation associated with the nanocrack growth and dimensional analysis on the number of active nano-scale cracks in the cyclic FPZ, the fatigue growth rate of a macrocrack in a finite specimen size can be written in the following form:

$$da/dN = \frac{A\Delta K^2}{U_c}\Phi(\Delta K^2/EU_c) \tag{7.5}$$

where $A = \omega^2 U_a \upsilon_a e^{-Q_0/kT}$, U_c = critical energy dissipation per unit growth of the macrocrack in a finite specimen and ΔK = SIF amplitude of a macrocrack. By borrowing the ideal on the Size Effect Law (SEL) of quasi-static loading to the cyclic loading scenario: $U_c = U_{c,\infty}[D/(D + D_{0c})]$ where D_{0c} can be considered as transitional size for cyclic loading, the following equation can be obtained:

$$da/dN = \frac{A\Delta K_D^2}{U_{c,\infty}}\Phi(\Delta K_D^2/EU_{c,\infty}) \tag{7.6}$$

If it is assumed that function Φ is self-similar which means that $\Phi(\Delta K_D^2/EU_{c,\infty})$ equals to $\Delta K_D^{2q}/E^q U_{c,\infty}^q$. By leveraging this, Eq.(7.6) can be further written as the following form:

$$da/dN = C\Delta K_D^m \tag{7.7}$$

where $C = AE^{1-n/2}U_{c,\infty}^{-n/2}$, $m = 2 + 2q$, $\Delta K_D = (1 + D_{0c}/D)^{0.5}\Delta K$ = size adjusted SIF amplitude.

After implementing Eq.(7.7) into the experimental data obtained from fatigue fracture tests, as illustrated in Figure 7.4, size effect on the fatigue threshold (K_{th}) and critical stress intensity factor amplitude ΔK_c are removed. To achieve this, cyclic FPZ size is about 1 mm, 3 times larger than the monotonic FPZ found by Mefford *et al.* [94]. However, size effect on the slope and initial crack growth rate still exist in the adjusted Paris-Erdogan curves.

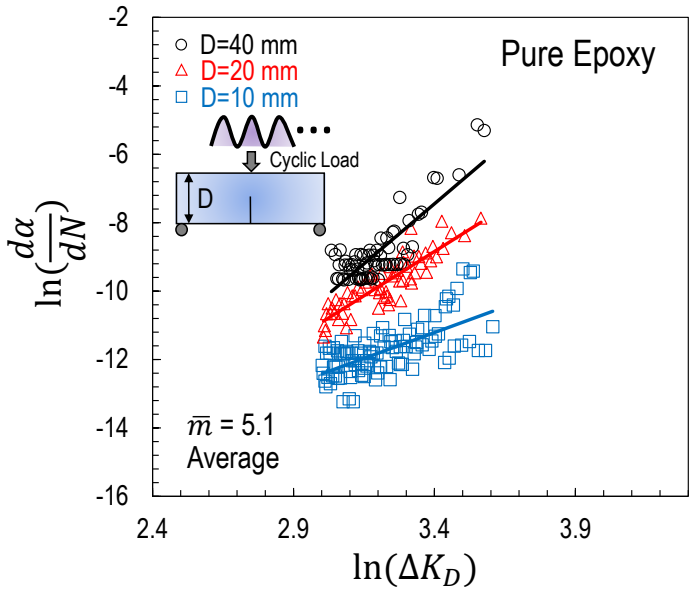

Figure 7.4: Size-adjusted Paris-Erdogan curves for pure epoxy.

7.1.4 Compliance method for fatigue crack growth and Paris-Erdogan curves

The foregoing method does not always provide an accurate measurement on the fatigue crack growth since the crack opening at the tip is typically in the magnitude of micron meter which can not be clearly captured by using a digital microscope. As a consequence, the measured crack length is possibly shorter than its real one which leads to an error for the calculation of crack growth rate and SIF amplitude. In this context, an indirect measurement was used to estimate fatigue crack growth. This is based on the compliance of the specimen since it is a function of the crack length. With knowing the evolution of the compliance of the specimen during the fatigue loading, crack length can be obtained through the compliance function with respect to the crack length which can be calculated either from the finite element analysis or analytical approach leveraging the LEFM as written in the following form:

$$c = \frac{9L^3}{2tD^2E}\int_0^{\alpha} g(\alpha)d\alpha + \frac{L^3}{48EI} \tag{7.8}$$

where I is the second moment of area and other symbols have the same definitions as described in the previous chapters. As can be noted from Figure 7.5, the evolution of normalized crack length with number of cycles based on the compliance method is different from the previous one obtained through a direct measurement. This is due to the fact that compliance method is based on the LEFM framework. As a consequence, to capture the fracturing behavior of the specimen during the fatigue loading, crack length must include an effective FPZ size which is not accounted into the crack length observed from a digital microscope. In this consideration, crack length estimated by means of the compliance method is considered as an equivalent crack length which includes the effects of the FPZ.

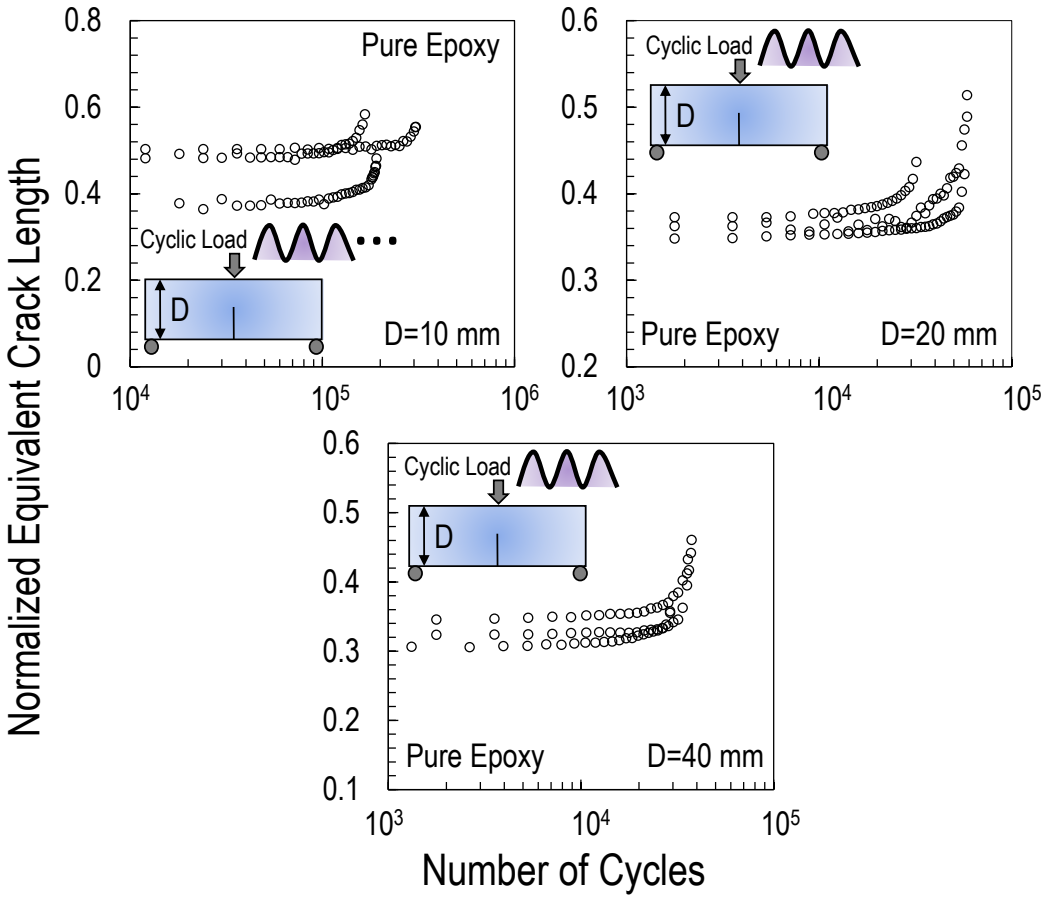

Figure 7.5: Compliance method: normalized equivalent crack length vs. number of cycles for pre-cracked SENB specimens of pure epoxy.

It is interesting to construct Paris-Erdogan curves based on the equivalent crack length to have a comparison with the foregoing curves by leveraging a different method for crack measurement. As illustrated in Figure 7.6, the curves for pure epoxy exhibit significantly larger slopes for all the investigated specimen sizes which are definitely different from the previous ones plotted in Figures 7.3-7.4 by leveraging a direct measurement of crack length. This aspect is due to the consideration for the cyclic evolution of the FPZ in the compliance method. The average slope (m) of the investigated pure epoxy with various sizes is approximately equal to 11 although the best fitting of these curves leads to the less significant differences on the slopes for different specimen sizes. Further computational studies are required to provide detailed information on the scaling of fatigue behavior which will be conducted in the following sections.

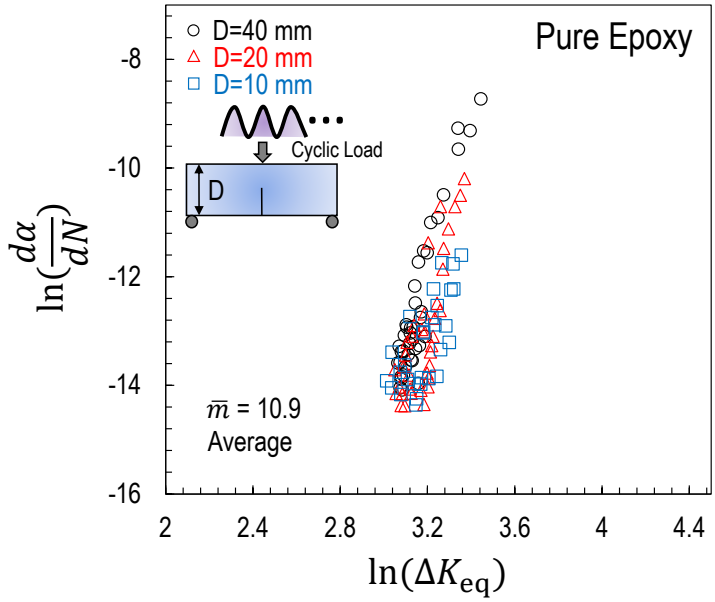

Figure 7.6: Paris-Erdogan curves of pure epoxy based on the compliance method.

7.1.5 Morphology of fatigue fracture

A further morphological study was conducted to investigate the main mechanisms of fatigue crack growth in the scaling of pure epoxy. To this end, the specimens were cut and the fracture surfaces were gold-coated in order to be used for Scanning Electron Microscopy (SEM) by a JSM-6010PLUS/LA Electron Microscope [136]. The SEM images of several samples with different sizes are showed in Figure 7.7.

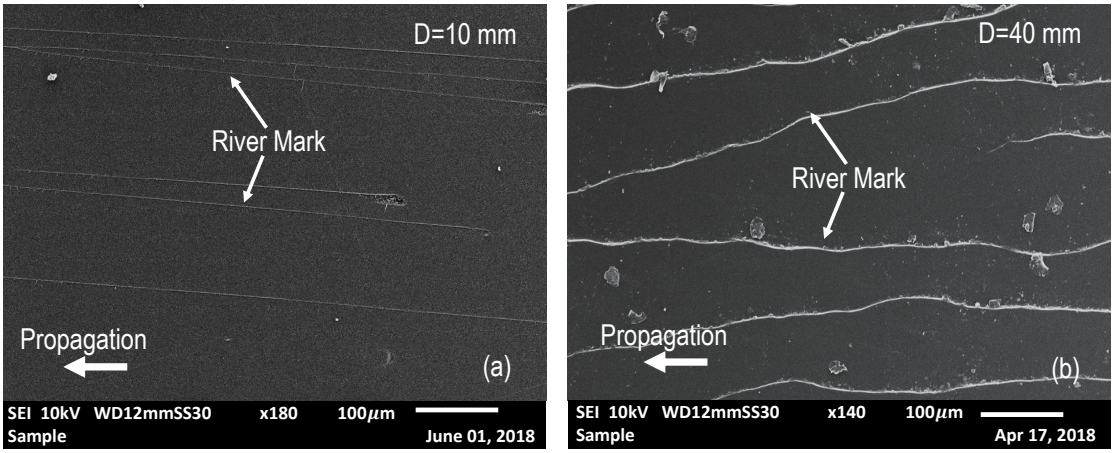

Figure 7.7: Fracture surfaces of specimens: (a) $D = 10$ mm; (b) $D = 40$ mm.

As can be noted from Figure 7.7, river marks parallel to the crack propagation direction were observed for all the investigated specimen sizes which contradicts the fact that beach marks perpendicular to the crack propagation direction features the fatigue fracture morphology in metals. This phenomenon can be explained by the fact that crack front propagates on the different planes in polymeric materials. In addition to this, river marks are more pronounced for large specimen while small specimen has less remarkable river marks.

7.1.6 Degradation of material strength at multiple length scales

Having discussed the effects of a non-linear FPZ size on the fatigue scaling of a thermoset polymer-based structure, this section focuses on studying the evolution of the material

strength throughout entire fatigue life. It is worth mentioning that the stress ratio of $R = 0.1$ and a low frequency of $f = 5$ Hz were selected for all the fatigue tests in this section. Before investigating the foregoing aspect, peak stress in the cyclic loading as a function of number of cycles (i.e. S-N curve) was obtained by conducting fatigue tests on dogbone specimens. The dimensions of the specimens are exactly the same as described in the previous chapters.

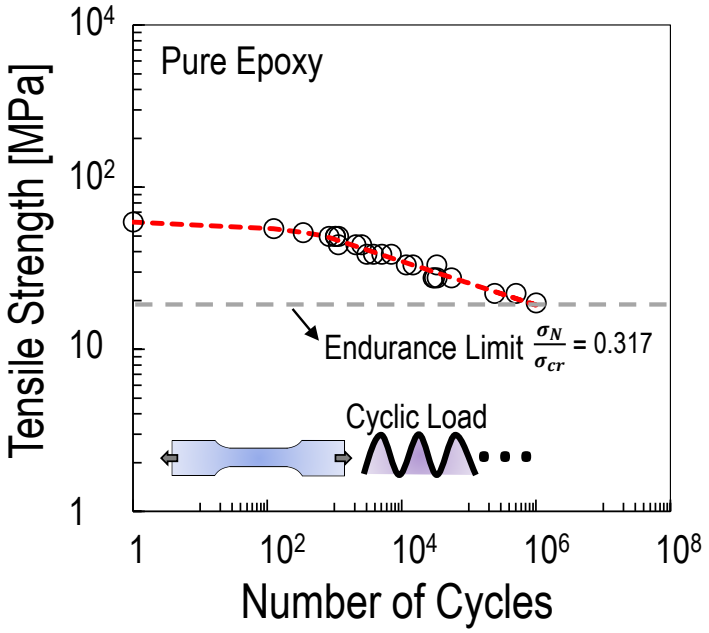

Figure 7.8: S-N curve for dogbone specimens of pure epoxy under tensile fatigue loading.

As can be noted in Figure 7.8, the S-N curve is characterized by three parts: (1) the initial part representing the low-cycle fatigue regime; (2) the second part describing the high-cycle fatigue regime which features larger slope compared to the initial part; (3) the last part referred as endurance limit representing no failure of the material below this threshold. The endurance limit was considered as one million cycles and found to be about 30% of the critical quasi-static load.

With knowing the S-N curve of the material, the evolution of the material strength with

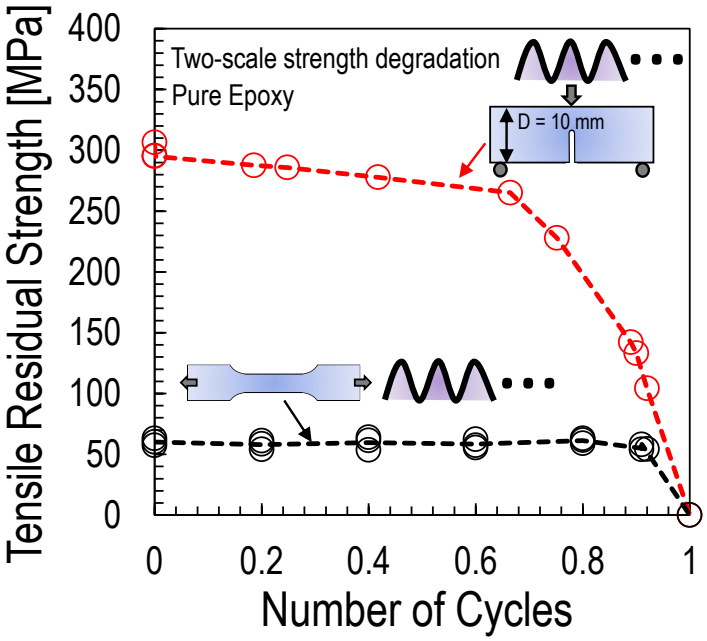

Figure 7.9: Evolution of residual strength at different scales throughout entire fatigue life.

respect to its fatigue life was investigated for the case that maximum applied cyclic load is about 50% of the critical quasi-static load. By conducting the quasi-static tests after the aforementioned fatigue fracture tests, the foregoing aspect was obtained as illustrated in Figure 7.9. It is interesting to notice from the figure that the material almost has no degradation on the macro-scale strength before about 90% of the entire fatigue life but it tends to exhibit degradation near the end of the entire fatigue life. On the other hand, with knowing the fact that pre-notched SENB specimens can be used to measure the micro-scale strength as discussed and analyzed in the previous chapters, the degradation of the material strength at the micro scale was investigated following the same procedure as described in the foregoing paragraph. The maximum applied cyclic load for this study is about 25% of the critical quasi-static load which is lower than the one used for dogbone specimens. This is due to the fact that high-cycle fatigue regime for pre-notched specimens happens at lower stress level. By testing the residual strength of the material as illustrated in Figure 7.9,

the material strength at the micro scale has significant degradation throughout the fatigue life and eventually tends to the evolution of macro-scale material strength. It is worth mentioning here that the calculation of the micro-scale strength does not take plasticity into the consideration. This interesting phenomenon requires further computational studies.

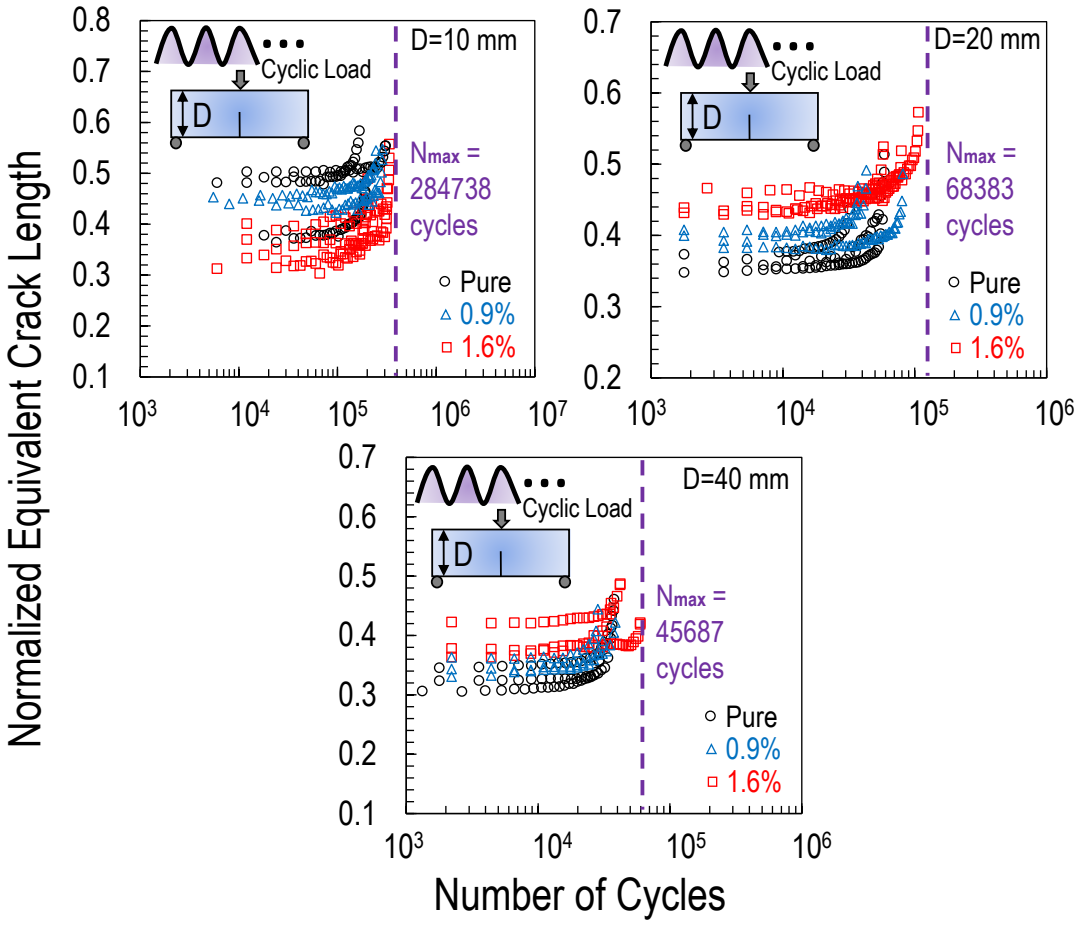

Figure 7.10: Compliance method: normalized equivalent crack length vs. number of cycles for geometrically scaled specimens featuring various graphene concentrations.

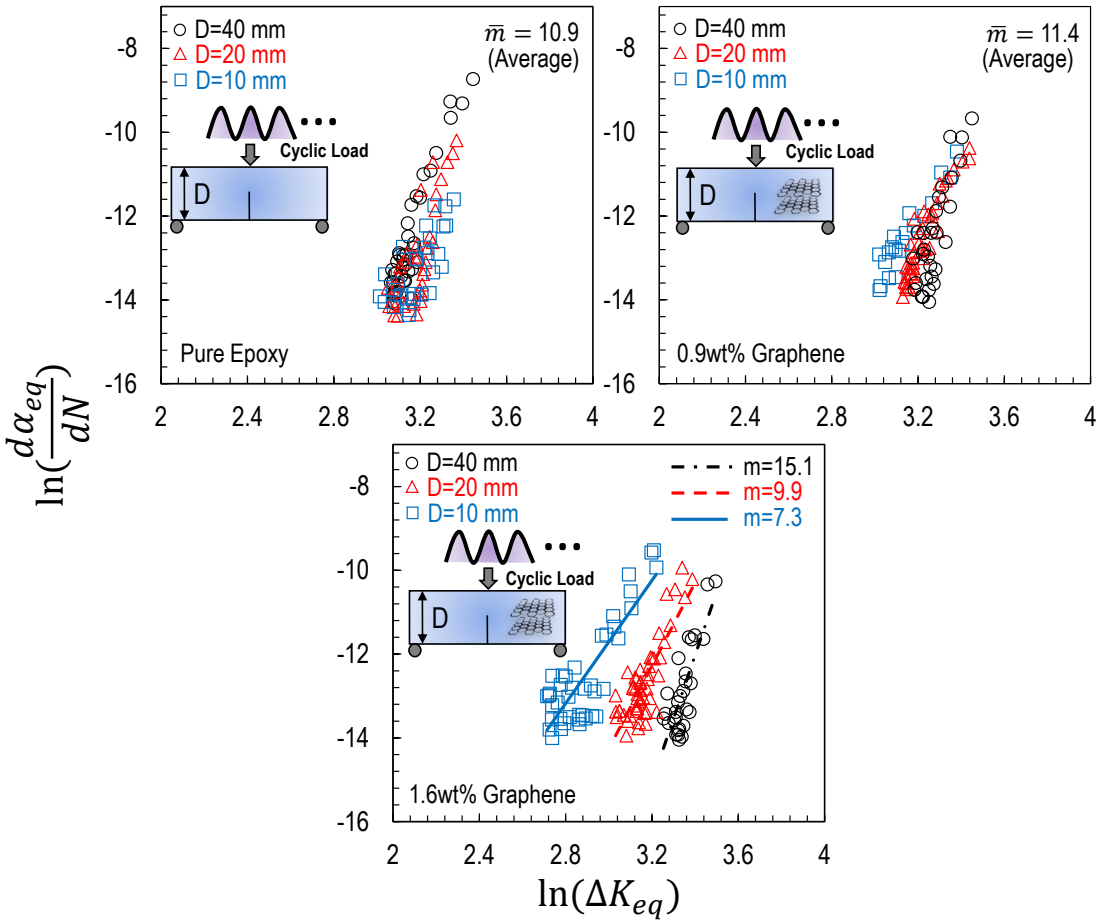

Figure 7.11: Paris-Erdogan curves for different graphene concentrations and specimen sizes.

7.2 Fatigue failure behavior of graphene nanocomposites

7.2.1 Compliance method for fatigue crack growth

The effects of a finite FPZ size on the fatigue behavior of thermoset polymer nano-modified by graphene nanoplatelets was further investigated. Two different contents of graphene nanoplatelets (0.9% and 1.6%) were selected for geometrically scaled specimens under fatigue loading condition. The dimensions of the specimens and loading conditions are exactly the same as described in the previous sections for fatigue fracture tests on pure specimens.

By using the compliance method for the determination of the fatigue crack growth as

described in the previous sections, the evolution of normalized equivalent crack length with number of cycles for geometrically-scaled specimens with various graphene contents is plotted in Figure 7.10. As can be noted from the figure, smaller specimens also feature higher number of cycles whereas lower fatigue life characterizes larger specimens which was also observed for the specimens without nanomodification.

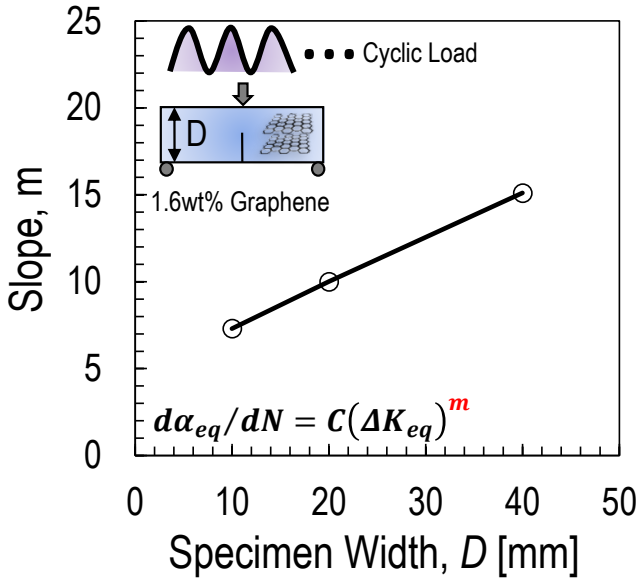

Figure 7.12: The slopes of Paris-Erdogan curves for the geometrically-scaled specimens with 1.6% graphene concentration.

7.2.2 Paris-Erdogan curves: compliance method for crack growth

With knowing the growth of the equivalent crack length, Paris-Erdogan curves for these cases can be plotted as illustrated in Figure 7.11, it is worth noticing from the figure that the fatigue threshold and critical SIF amplitude exhibit pronounced differences for geometrically-scaled specimens as graphene content increases. This is an indication that the fatigue crack growth is strongly affected by the evolution of the FPZ size. More interestingly, the Paris-Erdogan curves for higher graphene concentration exhibit more remarkable difference in the slopes and this aspect can be related to the function of the specimen size as shown in Figure 7.12.

This aspect is also attributed to the different evolution of the FPZ size for different specimen sizes which requires a further study by leveraging a computational modeling as it will be discussed in the following sections.

7.3 Past and current work in fatigue cohesive zone modeling

Fatigue crack growth of engineered materials via cohesive zone modeling is mainly categorized into Paris-Erdogan-law-based [169–172] and Non-Paris-Erdogan-law-based models [173–179]. The former one leverages on the experimental Paris-Erdogan curves to establish the formulation of the material degradation law. However, the experimental Paris-Erdogan curve is usually constructed by having a direct measurement of the crack growth in the material leveraging a traditional camera. As a consequence, this approach cannot determine the accurate location of the crack tip since the crack opening displacement close to the crack tip is in the order of few microns. This inappropriate method leads to the important fact that the non-linear Fracture Process Zone (FPZ) cannot be taken into the consideration but it was shown to be quintessential to characterize the failure behavior of polymeric materials depending on the structure size. In this context, Turon *et al.* [172] proposed the following degradation law by accounting for the length of the FPZ:

$$\frac{\partial d}{\partial N} = \frac{1}{l_{pz}} \frac{\left[\delta^f (1-d) + \delta^i d\right]^2}{\delta^f \delta^i} \frac{\partial a}{\partial N} \tag{7.9}$$

where $\partial d/\partial N$ is the damage degradation rate per cycle, l_{pz} is the length of the FPZ, δ^i is the displacement for damage initiation, δ^f is the displacement of failure and $\partial a/\partial N$ is the crack propagation rate expressed by the experimental Paris-Erdogan curves. It is worth mentioning here that the length of the FPZ used in the model is calculated under the critical quasi-static condition which leads to a constant length of the FPZ throughout the fatigue life. However, the evolution of the FPZ in the fatigue case must be included if the material degradation law is formulated with the consideration of the FPZ.

On the other hand, the Non-Paris-Erdogan-law-based models leverage on the assumption of damage kinematics laws to consider the degradation of the material strength and stiffness.

One of the outstanding examples is provided by Nguyen *et al.* [174] who introduced one parameter to govern the degradation of the material stiffness in the reloading scenario and assumed no plastic deformation in the unloading condition. Thanks to this, the degradation of the material stiffness for each loading cycle leads to an energy hysteresis loop representing the energy dissipation due to the microscopic damage in the material. This model was shown to successfully characterize the fatigue crack propagation in metals by matching the slopes of experimental Paris-Erdogan curves. Notwithstanding this success, the prediction for polymeric materials cannot be achieved since these materials typically exhibit steeper slopes of Paris-Erdogan curves. Towards this direction, Maiti *et al.* [180] introduced the following two-parameter power-law relation to govern the degradation of the cohesive stress in the reloading condition:

$$\frac{\partial \sigma}{\partial \delta} = \sigma \frac{1}{\alpha} N^{-\beta} \tag{7.10}$$

where α and β are the material parameters describing the material degradation in the reloading condition. This relation becomes equivalent to the foregoing one-parameter degradation law in the case of $\beta = 0$, The additional parameter (β) is related to the number of cycles experienced by the material after damage initiation. Thanks to this consideration, the material is characterized by a different degradation rate for each loading cycle compared to the foregoing model assuming the same degradation rate. This modified model was shown to successfully capture the higher slope of Paris-Erdogan curve for pure epoxy experimentally obtained by Brown *et al.* [181].

While the foregoing models made remarkable contribution to the understanding on the fatigue crack propagation in polymer matrix composites, an extremely important aspect for fatigue crack initiation has never been clearly stated in the open literature. The lack of information on the crack initiation in the foregoing models leads to the failure for characterizing the fatigue behavior of a notch-free structure. In this consideration, an outstanding study was provided by Dávila *et al.* [182] who proposed a fatigue cohesive zone model with the

following material degradation law:

$$\frac{\partial D}{\partial N} = (D + \gamma) \left[\frac{\sigma_{max}}{(1 - D)\sigma_c} \right]^{\beta} \tag{7.11}$$

where γ and β are the material parameters calibrated from the experimental S-N curves, σ_{max} is the maximum cohesive stress in the reloading condition and σ_c is the material strength. This model is on the assumption that both crack initiation and propagation can be sufficiently characterized by this unified degradation law. It was shown that this model successfully captured S-N curves and partially matched Paris-Erdogan curves. On the other hand, an interesting study was provided by Nojavan *et al.* [183] who introduced completely different degradation laws for crack initiation and propagation. In this model, the damage zone related to crack initiation is named as the critically stressed zone in which the material strength reduces without the degradation of the material stiffness. Two parameters are involved in this degradation law which can be calibrated from the experimental S-N curves for notch-free specimens. The transition from crack initiation to propagation is achieved by an immediate reduction of the material stiffness corresponding to the residual strength. The latter stage is named as fatigue cohesive zone in which the damage accumulation is controlled by different degradation laws depending on the relationship between the status of the cohesive stress and the boundary of the quasi-static cohesive law. In this case, additional two parameters are required by matching the experimental Paris-Erdogan curves.

The foregoing models with the consideration of both crack initiation and propagation leads to a further step towards understanding the fatigue behavior of polymer matrix composites. However, one important aspect often overlooked is the boundary of the quasi-static cohesive law which was shown to play a pivotal role in capturing the failure behavior of polymer matrix composites under quasi-static loading condition. In addition to this, the fatigue cohesive zone models in the open literature are never validated through the specimens with different sizes for polymeric materials. The goal of this study is to investigate the effects of the foregoing gaps on the fatigue characteristics of polymer matrix composites.

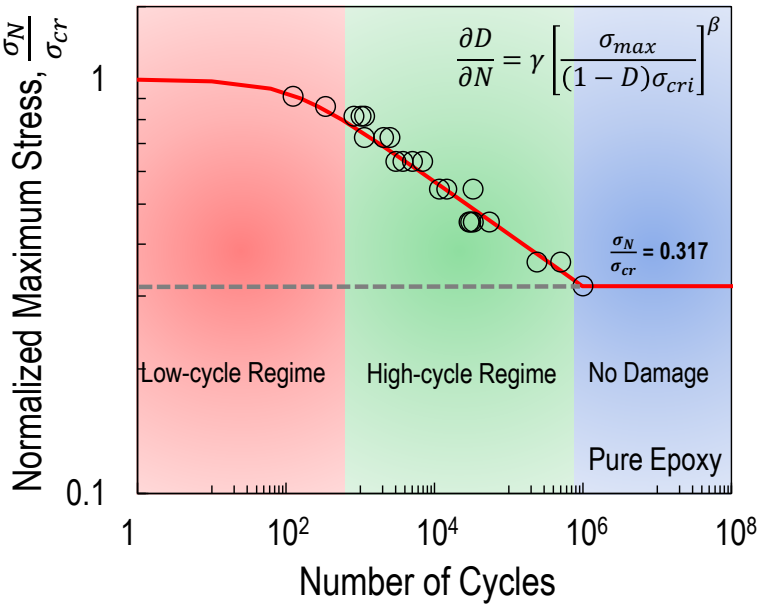

Figure 7.13: Fitting of experimental S-N curves obtained from uni-axial tensile tests on dog-bone specimens using the damage accumulation function as written in Eq.(7.12).

7.4 Selection of fatigue damage functions in computational study

7.4.1 Fatigue damage accumulation function: first expression

A possible material degradation law was initially selected to validate its fidelity through the comparison with the experimental Paris-Erdogan curves for geometrically-scaled thermoset polymer. This proposed damage accumulation function has the following expression:

$$\frac{\partial D}{\partial N} = \gamma \left[\frac{\sigma_{max}}{(1-D)\sigma_c}\right]^{\beta} \tag{7.12}$$

which is composed of a different pre-factor compared to the one proposed by Dávila *et al.* [182] as shown in the foregoing section. The modification of the pre-factor is due to the fact that, while a straight line of a S-N curve can be well described by the degradation law proposed in Dávila's model, an acceptable description for a S-N curve with two remarkable segments representing low-cycle and high-cycle fatigue regimes cannot be achieved. Thanks to the investigated expression as written in Eq. (7.12), two regimes of the experimental S-N

curves of pure epoxy obtained from uni-axial tensile tests can be seamlessly characterized as shown in Figure 7.13 and the calibrated parameters γ and β are 0.001 and 7.9 respectively.

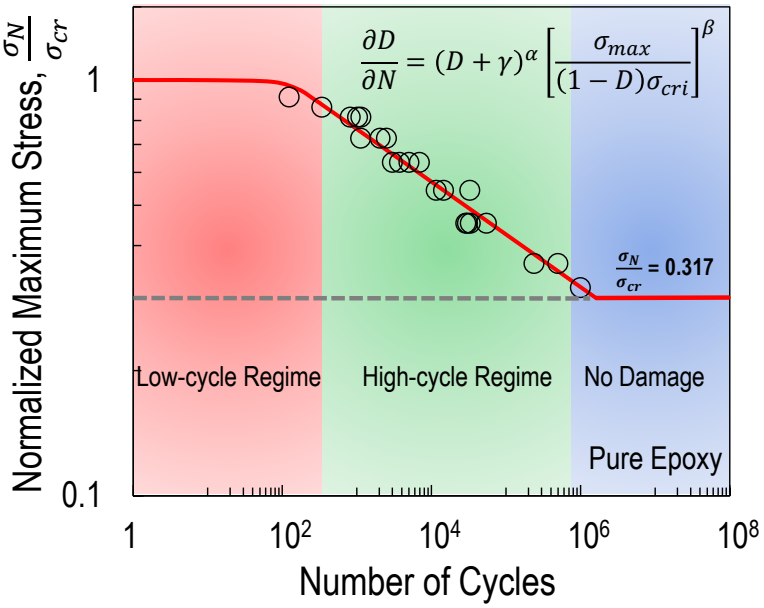

Figure 7.14: Fitting of experimental S-N curves obtained from uni-axial tensile tests on dog-bone specimens using the damage accumulation function as written in Eq.(7.13).

Parameters	γ	β	α
Low/high-cycle regime	0.012	7.9	2.15

Table 7.1: A set of parameters in the fatigue damage accumulation function (Eq.7.13) for the fitting of the experimental S-N curve.

7.4.2 Fatigue damage accumulation function: second expression

The selection of the damage accumulation functions on the computational results was further studied. Another possible function to describe the experimental S-N curves has the following

expression:

$$\frac{\partial D}{\partial N} = (D+\gamma)^{\alpha}\left[\frac{\sigma_{max}}{(1-D)\sigma_c}\right]^{\beta} \tag{7.13}$$

where α, γ and β are the material parameters which can be determined by matching the experimental S-N curves of pure epoxy as shown in Figure 7.14 and the corresponding values used in the simulation are tabulated in Table 7.1. It is worth mentioning here that the foregoing parameters are not the unique solution for the fitting of the experimental S-N curves. This aspect will be further discussed in the next section.

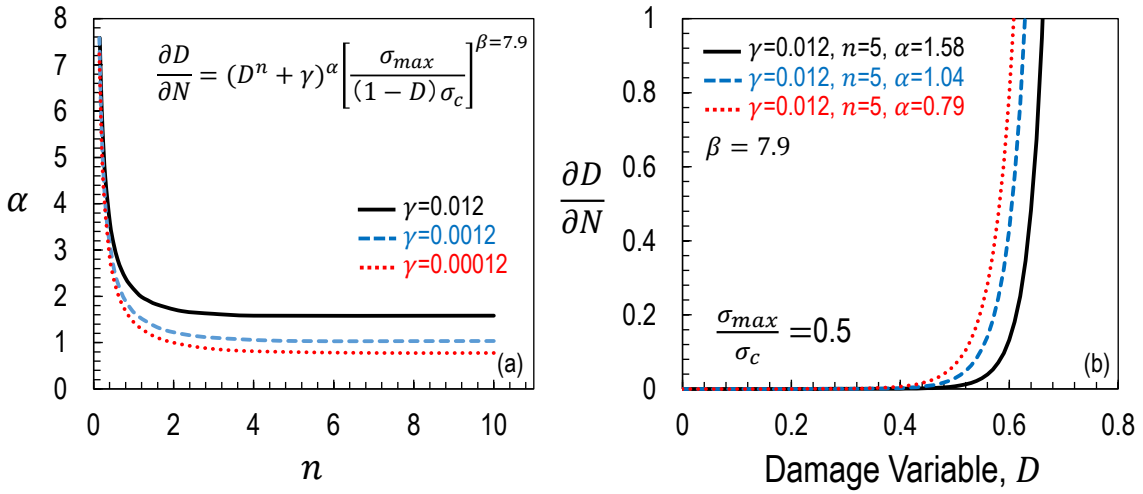

Figure 7.15: (a) Partial combinations of the parameters (n, γ, α) in the damage function (Eq.(7.14)) for the match of the experimental S-N curve of pure epoxy; (b) the evolution of the damage increment per cycle with the damage variable for the case of σ_{max}/σ_c =0.5. This figure compares the evolution for different combinations of the parameters.

7.4.3 Fatigue damage accumulation function: general expression

The forgoing expressions can be considered as the special cases of the damage accumulation function as described in following expression:

$$\frac{\partial D}{\partial N} = (D^n+\gamma)^{\alpha}\left[\frac{\sigma_{max}}{(1-D)\sigma_c}\right]^{\beta} \tag{7.14}$$

where n is an additional material parameter compared to the second expression of the proposed damage accumulation function in the previous section. The fitting of the experimental S-N curve can be achieved by infinite combinations of the parameters n, γ and α while the parameter β is typically in the range from 7 to 8 for pure epoxy which describes the slope of the S-N curve in the high-cycle fatigue region. The forgoing parameters to describe the experimental S-N curve of pure epoxy are partially plotted in Figure 7.15a showing the typical distribution of the combinations. In this figure, each set of the parameters n, γ and α generally leads to the different evolution of the damage as show in Figure 7.15b exemplifying the damage increment per cycle with respect to the damage variable for the case of σ_{max}/σ_c =0.5. The computational consequence of this aspect will be discussed in the following sections.

7.5 Boundary of fatigue cohesive zone model

On the other hand, both linear and bi-linear cohesive laws were used as the boundary of the fatigue cohesive zone model for the critical comparison. It is worth mentioning here that the damage variable has a different expression for a bi-linear cohesive law compared to the conventional one for a linear cohesive law. The expression for a bi-linear cohesive law is described in the following:

$$D = \left(\frac{\sigma_c - \sigma_k}{\varepsilon_k - \varepsilon_c}\right)\left(\frac{\varepsilon}{\sigma_c} - \frac{1}{E}\right), \varepsilon \in [\varepsilon_c, \varepsilon_k] \tag{7.15}$$

$$D = 1 - \left(\frac{\sigma_k}{\varepsilon_f - \varepsilon_k}\right)\left(\frac{\varepsilon_f - \varepsilon}{\sigma_c}\right), \varepsilon \in [\varepsilon_k, \varepsilon_f] \tag{7.16}$$

where σ_c is the material strength, ε_c is the critical strain for damage initiation, ε_f is the final strain for failure, σ_k is the stress at the kink point of a bi-linear cohesive law and ε_k is the strain related to the aforementioned stress. The specific values of these material properties were determined through the experimental and numerical characterization of graphene nanocomposites for quasi-static scenario as discussed in the previous chapters.

7.6 Validation of fatigue uni-axial tensile tests for pure epoxy

The computational validation on unnotched specimens was initially conducted before moving to the investigation on the fatigue crack growth of pre-cracked specimens. As illustrated in Figure 7.16, the fatigue behavior of unnotched specimens can be accurately captured by utilizing the foregoing damage accumulation functions since the predicted fatigue life is consistent with the experimental results. On the other hand, the simulations results are not significantly affected by the cohesive shape since the use of linear or bi-linear cohesive law leads to similar fatigue lifetime. The explanation will be discussed in the following sections. It is worth mentioning here that only the case for the stress level lower than 70% of the critical stress was validated due to the plastic deformation for even higher stress level. This aspect does not affect the computational modeling of fatigue Mode I fracture tests since the material at the crack tip is subjected to tri-axial stress state thus leading to brittle behavior with negligible plastic deformation as discussed in the previous chapters.

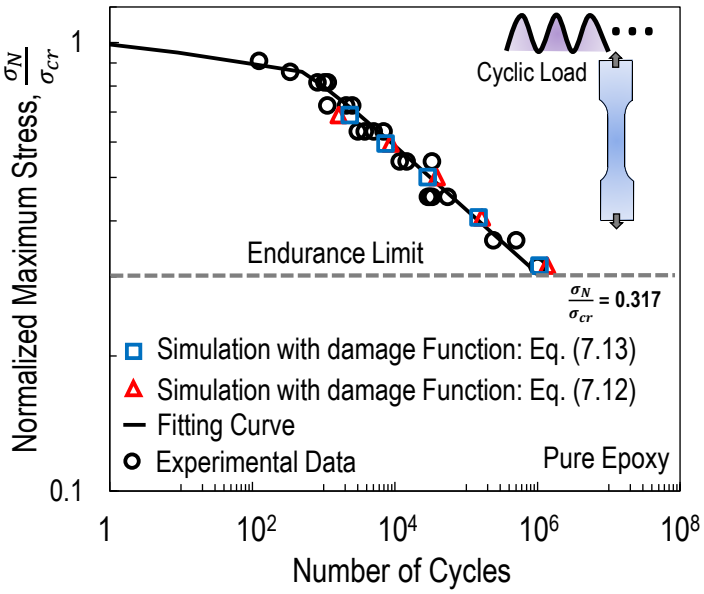

Figure 7.16: Comparison between the experimental S-N curve and the simulation results using damage accumulation functions as expressed in Eq. (7.12) and Eq. (7.13).

On the other hand, it is worth pointing out that the most degradation of the material in the simulation always happens in the region where the non-prismatic geometry transits into prismatic one. Eventually, the damage localizes in that region leading to the catastrophic failure of the specimen as shown in Figure 7.17. This is due to the fact that the statistical strength of the material and the defects are not considered in the simulation and this aspect can be included in the future work.

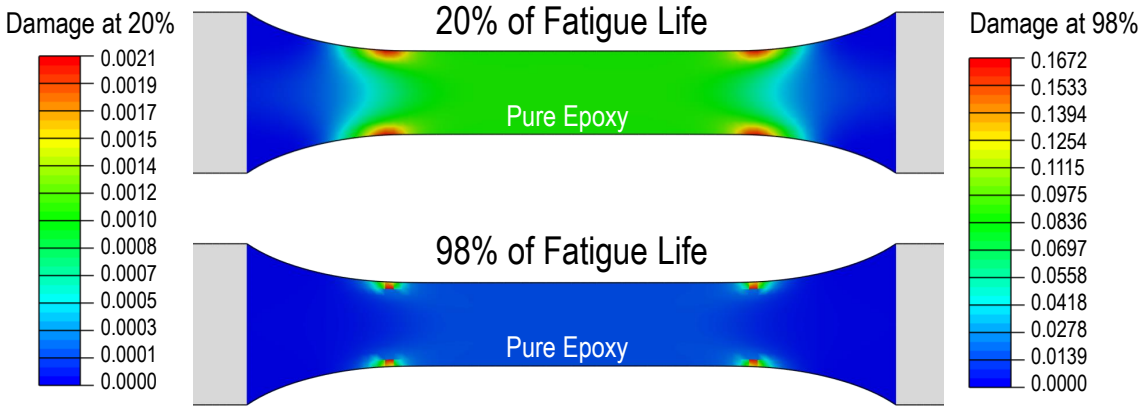

Figure 7.17: Damage region in the dogbone specimen under fatigue uni-axial tension with the maximum load about 50% of the quasi-static critical load. This figure compares the damage region at 20% and 98% of the total fatigue life.

7.7 Validation of fatigue Mode I fracture tests for pure epoxy

7.7.1 Evaluation of fatigue damage functions: Eqs.(7.12 and 7.13)

The fatigue damage accumulation functions (Eq.(7.12) and Eq.(7.13)) with the same calibrated parameters for unnotched specimens were further examined for the Mode I fatigue fracture tests. As illustrated in Figure 7.18, the numerical evolution of the compliance with the fatigue lifetime was plotted for the pre-cracked SENB specimen (D=10 mm) together with the corresponding experimental results. Both linear and bi-linear cohesive laws with

the same fracture energy estimated from the quasi-static fracture tests in the previous chapters was used as the boundary of the cyclic cohesive stress. The simulations were conducted by using an uniform cyclic jump after the initial 1000 cycles for the consideration of the computational efficiency and the results with the jumps of 200 to 500 cycles are consistent showing negligible differences in terms of the entire fatigue lifetime.

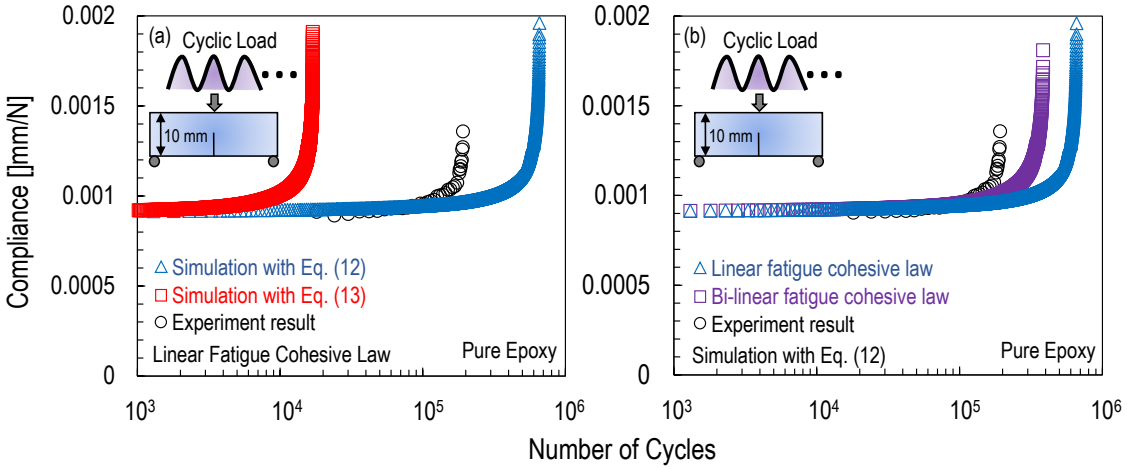

Figure 7.18: Comparison between the experimental data and the simulation results: (a) different fatigue damage accumulation functions (Eq.(7.12) and Eq.(7.13)) with the same linear cohesive law; (b) different cohesive laws with the same fatigue damage accumulation function (Eq.(7.12)).

As can be noted from Figure 7.18a , the predicted fatigue life of the specimen obtained by leveraging a linear cohesive law and Eq.(7.12) as the damage accumulation function is significantly overestimated compared to the experimental data. In contrast, the computational results by leveraging the same cohesive law but Eq.(7.13) exhibit a remarkable underestimation for the fatigue life. It is interesting to notice that the experimental data lies between the computational results. On the other hand, the simulation results for pre-cracked specimens are definitely affected by the cohesive shape as illustrated in Figure 7.18b showing the non-negligible difference on the fatigue lifetime by using linear and bi-linear fatigue cohesive laws. These results clearly showed that, while the fatigue behavior of unnotched specimens

can be successfully characterized by using the investigated fatigue damage functions, the Mode I fatigue fracture tests cannot be always captured with the same damage function and cohesive law.

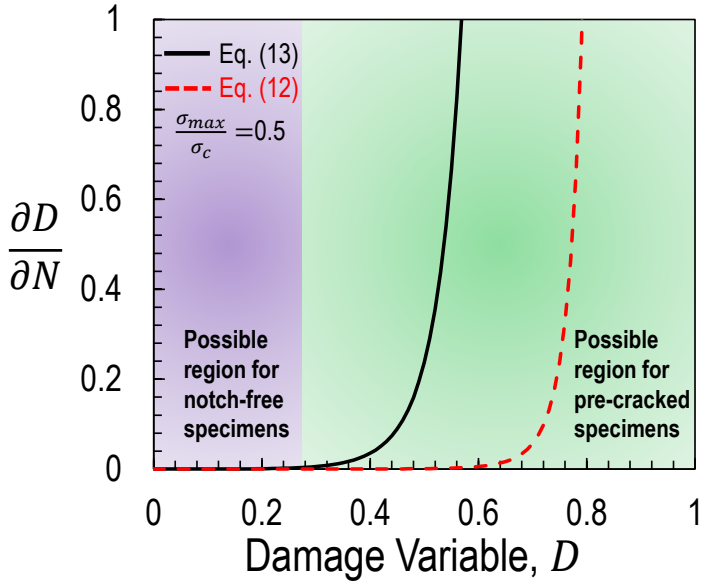

Figure 7.19: Evolution of damage increment rate with damage variable obtained by using the fatigue damage accumulation functions Eq.(7.12) and Eq.(7.13). Note that this plot only represents the case of σ_{max}/σ_c=0.5.

This phenomenon is actually due to the different damage evolution in unnotched and pre-cracked specimens under fatigue loading condition. As shown in Figure 7.19, the damage increment rate in unnotched specimens is typically slow leading to the lower damage values as highlighted in purple region before the catastrophic failure of the structure. In this region, all the investigated fatigue damage accumulation functions lead to similar damage evolution in the material and this is the main reason for the insensitivity on the simulation results for unnotched specimens by leveraging various fatigue damage accumulation functions and cohesive laws. However, this is not the truth anymore for pre-cracked specimens since the damage in front of the crack tip can enter the green region featuring higher damage values.

Accordingly, the investigated fatigue damage accumulation functions can generate completely different damage evolution in that region which substantially affects the simulation results for pre-cracked specimens as clearly shown in Figure 7.18. These results further confirm the insufficiency of only calibrating the model for unnotched specimens to characterize the fatigue fracturing behavior of pre-cracked specimens. To achieve the characterization for both unnotched and pre-cracked specimens under quasi-static and fatigue loading conditions, the correct boundary of cohesive law must be calibrated from quasi-static size effect tests on pre-cracked specimens as discussed in the previous chapters whereas the correct fatigue damage accumulation function must also be calibrated from fatigue size effect tests on pre-cracked specimens together with unnotched specimens under fatigue scenario.

On the other hand, it is worth mentioning here that the experimental compliance of the specimen close to the catastrophic failure is typically lower than the one of the specimen in the simulations as shown in Figure 7.18. This can be explained that the specimen has an unstable crack propagation close to the final failure due to the instability issue caused by the compliance of the testing system as similarly observed in the quasi-static fracture tests.

7.7.2 Evaluation of fatigue damage function: Eq.(7.14)

7.7.2.1 Experiment vs. simulation for size effect tests

The general expression of the fatigue damage accumulation function Eq.(7.14) was further investigated in the simulations to match the experimental data for both fatigue uni-axial tensile tests on unnotched specimens and Mode I fatigue fracture tests on pre-cracked SENB specimens with various sizes. As illustrated in Figure 7.20, the experimental fatigue lifetime for pre-cracked specimens with various sizes can be successfully captured by leveraging the foregoing fatigue damage accumulation function and the bi-linear cohesive law calibrated from the quasi-static size effect tests. The computational errors on the fatigue lifetime for all the investigated sizes are less than 25% which can be neglected considering the scatter of the experimental data for fatigue tests. These simulations were conducted with an uniform

cyclic jump of 50 to 500 cycles after the initial 200 cycles and the results have negligible differences in terms of the entire fatigue lifetime. It is worth mentioning here that a linear cohesive law can also be used to possibly capture the forgoing tests but it fails to describe the quasi-static fracturing behavior of pre-cracked specimens with various sizes as discussed in the previous chapters.

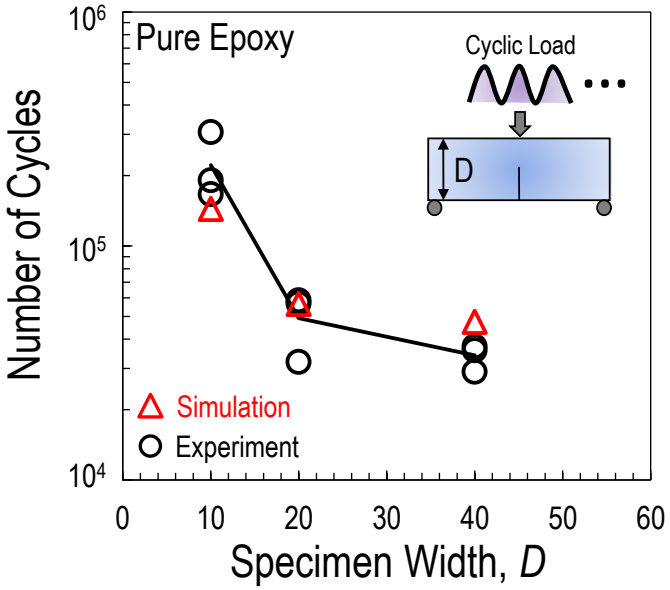

Figure 7.20: Experiment vs. simulation for the fatigue lifetime of pre-cracked specimens with various sizes. Note that the simulations were conducted with the calibrated bi-linear cohesive law and the fatigue damage accumulation function Eq.(7.14).

In addition to the excellent agreement on the fatigue lifetime, the evolution of the experimental compliance curves for pre-cracked specimens with various sizes can also be matched with the foregoing simulations as shown in Figure 7.21. In particular, the transitional region in the compliance curve from the stable crack propagation to the dramatic failure can be reasonably reproduced and this aspect further leads to the successful characterization of the experimental Paris-Erdogan curves for all the specimen sizes. As illustrated in Figure 7.22 for the numerical Paris-Erdogan curves analyzed through the previous compliance method, the fatigue threshold ΔK_{th} and the slope of the Paris-Erdogan curve can have an excel-

lent agreement with the experimental results although the critical stress intensity amplitude ΔK_{cr} was overestimated due to the simulations without modeling the compliance of the testing system.

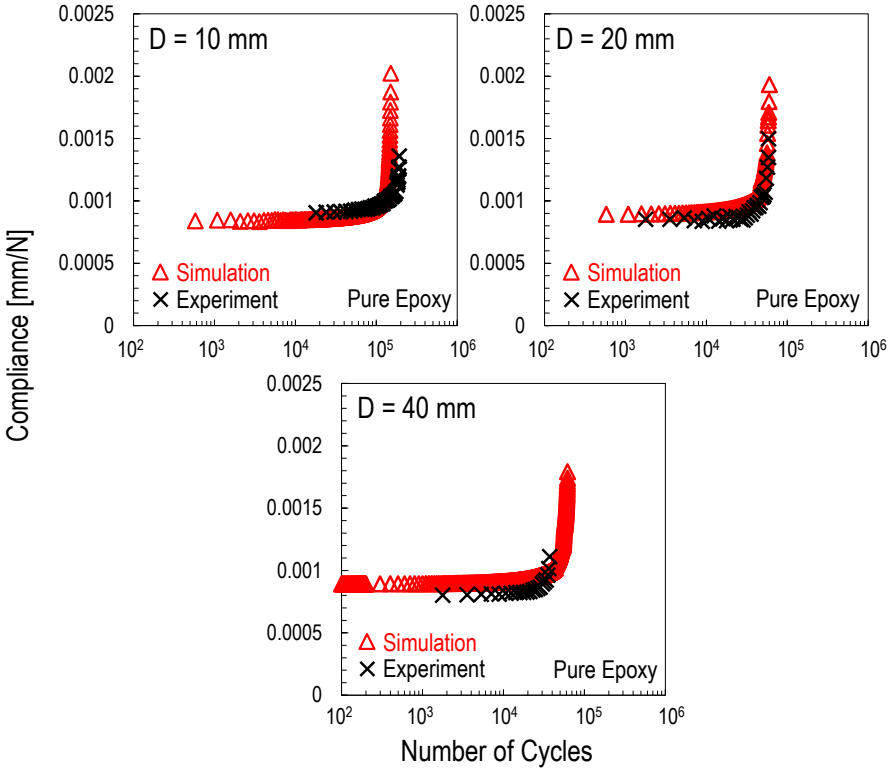

Figure 7.21: Experiment vs. simulation for the compliance curves of pre-cracked specimens with various sizes. Note that the simulations were conducted with the calibrated bi-linear cohesive law and the fatigue damage accumulation function Eq.(7.14).

The calibrated parameters for the foregoing simulations are tabulated in Table 7.2. It is worth mentioning here that this set of parameters is not the unique solution for the foregoing excellent match since other sets of parameters (e.g. n=4.3, γ=0.0012, α=1.06, β=7.9, etc.) can also provide similar results. However, these solutions lead to an unique evolution of the pre-factor in the fatigue damage accumulation function Eq.(7.14) as illustrated in Figure 7.23. This aspect implies that the evolution of the damage increment rate with the damage variable

is determined through the calibration of the fatigue size effect tests in spite of different sets of parameters in the fatigue damage accumulation function Eq.(7.14). It is worth mentioning here that the modeling of graphene nanocomposites can be similarly conducted which is undergoing and considered as the future investigation.

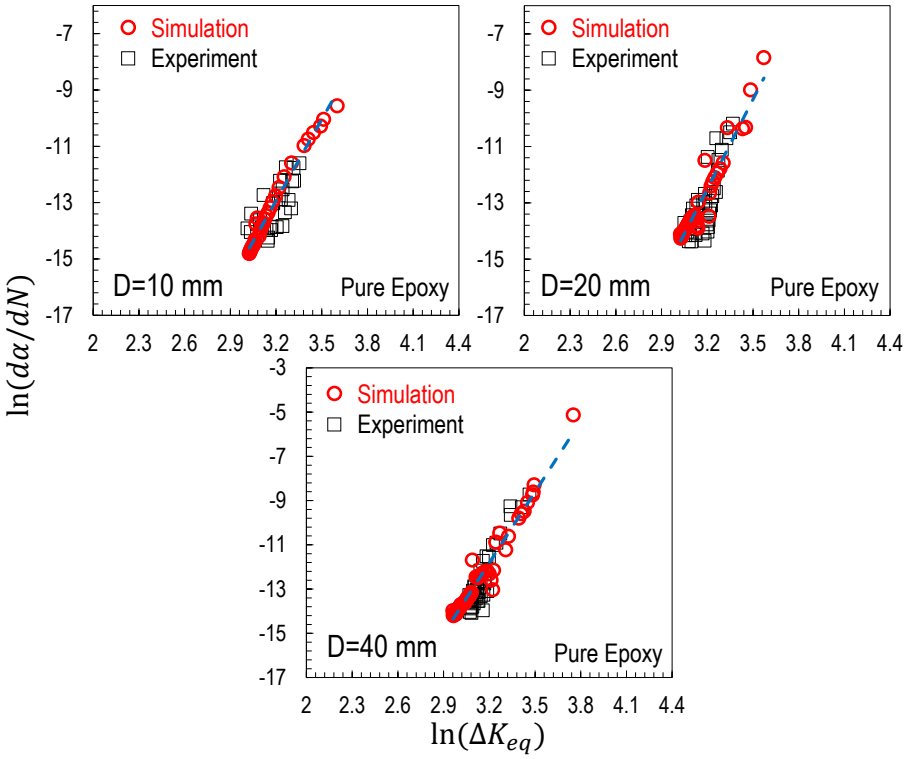

Figure 7.22: Experiment vs. simulation for the Paris-Erdogan curves of pre-cracked specimens with various sizes. Note that the simulations were conducted with the calibrated bi-linear cohesive law and the fatigue damage accumulation function Eq.(7.14).

Parameters	n	γ	α	β
Bi-linear cohesive boundary	3	0.012	1.62	7.9

Table 7.2: A set of parameters in the fatigue damage accumulation function (Eq.7.14) used for the simulations with the calibrated bi-linear cohesive law.

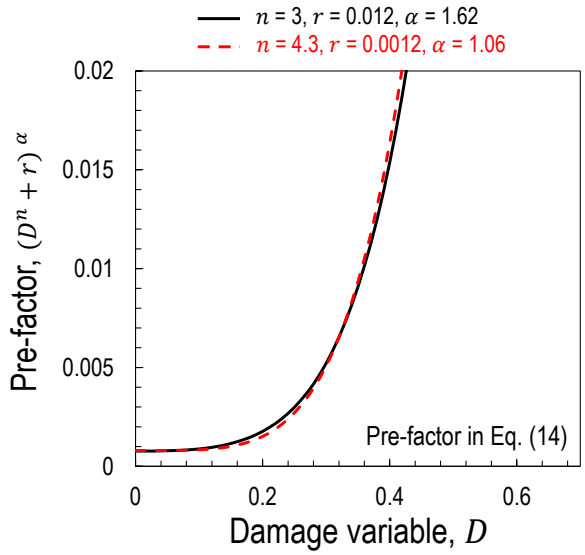

Figure 7.23: Evolution of the pre-factor in the fatigue damage accumulation function Eq.(7.14) with the damage variable for two sets of the parameters used for the successful characterization of the experimental results.

7.7.2.2 Characteristics of the fatigue fracturing in thermoset polymers

By leveraging the foregoing successful simulations, the characteristics of the fatigue fracturing in thermoset polymers can be further studied. As illustrated in Figure 7.24a-b, both primary and secondary damage zones constitute the total fracture process zone ahead of the crack tip in the fatigue scenario whereas only one damage zone characterizes the quasi-static scenario. The primary damage zone is considered as the region from the stress-free crack tip to the peak stress and the secondary damage zone is the region outside the foregoing damage zone where the material also experiences damage as illustrated in Figure 7.24c. The main reason for the additional damage zone in the fatigue scenario is due to the fact that the material can also have damage even if the local cyclic stress is not larger than the material strength and this aspect does not exist in the quasi-static condition. On the other hand, the material degradation due to the cyclic stresses in the fatigue scenario can also lead to the case that the peak stress ahead of the crack tip is not always the material strength anymore and this

value can evolve and reduce up to 50% of the original strength during the fatigue loading as illustrated in Figure 7.24c.

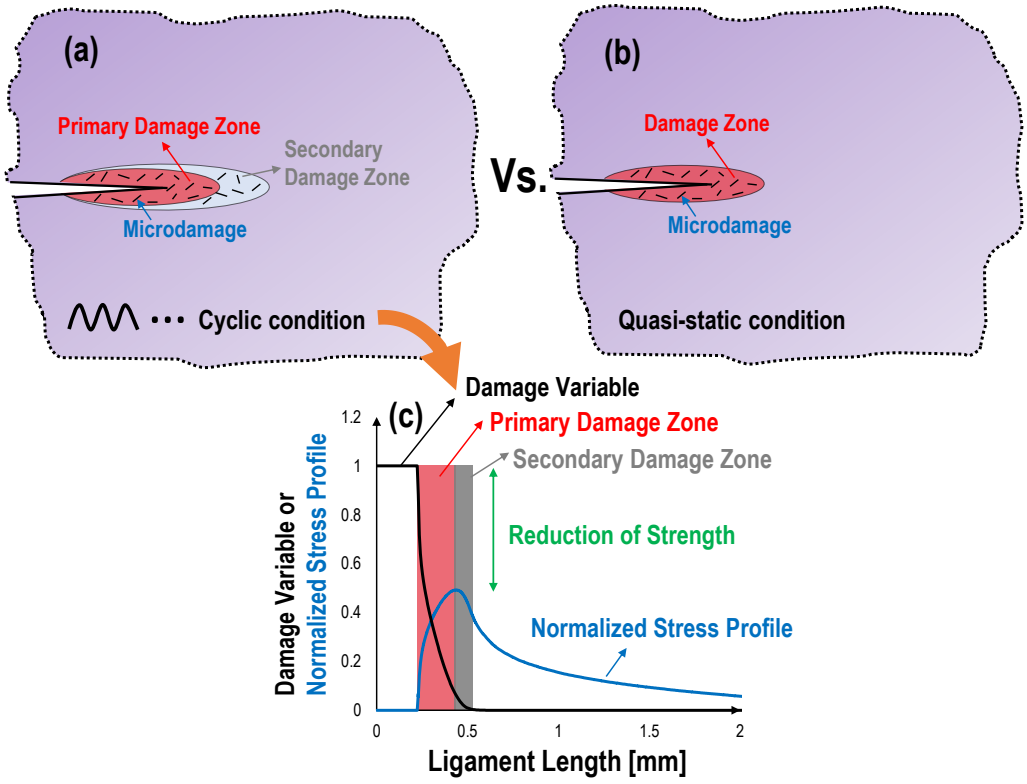

Figure 7.24: Damage zone in front of the crack tip: (a) fatigue condition; (b) quasi-static condition. (c) Evolution of damage variable or normalized stress profile with the ligament length ahead of the crack tip in fatigue condition.

It is interesting to further investigate the evolution of the individual damage zone in the fatigue scenario for all the investigated specimen sizes and make a critical comparison with the one in the quasi-static scenario. As illustrated in Figure 7.25a for the fatigue scenario, the primary damage zone typically becomes larger as the specimen size increases and the magnitude of these zones is generally smaller than the fully-developed damage zone in the quasi-static scenario. On the other hand, larger secondary damage zone in the fatigue scenario also characterizes larger specimen size as illustrated in Figure 7.25b. The summation of the foregoing two damage zones leads to the case that the total damage zone in the fatigue

scenario can be larger than the fully-developed damage zone in the quasi-static scenario depending on the specimen size as shown in Figure 7.25c. In addition, the evolution of the damage zone in fatigue and quasi-static conditions can be completely different as illustrated in Figure 7.25d. The quasi-static damage zone generally has rapid growth close to the end of the total life whereas the fatigue damage zone increases quickly at the early stage and then saturates for the most part of the remaining life. This difference was actually reported for the fracturing behavior of fiber-reinforced composites in the literature and the similar situation will also be shown in the following chapters for the studies focusing on the multi-axial fatigue behavior of polymer composites.

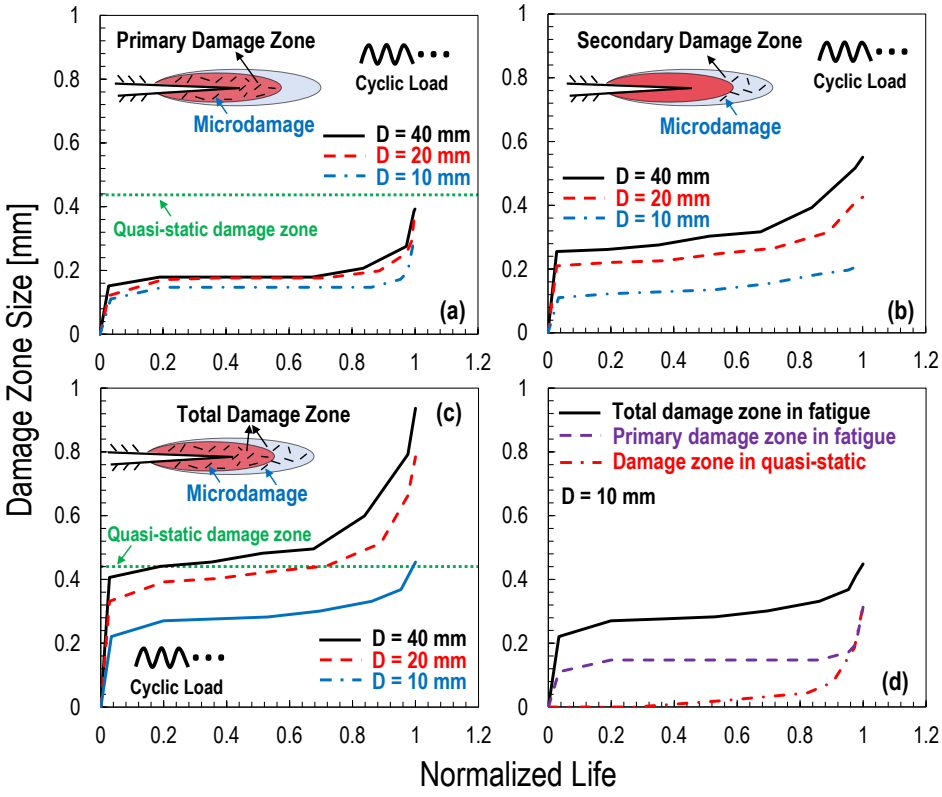

Figure 7.25: (a) Primary damage zone; (b) Secondary damage zone; (c) Total damage zone in fatigue scenario for various specimen sizes. (d) Comparison on the damage zone between quasi-static and fatigue conditions.

7.8 Conclusions

1. Fatigue crack growth in pure thermoset polymers features river marks which are parallel to the crack propagation direction. This phenomenon is completely opposite to the fatigue fracturing morphology of metallic materials exhibiting beach marks perpendicular to the crack propagation direction;

2. This interesting morphology for pure thermoset polymers can be explained that the crack propagates on the planes with different heights in the fatigue scenario thus leading to river marks. These marks are more pronounced for larger specimen sizes due to the relatively higher crack propagation rate leading to the larger height difference of the planes. In comparison with the quasi-static condition, the dynamic crack propagation at the final failure leads to the smooth fracture surfaces;

3. The classical Paris-Erdogan curves for pure thermoset polymers obtained through the direct measurement of crack length are strongly affected by the specimen sizes. This is due to the fact that the non-linear Fracture Process Zone (FPZ) has significant effects on the fatigue fracture scaling of pure thermoset polymers and this aspect is not the case for the same materials under quasi-static scenario. Such a great difference can be explained that the FPZ size in quasi-static case is relatively small compared to the specimen sizes but sufficiently large compared to the same ones in the fatigue case;

4. The fatigue size effect model based on the energetic-equivalence framework can not achieve the consistent Paris-Erdogan curves for all the investigated sizes since only the constant cyclic FPZ is considered in the model but not for the evolution of the FPZ in the fatigue scenario. By leveraging the compliance method, this aspect can be equivalently accounted and the consistent Paris-Erdogan curves for pure thermoset polymers can be achieved in spite of the different slopes through the best fitting due to the scatter of the experimental data for the fatigue case;

5. However, the Paris-Erdogan curves of graphene nanocomposites analyzed through the compliance method tend to exhibit difference as the graphene content increases. The most remarkable difference was observed for the thermoset polymer with the addition of 1.6% graphene nanoplatelets showing that mainly the fatigue threshold and the slope of Paris-Erdogan curves are not consistent for different specimen sizes;

6. The different fatigue thresholds are mainly attributed to the different FPZ sizes ahead of the crack tip in the 1.6% graphene nanocomposites at the early stage of the fatigue crack growth whereas the different slopes are possibly due to the shape of the bi-linear cohesive law for 1.6% graphene nanocomposites which is completely different from the one for pure thermoset polymers;

7. The proposed computational model can have a successful characterization of all the investigated specimens with various sizes in the fatigue and even quasi-static conditions. This must be achieved by calibrating the cohesive law through the quasi-static size effect tests and the fatigue damage accumulation function through the fatigue size effect tests otherwise the model fails to describe both quasi-static and fatigue behavior of the materials with various sizes. This aspect is significantly important but rarely investigated or even never explored in the open literature;

8. The successful simulation results revealed the interesting fracturing characteristics in the fatigue scenario. The cyclic damage zone in front of the crack tip is formed by two zones compared to the quasi-static case only featuring one damage zone at the same location. The additional damage zone in the fatigue scenario is due to the material degradation induced by the cyclic stresses lower than the material strength and this aspect does not exist in the quasi-static case;

9. On the other hand, the material degradation due to the lower stresses but larger than the stress level for the endurance limit can also lead to the reduction of the peak stresses ahead of the crack tip in the fatigue scenario. This is also different from the

quasi-static case since the peak stress at the edge of the damage zone is always the material strength which does not have degradation;

10. More importantly, the primary damage zone in the fatigue scenario is typically smaller than the fully developed damage zone in the quasi-static case whereas the summation of the primary and secondary damage zones can be larger than the foregoing quasi-static damage zone depending one the specimen size. This important aspect can explain the contradiction for the size of the cyclic damage zone in the open literature.

Chapter 8

STRESS STATE AND SIZE EFFECT IN FIBER-REINFORCED POLYMER COMPOSITES

Micro-scale modeling of sub-critical damage and their evolution (e.g. matrix cracking, delamination, etc) in fiber-reinforced polymer composites is still a challenging task since it was attempted by many studies in the past but a successful characterization for the macro-scale load-displacement curve and the micro-scale damage morphology was never achieved. In this chapter, the evolution of the sub-critical damage in cross-ply laminates under uni-axial tension and pure shear was computationally reproduced by leveraging the two-scale constitutive model which considers the micro-scale behavior of the polymer and the Drucker-Prager model which considers the complex stress states in the composites.

The effects of the size scaling on the splitting crack initiation and propagation in off-axis layers of fiber-reinforced polymer composites were further investigated. This aspect was also critically compared with the same geometrically-scaled pure thermoset polymers and the comparison is extremely insightful for understanding the fracture behavior of polymer matrix composites with various notch geometries and sizes.

8.1 Modeling of sub-critical damage in fiber-reinforced polymer composites

8.1.1 Past and current work on the micro-scale damage modeling

Many attempts on the micro-scale modeling of transverse matrix cracks and their evolution in cross-ply laminates, using macroscopic properties of thermoset polymer obtained from conventional tests, showed a significant deviation from the experimental damage morphology. Typically, the real damage feature of the 90° lamina in cross-ply laminates exhibits a pattern of individual matrix crack at a distance of roughly one to three times the thickness of the

lamina as illustrated in Figure 8.1. The foregoing mismatch was generally considered in the literature due to the fact that smeared crack approaches do not describe the stress field of interacting cracks accurately and do not capture the discontinuities induced by the large crack opening displacements correctly. Accordingly, approaches such as e.g. XFEM were proposed without actually solving the problem.

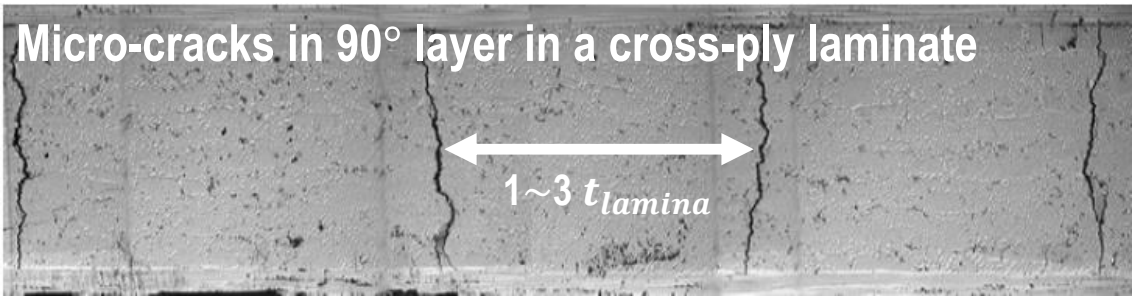

Figure 8.1: Micro-scale cracks in 90° layer in a cross-ply laminate. Image obtained from [41]

In this direction, another approach such as e.g. IGFEM was developed and used for the micro-scale modeling of transverse matrix cracks in fiber-reinforced polymer composites. One of the outstanding examples was provided by Zhang *et.al* [14] who modeled transverse matrix cracks using IGFEM and only considered the damage at the interface between fiber and matrix. The strength and fracture energy at the interface used in the modeling were about 25 MPa and 0.004 N/mm respectively. As can be noted from Figure 8.2, simulation results showed several matrix cracks at the distances which does not match the real damage morphology exhibiting the distance between the matrix cracks at least one lamina thickness.

On the other hand, an interesting study proposed by D'Mello and Waas who modeled the transverse matrix cracks by only considering the damage in the matrix [13]. The material strength used in the modeling was about 55 MPa but the fracture energy is around 0.02 N/mm which is almost one order of the magnitude lower than the value measured from conventional tests. As a consequence, a noticeable crack was observed in the simulation but multiple locations of fiber/matrix interface exhibited remarkable damage due to the stress

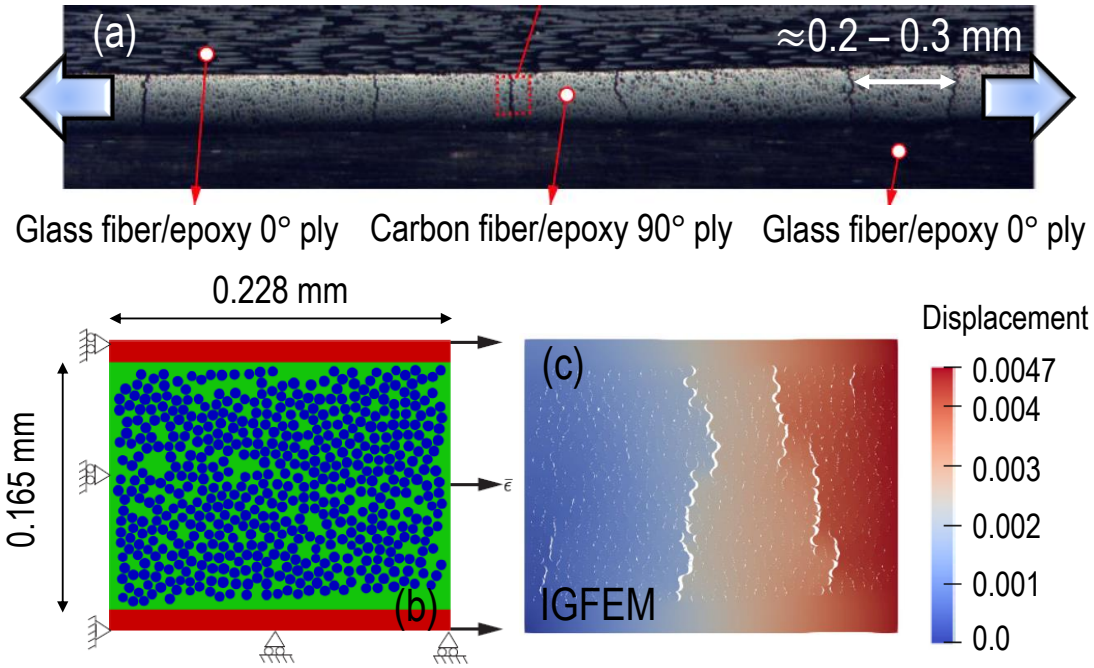

Figure 8.2: IGFEM-based modeling of transverse matrix cracking in a cross-ply laminate. Images obtained from [14]

concentration and the low fracture energy of the polymer. This is not consistent with the experimental damage morphology as shown in Figure 8.1.

The foregoing undesirable comparison between simulation and experiment is mainly due to the lack of understanding the proper cohesive behavior of the polymer across length scales. To support this statement, an interesting study on the micro-scale modeling for the initiation and propagation of the matrix-cracking in fiber-reinforced polymer composites under different loading conditions was performed. Before moving to the insightful discussion about the corresponding results for the remarkable differences between the simulations using macro- and micro-scale material properties in the following sections, a detailed description on the characteristics of the representative micro-structures of investigated laminates is presented in the next section.

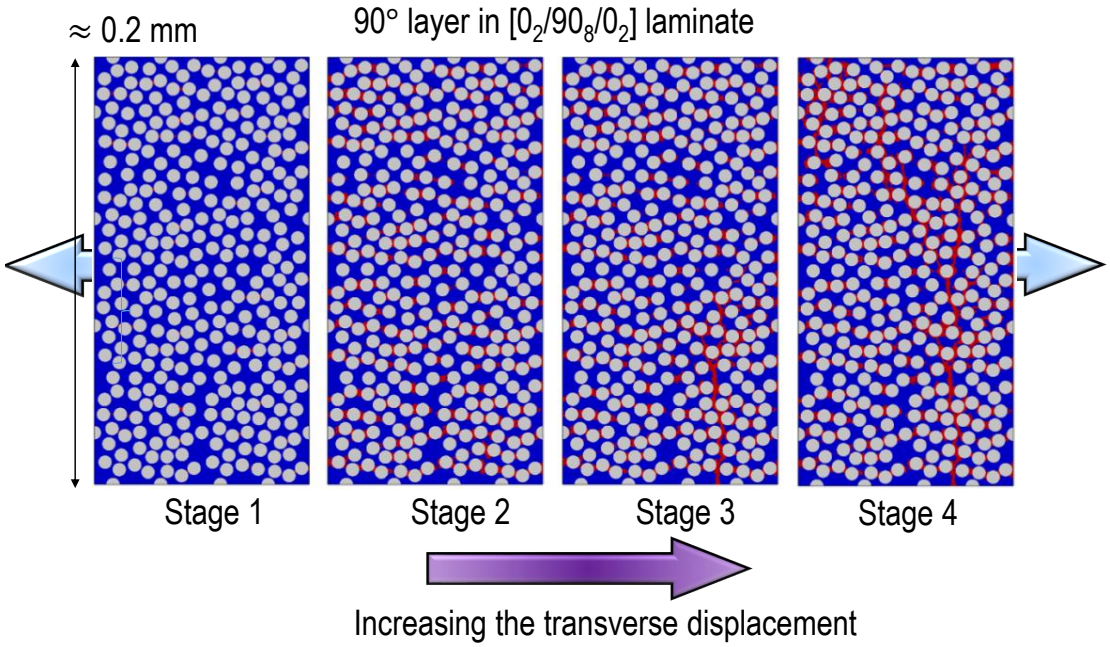

Figure 8.3: Micro-scale modeling of transverse matrix cracking in a cross-ply laminate. Images obtained from [13].

8.1.2 Description of micro-structure and modeling strategy

The investigated micro-structures include both $[90/0]_s$ and $[0/90]_s$ laminates which were generated by leveraging the Digimat-FE from MSC Software [184]. The choice of the foregoing laminates is due to the fact that the simulation results of micro-scale damage modeling can be used to have a qualitative comparison with the inspiring experimental results provided in the open literature [14, 15, 41, 185, 186]. Regarding the micro-structural features, all the fibers are located inside the representative micro-structures and there are about 820 fibers leading to a reasonable fiber volume fraction of roughly 53% as experimentally shown and commonly used in the literature [13, 14, 187]. The fiber diameter follows a normal distribution with the mean value about 7 μm and standard deviation about 0.14 μm whereas the minimum nearest-neighbor distance between fibers is about 0.2 μm and this distance is better described by a Weibull distribution. The foregoing information was adopted from

the outstanding study provided by Zhang *et al.* [14] and it is worth mentioning here that the fiber diameter distribution was also experimentally observed following a log-normal distribution [187] but this is also can be decently fitted by a normal distribution with a less difference compared to the log-normal fitting.

The micro-scale damage modeling of the foregoing micro-structures was conducted in ABAQUS Explicit 2019. A 6-node modified quadratic plane strain triangle (CPE6M) was adopted in the simulation featuring about 4 million elements for the entire model meshed by using an uniform element size about 0.4 μm. A linear elastic orthotropic constitutive model was used for the fibers in the 90° laminae and the entire 0° laminae whereas the matrix in the 90° laminae was modeled within the framework of Drucker-Prager model and the constitutive laws calibrated from dogbone and SENB specimens for the critical comparison. In addition to this, the fiber/matrix interface was simulated with a perfect bonding in this work due to the strong bonding between carbon fiber and matrix.

Configurations	Material Properties
Fiber in 90° lamina	$E_1 = 220$ GPa, $E_2 = 19.5$ GPa, $v_{12} = 0.28$
	$v_{23} = 0.45$, $G_{12} = 55$ GPa, $G_{23} = 6.72$ GPa
0° homogenized lamina	$E_1 = 147$ GPa, $E_2 = 10.3$ GPa, $v_{12} = 0.27$
	$v_{23} = 0.54$, $G_{12} = 7$ GPa, $G_{23} = 3.7$ GPa
Matrix in 90° lamina	$E = 2.38$ GPa, $\sigma_t^{macro} = 55$ MPa, $\sigma_t^{micro} = 300$ MPa
	$v = 0.43$, $G_F^{micro} = 0.02$ N/mm, $G_F^{macro} = 0.8$ N/mm

Table 8.1: Material properties used in the micro-scale damage modeling of $[90/0]_s$ and $[0/90]_s$ laminates under uni-axial tension and shear loading conditions. Note that the properties listed in the table for the matrix in 90° lamina lead to the successful characterization of the micro-scale fracturing morphology.

In fact, the weak bonding at the interface using the conventional material properties (i.e. low material strength and low fracture energy in the literature) for the micro-scale simulation typically leads to the undesirable comparison with the experimental micro-scale morphology. Most importantly, the delamination at the interface of laminae induced by splitting crack

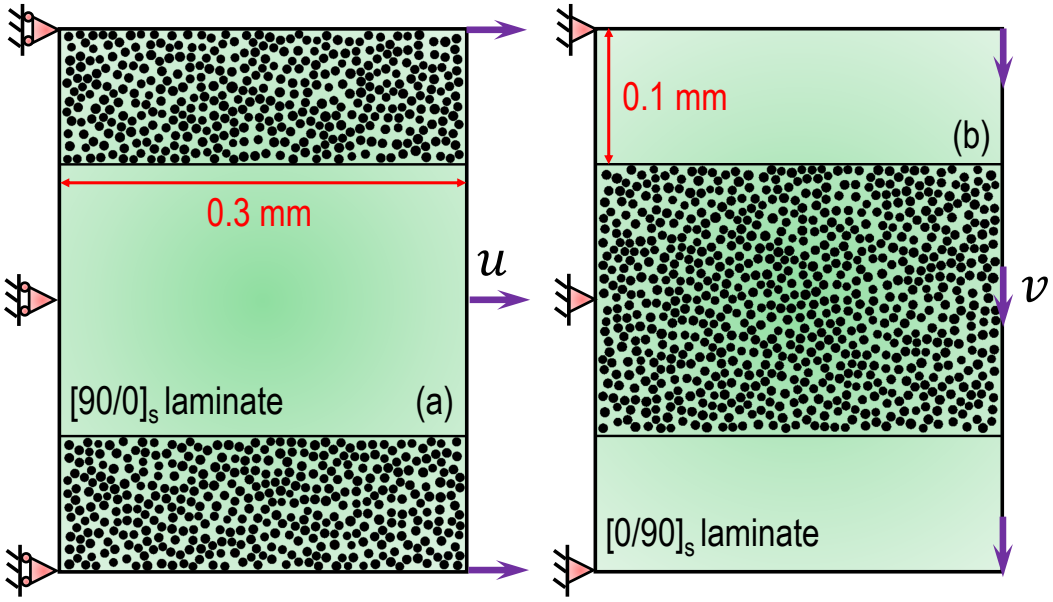

Figure 8.4: Representative micro-structures generated from Digimat and used in the micro-scale damage modeling: (a) $[90/0]_s$ laminate under uni-axial tension; (b) $[0/90]_s$ laminate under pure shear. Note that the thickness of each lamina is 0.1 mm and the width of this laminate is 0.3 mm.

cannot be captured. This is due to the fact that the carbon fiber/matrix interface should also be characterized by the higher interface strength rather than the lower value typically measured from pushout, fragmentation,and micro-bond tests [188–193]. The detailed discussion related to this aspect is considered as the future publications. The material parameters for carbon fiber and matrix are summarized in Table 8.1 which was partially obtained from the study provided by Zhang *et al.* [14].

Regarding to the loading conditions, both uni-axial tension and pure shear scenarios were selected for the micro-scale modeling of cross-ply $[90/0]_s$ and $[0/90]_s$ laminates respectively as illustrated in Figure 8.4 aiming to provide a solid confirmation on the reliability of the simulation results in comparison with the corresponding experimental morphologies. An insightful discussion about the computational results of the foregoing simulations is presented in the next section.

8.1.3 Simulation results: microscopic vs. macroscopic properties

To elucidate how the foregoing size effect and stress state of the polymer computationally affects the micro-scale damage modeling of fiber-reinforced polymer composites, simulation results by using the traditional material properties for the matrix, obtained from the conventional tests on the large-scale specimens, were compared with the ones by leveraging the proposed two-scale constitutive model, calibrated from Mode I fracture tests on the investigated SENB specimens and micro-scale SENT specimens, as illustrated in Figures 8.5-8.7. The traditional material properties of the matrix represent the macro-scale behavior featuring uni-axial tensile strength $\sigma_t^{macro} \approx 60$ MPa and Mode I fracture energy $G_F^{macro} \approx 0.8$ N/mm whereas the two-scale constitutive model describes both micro-scale and macro-scale behavior. While the latter behavior is exactly the same as the aforementioned macroscopic properties, the former one features high uni-axial tensile strength $\sigma_t^{micro} \approx 200$ to 300 MPa and low Mode I fracture energy $G_F^{micro} \approx 0.02$ N/mm.

As can be noted from Figure 8.5, the only assignment of the foregoing macro-scale material properties for the matrix in the 90° laminae leads to the distributed damage in the matrix without significant crack opening showing the maximum damage variable smaller than 0.1 for both uni-axial tension and pure shear scenarios. This computational micro-scale damage morphology is completely wrong in the consideration of the experimental morphology as provided by many authors in the literature [14, 15, 41, 185, 186] showing a pattern of individual matrix crack at a distance of roughly one to three times the thickness of the lamina.

However, the foregoing wrong morphology does not happen again for the simulations by leveraging the proposed two-scale constitutive model considering the micro-scale matrix properties. As illustrated in Figure 8.6, the evolution of the sub-critical damage in cross-ply $[90/0]_s$ laminate under uni-axial tension was successfully reproduced which is consistent with the experimental observation. Typically, the damage initiates at several locations of the fiber/matrix interfaces as shown in Figure 8.6a and this is followed by a fast propagation of the transverse matrix cracking as shown in Figure 8.6b. A further development of this

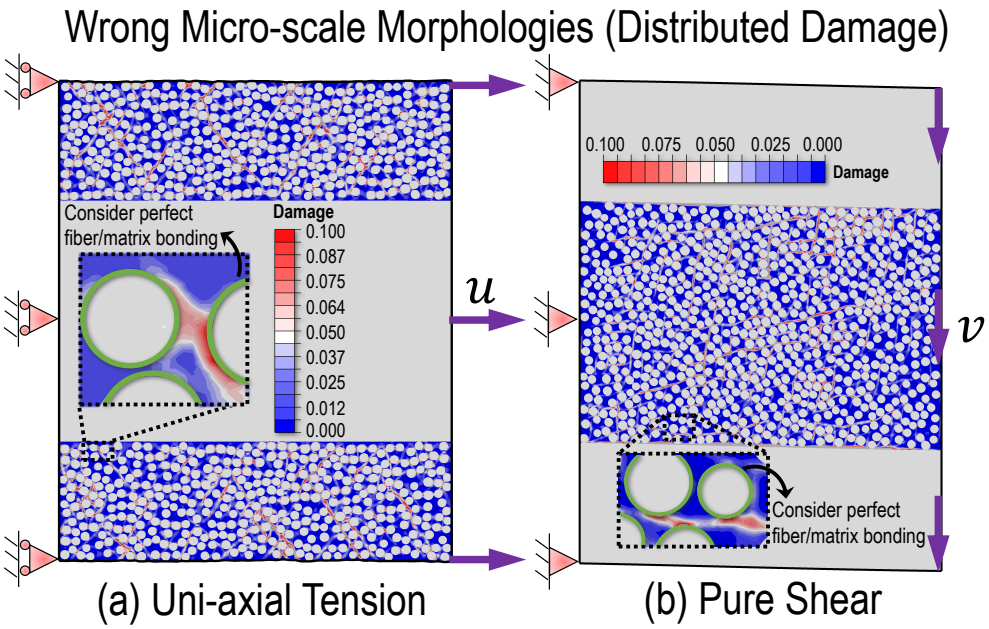

Figure 8.5: Micro-scale simulation with perfect bonding for fiber/matrix interface and material properties of matrix obtained from dogbone specimen for $[90/0]_s$ laminate under uni-axial tension and pure shear scenarios. Note that the labels u and v represent horizontal and vertical displacements.

matrix splitting is hindered by the 0° lamina leading to the significant delamination at the interface of two different laminae as shown in Figure 8.6b. Eventually, additional transverse cracks happen at a distance of at least one lamina thickness from the pre-existing transverse cracks as shown in Figure 8.6c.

In addition to the uni-axial tension, the micro-scale damage morphology of cross-ply $[0/90]_s$ laminate under pure shear was also successfully captured as shown in Figure 8.7. Similar to the previous case under uni-axial tension, the damage also initiates at the fiber/matrix interface as shown in Figure 8.7a. The following event is the fast splitting crack happening at an angle of roughly 30° corresponding to the direction of the 0° fibers due to the complex multi-axial stress state in the micro-structural composite. The foregoing damage further drives the delamination at the interface of laminae and this delamination pattern typically has a connection with the damage at the closest fiber/matrix interface which is slightly dif-

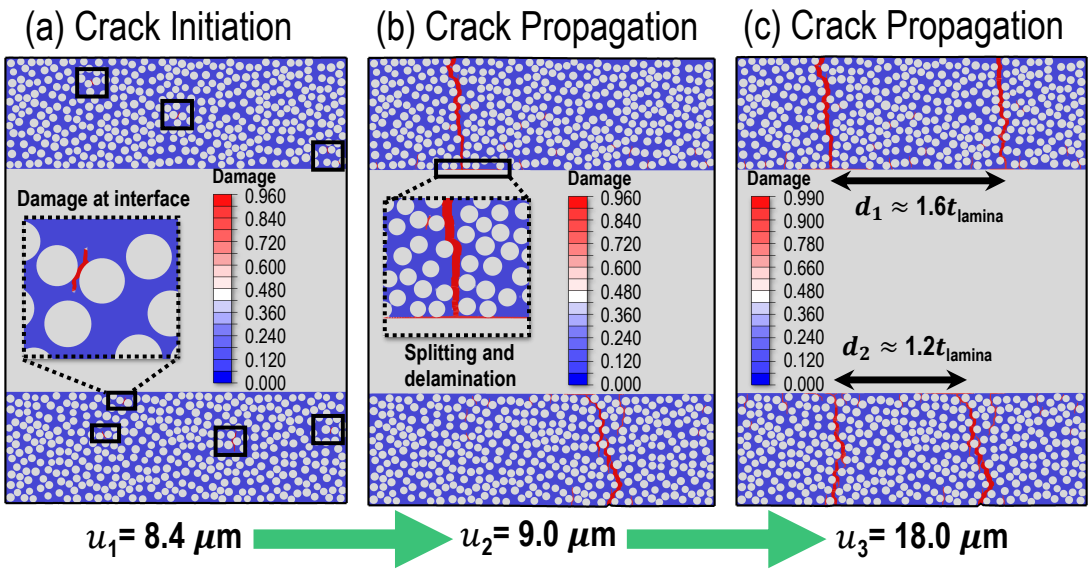

Figure 8.6: Micro-scale simulation for $[90/0]_s$ laminate under uni-axial tension. Note that microscopic material properties and Drucker-Prager model were used in this simulation whereas the debonding between fiber and matrix is not considered. The thickness of the lamina is 0.1 mm and the width of the micro-structure is 0.3 mm.

ferent from the uni-axial tension case due to the different local multi-axial stress state. This phenomenon was also reported in the work by Mortell *et al.* [186] showing similar micro-delamination at the boundary of two laminae under shear-dominated loading condition. On the similar grounds with the uni-axial tension case, an additional splitting crack eventually occurs at a distance about one lamina thickness from the foregoing splitting crack.

It is worth mentioning here that, in a typical fiber-reinforced polymer composite, the matrix experiences a high level of volumetric stress components leading to the brittleness of the material. This is consistent with the fact that the cumulative plastic strain in the range from 0 to 1% was used in the successful simulations leveraging the two-scale constitutive model rather than the use of a higher plastic strain greater than few percent leading to more damage occurring at the fiber/matrix interface during the initiation stage.

These excellent computational characterizations for different loading conditions also clearly show the importance of the full description of the multi-axial tensorial stress states in the

composite otherwise the correct damage pattern cannot be successfully captured for a wide range of loading scenarios. However, the traditional Cohesive Zone Models (CZMs) and basic XFEM or phase field models widely used in the literature may not be the best candidates due to the lack of considering entire stress field.

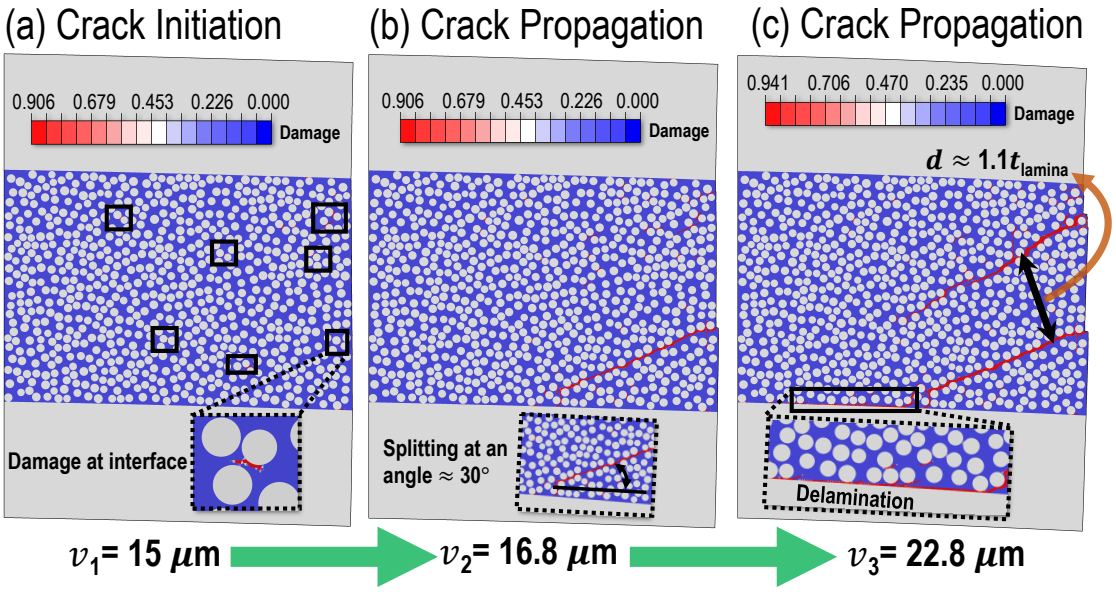

Figure 8.7: Micro-scale simulation for $[0/90]_s$ laminate under pure shear. Note that microscopic material properties and Drucker-Prager model were used in this simulation whereas the debonding between fiber and matrix is not considered. The thickness of the lamina is 0.1 mm and the width of the micro-structure is 0.3 mm.

Last but not least, several other aspects (e.g. thermal residual stresses induced by the curing of the composite, statistical strength distribution of the matrix, etc.) may also need to be considered in the micro-scale polymer damage modeling of fiber-reinforced composites to provide an even better quantitative characterization of the sub-critical damage and their evolution. This interesting aspect will be the subject of the future publications.

8.2 Size Effect on Splitting Crack Initiation and Propagation

This section aims to experimentally and computationally clarify the effects of size scaling on the transverse fracturing behavior of fiber-reinforced polymer composites and the interfacial behavior between fiber and matrix. The latter aspect is still considered as a controversial topic in the literature due to the testing method and size scaling effect. Before moving to the experimental results and related analysis, the manufacturing procedure and the testing methods are described in the following sections.

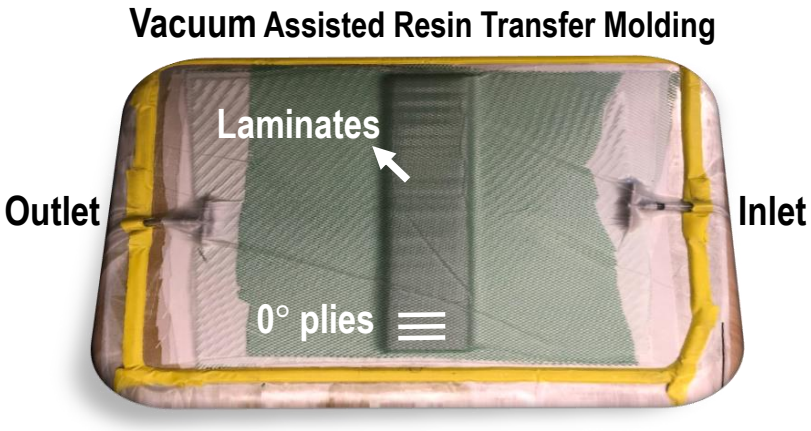

Figure 8.8: Vacuum Assisted Resin Transfer Molding (VARTM) technique for the manufacturing of the laminates composed of pure epoxy and unidirectional dry carbon fabrics.

8.2.1 Materials and methods

8.2.1.1 Specimen preparation

The transverse fracturing behavior of fiber-reinforced polymer composites was investigated by leveraging the same pure epoxy as described in the previous chapters and the addition of non-crimp 2253 unidirectional carbon fabrics [194]. The laminates were manufactured by using the Vacuum Assisted Resin Transfer Molding (VARTM) technique as illustrated in Figure 8.8 leading to the fiber volume fraction about 60%. It is worth mentioning here

that only small panel was manufactured every time and the uncured pure epoxy was infused through the vacuum pressure about 100 KPa at least three times in order to provide a better distribution of the matrix in the investigated laminates.

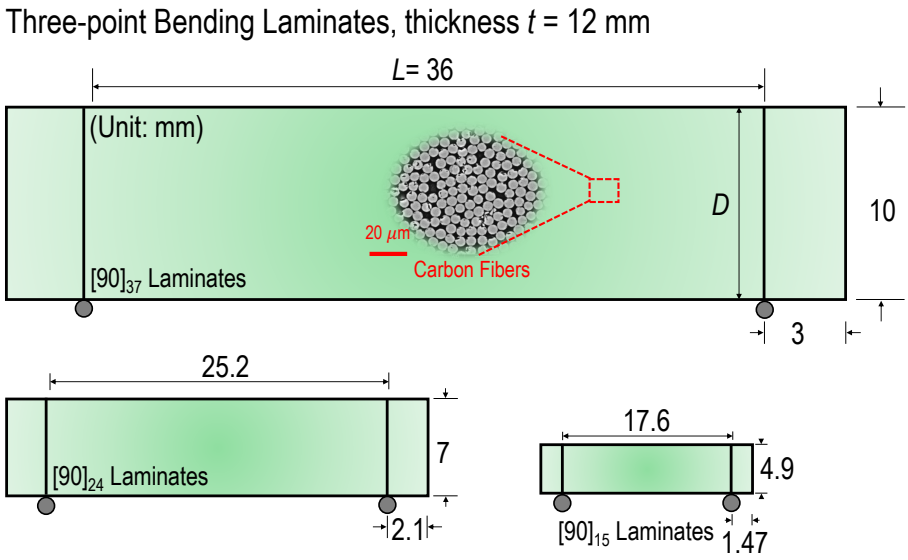

Figure 8.9: Geometrically-scaled rectangular specimens featuring 90° carbon fibers manufactured by leveraging the VARTM technique.

8.2.1.2 Three-point bending tests

The size effect study on the splitting crack initiation was achieved by conducting three-point bending tests on geometrically-scaled rectangular laminates as illustrated in Figure 8.9. The specimens feature 90° carbon fibers which are perpendicular to the longitudinal and out-of-plane directions of the specimen. The dimensions, scaled as $1 : 1.43 : 2.04$, were 4.9×17.64 mm, 7×25.2 mm, and 10×36 mm, respectively. The geometrical scaling on the width of the specimen leads to the different number of plies exhibiting $[90]_{15}$, $[90]_{24}$, and $[90]_{37}$ laminates. The thickness of the specimen was not scaled and kept about 12 mm for all the sizes. It is worth mentioning here that the specimen featuring 4.9 mm in width is not manufactured and tested yet due the unprecedented situation caused by COVID-19. This is one of the

future works as it will be discussed in the last chapter.

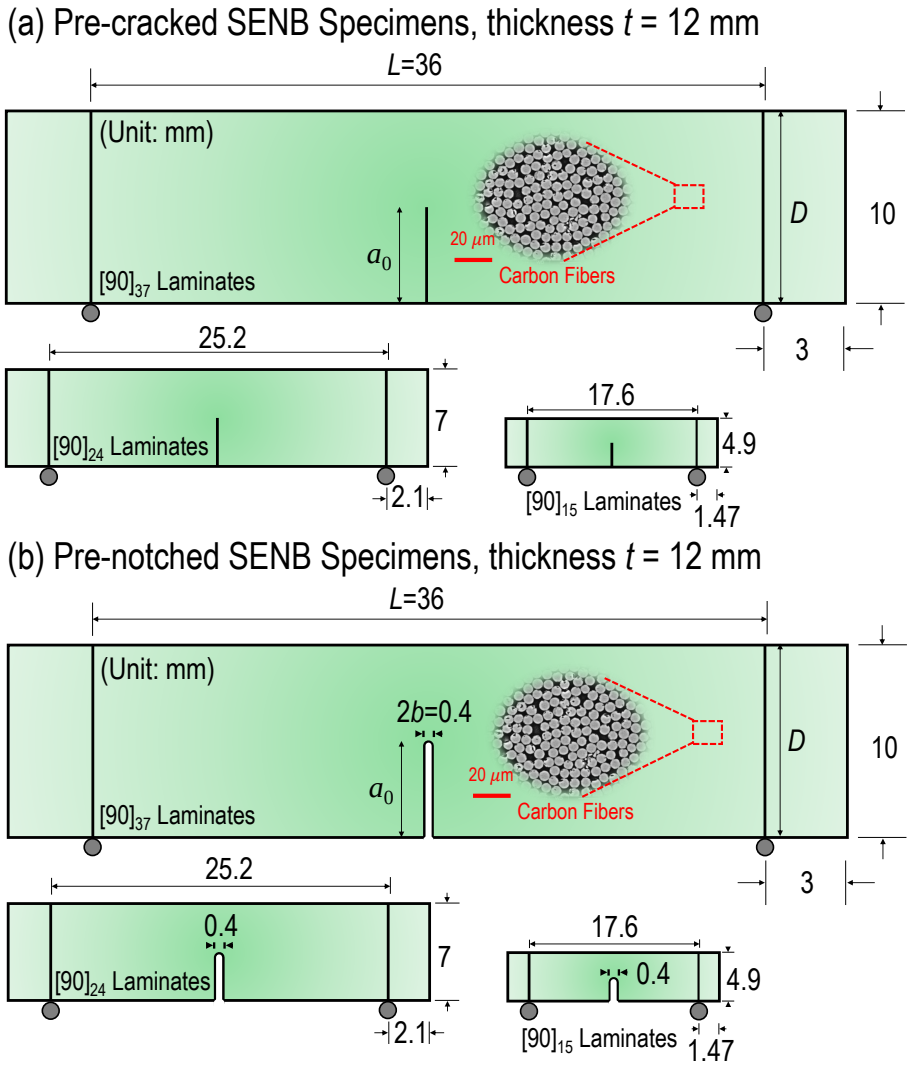

Figure 8.10: Geometrically-scaled SENB specimens featuring 90° carbon fibers manufactured by leveraging the VARTM technique: (a) pre-cracked specimens; (b) pre-notched specimens.

8.2.1.3 Mode I fracture tests

In addition, geometrically-scaled Single Edge Notch Bending (SENB) laminates were prepared for Mode I fracture tests to investigate the size effect on the splitting crack initiation

and propagation. The specimens have the same scaling dimensions as the foregoing rectangular specimens used fro three-point bending tests. As illustrated in Figure 8.10, both pre-cracked and pre-notched specimens were investigated to clarify the effects of the notch type in fiber-reinforced polymer composites and make a critical comparison with the corresponding behavior of pure epoxy. The detailed manufacturing of the crack and notch follows the same procedures as described in the previous chapters. The length of the initial notch was about $0.5D$ where D is the width of the specimen but the length of the initial crack was scaled with the range approximately from $0.45D$ to $0.55D$ due to the difficulties in tapping the crack with consistent length. It is worth mentioning here again that the specimen featuring 4.9 mm in width is not manufactured and tested yet due the unprecedented situation caused by COVID-19. This is one of the future works as it will be discussed in the last chapter.

8.2.2 Experimental results and analysis

8.2.3 Size effect on the transverse strength of fiber-reinforced composites

The load-displacement curves obtained from three-point bending tests are plotted in Figure 8.11b. As can be noted from the figure, the specimen features pronounced brittleness before reaching the critical load and then exhibits unstable crack propagation due to snap-back instability. In comparison with the mechanical behavior of the pure epoxy featuring the same dimension and loading condition as shown in Figure 8.11a, the addition of 90° carbon fibers not only reduces the ductility but also lowers the structural strength in the transverse direction of the material. This interesting phenomenon is mainly attributed to the stress concentration and possible defects at the fiber/matrix interface due to the heterogeneity of the materials [195]. In addition to this aspect, the existence of the hydrostatic stress in a typical fiber-reinforced composite also makes non-negligible contribution to the worse transverse behavior of the investigated laminates. On the other hand, the transverse stiffness of the specimen with the addition of carbon fibers was noticeably increased compared to the

one of pure epoxy as illustrated in Figure 8.11a. This aspect is reasonable considering the fact that about 60% volume fraction of carbon fibers was bounded with epoxy resin thus exhibiting higher transverse stiffness.

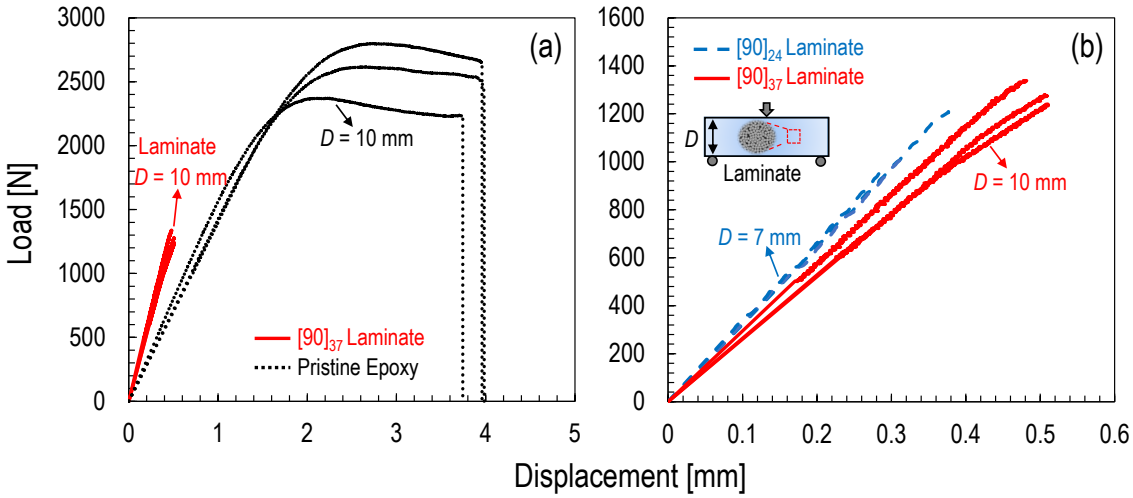

Figure 8.11: (a) Critical comparison between $[90]_{37}$ laminates and pure epoxy on the experimental load-displacement curves obtained from three-point bending tests; (b) Geometrically-scaled rectangular specimens featuring 90° carbon fibers under three-point bending condition.

With knowing the distinct mechanical behavior between pure epoxy and the one modified by carbon fibers, it is interesting to further study the size scaling effect on the structural strength of both investigated materials and make a critical comparison. The definition of the structural strength has the same meaning as described in the previous chapters. As illustrated in Figure 8.12, while the pure epoxy exhibits relatively weak size effect on the structural strength of investigated specimens, a remarkable size effect on the counterpart was observed for the investigated fiber-reinforced specimens in the transverse direction due the higher slope featuring the investigated specimens. In this context, the structural strength of the fiber-reinforced composite in the transverse direction can reach a significantly higher value as specimen size decreases and this aspect is considered as one of the future works. On the other hand, the failure probability distribution of the fiber-reinforced specimens with

the investigated size ranges possibly still follows Weibull distribution with a lower Weibull modulus compared to the one measured from pure epoxy as mentioned in the previous chapters. More studies are required in the future to clarify the size ranges for entering the Gaussian distribution part.

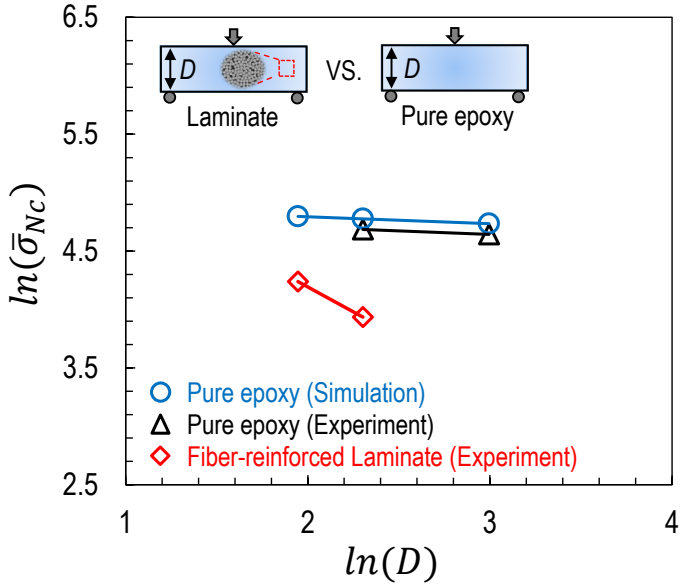

Figure 8.12: Average structural strength vs. specimen size measured from pure epoxy and the one modified by carbon fibers under three-point bending condition. Note that the computational results for pure epoxy was simulated by leveraging calibrated Ramberg-Osgood relation as discussed in the previous chapters.

8.2.4 Size effect on the Mode I fracturing behavior of fiber-reinforced composites

The intralaminar mode I fracturing behavior of fiber-reinforced composites was further investigated in this section. The load-displacement curves obtained from both pre-cracked and pre-notched SENB specimens are plotted in Figure 8.13. As can be noted from the figure, the pre-notching method does not significantly affect the transverse stiffness of the material. However, the critical loads of pre-cracked specimens are generally higher than the ones of pre-notched specimens showing about 25% in difference for all the investigated sizes. The

possibility can be either due to the hydrostatic stress or the higher stress intensity at the crack tip which is substantially different from the one at the notch tip as discussed in the previous chapters.

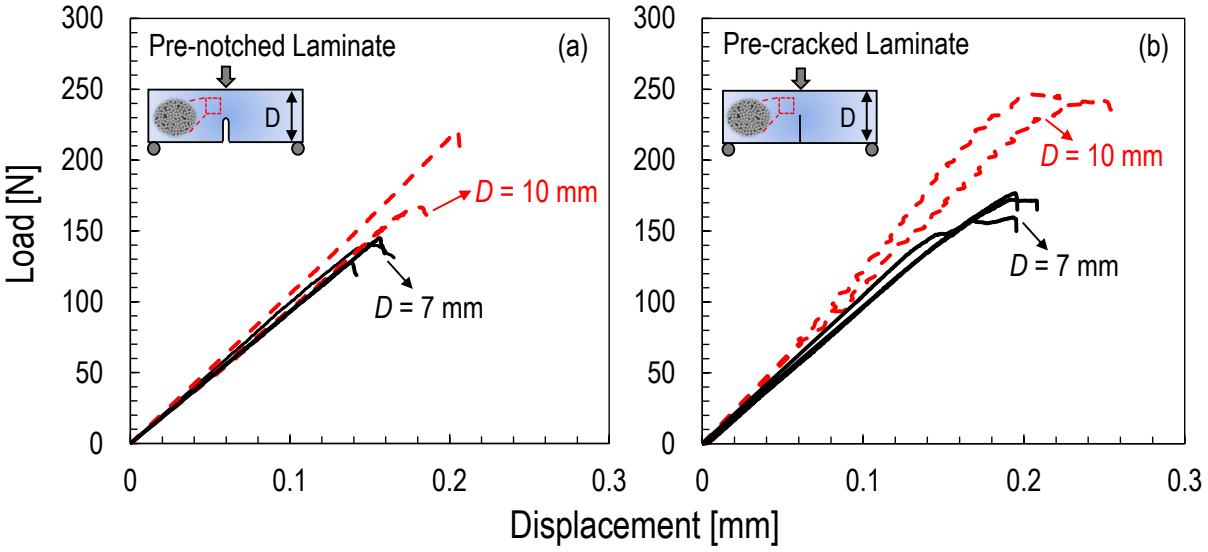

Figure 8.13: Experimental load-displacement curves obtained from Mode I fracture tests on geometrically-scaled fiber-reinforced composites featuring notch and crack.

The foregoing weak effects of pre-notching methods on the investigated fiber-reinforced composites are significantly different from the ones of pure epoxy as presented in the previous chapters. As illustrated in Figure 8.14, the pre-cracked fiber-reinforced specimen exhibits better structural capacity in comparison with the corresponding pure epoxy. This can be explained due to the fact that high stress concentration at the crack tip leads to significantly increased damage initiation at the fiber/matrix interface thus generating larger FPZ for energy dissipation. However, this is not the truth for the pre-notched fiber-reinforced specimen since the addition of carbon fibers significantly reduce the critical load being more than two times lower than the one of pre-notched pure epoxy. This interesting phenomenon is probably due to the fact that the foregoing larger FPZ at the notch tip is at least comparable with the notch radius thus deactivating the micro-scale strength of the polymer as comprehen-

sively analyzed in the previous chapters. In addition to these insightful differences between pure epoxy and fiber-reinforced laminate, it is worth mentioning here that both pre-cracked and pre-notched specimens with the addition of carbon fibers also exhibit noticeably higher stiffness in the transverse direction which is ascribed to the same reason as discussed in the previous section for the rectangular fiber-reinforced specimens under three-point bending condition.

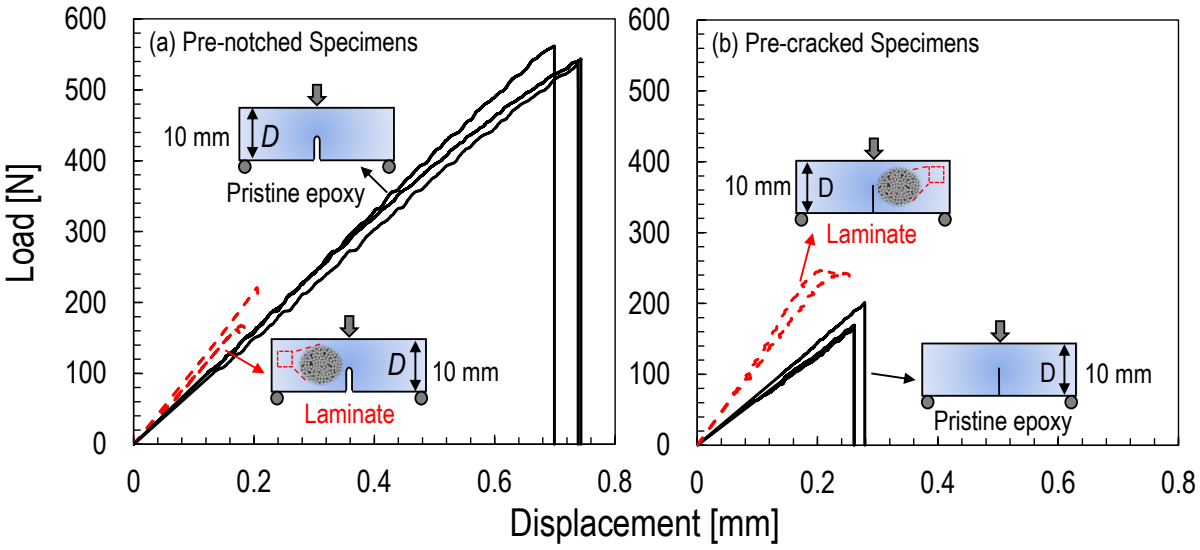

Figure 8.14: Experimental load-displacement curves obtained from Mode I fracture tests on geometrically-scaled pure epoxy and related fiber-reinforced composites. This plot compares the effects of pre-notching methods on both materials.

8.3 Conclusions

1. The long-standing problem on the undesirable computational modeling of sub-critical damage and their evolution in fiber-reinforced composites at the micro scale is not actually due to the methods for describing the complex stress field for crack formation and propagation but mainly due to the following two important aspects which were computationally confirmed through the successful micro-scale modeling of fiber-

reinforced composites under either uni-axial tension or pure shear showing excellent reproduction with the experimental morphologies reported in the literature;

2. One of the key aspects for the solution of this problem as illustrated in this chapter is mainly associated to the versatile material behavior of the polymer at different stress states as clearly shown in chapter 2. In this context, the damage initiation can only be captured upon the condition that the full multi-axial tensorial stress state in the composite is correctly described. This is possible in the crack band approach but not feasible in traditional Cohesive Zone Models (CZMs) and basic XFEM or phase field models widely used in the literature;

3. Another leading aspect for the solution of the foregoing problem is related to the distinguishable material properties of the polymer at the microscale (i.e. high material strength and low fracture energy) compared to the opposite values at the large scales (i.e. low material strength and high fracture energy) obtained from conventional laboratory tests. This aspect is extremely important to capture the matrix cracking and the following delamination for polymer matrix composites under either uni-axial tension or pure shear loading condition as shown in this chapter;

4. On the other hand, the transverse behavior of the investigated fiber-reinforced composites under three-point bending condition exhibits significant difference showing remarkable brittleness and lower structural capacity compared to the corresponding behavior of the investigated pure thermoset polymer as experimentally shown in this chapter. This worse behavior is mainly due to the heterogeneity of the materials and the possibility of the defects leading to the higher stress concentration at the interface between fiber and matrix;

5. Moreover, the notch type has significant effects on the transverse behavior of fiber-reinforced composites. The addition of the transverse fibers can lead to a noticeable improvement for the thermoset polymer in presence of a sharp crack whereas this is

not the truth for the material in presence of a blunt notch showing the structural capacity being almost three times lower than the one of the investigated thermoset polymer. This pronounced difference is actually due to the larger fracture process zone happening in front of the crack or notch tip thus deactivating the micro-scale behavior of the investigated thermoset polymer but dissipating more energy leading to the better performance of pre-cracked composites.

Chapter 9

MULTI-AXIAL QUASI-STATIC AND FATIGUE BEHAVIOR OF FIBER-REINFORCED POLYMER COMPOSITES

This chapter presents an investigation on the global mechanical behavior of fiber-reinforced composites under multi-axial quasi-static and cyclic loading conditions. The unprecedented comprehensive experimental results clarified the effects of multiaxiality ratio, stacking sequence, loading condition, and notch configuration on the fracturing behavior of fiber-reinforced composites. These aspects are important for the future formulation and validation of an efficient computational model for composites.

9.1 Past and current work on the multi-axial fatigue studies

Far less attention has been devoted to fatigue compared to quasi-static loading despite the fact that the characterization and modeling of the behavior of composite materials under uni-axial and multi-axial loading have been the subjects of countless advances since the pioneering works of Owen and co-authors [28–33]. Still today, these are considered among the most comprehensive experimental investigations of the multi-axial fatigue behavior of polymer composites. A formidable set of data was also provided by Fujii *et al.* [34–37], who investigated the fatigue behavior of woven Glass Fiber Reinforced Polymers (GFRPs) under a variety of multi-axial stress states and even in the presence of stress concentrations induced by notches [38–40].

A very insightful discussion of fatigue damage in composites under on-axis tension was provided by Talreja in [41, 196] who identified three distinct mechanisms: (i) fiber failure at high applied strains with non-progressive failure, (ii) matrix fatigue cracking and progression by failing fibers or by debonding, and (iii) matrix cracking confined by fibers preventing its

propagation.

The damage mechanisms under multi-axial fatigue were investigated, among others, by Wang *et al.* [42, 43] who conducted cryogenic tests in tension/torsion on tubular specimens. They found that the dominating damage mechanisms included matrix cracking, fiber/matrix debonding, microbuckling of fiber bundles, and delamination. The relative contribution of each mechanism was found to be a function of the multiaxiality ratio. By testing cruciform GFRP specimens, Smith and Pascoe [44] identified rectilinear cracking, shear degradation of the fiber/matrix interface, and delamination as the main fatigue mechanisms. Similar results were obtained on carbon/epoxy composites by Chen and Matthews [45].

A step towards the quantification of microscale fatigue damage is represented by the work of Adden and Horst [46] who characterized the crack density evolution in tension/torsion loading in NCF glass/epoxy composites. In this context, a significant contribution was provided by Quaresimin and co-workers who investigated the damage evolution *in-situ* in various loading configurations and geometries [47–52].

On the modeling side, an early attempt of capturing the fatigue behavior of composites is due to Sims and Brogdon [197] who tried to extend the Tsai-Hill [198] static failure criterion to fatigue by substituting the strength parameters with suitable S-N curves. A similar approach was pursued by Francis *et al* [199] while Fujii and Lin [37] investigated the extension of the Tsai-Wu criterion [200] for the description of tension-torsion fatigue of glass/polyester tubes under different multiaxiality ratios. On similar grounds, several other authors proposed alternative extensions (see e.g. [201–203]).

An excellent discussion on polynomial criteria for multi-axial fatigue was provided by Quaresimin *et al.* [53] who verified their predictive capability through a comprehensive re-analysis of a large bulk of experimental data. They concluded that the accuracy of some multi-axial criteria was fair although, in few cases, largely unsafe predictions were obtained undermining the general validity of the models. They also stressed the importance of an insightful understanding of the local fatigue damage mechanisms and their incorporation in micro-mechanical models as an answer to the foregoing limitations.

In this context, a notable example is the Synergistic Damage Mechanics (SDM) approach proposed by Singh and Talreja [204] which combines micro-damage mechanics and continuum damage mechanics to predict the stiffness degradation due to presence of transverse cracks. Thanks to the micro-scale description of damage, the model can be used for various stacking sequences and loading conditions. In this direction is the outstanding work of McCartney and co-workers [205–210] and Lundmark and Varna [211, 212] on the modeling of matrix microcracking in transverse plies.

Later, Carraro *et al.* [213, 214] proposed an analytical model that can capture the microcracking in multidirectional laminates with any stacking sequence. Thanks to analytical framework, the model is extremely robust and inexpensive from the computational point of view while still extremely accurate. The foregoing results show the significant progress in the understanding of the fatigue behavior of composites. However, while the uni-axial and multi-axial fatigue response in smooth specimens has been the subject of extensive research, the study of notched structures is yet elusive.

As a first step towards addressing this important problem, the following sections presents an experimental investigation of the fracturing behavior of notched $[+45/90/-45/0]_s$ and $[0/90]_{2s}$ laminates under multi-axial quasi-static and fatigue loading. 3D woven composites in presence of blunt notch under multi-axial quasi-static loading were also investigated in this work. To have full control of both the multiaxiality ratio and the notch configuration relative to the fiber orientation and specimen geometry, the tests were conducted leveraging an Arcan rig which enables the application of combinations of nominal normal and shear stresses. Thanks to the synergistic use of stiffness degradation data, Digital Image Correlation (DIC), and X-ray Micro-computed tomography the study sheds more light on the effect of the multi-axial stress state, the layup and notch configuration on the fatigue behavior.

Before moving to the next sections, it is worth pointing out that all the results reported in this work are presented in terms of nominal stresses. Accordingly, the multiaxiality ratio refers to the "global" multi-axial state of stress rather than the "local", which may differ from lamina to lamina. Although it is well known that the damage mechanisms driving the

fatigue behavior in composites are controlled by the *in-situ* stress field, the choice of using the nominal stress was made to provide objective results for the calibration and validation of multi-axial fatigue models. In fact, in the presence of a stress raiser, the local stress state is in continuous evolution due to the stress/strain re-distribution associated to the progressive damage occurring in the Fracture Process Zone (FPZ). The calculation of such a stress state depends on the ability of the damage model to capture the main damage mechanisms and their evolution.

9.2 Materials and methods

9.2.1 Specimen preparation for two-dimensional composite laminates

The unidirectional system used for all the tests was a Glass Fiber Reinforced Polymer (GFRP) by Mitsubishi Composites [215]. This prepreg was made of 7781 unidirectional E-glass fiber and NB301 epoxy resin leading to a 0.28 mm lamina with 68% fiber volume fraction. The glass transition temperature for epoxy resin is about 120°C.

The investigated stacking sequences included a quasi-isotropic $[+45/90/-45/0]_s$ and a cross-ply $[0/90]_{2s}$ layup which are extensively studied in the literature and commonly used in composite structures. In the Quasi-Isotropic (QI) laminates, the decision of placing the 45° layers on top was made to facilitate the investigation of the matrix microcracking by optical microscopy. This information was instrumental to validate the non-destructive damage analysis conducted via micro-computed tomography which will be presented in the following sections. To manufacture the laminates, the prepreg was hand laid-up and then vacuum-bagged by using a Vacmobile mobile vacuum system [62]. A Despatch LAC1-38A programmable oven was used to cure the panels by ramping up the temperature from room temperature to 135°C in one hour, soaking for one hour, and cooling down to room temperature. After curing, the panels were cut into specimen of about 200 × 44 mm by using a water-cooled circular saw with a diamond-coated blade. The specimen thickness was about 1.72 mm and the gauge length was about 25 mm.

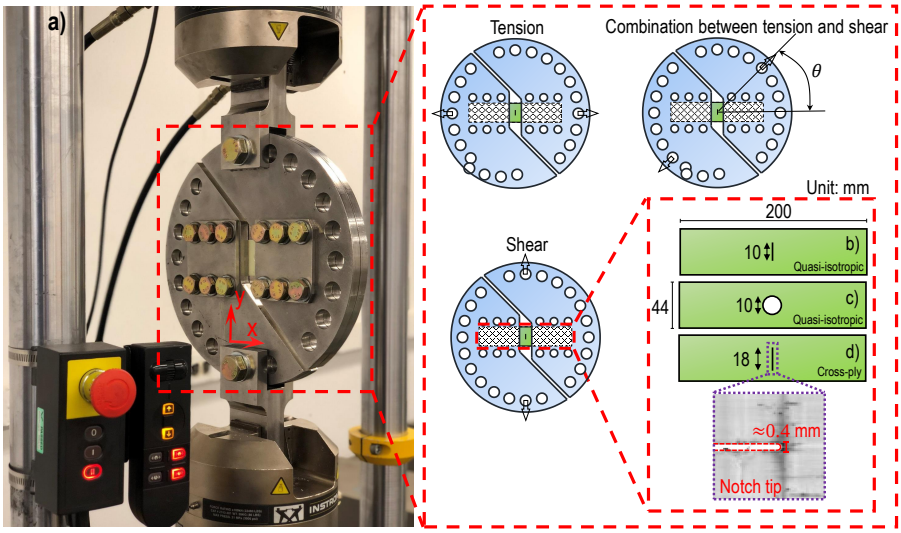

Figure 9.1: (a) Test setup and Arcan rig used for the multi-axial tests. Geometry of notched specimens used for the multi-axial tests: (b) $[+45/90/-45/0]_s$ specimen with a 10 mm central crack, (c) $[+45/90/-45/0]_s$ specimen with a 10 mm hole, and (d) $[0/90]_{2s}$ specimen with a 18 mm central crack. Note that the gauge length is about 25 mm.

The effect of an open hole or an intra-laminar central crack on composite materials under multi-axial quasi-static and fatigue loading was studied. To this end, three different geometries, illustrated in Figure 9.1b-d, were prepared: (1) specimen with a central circular hole of diameter $a_0 = 10$ mm, (2) specimen with a central crack of 10 mm, and (3) specimen with a central crack of 18 mm. The open-hole specimens featured only one stacking sequence of $[+45/90/-45/0]_s$ and a circular hole drilled by a tungsten carbide drill bit. In contrast, the cracked specimens featured both $[0/90]_{2s}$ and $[+45/90/-45/0]_s$ as stacking sequence. For the former layup, a crack $a_0 = 18$ mm was considered while, for the latter a_0 was equal to 10 mm. The crack was manufactured by firstly drilling a pre-notch using a 0.4 mm tungsten carbide drill bit and then completing the crack leveraging a 0.4 mm wide diamond-coated saw.

In addition to the forgoing notched specimens, unnotched specimens with different dimensions and layups were tested under quasi-static and fatigue loading conditions. The

purpose of these tests was to complete the information on the quasi-static and fatigue behavior provided by the manufacturer. The dimensions of the specimens followed ASTM D3039/D3039M [216] and the details can be found in Table 9.1.

Stacking Sequences	Dimension [mm]	Measured Properties
$[0]_8$	190x20x1.7	E_1=42.9 GPa, f_{1t}=900 MPa
$[90]_8$	210x30x1.7	E_2=8.3 GPa, f_{2t}=43 MPa
$[+45/\text{-}45]_{2s}$	210x30x1.7	G_{12}=5.8 GPa
$[0/90]_{2s}$	200x20x1.7	f_t=540 MPa
$[+45/90/\text{-}45/0]_s$	200x20x1.7	f_t=423 MPa

Table 9.1: Mechanical properties of unnotched specimens under tensile quasi-static loading condition. Note for the subscripts: 1 - axial direction, 2 - transverse direction.

9.2.2 Specimen preparation for three-dimensional woven composites

The three-dimensional woven composite features a ply to ply angle interlock fiber architecture and is composed of 48K hexcel IM7 carbon fiber and Cytec PR520 toughened epoxy resin. The particular architecture has 6×6 columns of warp and weft tows in each unit cell and the warp tows also work as binders to provide through-thickness reinforcement leading to the overall fiber volume fraction about 0.58. The planar composite panels were prepared by Albany Engineered Composites (AEC).

The effects of an intra-laminar central notch on the three-dimensional woven composites under multi-axial quasi-static load were studied. Two different geometries were prepared for the multi-axial tests including the rectangular specimens cut along the warp and weft directions. The intra-laminar central notch was manufactured by firstly drilling a hole using a 0.8 mm tungsten carbide drill bit and then completing the notch with a 0.8 mm wide diamond-coated saw. The dimensions of the specimens are illustrated in Figure 9.2.

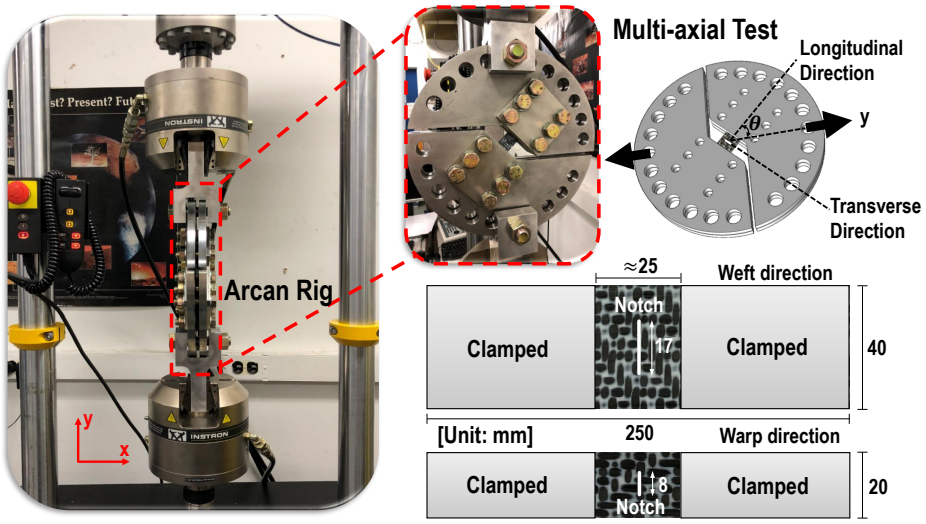

Figure 9.2: Test setup and Arcan rig used for the multi-axial tests on notched three-dimensional woven composites. Both warp and weft directions oriented towards the longitudinal direction of the specimen were investigated in this work.

9.2.3 Test method

A modified version of Arcan rig, illustrated in Figure 9.2, was specifically designed to guarantee infinite life for multi-axial fatigue tests on composite materials. This modified Arcan rig comprises four identical plates (two fronts and two backs) which are used to clamp the specimens by friction. A 17-4 PH stainless steel was used to manufacture these four plates.

The specimens were clamped to the modified Arcan rig by using twelve M14 high-strength bolts, with each bolt torqued at 130 N m. This ensures that enough clamping pressure was applied on the specimen tabs to avoid slipping during the tests. The modified Arcan rig is capable of applying multi-axial loads by varying loading angle θ, the angle between loading direction and the longitudinal direction of the specimen. As illustrated in Figures 9.1a and 9.2, tension is applied when θ equals 0° while pure shear is applied when θ equals 90°. A combination of tension and shear is achieved by an intermediate loading angle between 0° and 90°. To describe the loading configuration, multiaxiality ratio can be defined as

$\lambda = \arctan(\tau_N/\sigma_N)$ where $\sigma_N = P\cos\theta/[(w-a_0)t]$ is the nominal normal stress and $\tau_N = P\sin\theta/[(w-a_0)t]$ is the nominal shear stress applied to the specimen. It is worth mentioning here that $\sigma_N = P\cos\theta/(wt)$ and $\tau_N = P\sin\theta/(wt)$ are defined for 3D woven composites. In the definitions of stress, P is the instantaneous load, θ is the loading angle, w is the specimen width, a_0 is the crack length or hole diameter and t is the specimen thickness. On the other hand, in-plane and out-of-plane bending are negligible in the foregoing tests and this was verified by using multiple strain gauges on the different locations of the specimen or Digital Image Correlation (DIC) on the displacement contours of the specimen under multi-axial loading condition as discussed by Tan *et al.* [217]. The multi-axial, quasi-static, and fatigue tests were performed in a servo-hydraulic 8801 Instron machine with closed-loop control. The speckled specimens were analyzed by means of an open source Digital Image Correlation system programmed in MATLAB software developed at Georgia Tech [218, 219].

9.2.4 Uni-axial tests on notch-free specimens

Notch-free specimens were tested under quasi-static and fatigue loading conditions to characterize the uni-axial constitutive behavior and S-N curves. The quasi-static tests were performed under displacement control with a displacement rate of 0.01 mm/s whereas the fatigue tests were under load control with a stress ratio of $R = 0.1$ and a low frequency of $f = 5$ Hz. It is worth mentioning that both $[0/90]_{2s}$ and $[+45/90/-45/0]_s$ stacking sequences were investigated. These configurations were the same adopted for the multi-axial tests. The forgoing experimental campaign was performed to provide sufficient information on the uni-axial tensile behavior of the material before investigating the multi-axial behavior.

9.2.5 Multi-axial tests on notched specimens

9.2.5.1 Two-dimensional composite laminates

To study the failure behavior of notched laminates under multi-axial quasi-static loading, five sets of multiaxiality ratios were investigated: $\lambda = 0$, 0.262, 0.785, 1.309 and 1.571. Such

multiaxiality ratios corresponded to $\theta = 0°$, $15°$, $45°$, $75°$ and $90°$. At least three specimens were tested for each configuration. As for the tensile quasi-static tests on unnotched specimens, the load rate for the multi-axial quasi-static tests was 0.01 mm/s.

In the case of multi-axial fatigue tests, the same multiaxiality ratios as the quasi-static tests on notched specimens were investigated. At least three specimens were tested for each multiaxiality ratio in order to produce a statistically significant set of data. To study the fatigue failure behavior of notched laminates under multi-axial fatigue loading, three sets of loading cases were studied: 70% P_{max}, 55% P_{max} and 40% P_{max} where P_{max} is the average peak force determined from quasi-static tests for each multiaxiality ratio. A stress ratio of $R = 0.1$ and a low frequency of $f = 5$ Hz were kept for all the forgoing loading cases.

9.2.5.2 Three-dimensional woven composite specimens

The comprehensive information on the multi-axial behavior of notched three-dimensional woven composites was achieved by investigating six sets of multiaxiality ratios with $\lambda = 0, 0.262, 0.524, 0.785, 1.047$ and 1.571 in this study. Such multiaxiality ratios corresponded to $\theta = 0°$, $15°$, $30°$, $45°$, $60°$ and $90°$. Only multi-axial quasi-static tests were conducted for the notched three-dimensional woven composites with the displacement rate about 0.01 mm/s whereas the multi-axial fatigue tests were not performed in this work.

9.3 Experimental results and analysis

9.3.1 Uni-axial tests on notch-free specimens

The mechanical properties of the unnotched specimens under quasi-static loading conditions are tabulated in Table 9.1. These properties were measured based on the stress and strain curves with the strain obtained from Digital Imaging Correlation (DIC) to exclude the compliance of the testing system. On the other hand, in terms of the fatigue behavior of unnotched specimens, the normalized S-N curves of unnotched $[+45/90/-45/0]_s$ and $[0/90]_{2s}$ specimens under tensile fatigue loading conditions are plotted in Figure 9.3a. As can be noted

from the figure, the slope of S-N curve for the cross-ply specimen is slightly larger than the one of the quasi-isotropic specimen. The larger slope of S-N curve reflects the specimen with better resistance to fatigue loading. This is consistent with the results on the normalized stiffness degradation curves, as shown in Figure 9.3b, in which the structural stiffness of the cross-ply specimen deteriorates less significantly in comparison with the one of the quasi-isotropic specimen. The structural stiffness is defined as $K = (P_{peak} - P_m)/(u_{peak} - u_m)$ where P_{peak} is the peak load, P_m is the mean load, u_{peak} is the displacement at the peak load for each cycle, and u_m is the displacement at the mean load for each cycle. However, the endurance limit, generally considered as 2 million cycles, was achieved when the peak load in applied cyclic load reached roughly 30%-35% of the critical quasi-static load for both unnotched specimens.

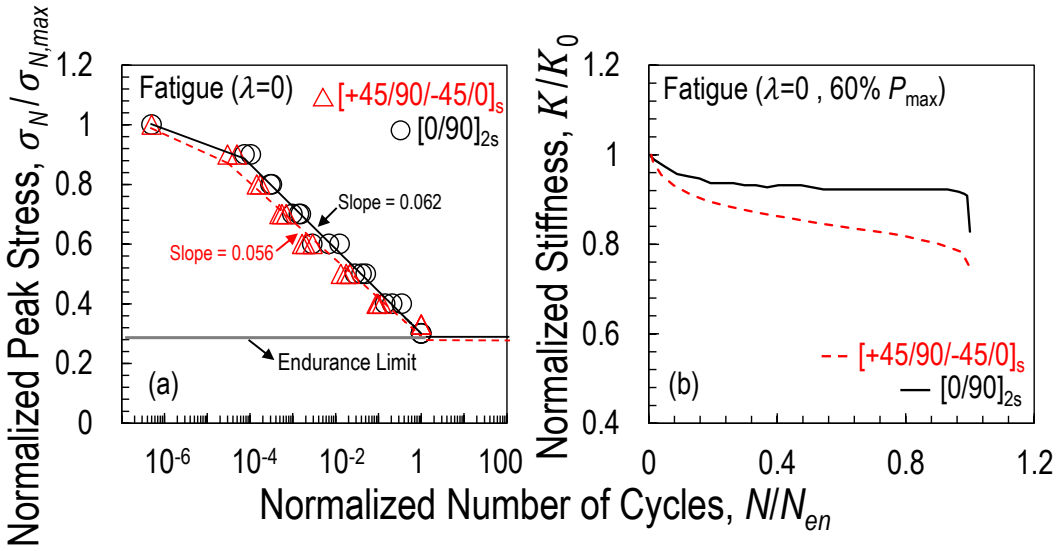

Figure 9.3: (a) Normalized S-N curves for unnotched quasi-isotropic and cross-ply specimens under tensile fatigue loading conditions; (b) Normalized stiffness vs. number of cycles (60% P_{max}). Note that N_{en} equals to 2 million cycles as endurance limit in this work and $\sigma_{N,max}$ represents the quasi-static uni-axial strength of the specimen.

9.3.2 Multi-axial quasi-static tests on notched specimens

9.3.2.1 Two-dimensional composite laminates

The nominal stress and strain curves obtained from the multi-axial quasi-static tests are plotted in Figures 9.4-9.7 for the following three specimen configurations: (1) $[0/90]_{2s}$ layup with a 18 mm central crack, (2) $[+45/90/-45/0]_s$ layup with a 10 mm hole, and (3) $[+45/90/-45/0]_s$ layup with a 10 mm central crack. In these figures, the normal and shear stresses are the nominal stresses in the net section, $\sigma_N = P\cos\theta/[(w-a_0)t]$ and $\tau_N = P\sin\theta/[(w-a_0)t]$, whereas the strain is calculated based on the difference in the displacements at two ends of the gauge area of the specimen obtained from Digital Imaging Correlation (DIC).

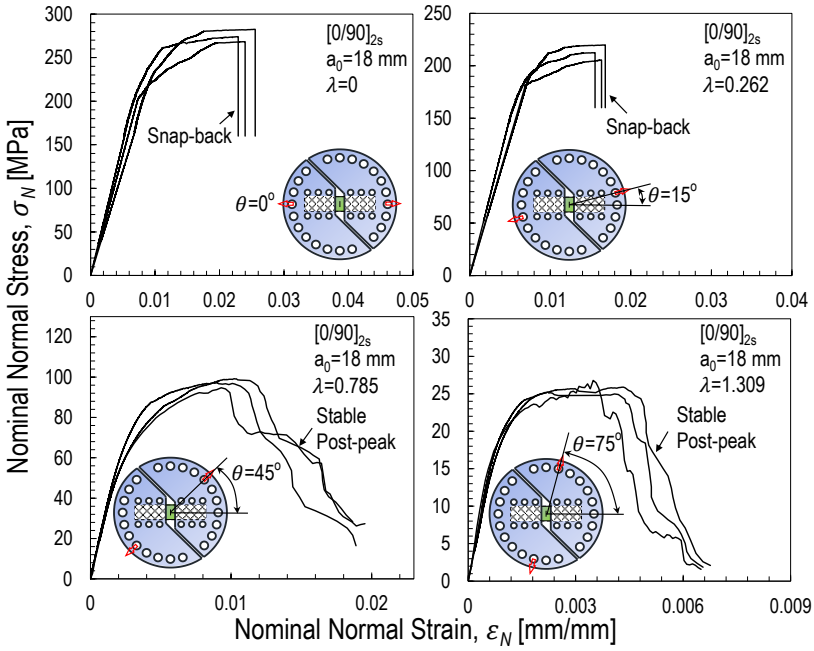

Figure 9.4: Nominal normal stress vs. nominal normal strain obtained from the multi-axial quasi-static tests on the $[0/90]_{2s}$ specimen weakened by a 18 mm central crack.

As can be noted from Figures 9.4-9.7, the stress-strain curves under multi-axial quasi-static loading are characterized by a significant non-linear behavior when the specimens are

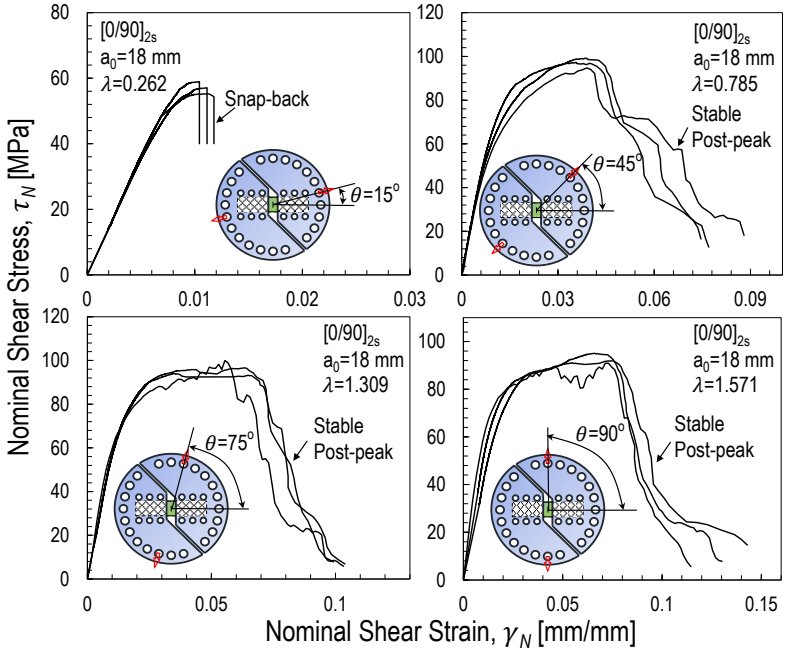

Figure 9.5: Nominal shear stress vs. nominal shear strain obtained from the multi-axial quasi-static tests on the $[0/90]_{2s}$ specimen weakened by a 18 mm central crack.

subjected to a combination of tension and shear, regardless of the layup. This phenomenon becomes more and more significant with increasing multiaxiality ratios due to the emergence of diffused, sub-critical matrix micro-cracking, splitting and delamination. These damage mechanisms contribute to the dissipation of the strain energy stored in the specimen inducing a significant non-linearity before reaching the failure load. A similar mechanism was reported in uni-axial tests on unidirectional laminates and two dimensional textile composites [220–222]. The mechanical behavior after peak stress is characterized by catastrophic failure due to snap-back instability [223, 224] for all the investigated layups when the specimens are subjected to tension-dominated loading. On the other hand, the failure behavior becomes more and more stable with increasing the shear load component. Eventually, as shown in Figures 9.4-9.7, the post-peak behavior becomes stable and strain softening becomes evident. This is an indication of more pronounced quasi-brittleness with increasing the shear

load component, a phenomenon even more pronounced for the $[+45/90/-45/0]_s$ specimens. It is worth mentioning here that the snap-back instability in tension-dominated loads is a structural, not a material phenomenon. To explore the post-peak behavior, one could leverage the new device proposed by the authors [225]. However, this is beyond the scope of the present work.

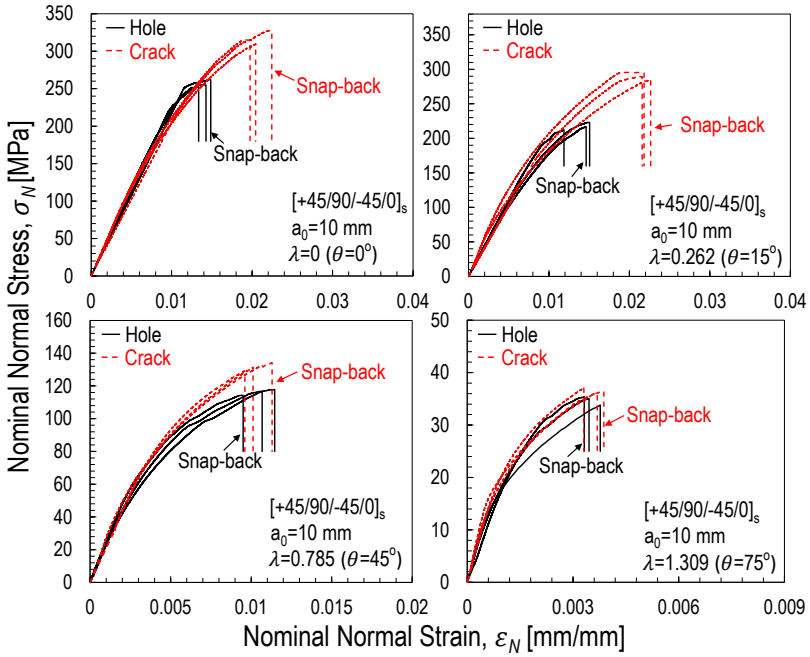

Figure 9.6: Nominal normal stress vs. nominal normal strain obtained from the multi-axial quasi-static tests on the $[+45/90/-45/0]_s$ specimens weakened by a 10 mm central crack and a 10 mm hole respectively. All the tests summarized in this figure exhibited snap-back instability.

It is interesting to investigate the relationship between the normal and shear strength (critical net cross-section stress) as a function of the multiaxiality ratio. The failure envelopes for the foregoing notched specimens under multi-axial quasi-static tests are plotted in Figure 9.8 and the details can be found in Table 9.2. In this plot, the normal and shear strengths are defined as $\sigma_{N,max} = P_{max}\cos\theta/[(w-a_0)t]$ and $\tau_{N,max} = P_{max}\sin\theta/[(w-a_0)t]$ respectively where P_{max} is the critical load. As can be noted from Figure 9.8, the failure envelope of

quasi-isotropic $[+45/90/-45/0]_s$ layup with a 10 mm central crack encompasses the one with a 10 mm open hole hinting the fact that the hole affects the structural strength more severely than a crack. A similar phenomenon, associated to the greater splitting development in load-bearing plies for the specimens with an intra-laminar central crack compared to the ones with an open hole, has been reported by several authors on notched Carbon Fiber Reinforced Polymer (CFRP) laminates [217, 226].

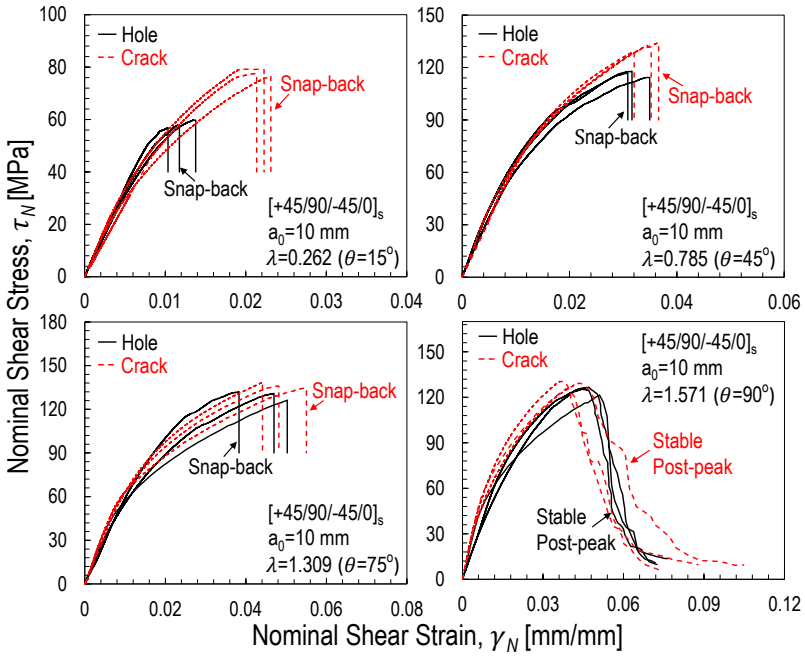

Figure 9.7: Nominal shear stress vs. nominal shear strain obtained from the multi-axial quasi-static tests on the $[+45/90/-45/0]_s$ specimens weakened by a 10 mm central crack and a 10 mm hole respectively.

However, since the failure behavior of notched composites depends on the size of the non-linear Fracture Process Zone (FPZ) occurring in the presence of a large stress-free crack compared to the specimen width [94–103, 227, 228], geometrically-scaled specimens with an open hole or a central crack need to be investigated to better understand this phenomenon. The size effect tests are undergoing and will be presented in future publications. Another subject of future investigations is the evolution of the fracture toughness with the multiaxi-

ality ratio which has been studied in nanocomposites [72, 73].

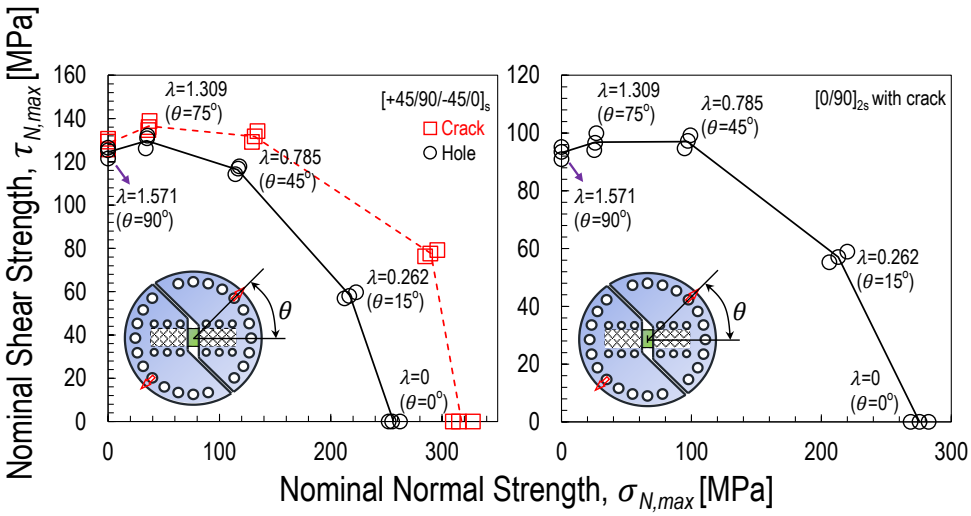

Figure 9.8: Failure envelopes of notched $[0/90]_{2s}$ and $[+45/90/-45/0]_s$ specimens under multi-axial quasi-static loading conditions.

9.3.2.2 Three-dimensional woven composites

The representative nominal stress and strain curves for the three-dimensional woven composites in presence of an intra-laminar central notch under multi-axial loads were plotted in Figure 9.9. For both warp and weft scenarios, the mechanical response of the materials in the longitudinal direction of the specimen exhibits less non-linearity up to the peak load with the curves departure from the linear part at least after 35% of the strain at the peak load. However, the emergence of the material ductility in the transverse direction of the specimen was observed with increasing the proportion of shear to tension since the significant non-linear curves depart from the linear part only after 20% of the strain at the peak load and followed by a stable post-peak behavior. Similar phenomenon was also reported in other related studies [74, 217, 229–231]. The non-linearity of the materials under shear-dominated loads can be explained mainly due to the formation of the significant matrix and debonding

Stacking Sequences	Multiaxiality Ratio	Normal Strength, $\sigma_{N,max}$ [MPa]	Shear Strength, $\tau_{N,max}$ [MPa]
$[0/90]_{2s}$ with central crack	0	275.57	0
	0.262	213.02	57.08
	0.785	97.05	97.05
	1.309	25.96	96.87
	1.571	0	93.18
$[+45/90/-45/0]_s$ with central crack	0	317.52	0
	0.262	289.99	77.70
	0.785	131.71	131.71
	1.309	36.57	136.48
	1.571	0	128.56
$[+45/90/-45/0]_s$ with open hole	0	256.47	0
	0.262	217.24	58.21
	0.785	116.33	116.33
	1.309	34.76	129.72
	1.571	0	124.46

Table 9.2: Average nominal normal and shear strengths of notched specimens under multi-axial quasi-static loading condition.

cracks for the energy dissipation in this case rather than the plasticity of the material as it will be shown through the morphological study in the next section. On the other hand, it is interesting to notice from the figure that the evolution of the nominal stress and strain curves can be dependent on the global multi-axial stress states. This implies the significant effects of the local stress states on the plastic deformation and fracture behavior of the materials which was also reported in other studies for various materials [22, 123, 125, 126, 130, 232].

The correlation between the nominal normal and shear strength as a function of the multiaxiality ratio for the notched three-dimensional woven composites was further investigated and plotted in Figure 9.10. As illustrated in Figure 9.10a for the warp tows oriented towards the longitudinal direction of the specimen, the failure envelope features two distinguishable segments which represent both tension dominated ($\lambda = 0$ to 0.262) and shear-dominated ($\lambda = 0.262$ to 1.571) loading conditions. This is an indication of two different damage mechanisms with respect to the multiaxiality ratio as it will be clarified in the next section. On the

other hand, the forgoing failure envelop is located in the area featuring the boundary with the in-plane tensile strength and shear strength measured from the previous uni-axial tensile tests on the notch-free specimens. This aspect is not surprising but mainly attributed to the significant reduction on the nominal normal strength of the specimen since the nominal shear strength does not exhibit sensitive degradation for the existence of an intra-laminar central notch in the specimen compared to the one estimated from the uni-axial tensile tests on the previous off-axis specimens. In addition, the experimental results obtained from the previous Mode I fracture tests were further used through the LEFM analysis to predict the nominal normal and shear strength of the geometry in this case with the warp tows parallel to the longitudinal direction of the specimen.

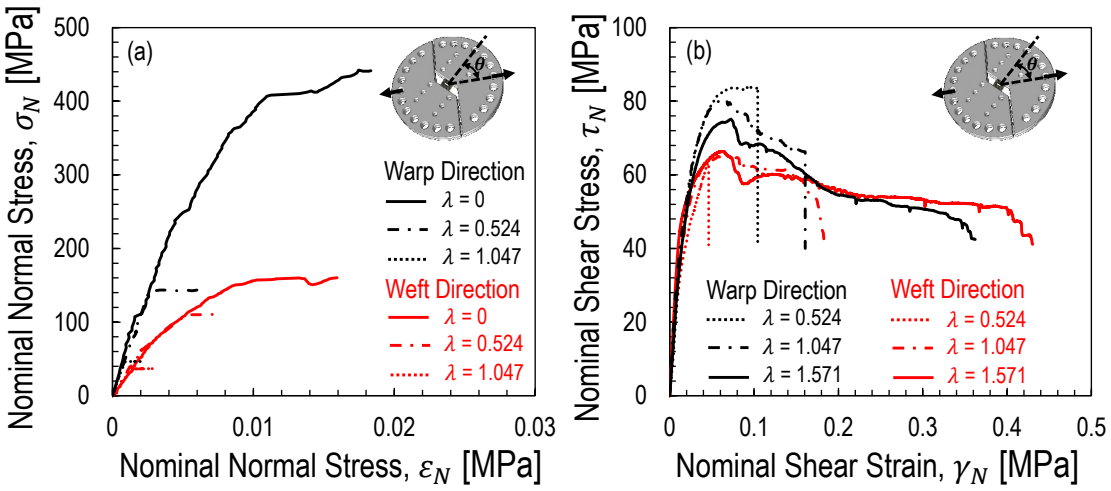

Figure 9.9: Nominal stress vs. strain curves in (a) longitudinal direction and (b) transverse direction obtained from the multi-axial tests on the notched three-dimensional woven composites with the longitudinal direction oriented in both warp and weft directions. Note that the nominal strain was measured based on the difference in the displacements close to the two ends of the gauge area of the specimen by means of the Digital Imaging Correlation.

As can be noted from Figure 9.10a, the prediction by means of the LEFM analysis can lead to a remarkable over-estimation for both nominal normal and shear strength and this mismatch confirms the quasi-brittleness of the investigated three-dimensional woven

composites which cannot be simply analyzed by leveraging the LEFM approach. It is worth mentioning here that the LEFM prediction on the nominal shear strength of the specimen in Figure 9.10a is based on the assumption that the apparent Mode II fracture energy G_f^{II} of the material with the warp tows oriented toward the longitudinal direction of the specimen is equivalent to the apparent Mode I values as reported in the recent work [233] due to the lack of data on this aspect in the open literature. In fact, the larger Mode II fracture energy of the laminates compared to the Mode I counterparts was typically reported in the literature [227] and this can lead to even more pronounced over-prediction on the forgoing nominal shear strength of the specimen.

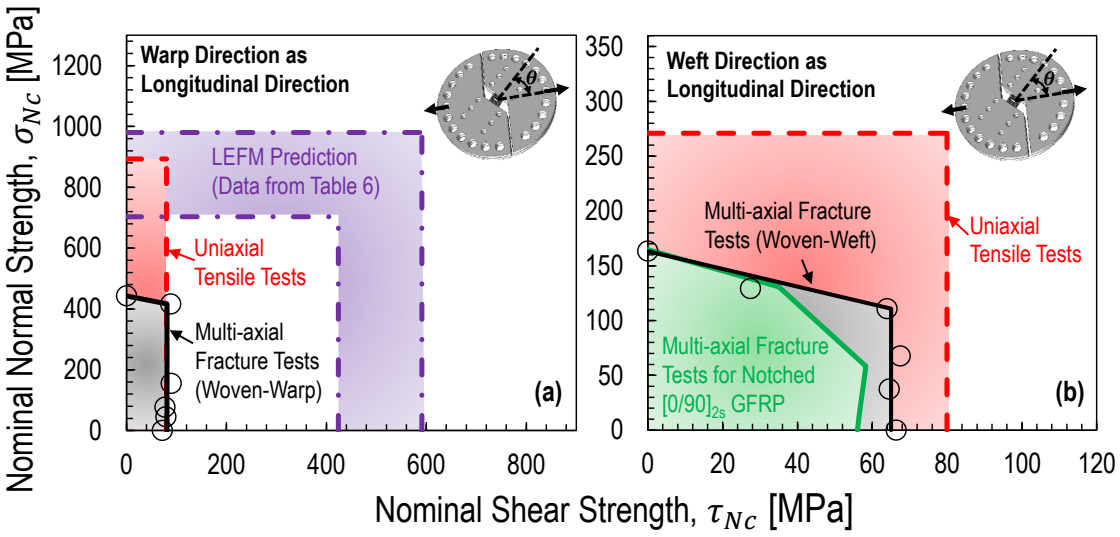

Figure 9.10: Failure envelops for the notched three-dimensional woven composites with the longitudinal direction of the specimen towards the (a) warp tows and (b) weft tows. Figure (a) compares the failure envelop measured from the multi-axial tests with the associated results obtained from the uni-axial tensile tests and predicted through the LEFM analysis. Figure (b) has a similar comparison but includes the previous results measured from the multi-axial tests on the notched $[0/90]_{2s}$ GFRP laminates.

Similar analysis was further performed on the notched three-dimensional woven composites with the weft tows in the longitudinal direction of the specimen. As it can be noted from Figure 9.10b, the failure envelope of the foregoing specimens under multi-axial loads

is also composed of two noticeable parts representing the transition of the damage mechanism from tension to shear. Moreover, this aforementioned failure envelop was reasonably compared with the one in the previous study [229] for the notched cross-ply $[0/90]_{2s}$ laminates made of glass fiber and thermoset polymer (GFRP) in the consideration of similar in-plane dimensions. As illustrated in Figure 9.10b, the mechanical behavior of the foregoing cross-ply laminates is similar to the one of the notched woven composites plotted in this figure under tension-dominated loading conditions. However, this does not happen in the shear-dominated scenarios since this notched woven composites exhibit higher nominal shear strength indicating the better shear resistance of the materials than the two-dimensional GFRP laminates with similar fiber orientations. On the other hand, the investigated intralaminar central notch leads to the reduction on both nominal tensile and shear strength of the notched woven composites with the weft tows in the longitudinal direction of the specimen and this aspect differs from the warp case as plotted in Figure 9.10a showing almost no degradation on the nominal shear strength of the material with the non-negligible intralaminar central notch. This can be explained by either the contribution of the warp tows to the better shear performance or the geometrical effects considering the different specimen sizes for both warp and weft cases. This requires further computational studies which will be covered in the future publications.

9.3.3 Multi-axial fatigue tests on notched specimens

9.3.3.1 Evolution of structural stiffness vs. multiaxiality ratio

Having discussed the failure behavior of notched laminates under multi-axial quasi-static loading, the fatigue failure behavior needs to be investigated. The evolution of the structural stiffness obtained from the multi-axial fatigue tests is represented in Figures 9.11-9.14 for all the studied notched specimens and two loading cases (70% and 55% of P_{max}). In these plots, the stiffness has the same meaning defined for the analysis of unnotched specimens under tensile fatigue loading condition.

As can be noted from Figures 9.11-9.12, for cross-ply $[0/90]_{2s}$ specimen with a central crack, the stiffness decreases of roughly 10% in the early stage of tension-dominated fatigue tests ($\lambda = 0, 0.262$) while no significant degradation can be observed throughout fatigue life of specimens subjected to shear-dominated fatigue loading. This is mainly due to the growth of transverse matrix cracking during tension-dominated fatigue loading [196]. Eventually, as illustrated in Figure 9.15c, the stiffness decreases of about 20% before catastrophic failure for multiaxiality ratio $\lambda = 0$ whereas only 5% degradation in stiffness was observed for multiaxiality ratio $\lambda = 1.571$. This can be attributed to a significant reduction of the splitting in 90° plies under shear-dominated loading compared to tension-dominated loading before catastrophic failure as shown in Figure 9.16 through the quantitative damage analysis by using X-ray micro-computed tomography (μ-CT) as it will be discussed later. Despite this reduction leading to a lower total crack volume for shear-dominated loading, the final failure is eventually triggered by the rapid growth of delamination in the late stage of fatigue tests as it will be shown in the next chapter.

However, this is not the case for quasi-isotropic $[+45/90/-45/0]_s$ specimen with an open hole or a central crack since in both cases a gradual stiffness degradation throughout the fatigue life can be noted for various multiaxiality ratios. In contrast to cross-ply $[0/90]_{2s}$ specimens, the stiffness of quasi-isotropic specimens with an open hole or a central crack deteriorates roughly 19% to 25% for all the investigated multiaxiality ratios as shown in Figures 9.15a-b. This consistent deterioration is mainly due to the significant development of splitting and delamination before catastrophic failure for all the multi-axial tests as shown in Figure 9.17 exemplifying the typical damage in specimens featuring an open hole. Similar damage was observed in specimens featuring a central crack.

In addition to the foregoing observations, it can be noted from Figures 9.13-9.14 that the fatigue performance of quasi-isotropic $[+45/90/-45/0]_s$ specimens with a central crack is generally worse than the one of the same layup featuring an open hole. As it will discussed in section 10.4, the quantitative damage analysis by using μ-CT technique confirms that the worse performance of the quasi-isotropic specimens weakened by a central crack compared

to the ones weakened by a central hole is associated to a significant larger amount of crack volume. It is interesting to note that this is in contrast to the quasi-static results which pointed to the central hole case as being the most critical. This structural phenomenon is due to a different evolution of the Fracture Process Zone (FPZ) in quasi-static regime compared to fatigue. There is no doubt that the process of FPZ development is strongly affected by the size of the specimens (width, notch size, etc.). This size effect deserves further studies and it will be the subject of future publications by the authors.

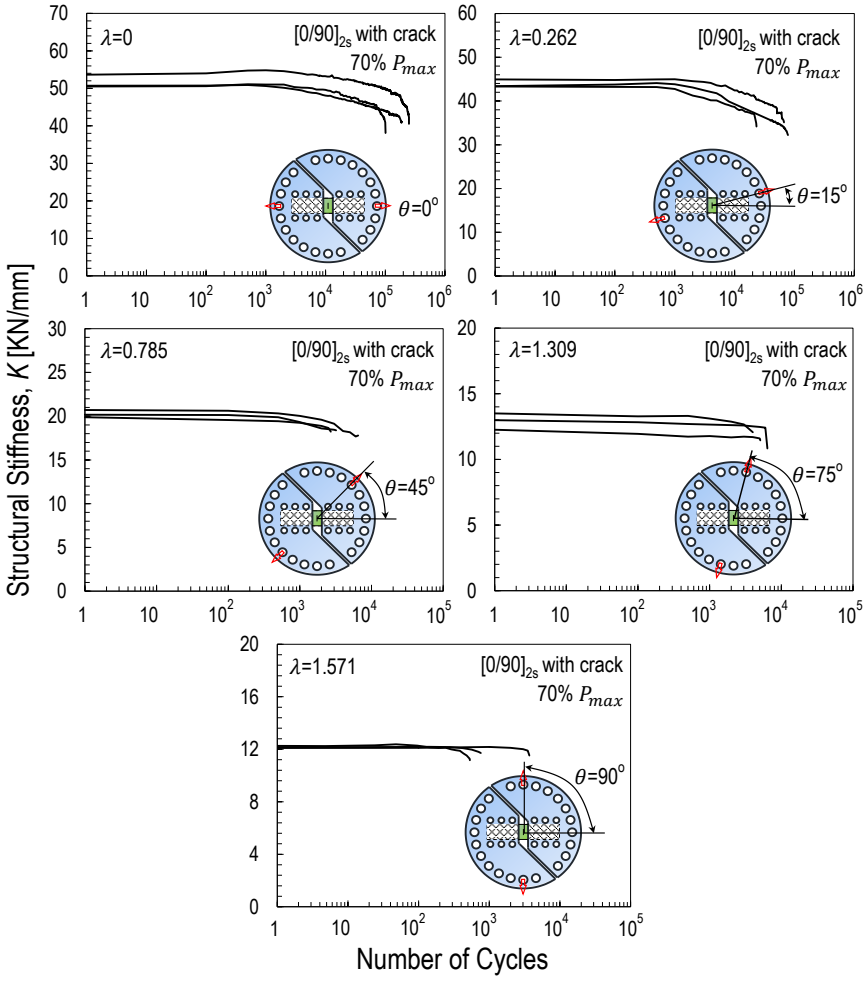

Figure 9.11: Evolution of structural stiffness vs. number of cycles measured during the multi-axial fatigue tests (70% P_{max}) on the $[0/90]_{2s}$ specimen with a 10 mm central crack.

It is interesting to note that this is in contrast to the quasi-static results which pointed to the central hole case as being the most critical. This structural phenomenon is due to a different evolution of the Fracture Process Zone (FPZ) in quasi-static regime compared to fatigue. There is no doubt that the process of FPZ development is strongly affected by the size of the specimens (width, notch size, etc.). This size effect deserves further studies and it will be the subject of future publications by the authors.

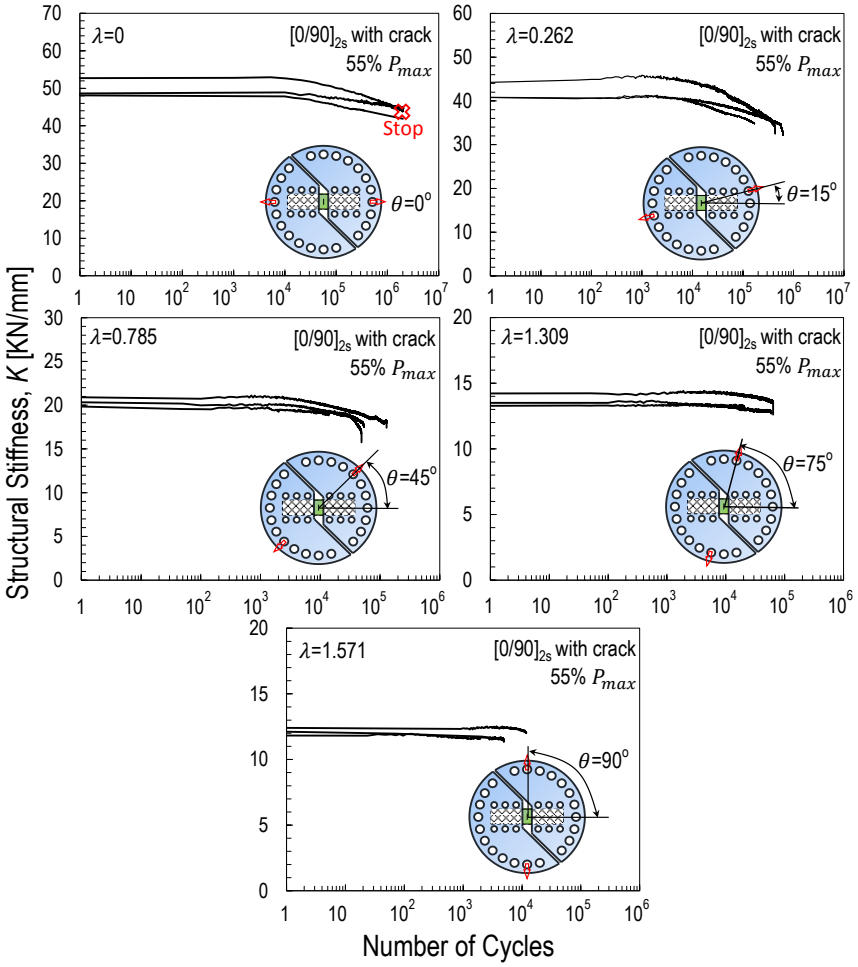

Figure 9.12: Evolution of structural stiffness vs. number of cycles measured during the multi-axial fatigue tests (55% P_{max}) on the $[0/90]_{2s}$ specimen with a 10 mm central crack.

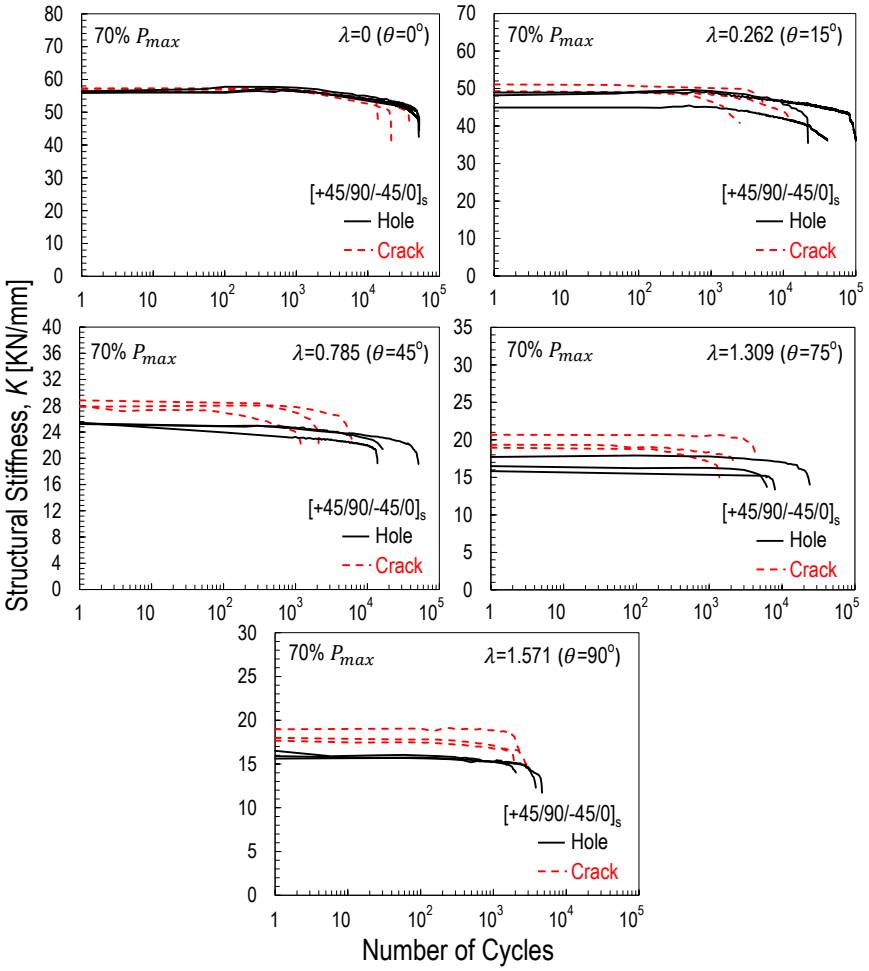

Figure 9.13: Evolution of structural stiffness vs. number of cycles measured during the multi-axial fatigue tests (70% P_{max}) on the $[+45/90/-45/0]_s$ specimens with a 10 mm central crack and a 10 mm hole.

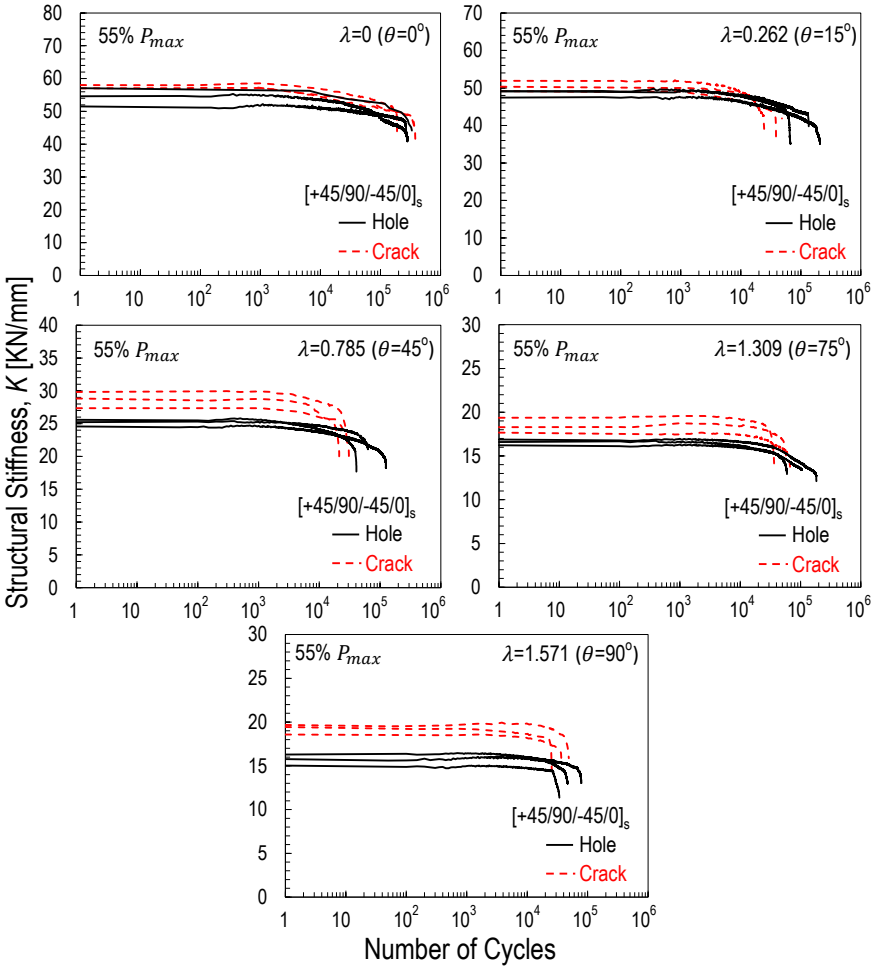

Figure 9.14: Evolution of structural stiffness vs. number of cycles measured during the multi-axial fatigue tests (55% P_{max}) on the $[+45/90/-45/0]_s$ specimens with a 10 mm central crack and a 10 mm hole.

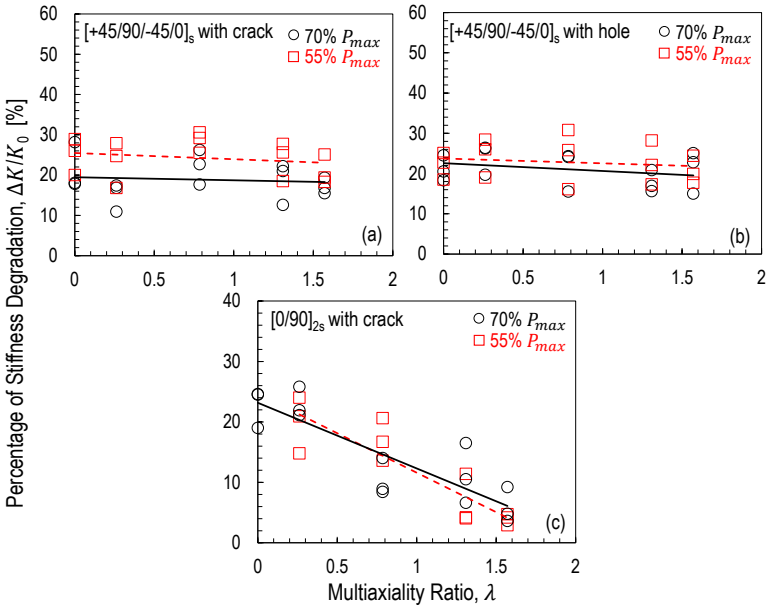

Figure 9.15: The percentage of stiffness degradation right before catastrophic failure vs. multiaxiality ratio for notched quasi-isotropic and cross-ply specimens. Note that K_0 is the initial stiffness.

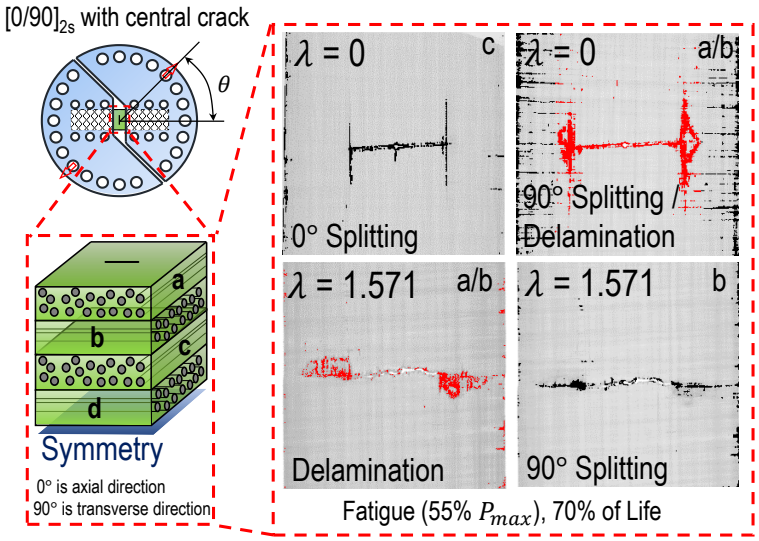

Figure 9.16: Analysis of main fatigue damage mechanisms before final failure by micro-computed tomography. Comparison on fatigue damage in $[0/90]_{2s}$ specimens weakened by a 18 mm central crack for multiaxiality ratio $\lambda = 0$ and $\lambda = 1.571$. Note that the original colors of the images were inverted for a better visualization on the damage.

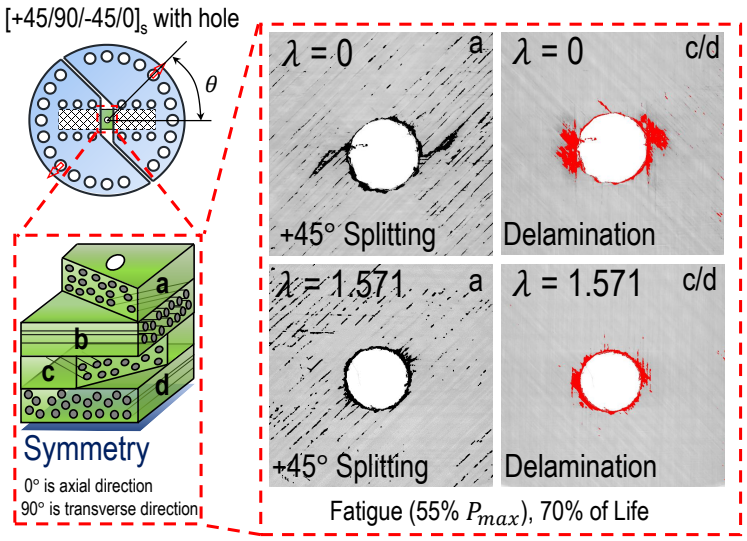

Figure 9.17: Analysis of main fatigue damage mechanisms before final failure by micro-computed tomography. Comparison on fatigue damage in $[+45/90/-45/0]_s$ specimens weakened by a 10 mm open hole for multiaxiality ratio $\lambda = 0$ and $\lambda = 1.571$. Note that the original colors of the images were inverted for a better visualization on the damage.

9.3.3.2 S-N curve vs. multiaxiality ratio

To gain a better understanding of the fatigue behavior of notched laminates under various multiaxiality ratios, S-N curves were constructed by leveraging the fatigue tests with three different loading cases (70%, 55% and 40% of P_{max}). As illustrated in Figure 9.18, the peak nominal normal stress is plotted as a function of number of cycles in the semi-logarithmic coordinate for notched specimens. In these plots, the slopes of S-N curves decrease as multiaxiality ratio increases which indicates that the deterioration of the fatigue behavior happens severely when the loading condition transits from tension to shear. This phenomenon is consistent with the previous experimental investigations on both tabular and cruciform specimens featuring a circular hole [38–40, 199, 234, 235]. It is worth mentioning here that, for specimens under the fatigue loading of pure shear ($\lambda = 1.571$), the slope of S-N curve is zero due to the definition of the multiaxiality ratio. Thus, additional S-N curves are plotted

in Figure 9.18 for these specific cases.

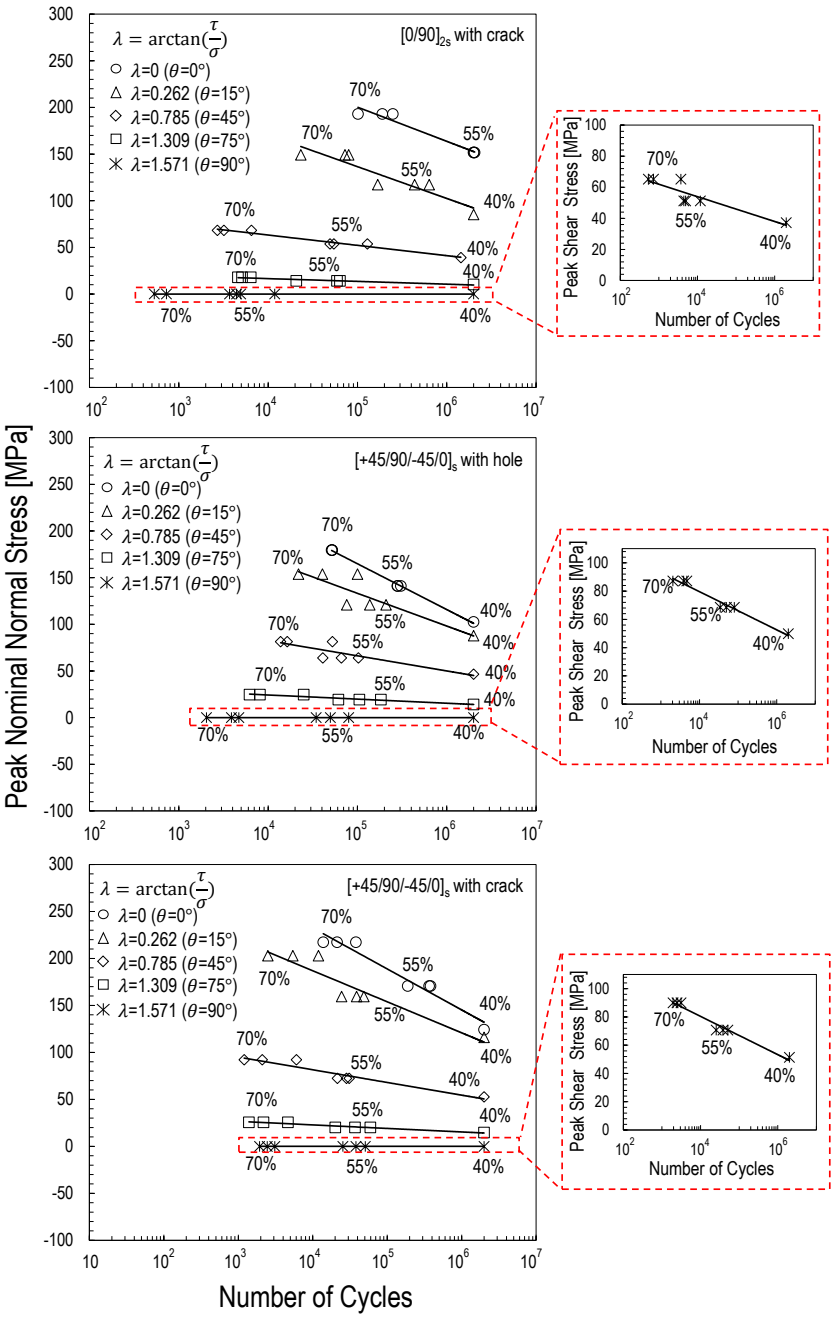

Figure 9.18: S-N curves vs. multiaxiality ratio measured from the multi-axial fatigue tests on notched quasi-isotropic and cross-ply specimens.

Multiaxiality Ratio	Percentage of P_{max}	$[0/90]_{2s}$ (crack)	$[+45/90/\text{-}45/0]_s$ (crack)	$[+45/90/\text{-}45/0]_s$ (hole)
	70 %	1.8×10^5	2.4×10^4	5.2×10^4
0	55 %	2×10^6	3.1×10^5	2.9×10^5
	40 %	2×10^6	2×10^6	2×10^6
	70 %	5.8×10^4	6617	5.4×10^4
0.262	55 %	4.1×10^5	3.7×10^4	1.4×10^5
	40 %	2×10^6	2×10^6	2×10^6
	70 %	4133	3117	2.8×10^4
0.785	55 %	7.7×10^4	2.7×10^4	7×10^4
	40 %	1.4×10^6	2×10^6	2×10^6
	70 %	5367	2741	1.3×10^4
1.309	55 %	4.8×10^4	3.9×10^4	1.2×10^5
	40 %	2×10^6	2×10^6	2×10^6
	70 %	1664	2493	3545
1.571	55 %	7070	3.8×10^4	5.5×10^4
	40 %	2×10^6	2×10^6	2×10^6

Table 9.3: Average fatigue lifetimes measured from the multi-axial fatigue tests on both notched cross-ply and quasi-isotropic laminates. Note that two million cycles represents run-out.

As far as the fatigue life is concerned, as illustrated in Figure 9.19 and tabulated in Table 9.3, the number of cycles to failure decreases with increasing the multiaxiality ratio for both two fatigue loading conditions (70% and 55% of P_{max}). This cause the decrease of the slopes of S-N curves as mentioned in the forgoing discussion. Furthermore, it was shown in Figure 9.19a that the endurance limit (2 million cycles) of notched cross-ply $[0/90]_{2s}$ specimens under the fatigue loading of pure tension can be achieved approximately when 55% of P_{max} is applied as a peak load in the cyclic load. This is much higher than the condition for the forgoing unnotched specimens featuring the same layup under tensile fatigue loading condition. This is probably due to the reduced stress concentration of a central crack caused by splitting in 0° plies occurring at the notch tip during the fatigue [236–238]. However, the fatigue loading condition for the endurance limit of notched cross-ply $[0/90]_{2s}$ specimens

at multiaxiality ratios except for pure tension is about 40% of P_{max}, the similar condition for notched quasi-isotropic $[+45/90/-45/0]_s$ specimens at all the investigated multiaxiality ratios in order to reach the endurance limit during the fatigue.

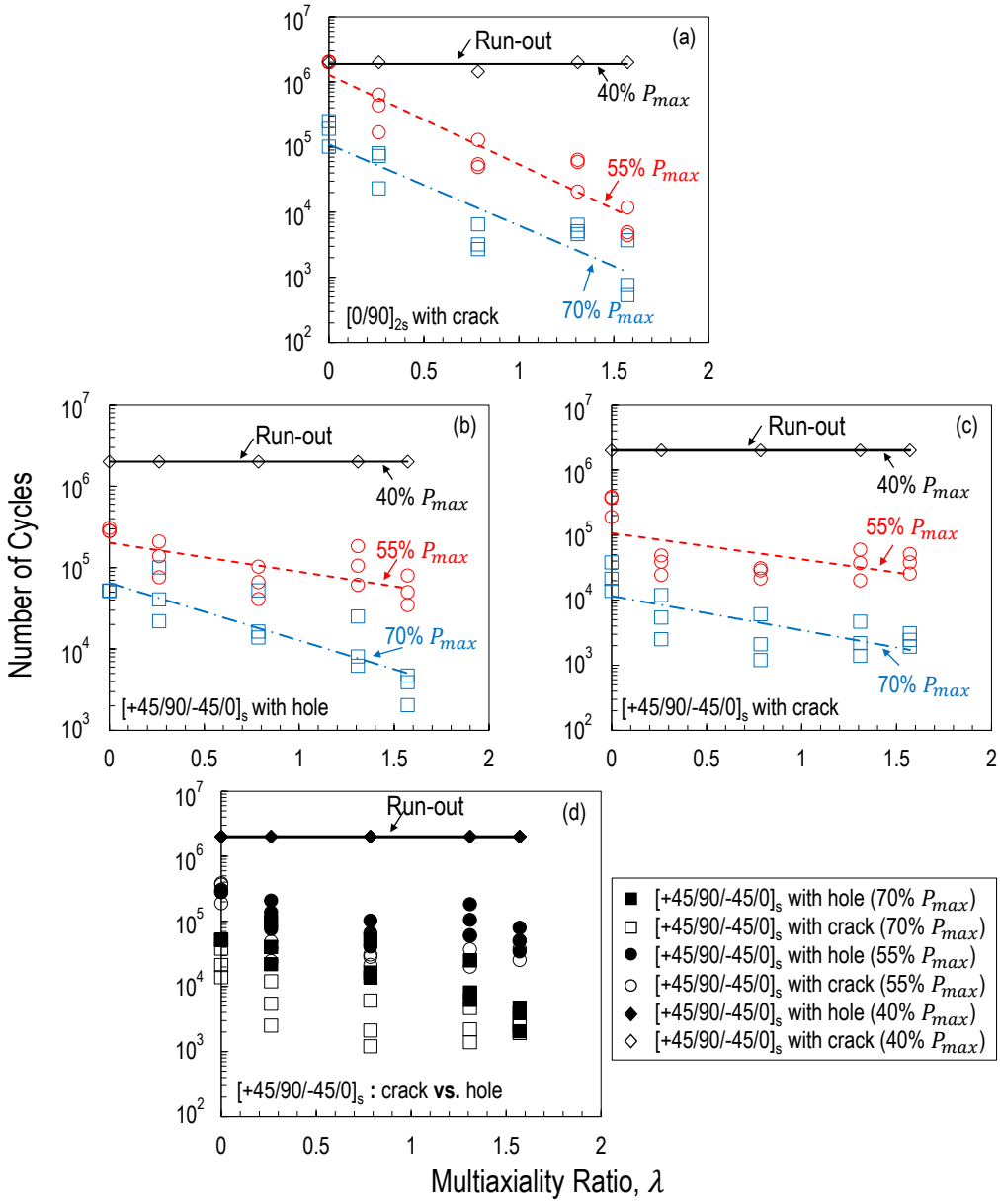

Figure 9.19: Number of cycles to failure vs. multiaxiality ratio for notched quasi-isotropic and cross-ply specimens.

9.4 Conclusions

1. For notched laminates under multi-axial quasi-static loading, the stress-strain behavior is characterized by a significant non-linearity. This phenomenon becomes more and more significant with increasing shear load components due to the emergence of diffused, sub-critical matrix micro-cracking and delamination. This conclusion is supported by micro-computed tomography analysis;

2. The multiaxiality ratio influences significantly also the post-peak behavior. Catastrophic failure due to snap-back instability occurs when the specimens are subjected to tension-dominated loading whereas the post-peak behavior becomes stable and strain softening becomes evident in the case of shear-dominated loading;

3. Leveraging the multi-axial data, failure envelops in terms of peak nominal normal and shear stresses were constructed. Interestingly, the quasi-isotropic laminates featuring an open hole of diameter a_0 exhibited a lower strength compared to specimens weakened by a central crack with length equal to a_0. This phenomenon depends on the evolution of the Fracture Process Zone (FPZ) as a function of the multiaxiality ratio and specimen size;

4. The forgoing quasi-static data are in contrast to the results of the fatigue tests showing the central crack case being the most critical. This structural phenomenon may be due to a different evolution of the Fracture Process Zone (FPZ) in quasi-static regime compared to fatigue. This aspect is particularly important for structural design since it shows that failure under quasi-static loading and fatigue can occur by a completely different damage progression. The efficient fatigue design of composite structures demands the formulation of damage models that can capture such evolution in the context of the loading configuration, stacking sequence, and structure size and geometry;

5. The evolution of the structural stiffness degradation in notched quasi-isotropic and

cross-ply laminates is substantially different. While the structural stiffness exhibits a similar amount of degradation before catastrophic failure for quasi-isotropic laminates at different multiaxiality ratios, the stiffness of cross-ply laminates deteriorates about 20% before catastrophic failure for a multiaxiality ratio $\lambda = 0$ but only 5% degradation for a multiaxiality ratio $\lambda = 1.571$;

6. The S-N curves clearly shows the detrimental effects of the shear load component on the fatigue life of all the investigated notched laminates since the slopes of S-N curves decrease with increasing the shear load component. This is mainly due to the emergence of the damage (e.g. delamination, fiber kinking, micro-bucking, etc) induced by the shear load component which is even critical compared to the matrix cracking in the tension-dominated loading conditions and the details will be shown in the next chapter;

7. On the other hand, the conditions to achieve the endurance limit are approximately the same (40% of P_{max}) for both notched and notch-free laminates at different multiaxiality ratios except for notched cross-ply laminates under tensile fatigue loading. In this case, the endurance limit is about 55% of P_{max} which is much higher than the one of notch-free laminates featuring the same layup. This is probably due to the reduced stress concentration of a central crack caused by splitting occurring at the notch tip during the fatigue since the development of splitting is the main damage mechanism for this loading case.

Chapter 10

DAMAGE MECHANISMS OF FIBER-REINFORCED POLYMER COMPOSITES UNDER MULTI-AXIAL LOADS

This chapter focuses on the experimental investigation on the morphological characteristics of the sub-critical damage in polymer matrix composites (e.g. matrix cracking, delamination, fiber kinking, etc.) under multi-axial quasi-static and cyclic loading conditions. By leveraging the synergistic approach combining several damage evaluation methods, the detailed damage mechanisms of the investigated fiber-reinforced composites with respect to the multi-axiality ratio were revealed. In addition, the common aspects and the minor differences between quasi-static and cyclic loading on the mechanical behavior of fiber-reinforced composites were also clarified.

10.1 Damage inspection techniques

A range of non-destructive inspection techniques has been developed and applied in the last few decades. The most attractive techniques include acoustic emission [239–243], infrared thermography [244–248], ultrasonic C-scan [249], Digital Imaging Correlation [250–252] and X-ray micro-computed tomography [253–259]. An analysis to combine the mechanical behavior of the materials with the damage evaluation via the forgoing useful tools promotes a better understanding on the fracturing behavior of composite structures under a variety of loading conditions. This is a condition of utmost importance for the development of safe and reliable designs and certification guidelines.

Among these techniques, acoustic emission method is widely used for monitoring damage initiation. An excellent investigation on the initiation of transverse cracking and delamination in textile composite under uni-axial tensile test was provided by Lomov *et al.* [241].

Similar studies were reported on the unidirectional and woven composites by Silversides *et al.* [240].

However, infrared thermography and ultrasonic C-scan are typically employed to have a rough estimation of the damage progression in composite structures. A noticeable example was provided by Meola and Carlomagno [245] who evaluated impact damage in Glass Fiber Reinforced Polymer (GFRP) leveraging the thermographic technique. Thanks to this method, the impact damage progression throughout the thickness of the laminates was successfully reconstructed. By conducting an ultrasonic inspection on the damaged specimens, Scarponi and Briotti [249] identified significant development of delamination in thermoset polymer reinforced by various types of fibers.

Although the forgoing techniques led to a remarkable progress in the damage characterization, the identification of individual damage types is still not clear since the damage analyzed using the forgoing inspection tools is usually homogenized. In this context, microscopic techniques (Optical and Scanning Electron Microscopy) are extensively used to visualize different damage types in specimens. Carraro *et al.* [260], for instance, conducted an optical microscopic inspection which was capable of capturing the delamination induced by transverse cracking in cross-ply laminates under tensile fatigue loading. On similar grounds, a micro-damage study leveraging Scanning Electron Microscopy (SEM) was provided by Nguyen *et al.* [261] who identified shear hackles between the fibers in specimens featuring $[+45/-45]_{4s}$ layup under uni -axial tensile test. However, these techniques can only provide a local visualization of a detailed damage morphology since the specimens must be cut into a small portion which can be properly operated by microscopic techniques.

Thanks to the emergence and development of X-ray micro-computed tomography (μ-CT), a detailed damage morphology throughout the entire composite structure can be obtained even under an in-situ inspection test. An interesting study was provided by Yu *et al.* [254] who investigated the damage evolution in 3D woven composite under tensile fatigue loading. It was concluded that the dominating damage mechanism before final failure is the debonding cracks spreading along the interface between binder yarns and matrix. By leveraging μ-

CT technique, the growth of different type of damage was also successfully quantified as a function of fatigue lifetime.

A further step towards an even more insightful damage analysis requires a synergistic approach combining μ-CT technique and other aforementioned methods. In this way, the following sections present a comprehensive damage analysis via X-ray micro-computed tomography and Digital Imaging Correlation techniques on notched quasi-isotropic $[+45/90/-45/0]_s$ and cross-ply $[0/90]_{2s}$ laminates under multi-axial quasi-static and fatigue loading. 3D woven composites in presence of blunt notch under multi-axial quasi-static loading were also studied in this work. Thanks to the synergistic approach, a detailed analysis of the damage mechanisms and quantification of damage evolution was achieved. This result, which is of utmost importance for the development and validation of fatigue computational models for notched composite structures under multi-axial loading, has never been obtained before.

10.2 Damage evaluation strategy

To study the damage evolution of notched laminates under multi-axial tests, specimens with the same dimensions but featuring different types of notches as described in the previous sections were prepared. The detailed description on the manufacturing and testing method can be found in the work by Qiao *et al.* [229]. The procedure of damage evaluation leveraging Digital Image Correlation (DIC) and X-ray micro-computed tomography (μ-CT) is illustrated in Figure 10.1 and described in the following sections.

10.2.1 Digital Image Correlation (DIC)

The strain distribution of notched laminates was investigated by using an open source DIC system programmed in MATLAB software developed at the Georgia Institute of Technology [218, 219]. To this end, specimens were painted white and then speckled black with a refinement pattern close to the edge of hole and notch tip. This is significantly important to guarantee that enough speckles can be used for DIC analysis to describe the strain field at that location. A recording of videos with a frame rate of 30 fps for speckled specimens

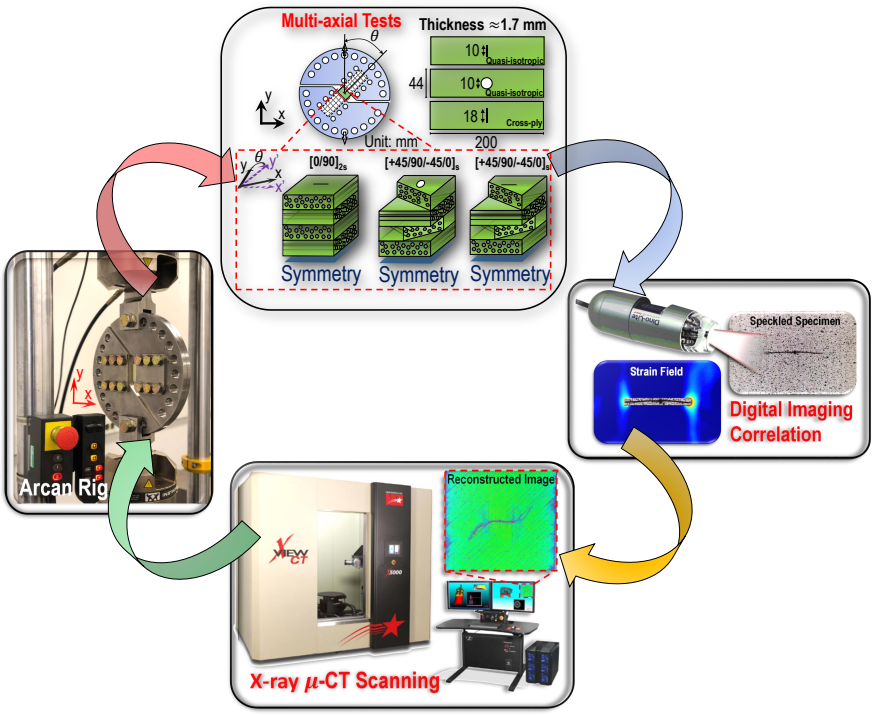

Figure 10.1: Notched specimen geometries and damage evaluation leveraging Digital Imaging Correlation (DIC) and X-ray micro-computed tomography (μ-CT).

was analyzed at roughly 97% of total quasi-static or fatigue life. The total quasi-static life corresponded to its final catastrophic failure whereas the total fatigue life corresponded to its lifetime to failure and the percentage of this life represented its performance at the peak load of applied cyclic load (55% of quasi-static critical load). The loading situation for the specimens analyzed by DIC is summarized in Table 10.1 and the details can be found in [229]. The moments analyzed for 3D woven composites can be found in Figures 10.18 and 10.19.

10.2.2 X-ray micro-computed tomography (μ-CT)

The multi-axial tests were stopped and notched specimens were unloaded and demounted from the testing system for the observation of the sub-critical damage by means of a NSI X5000 X-ray micro-tomography scanning system [262]. A X-ray tube setting of 90 kV in

voltage and 220 μA in current was used in the analyses. It is worth mentioning here that μ-CT scanning was also performed before multi-axial tests to guarantee that no damage was induced by the manufacturing of the specimen. To have a better understanding of the damage evolution under multi-axial tests, damaged specimens taken from the multi-axial quasi-static tests were analyzed at 90% and even later stage of the entire life whereas the ones taken from the multi-axial fatigue tests were analyzed at 40% and 70% of the entire life. It is worth mentioning here that the total quasi-static life corresponded to its life reaching the critical load whereas the total fatigue life corresponded to its lifetime to failure. The loading situation for the specimens analyzed by μ-CT is summarized in Table 10.2 and the details can be found in [229]. The moments analyzed for 3D woven composites can be found in Figures 10.18 and 10.19.

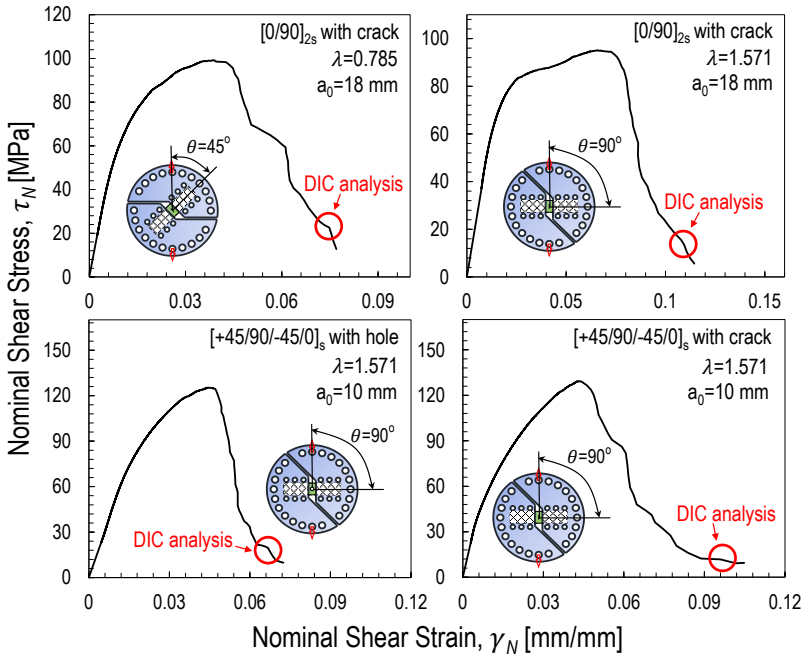

Figure 10.2: Nominal shear stress vs. nominal shear strain for representative notched specimens. The detailed description of this figure can be found in section 9.3.2 . This figure corresponds to Table 10.1 explaining the loading situations analyzed by DIC for the case that the specimen has stable post-peak behavior.

DIC		Quasi-static	Fatigue	
Layups	Multiaxiality Ratio	Load for Analysis (KN)	Peak Value in Cyclic Load (KN)	Cycles for Analysis
$[0/90]_{2s}$ with crack	0	11.95	6.78	1.94×10^6
	0.785	See Fig.10.2	3.38	7.52×10^4
	1.571	See Fig.10.2	2.29	6.86×10^3
$[+45/90/-45/0]_s$ with hole	0	14.55	8.25	2.81×10^5
	0.785	9.33	5.29	6.78×10^4
	1.571	See Fig.10.2	4.01	5.31×10^4
$[+45/90/-45/0]_s$ with crack	0	17.80	10.09	3.03×10^5
	0.785	10.44	5.92	2.61×10^4
	1.571	See Fig.10.2	4.09	3.69×10^4

Table 10.1: Load and number of cycles for DIC analysis of investigated notched specimens at 97% of total quasi-static or fatigue life. This table includes the foregoing information for three multiaxiality ratios. Note that the text "See Fig.2" in the table represents the case that the specimen has stable post-peak behavior.

μ-CT		Quasi-static		Fatigue		
Layups	Multiaxiality Ratio	Percentage of Life	Load for Analysis (KN)	Peak Load in Cyclic Load (KN)	Percentage of Life	Cycles for Analysis
$[0/90]_{2s}$ with crack	0	90%	11.09	6.78	40%	8.00×10^5
		95%	11.71		70%	1.40×10^6
	0.785	90%	5.52	3.38	40%	3.10×10^4
		95%	5.83		70%	5.43×10^4
	1.571	90%	3.75	2.29	40%	2.83×10^3
		95%	3.96		70%	4.95×10^3
$[+45/90/-45/0]_s$ with hole	0	90%	13.50	8.25	40%	1.16×10^5
		95%	14.25		70%	2.03×10^5
	0.785	90%	8.66	5.29	40%	2.80×10^4
		98%	9.43		70%	4.89×10^4
	1.571	90%	6.55	4.01	40%	2.19×10^4
		98%	7.13		70%	3.83×10^4
$[+45/90/-45/0]_s$ with crack	0	90%	16.52	10.09	40%	1.25×10^5
		95%	17.43		70%	2.19×10^5
	0.785	90%	9.69	5.92	40%	1.08×10^4
		95%	10.23		70%	1.88×10^4
	1.571	90%	6.69	4.09	40%	1.52×10^4
		98%	7.28		70%	2.67×10^4

Table 10.2: Load and number of cycles for μ-CT analysis of investigated notched specimens at selected percentage of total quasi-static or fatigue life. This table includes the foregoing information for three multiaxiality ratios.

A dye penetrant was used as a supplement to improve the contrast of damage in the X-ray images [263–265]. Before conducting the scanning, the specimens were soaked approximately one day in the dye penetrant mixture containing zinc iodide powder (250 g), isopropyl alcohol (80 ml), Kodak photo-flow solution (1 ml) and distilled water (80 ml). The sub-critical damage in each ply and interface were identified by slicing through the reconstructed 3D images of the specimens via the softwares ImageJ [266] and ParaView [267].

10.3 Digital Image Correlation (DIC) Analysis

The sub-critical, distributed damage occurring under fatigue loading of notched composite structures generally leads to a local reduction of the material stiffness with consequent increase of the local strain. Accordingly, to have a qualitative idea of the overall damage distribution notched $[0/90]_{2s}$ and $[+45/90/-45/0]_s$ specimens were analyzed through DIC as described in section 10.2.

As illustrated in Figure 10.3 which compares the maximum principal strain distribution of the quasi-static and fatigue loading, the overall damage distribution under fatigue loading appears to be more diffuse compared to the quasi-static case. A similar phenomenon was found by Fujii *et al.* [38–40] who tested tabular specimens featuring a circular hole under the multi-axial fatigue loading of tension and torsion. This result is an indication of a larger non-linear Fracture Process Zone (FPZ) in the specimens subject to fatigue loading. It is worth mentioning that the maximum principle strains were normalized against their maximum values in the area of interest in order to have a comparison between quasi-static and fatigue loading condition. In fact, the focus was not on the magnitude of the strain field but the overall damage distribution.

However, the critical magnitude in the maximum principle strain field for quasi-isotropic specimens featuring a central hole under multi-axial tests provides an insightful information on the quasi-static and fatigue fracturing behavior. As can be noted in Figure 10.4, the critical magnitude of the maximum principle strain in fatigue case is significantly lower than the one in quasi-static case almost before catastrophic failure. This result is an indication

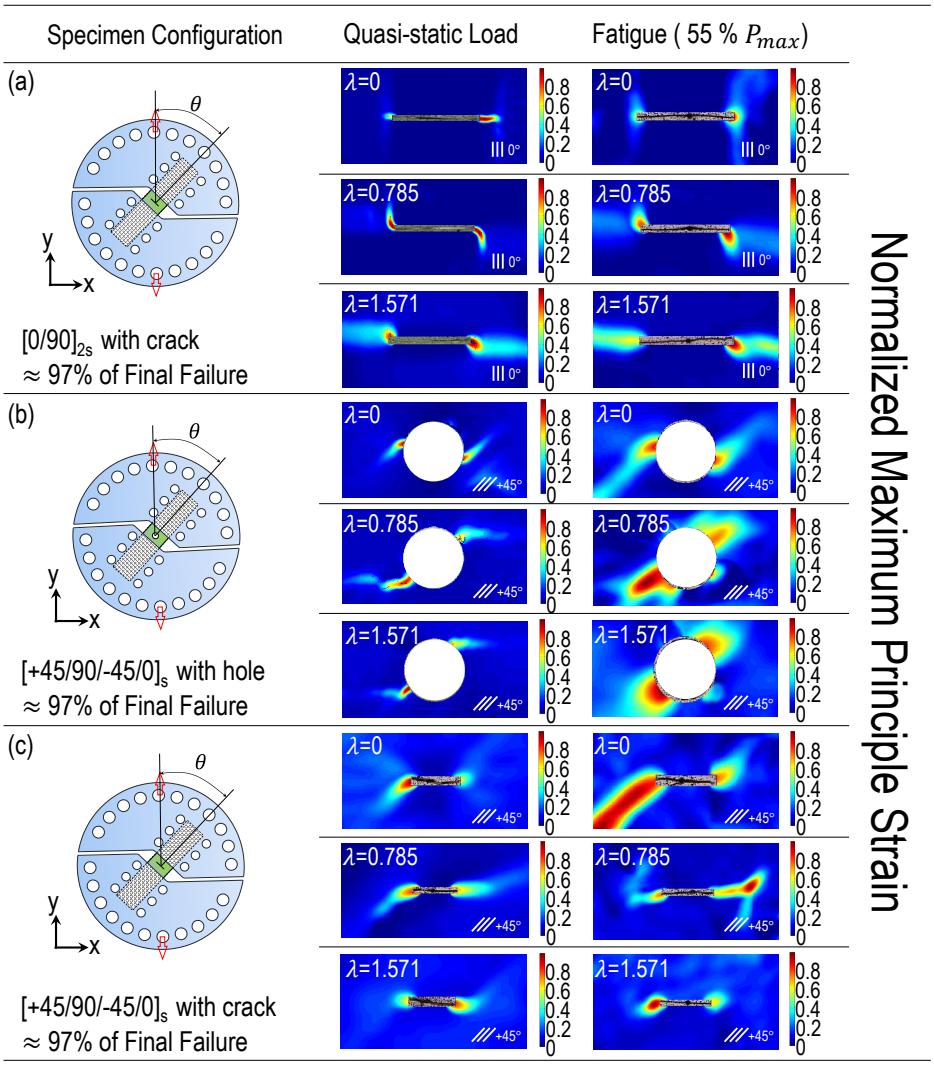

Figure 10.3: Digital Imaging Correlation (DIC) analysis of investigated notched specimens at 97% of total quasi-static or fatigue life. This figure compares three multiaxiality ratios. From the contour plots of the normalized maximum principle strain, it can be noted that the region of high deformation in fatigue is generally more spread compared to quasi-static loading. This is an indication that fatigue damage is generally more distributed than its quasi-static counterpart.

of substantially different failure criteria for quasi-static and fatigue case which is typically reported in fatigue fracturing behavior of thermoset polymers showing that the Mode I critical stress intensity factor in fatigue case is generally lower than the one in quasi-static

case [180, 268, 269].

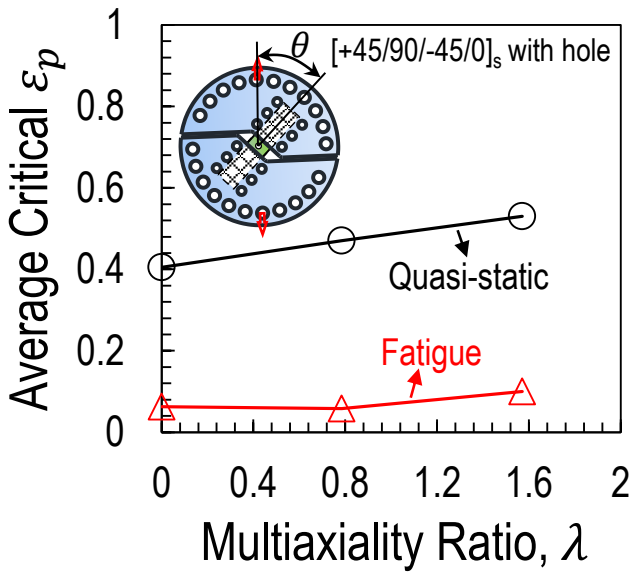

Figure 10.4: The evolution of critical maximum principle strain at 97% of final failure for the specimen weakened by a central hole as a function of multiaxiality ratio. The graph compares quasi-static and fatigue results. Note that ε_p refers to the maximum principle stress and these values in the figure were obtained by averaging the results over at least three specimens.

On the other hand, before moving to the following section on the investigation of damage mechanisms via μ-CT technique, the fracturing features can be roughly known based on the overall strain distribution leveraging DIC. As can be noted in Figure 10.3, the region of high deformation for notched laminates at various multiaxiality ratios does not show significant differences in terms of shape and location for quasi-static and fatigue case. For notched cross-ply laminates as shown in Figure 10.3a, the specimen under pure tension is characterized by a region of high deformation in 0° plies at the notch tip whereas the one under pure shear features a noticeable damage band in 90° plies ahead of the notch. This corresponds to splitting and fiber kinking for pure tension and pure shear case respectively. For notched quasi-isotropic laminates as shown in Figures 10.3b-c, the specimens at various multiaxiality

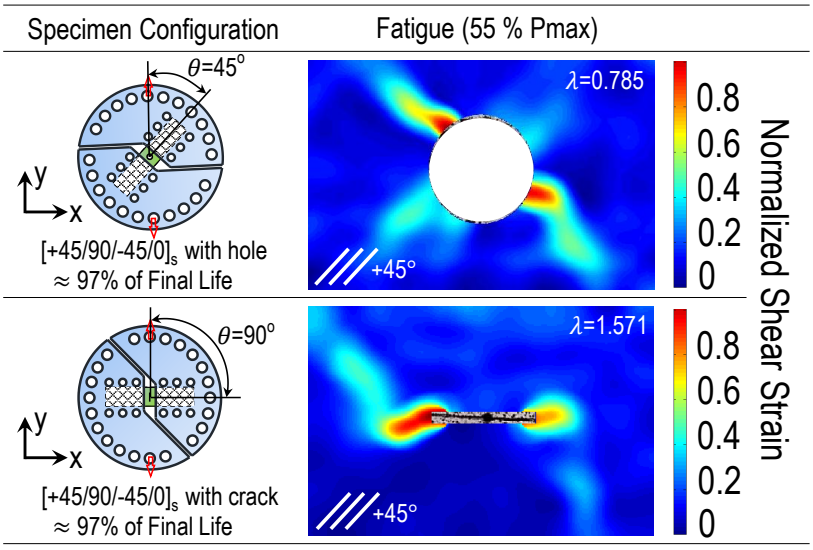

Figure 10.5: Digital Imaging Correlation (DIC) analysis of notched quasi-isotropic specimens for multiaxiality ratio $\lambda = 0.785$ and $\lambda = 1.571$ at 97% of total fatigue life. Note that the shear strain was normalized against its maximum value in the area of interest.

ratios are mainly characterized by a highly-deformed region in +45° plies in front of the notch which is associated to significant splitting. In addition to this, a highly-deformed region due to shear strain almost perpendicular to the +45° plies was observed for the specimens under shear-dominated loading as shown in Figure 10.5. This indicates that the +45° plies are under compression leading to the potential micro-buckling of the fibers.

10.4 Quantitative analysis of damage mechanisms

To shed more light on the characteristics of the fracturing morphology of notched laminates under multi-axial quasi-static and fatigue loading, representative damaged specimens at various multiaxiality ratios selected from three tested specimens were analyzed leveraging X-ray μ-CT using the parameters described in the section 10.2.2. It is worth mentioning that, for each loading configuration, at least three tests were conducted and the results were found to be very consistent in terms of both mechanical behavior and damage morphology.

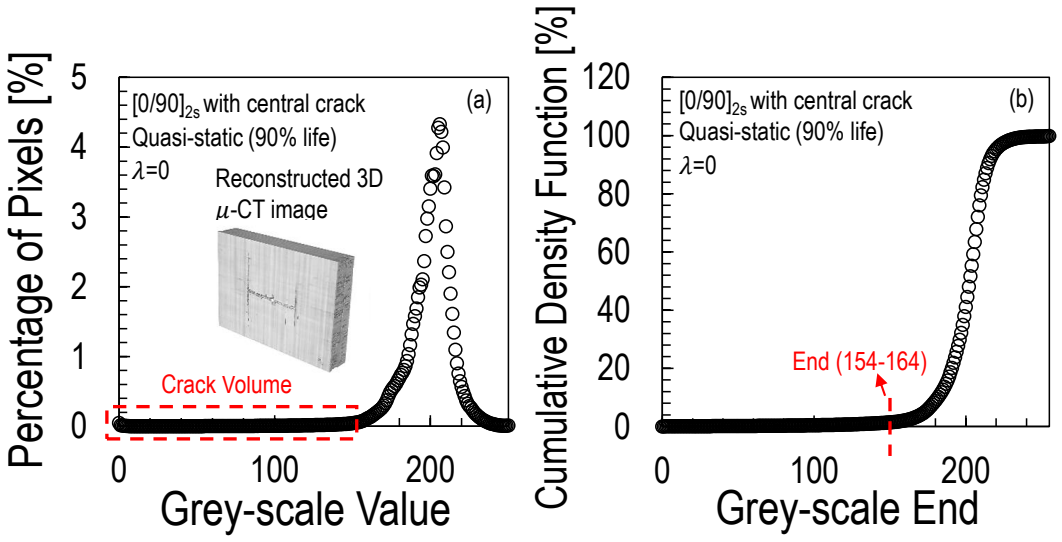

Figure 10.6: (a) Typical graph of the percentage of pixels vs. grey-scale value in the gauge volume of the $[0/90]_{2s}$ specimens weakened by a 18 mm central crack for a multiaxiality ratio $\lambda = 0$ based on the reconstructed 3D image obtained by micro-computed tomography; (b) The evolution of cumulative density function of grey-scale distribution as a function of grey-scale end. All the grey-scale values lower than this end was considered as the damage. In this case, the grey-scale end (159) was selected and ± 5 was considered to account for the measurement errors on the accuracy of this selective end value.

The use of micro-computed tomography was particularly important to guarantee that no additional damage was created during the damage visualization process. Thanks to this technique, the sub-critical damage can be observed through the reconstructed 3D images in order to have a quantitative comparison on the crack volume and delamination area of the specimens under multi-axial tests. With the supplement of the dye penetrant, the sub-critical damage can be easily visualized as illustrated in Figures 10.8-10.16. Thanks to the great contrast provided by the use of the dye penetrant, the analysis of the grey-scale value can be used to roughly estimate the crack volume and delamination area of the specimen. Figure 10.6a shows an example of such analysis for a cross-ply specimen featuring a central crack under the quasi-static loading in pure tension. In this plot, the lower grey-scale values

represent the sub-critical damage in the gauge volume of the specimen while the higher grey-scale values, constituting the most part of the percentage of pixels, characterize the remaining part of the gauge volume of the specimen. It is worth mentioning here that there are roughly 90 reconstructed images throughout the thickness of the specimen leading to about 2.5×10^7 pixels for the gauge volume of the specimen. To quantify the sub-critical damage, as illustrated in Figure 10.6b, the cumulative density function of grey-scale distribution up to a range of grey-scale end was treated as crack volume to provide a safe estimation. This range was based on a reference value with the upper and lower bounds of 5 grey-scale values while this reference value was about 144 to 179 for different specimens and reasonably taken on the location of the specimen where no significant damage was observed.

10.4.1 $[0/90]_{2s}$ *laminate with a central crack*

10.4.1.1 Fatigue loading condition

(a) Mechanism A

In the case of specimens subjected to tension-dominated loading conditions ($\lambda = 0, 0.262$), the dominant mechanisms before sudden failure are the splitting in 0° plies at the notch tip and the splitting in 90° plies. The final failure is triggered by the additional splitting in 0° plies away from the notch tip and the breakage of 0° fibers. As illustrated in Figure 10.8, the damage evolution as a function of fatigue lifetime for mechanism A can be summarized as follows:

(1) splitting initiates in 90° plies (Fig. 10.8D);

(2) splitting initiates in 0° plies at notch tip (Fig. 10.8D);

(3) splitting develops in the corresponding plies (Fig. 10.8E);

(4) a small amount of delamination between 0°/90° plies starts to initiate. (Fig. 10.8E);

(5) additional splitting in 0° plies away from the notch tip happens simultaneously with the breakage of 0° fibers (Fig. 10.8F).

(b) Mechanism B

When the multiaxiality ratio $\lambda = 0.785, 1.309$, a mix of nominal normal and shear stresses is applied on specimens and failure behavior follows Mechanism B. In this case, the dominant mechanism transits from splitting to a combination of delamination and splitting. The final failure happens with the growth of splitting in 0° plies at the notch tip and the delamination between 0° and 90° plies. As illustrated in Figure 10.9, the damage evolution of mechanism B can be summarized by the following steps:

(1) splitting initiates in 90° plies (Fig. 10.9D);
(2) splitting initiates in 0° plies at notch tip simultaneously with the formation of delamination between 0° and 90° plies (Fig. 10.9D);
(3) splitting and delamination develop in and between the corresponding plies (Fig. 10.9E);
(4) fibers in 0° plies start to kink due to the shear stress (Fig. 10.9E);
(5) delamination between 0° and 90° plies grows together with the significant splitting at notch tip (Fig. 10.9E-F).

(c) Mechanism C

When the specimens are only subjected to pure shear loading ($\lambda = 1.571$), the dominant mechanisms are the delamination between 0° and 90° plies and then fiber kinking in 0° plies. The final failure is due to the unstable growth of the inter-laminar crack enabling the splitting in 0° plies at notch tip. As illustrated in Figure 10.10, the damage evolution of mechanism C consists of the following phases:

(1) a small amount of splitting initiates in 90° plies at notch tip (Fig. 10.10D);
(2) delamination initiates between 0° and 90° plies (Fig. 10.10D);
(3) fibers in 0° plies start to kink significantly due to the shear stress (Fig. 10.10E);
(4) delamination develops between the corresponding plies (Fig. 10.10E);
(5) delamination grows dramatically and drives the significant splitting in 0° plies

at notch tip (Fig. 10.10E-F).

10.4.1.2 Quantitative analysis: fatigue vs. quasi-static loading

The crack volume and delamination area as a function of the percentage life were plotted in Figures 10.17a-d for specimens under quasi-static and fatigue loading. As illustrated in Figure 10.17c, in the fatigue case, the specimens following mechanism B and C feature larger delamination area compared to the specimens following mechanism A at 70% of total fatigue life, with 1.6% for $\lambda = 0.785$ and 2% for $\lambda = 1.571$ but only 1% for $\lambda = 0$. This is an indirect evidence of the foregoing damage mechanisms showing that delamination contributes to most of the energy dissipation in notched cross-ply laminates under shear-dominated loading. However, this is not the case for total crack volume in specimens at the corresponding life as shown in Figure 10.17a, with the lowest value (2.2%) featuring $\lambda = 1.571$ but 4.1% for $\lambda = 0$ and 0.785. This lower crack volume explains the less pronounced stiffness degradation of specimens under the fatigue of pure shear as shown in [229] and is associated to the significant reduction of splitting in 90° plies.

With the comparison to the fatigue case, similar damage mechanisms were observed in the case of quasi-static loading for all the multiaxiality ratios as shown in Figures 10.8-10.10. However, the overall sub-critical damage during quasi-static loading is less diffused, consistent with the DIC results discussed in section 10.3 and the quantitative analysis via $\mu-$CT. In Figures 10.17a-d, for all the multiaxiality ratios, both crack volume and delamination area for the quasi-static case above 90% of total quasi-static life are significantly less than the fatigue case at even lower percentage of the life. Only about 2.4% crack volume and 0.7% delamination area in average for different multiaxiality ratios were observed at 95% of total quasi-static life. Notwithstanding this, these sub-critical damage grows rapidly close to the end of total quasi-static life leading to the catastrophic failure of the specimen. It is worth mentioning here that the specimen only at 90% and even later stage of its quasi-static life was prepared for the quantitative analysis due to the less pronounced damage at the early stage of the quasi-static loading and the difficulties for the damage visualization.

10.4.2 $[+45/90/-45/0]_s$ laminate with an open hole

10.4.2.1 Fatigue loading condition

(a) Mechanism A

In the case of specimens subjected to tension-dominated loading conditions ($\lambda = 0, 0.262$), the dominant mechanisms before the dramatic failure are the delamination between all the plies except for the middle plies and the significant splitting in $\pm$ 45° plies. These damage is not the only contribution to the catastrophic failure and the breakage of 0° piles also plays a pivotal role. As illustrated in Figure 10.11, the damage evolution as a function of fatigue lifetime for mechanism A can be summarized in the following:

(1) splitting initiates in 90° plies at notch tip (Fig. 10.11D);
(2) splitting initiates in 0° and $\pm$ 45° plies at notch tip (Fig. 10.11D);
(3) delamination between the foregoing plies initiates (Fig. 10.11D);
(4) splitting and delamination develop in and between the corresponding plies (Fig. 10.11E);
(5) splitting in $\pm$ 45° plies grows significantly and delamination reaches critical condition accompanying the emergence of 0° plies breakage (Fig. 10.11E-F).

(b) Mechanism B

The specimens fail following Mechanism B when the shear load component is involved ($\lambda = 0.785, 1.309$ and 1.571). In contrast to mechanism A, a significant reduced delamination between all the plies was observed. On the other hand, the direction of shear loading was established so that the +45° plies are in compression while the -45° plies are in tension. Considering the fact that the compressive strength of an unidirectional ply is generally lower than its tensile strength, the dominant mechanism is the micro-buckling in +45° plies and the final failure is triggered by the significant growth of the micro-buckling due to the compression at the very late stage of the fatigue life. The paths of the micro-buckling usually start in a straight way at the two ends of the hole but not on the same line and then additional micro-

buckling paths almost perpendicular to the +45° plies happen. These micro-buckling paths are usually in collaboration with the significant splitting in +45° plies as mentioned in the foregoing discussion of DIC analysis in Section 10.3. Similar conclusions were drawn by Tan *et al.* [217, 270] on the quasi-static fracturing behavior of notched Carbon Fiber Reinforced Polymer (CFRP) laminates. As illustrated in Figures 10.12-10.13, the damage evolution of mechanism B can be summarized in the following:

(1) splitting initiates in 90° plies at notch tip (Fig. 10.12D) ;
(2) splitting initiates in 0° and ± 45° plies at notch tip (Fig. 10.12D);
(3) a small amount of delamination between 90° and ± 45° plies starts to initiate (Fig. 10.12D);
(4) splitting and delamination develop in and between the corresponding plies (Fig. 10.12E);
(5) micro-buckling initiates in +45° plies at notch tip (Fig. 10.12F);
(6) micro-buckling in +45° plies grows unstably in collaboration with the significant splitting in +45° plies (Fig. 10.12F).

10.4.2.2 Quantitative analysis: fatigue vs. quasi-static condition

The similar quantitative analysis on the sub-critical damage as discussed in section 10.4.1.2 was proceeded. As can be noted from Figure 10.17g for the fatigue case, the specimen following mechanism A has larger delamination area compared to the one following mechanism B at 70% of total fatigue life, with the highest value (1.13%) for $\lambda = 0$ and the lowest value (0.33%) for $\lambda = 1.571$. This is supported by the foregoing damage mechanisms showing that delamination takes less important role but micro-buckling dominates the fracturing behavior of notched quasi-isotropic laminates under shear-dominated loading. On the other hand, the evolution of total crack volume before 70% of total fatigue life is close for each multiaxiality ratio as shown in Figure 10.17e. This explains the observation, reported in the previous work by Qiao *et al.* [229], that the stiffness deteriorates roughly 19 % to 25 % before catastrophic

failure for various multiaxiality ratios.

In the case of quasi-static loading, specimens follow the similar damage mechanisms for the foregoing fatigue case. However, in mechanism B, the straight paths of the micro-buckling in $+45^{\circ}$ plies at the two ends of the hole have a pronounced propagation with the increasing multiaxiality ratio as can be noted in Figures 10.12B and 10.13B . This difference is much more obvious in the quasi-static case compared to the fatigue case. Additionally, the overall sub-critical damage during quasi-static loading is also less diffused which is similar to the foregoing discussion on notched cross-ply laminates. As shown in Figures 10.17e-h, total crack volume only has 2.7% in average for different multiaxiality ratios and the highest delamination area has 0.13% for multiaxiality ratio $\lambda = 0.785$ at 90% of total quasi-static life but these sub-critical damage grows rapidly close to the catastrophic failure.

10.4.3 $[+45/90/-45/0]_s$ *laminate with a central crack*

Having discussed the fracturing features and damage mechanisms for the quasi-isotropic specimens in presence of an open hole, similar damage mechanisms were observed for the same layup but featuring a central crack as shown in Figures 10.14-10.16. The only difference in mechanism B (micro-buckling dominant) is the location of the micro-buckling paths ahead of the notch. As can be noted from Figures 10.15-10.16, the straight micro-buckling paths in front of the notch are on the same line for multiaxiality ratios related to shear-dominated loading.

10.4.3.1 Quantitative analysis: fatigue vs. quasi-isotropic condition

In the fatigue case as shown in Figure 10.17k, the larger delamination area was also observed for the specimen following mechanism A compared to the one following mechanism B before catastrophic fatigue failure. At 70% of total fatigue life, the delamination reaches approximately 1.4% for $\lambda = 0$ whereas a significant reduction characterizes the other multiaxiality ratios, with 0.8% for $\lambda = 0.785$ and 0.55% for $\lambda = 1.571$. This is similar to the quasi-isotropic specimens featuring an open hole as discussed in the foregoing section. Another

similarity was found in terms of the evolution of total crack volume confirming a similar gradual stiffness degradation throughout the fatigue life for various multiaxiality ratios as shown in Figure 10.17i. Despite these similarities, the specimens weakened by a central crack have a significant larger amount of total crack volume compared to the ones weakened by an open hole.

However, this does not occur for the quasi-static scenario which shows the central crack case having less amount of total crack volume. This indicates a different evolution of the Fracture Process Zone (FPZ) in quasi-static regime compared to fatigue. A structural design must take this into consideration since the previous study shows that specimens featuring a central hole behave better than the ones with the same layup but featuring a central crack in fatigue case but not for the quasi-static case [229]. It is worth mentioning again that less diffused sub-critical damage was also observed on the specimens featuring a central hole under quasi-static loading. As shown in Figure 10.17i-l, total crack volume has roughly 1.96% and the delamination area is significantly low (0.2%) for different multiaxiality ratios at 90% of total quasi-static life but these sub-critical damage also grows rapidly close to the catastrophic failure similar to the foregoing discussion on the quasi-static fracturing behavior.

10.4.4 Three-dimensional woven composite with a central notch

10.4.4.1 Warp tow as longitudinal direction

In the case that the warp tows are oriented towards the longitudinal direction of the specimens and these notched three-dimensional woven composites are subjected to multi-axial load, the damage mechanisms can be reasonably categorized into two different scenarios. The damage characteristics belong to *Mechanism A* when the tension-dominated loading conditions ($\lambda = 0, 0.262$) are applied on the specimens. In this mechanism, the fracturing features at the peak load are characterized by a remarkable distributed region of high deformation at both sides of the notch as illustrated in Figure 10.18a through the two-dimensional DIC analysis. This deformed region is mainly formed by the significant splitting in the transverse

direction distributed in the gauge area of the specimen and the noticeable splitting in the longitudinal direction at the notch tip as can be clearly seen from Figure 10.18b by leveraging micro-computed tomography analysis. Thanks to this three-dimensional damage inspection technique, the significant damage through the entire thickness of the specimen at the peak load was also observed as illustrated in Figure 10.18b showing the multiple debonding cracks spreading along the interfaces between tows and matrix as similarly reported in other related studies [254]. Interestingly, these debonding cracks are characterized by a distance about two times the thickness of the specimen and this important feature is similar to the experimental morphology of the cross-ply laminates under uni-axial tension exhibiting individual transverse matrix crack at a distance of roughly one to three times the thickness of the lamina [14, 15, 41, 186]. Based on the foregoing description, the damage evolution of *Mechanism A* can be summarized into the following:

(1) splitting initiates in the transverse direction and has a distributed development (Figure 10.18b);

(2) splitting in the longitudinal direction initiates and develops near the notch tip (Figure 10.18b);

(3) matrix and debonding cracks initiate and develop through the specimen thickness (Figure 10.18b);

(4) fibers break mainly in the longitudinal direction together with the further splitting propagation mainly in the transverse direction near the notch tip.

On the other hand, the specimens exhibit completely different damage characteristics compared to the previous ones following *Mechanism A* when the shear load component is involved ($\lambda = 0.524, 0.785, 1.047$ and 1.571). This significant difference was exemplified in Figures 10.18c-f for the DIC and micro-computed tomography analyses on the specimens with the multiaxiality ratio $\lambda = 0.7857$ and 1.571. In these scenarios, the damage characteristics follow *Mechanism B* which features localized region of high deformation at both sides of the notch at the peak load as shown in Figures 10.18c and 10.18e. The detailed damage morphology with respect to the forgoing localized damage region was illustrated in Figures

10.18d and 10.18f showing that the in-plane damage band is the combination of the localized splitting in both transverse and longitudinal directions whereas the minor matrix cracks and the pronounced debonding cracks between tows and matrix lead to the out-of-plane damage band which was not obtained from the two-dimensional DIC analysis. In addition to this, the splitting in the longitudinal direction is more pronounced in terms of both length and quantity as the multiaxiality ratio increases representing the transition from uni-axial tension to pure shear condition as illustrated in Figure 10.18. Based on the foregoing discussion, the damage evolution of *Mechanism B* consists of the following phases:

(1) splitting initiates in the transverse direction and has a localized development near the notch (Figures 10.18d,e);

(2) matrix and debonding cracks initiate and develop through the specimen thickness (Figures 10.18d,e);

(3) splitting in the longitudinal direction initiates and develops in the specimen with the noticeable longer length for the pure shear loading condition (Figures 10.18e);

(4) fiber breaking leads to the final separation of the specimen.

10.4.4.2 Weft tow as longitudinal direction

On similar grounds, the damage mechanisms can also be reasonably categorized into two different situations when the notched three-dimensional woven composites are subjected to multi-axial load but the weft tows are oriented towards the longitudinal direction of the specimens. In this case, the application of tension-dominated loading conditions ($\lambda = 0, 0.262$ and 0.524) on the specimens leads to the damage characteristics following *Mechanism A*. As illustrated in Figure 10.19a, a distributed region of high deformation at both sides of the notch was also observed at the peak load through the DIC analysis and the forgoing region is still the consequence of the distributed splitting in the transverse direction as shown in Figure 10.19b through the micro-computed tomography analysis. These aspects are almost similar to the morphological features as discussed in the previous section for the warp tows parallel to the longitudinal direction of the specimen but the difference lies in the disappearance of

the noticeable splitting in the longitudinal direction near the notch tip as clearly shown in Figure 10.19b. On the other hand, the matrix and debonding cracks with an approximate distance of roughly two times the thickness of the specimen were also observed as can be noted in Figure 10.19b. In summary, the damage evolution of *Mechanism B* has the following steps:

(1) splitting initiates in the transverse direction and has a distributed development (Figure 10.19b);

(2) matrix and debonding cracks initiate and develop through the specimen thickness (Figure 10.19b);

(3) fibers break mainly in the longitudinal direction together with the further splitting propagation in the transverse direction near the notch tip.

When the specimens are subjected to shear-dominated loading conditions ($\lambda = 0.785, 1.047$ and 1.571), the damage characteristics can be categorized into *Mechanism B* which has similar features compared to the previous ones for the materials with the warp tows parallel to the longitudinal direction of the specimen under the same global multi-axial loads. As it can be noted in Figures 10.19c-f for both DIC and μ-CT analyses at the peak load, the specimens exhibit localized three-dimensional damage bands at both sides of the notch due to the mixed splitting in both longitudinal and transverse directions near the notch and the combination of matrix and debonding cracks through the entire thickness of the specimen. However, the splitting in the longitudinal direction of the specimen was significantly reduced in these scenarios which is substantially different from the previous *Mechanism B* showing remarkable splitting in the longitudinal direction of the specimen. Based on these interesting morphological studies, the damage evolution of this *Mechanism B* can be summarized in the following:

(1) splitting initiates in the transverse direction and has a localized development near the notch (Figures 10.19d,e);

(2) matrix and debonding cracks initiate and develop through the specimen thickness (Figures 10.19d,e);

(3) minor splitting initiates and develops in the longitudinal direction (Figures 10.19d,e);

(4) fiber breaking leads to the final separation of the specimen.

10.4.4.3 Crack volume vs. multiaxiality ratio

The crack volume in the notched three-dimensional woven composites as a function of the multiaxiality ratio at almost the peak load was further estimated as illustrated in Figure 10.7. As can be noted from this figure for both warp and weft cases, the crack volume increases in a non-linear way as the multiaxiality ratio increases. This is a confirmation that the material exhibits more quasi-brittleness when the loading condition transits from tension to shear. On the other hand, the foregoing phenomenon is also consistent with the previous nominal stress-strain curves of the notched three-dimensional woven composites under multi-axial loads since the less crack volume in the material for the tension-dominated loads leads to the less non-linearity of the curves whereas the energy dissipation due to the large crack volume can be the main reason for the significant non-linearity of the curves under shear-dominated loads.

10.4.5 Effect of laminate thickness

The foregoing damage mechanisms can be significantly affected by the thickness of the laminate and by way it is increased or decreased in the context of a ply-level or a sub-laminate level scaling [271]. For the cross-ply and quasi-isotropic laminates investigated in this work, ply-level scaling means stacking the plies with the same orientation leading to $[0_n/90_n]_{2s}$ and $[+45_n/90_n/-45_n/0_n]_s$ layups where n is equal or greater than one. In contrast, sub-laminate level scaling is obtained by repeating the sub-laminate groups, leading to $[0/90]_{ns}$ and $[+45/90/-45/0]_{ns}$ layups. The former scaling in thickness allows damage to coalesce and propagate through the thickness of the laminate whereas the damage in the latter scaling can be constrained to the sub-laminate thus leading to a different damage mechanism.

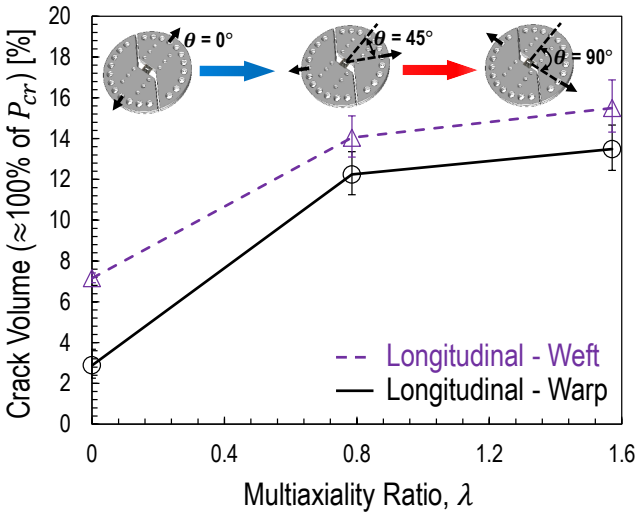

Figure 10.7: Crack volume as a function of the multiaxiality ratio at almost the peak load for the notched three-dimensional woven composites with the longitudinal direction in both warp and weft directions.

10.4.6 Effect of notch acuity

The notch acuity of the specimen also plays an important role in the damage mechanisms and it is related to the comparison between the notch radius R of the specimen and the Irwin's characteristic length l_{ch}. This length is associated to the size of the Fracture Process Zone and defined as $l_{ch} = EG_f/f_t^2$ where E is the Young's modulus, G_f is the fracture energy and f_t is the material strength. In the case for $R < l_{ch}$, the specimen featuring a notch behaves like crack leading to the similar damage phenomena in polymer matrix composites. However, in the case for a sufficiently large notch radius $R \geq l_{ch}$, the specimen in presence of a notch can have a significantly different behavior compared to the one with a crack. The foregoing difference was shown in many studies [88,226,229] focusing on the fracture behavior of geometrically-scaled quasi-brittle materials featuring a sharp or blunt notch. The effect of the notch acuity is confirmed by the results of the present work. In fact, it has been shown that, while the mechanisms involved in the FPZ formation where substantially the same for the crack and hole cases, the damage evolution and extent of the FPZ were significantly

different.

10.4.7 Effect of structural scaling

Composites are quasi-brittle materials featuring strain softening due to the emergence of several distributed damage mechanisms in the Fracture Process Zone (FPZ). The evolution of the FPZ, its size, and the type of damage mechanisms are generally affected significantly by the size of the structure and its geometry as well as the composite layup and material properties. In turn, the energy dissipation due to the nonlinear phenomena occurring in the FPZ drives the structural behavior of the composite. These effects become increasingly important when the structure is not significantly larger than the FPZ and a large volume of material features nonlinear damage. The dependence of the structural behavior of notched quasi-brittle components on the structure size is typically referred to as "Type II" size effect and it has been reported for both quasi-static and fatigue loading [94–100, 102, 103, 164–166, 269]. In this context, the results presented in this work are surely size-dependent in terms of both structural performance and damage morphology. A way to address these important aspects is leveraging quasi-brittle mechanics and high-fidelity computational models that are capable of capturing the main damage mechanisms and the related energy dissipation. To achieve this goal, such computational models must be calibrated and their ability to describe the damage morphology must be validated against quantitative damage data for at least one specimen size. Providing this data is one of the results achieved by the present contribution. A large bulk of literature [82, 88, 94–96, 164, 166, 221, 222, 228] has shown that, once the computational framework is properly set up using the data of at least one size, quasi-brittle fracture mechanics can adequately predict the structural size effect in both the quasi-static and fatigue performance.

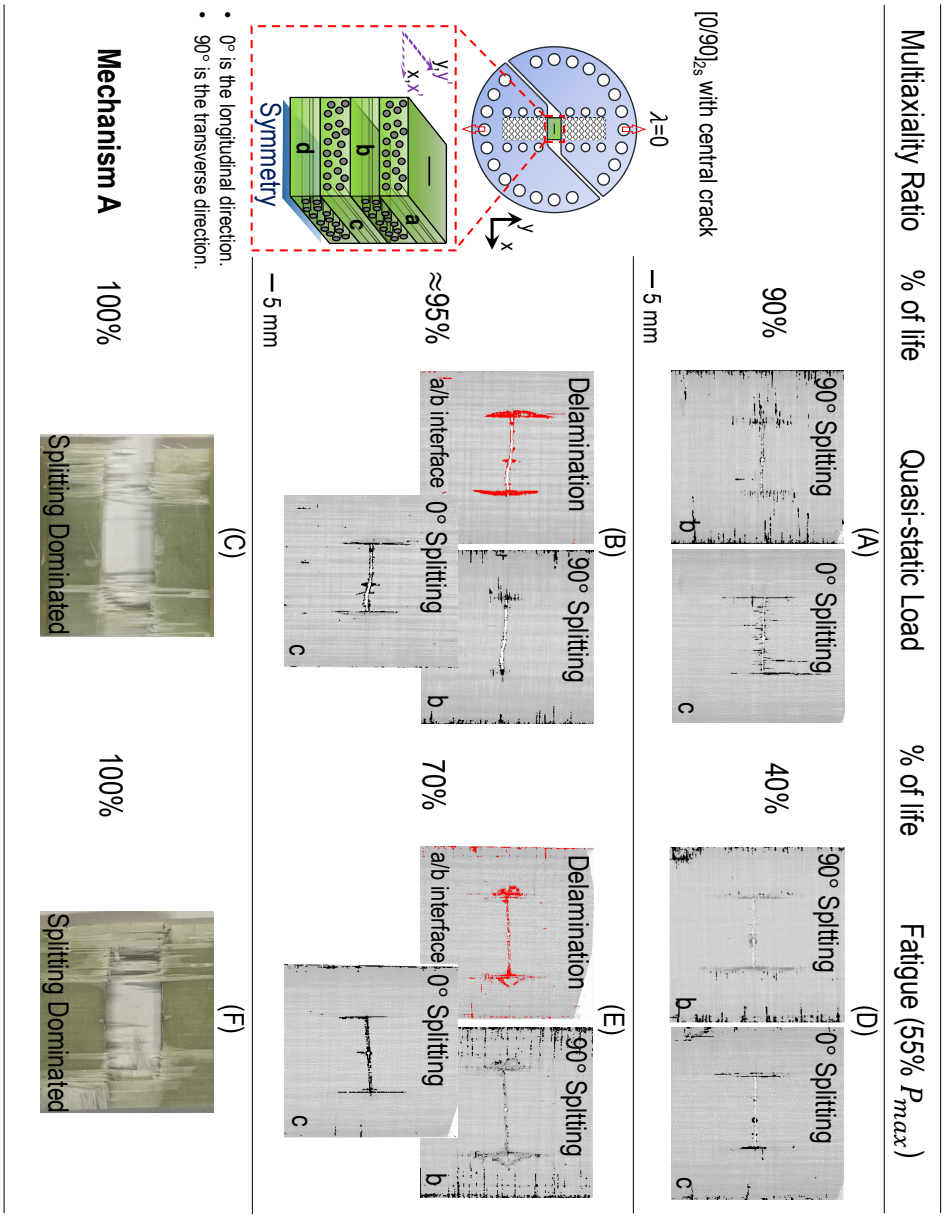

Figure 10.8: Analysis of quasi-static and fatigue damage mechanisms by micro-computed tomography. Comparison between quasi-static and fatigue damage in $[0/90]_{2s}$ specimens weakened by a 18 mm central crack for a multiaxiality ratio $\lambda = 0$ in the 0°, 90° layers and at the interface. Note that the original colors of the images were inverted for a better visualization on the damage and the figure should be viewed by rotating 90° in a counter-clockwise direction. Note that the schematic drawing of notched laminates corresponds to x'-y' coordinate.

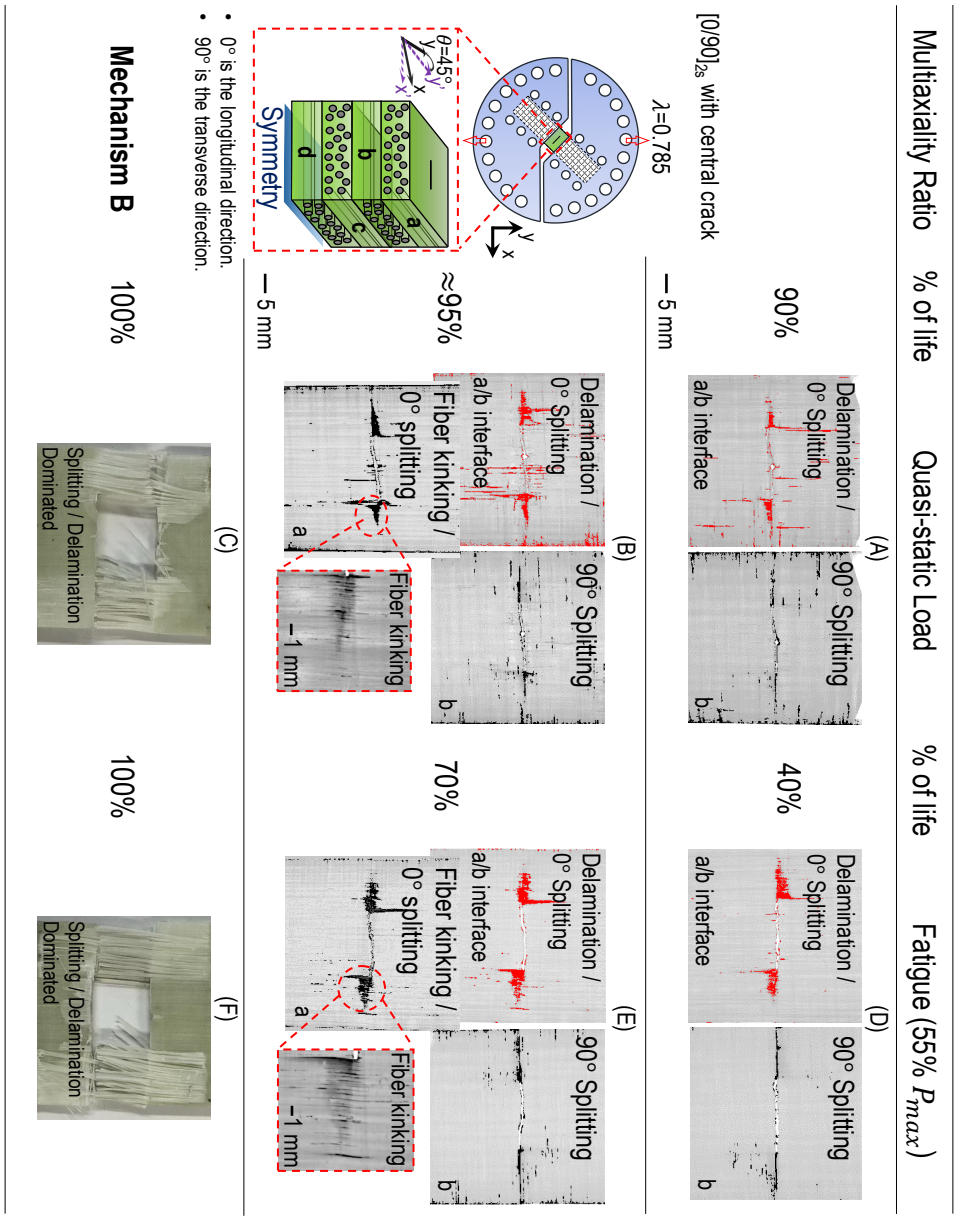

Figure 10.9: Analysis of quasi-static and fatigue damage mechanisms by micro-computed tomography. Comparison between quasi-static and fatigue damage in $[0/90]_{2s}$ specimens weakened by a 18 mm central crack for a multiaxiality ratio $\lambda = 0.785$ in the 0°, 90° layers and at the interface. Note that the original colors of the images were inverted for a better visualization on the damage and the figure should be viewed by rotating 90° in a counter-clockwise direction. Note that the schematic drawing of notched laminates corresponds to x'-y' coordinate.

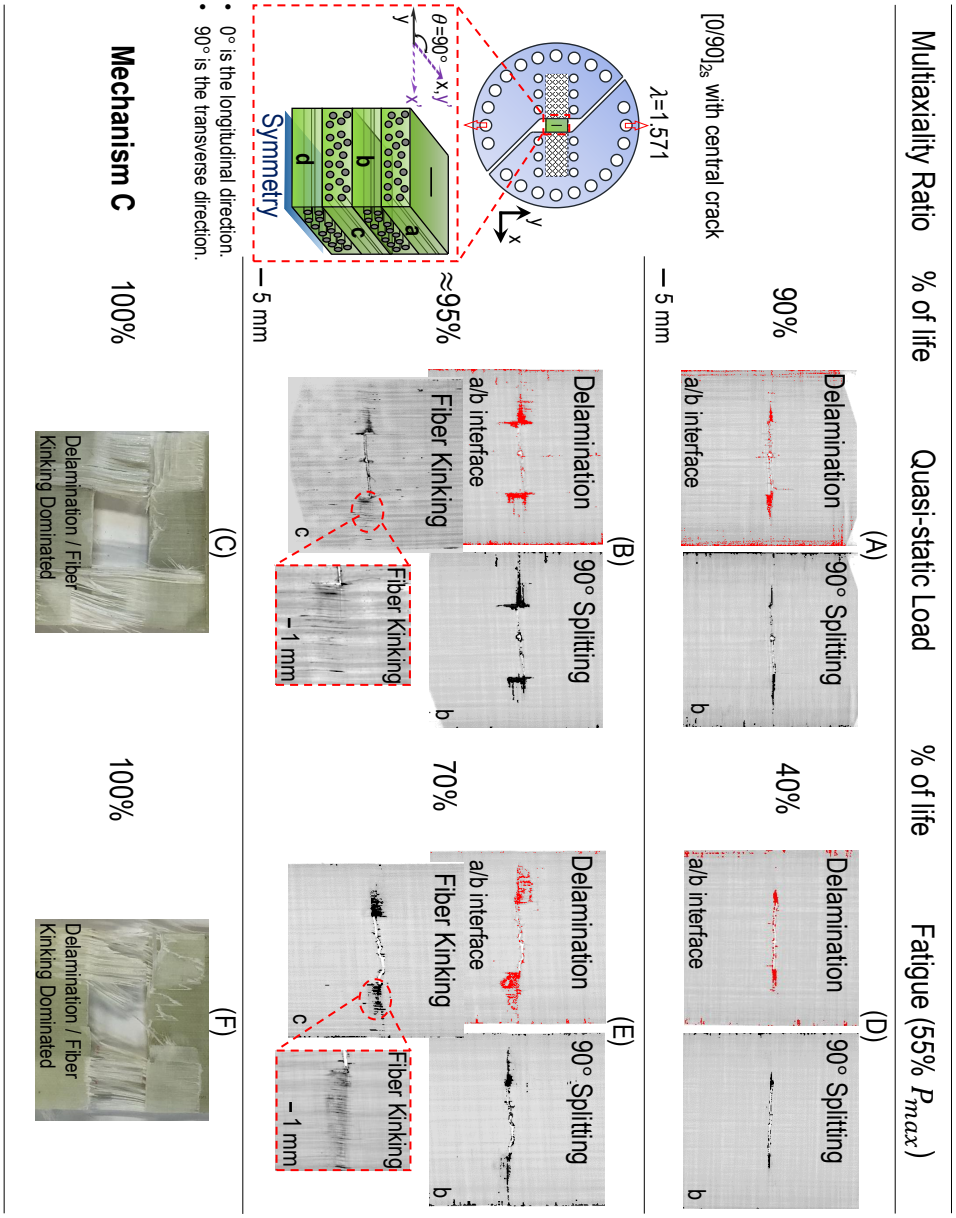

Figure 10.10: Analysis of quasi-static and fatigue damage mechanisms by micro-computed tomography. Comparison between quasi-static and fatigue damage in $[0/90]_{2s}$ specimens weakened by a 18 mm central crack for a multiaxiality ratio $\lambda = 1.571$ in the 0°, 90° layers and at the interface. Note that the original colors of the images were inverted for a better visualization on the damage and the figure should be viewed by rotating 90° in a counter-clockwise direction. Note that the schematic drawing of notched laminates corresponds to x'-y' coordinate.

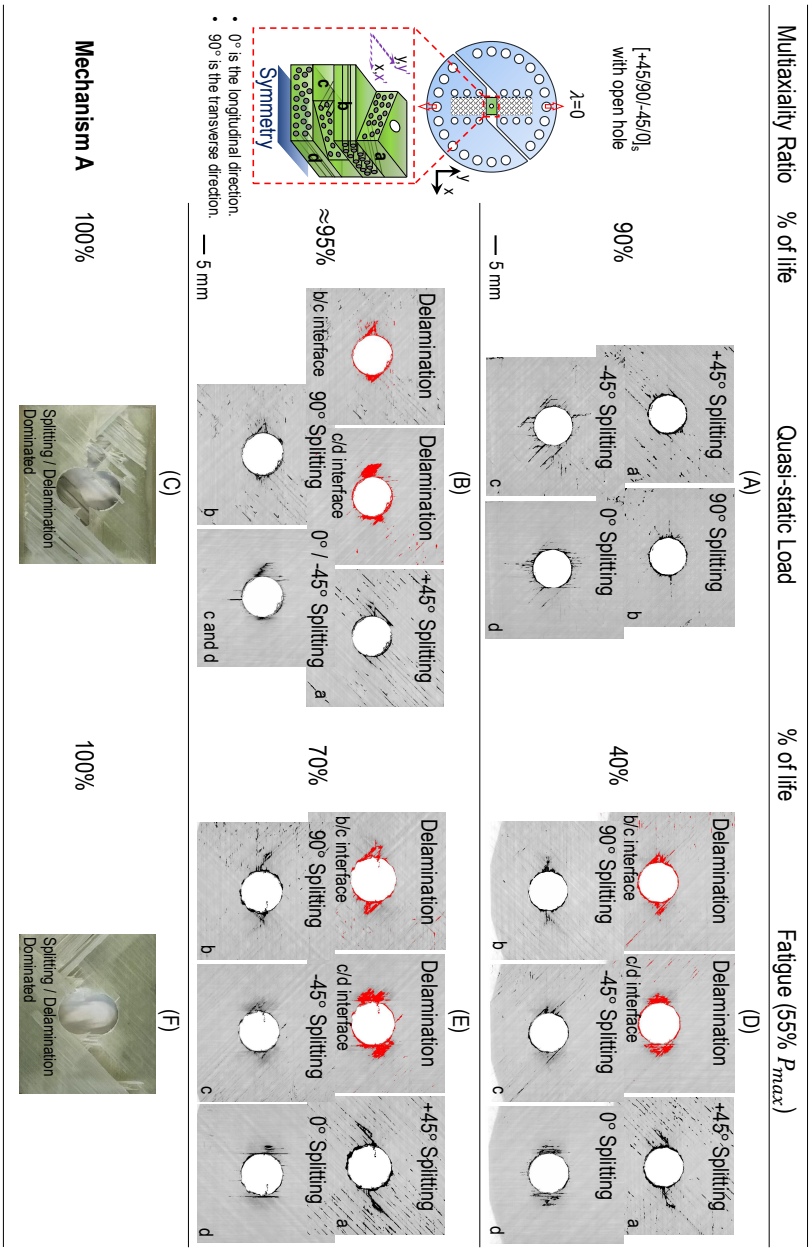

Figure 10.11: Analysis of quasi-static and fatigue damage mechanisms by micro-computed tomography. Comparison between quasi-static and fatigue damage in $[+45/90/-45/0]_s$ specimens weakened by a 10 mm open hole for a multiaxiality ratio $\lambda = 0$ in the $+45°$, $90°$, $-45°$, $0°$ layers and at the interfaces. Note that the original colors of the images were inverted for a better visualization on the damage and the figure should be viewed by rotating $90°$ in a counterclockwise direction. Note that the schematic drawing of notched laminates corresponds to x'-y' coordinate.

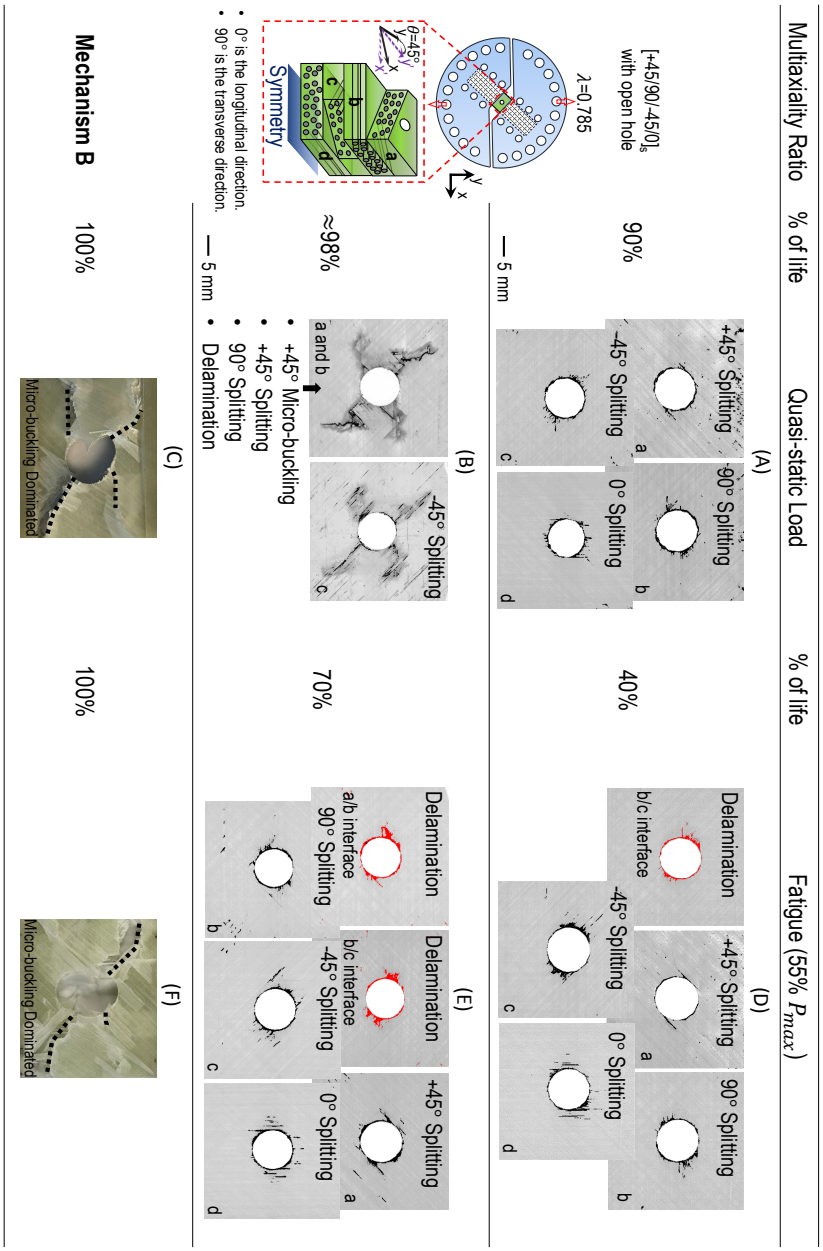

Figure 10.12: Analysis of quasi-static and fatigue damage mechanisms by micro-computed tomography. Comparison between quasi-static and fatigue damage in $[+45/90/-45/0]_s$ specimens weakened by a 10 mm open hole for a multiaxiality ratio $\lambda = 0.785$ in the $+45°$, $90°$, $-45°$, $0°$ layers and at the interfaces. Note that the original colors of the images were inverted for a better visualization on the damage and the figure should be viewed by rotating $90°$ in a counterclockwise direction. Note that the schematic drawing of notched laminates corresponds to x'-y' coordinate.

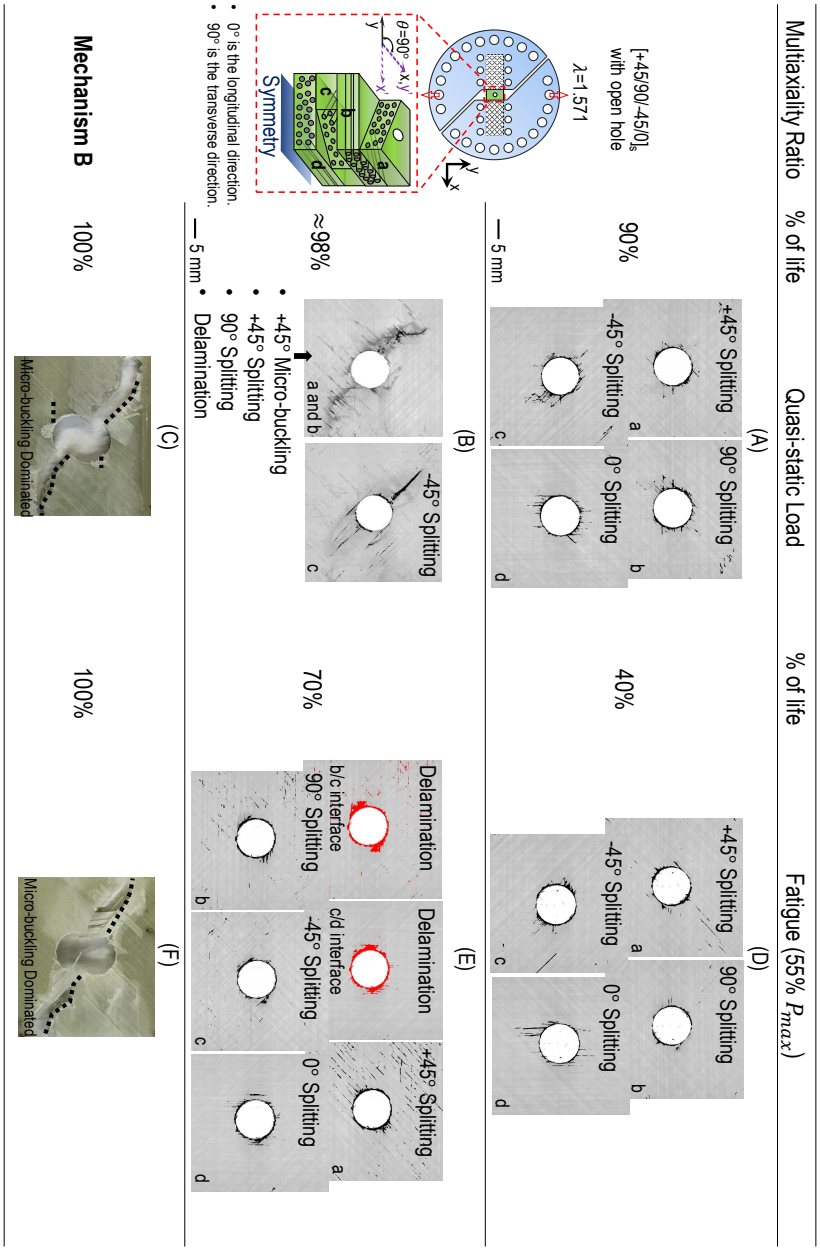

Figure 10.13: Analysis of quasi-static and fatigue damage mechanisms by micro-computed tomography. Comparison between quasi-static and fatigue damage in $[+45/90/-45/0]_s$ specimens weakened by a 10 mm open hole for a multiaxiality ratio $\lambda = 1.571$ in the $+45°$, $90°$, $-45°$, $0°$ layers and at the interfaces. Note that the original colors of the images were inverted for a better visualization on the damage and the figure should be viewed by rotating $90°$ in a counterclockwise direction. Note that the schematic drawing of notched laminates corresponds to x'-y' coordinate.

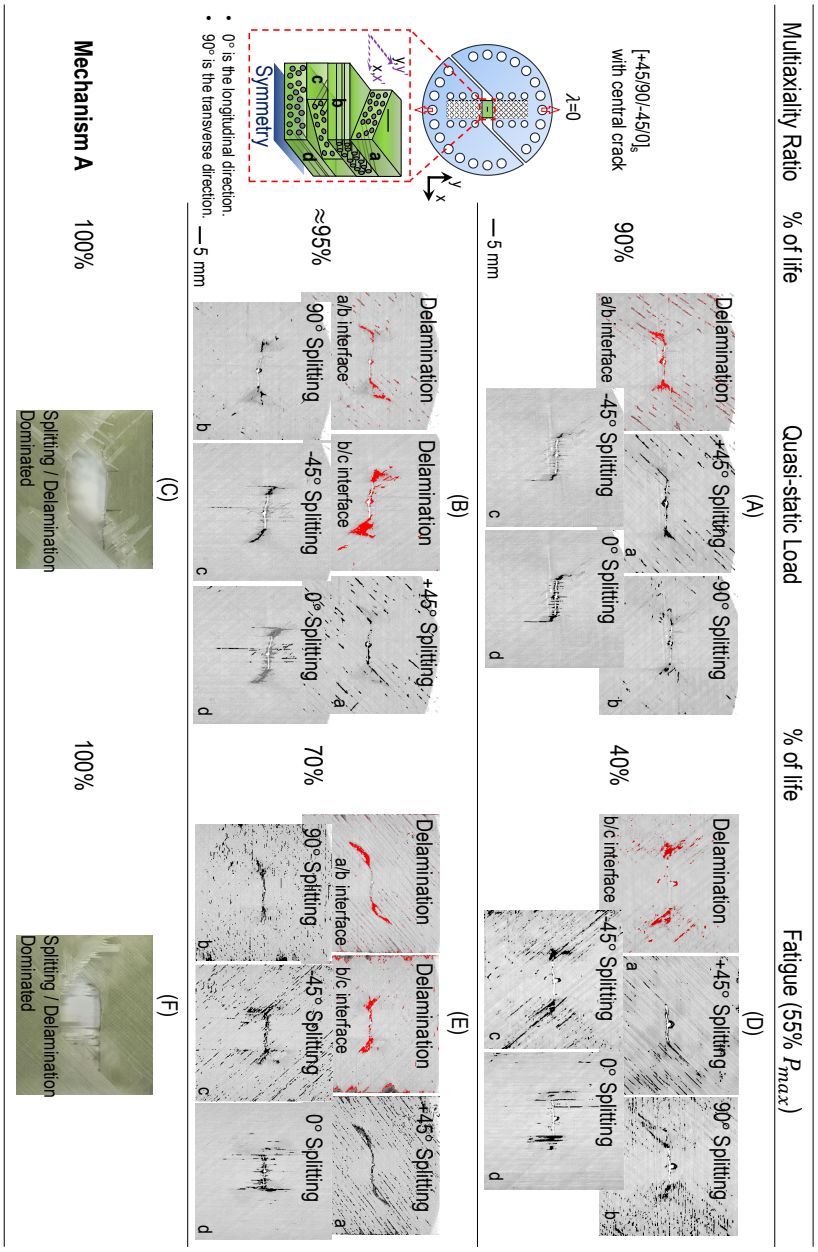

Figure 10.14: Analysis of quasi-static and fatigue damage mechanisms by micro-computed tomography. Comparison between quasi-static and fatigue damage in $[+45/90/-45/0]_s$ specimens weakened by a 10 mm central crack for a multiaxiality ratio $\lambda = 0$ in the $+45°$, $90°$, $-45°$, $0°$ layers and at the interfaces. Note that the original colors of the images were inverted for a better visualization on the damage and the figure should be viewed by rotating $90°$ in a counterclockwise direction. Note that the schematic drawing of notched laminates corresponds to x'-y' coordinate.

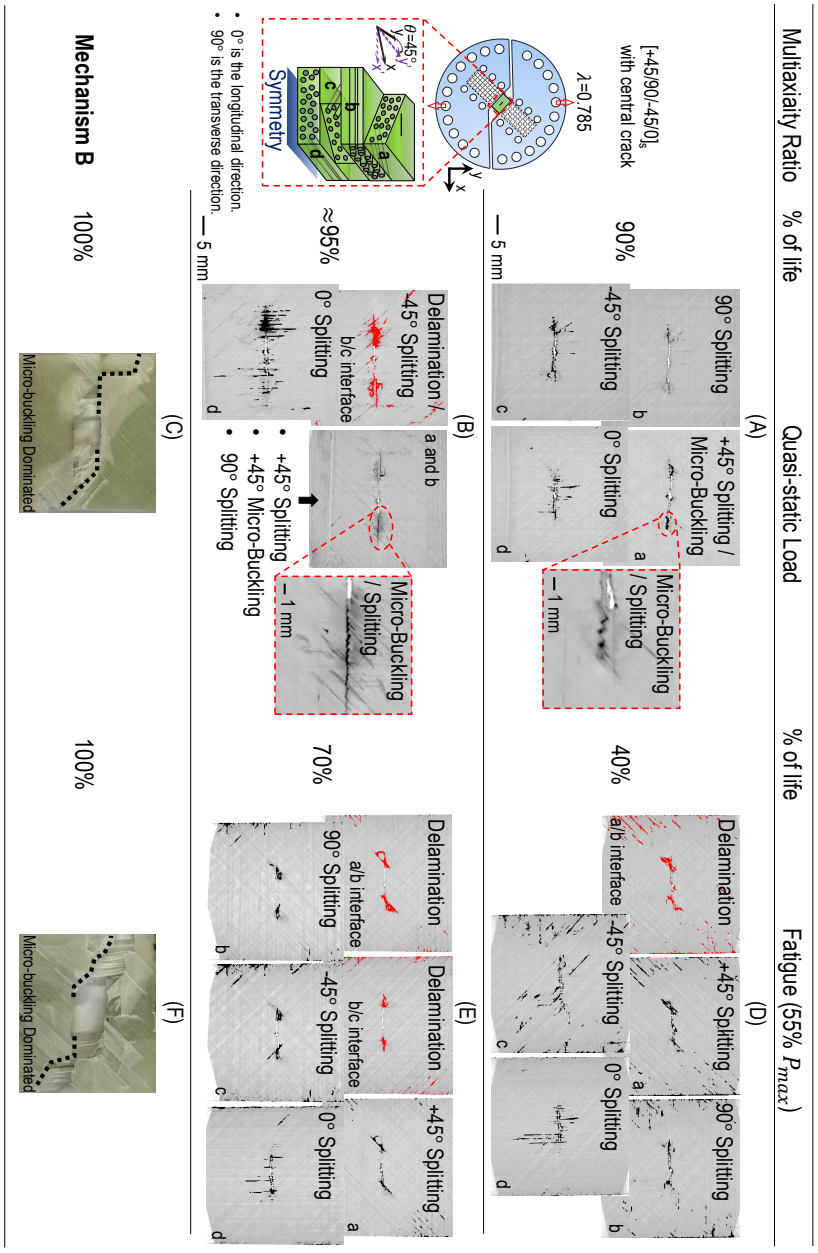

Figure 10.15: Analysis of quasi-static and fatigue damage mechanisms by micro-computed tomography. Comparison between quasi-static and fatigue damage in $[+45/90/-45/0]_s$ specimens weakened by a 10 mm central crack for a multiaxiality ratio $\lambda = 0.785$ in the $+45°$, $90°$, $-45°$, $0°$ layers and at the interfaces. Note that the original colors of the images were inverted for a better visualization on the damage and the figure should be viewed by rotating 90° in a counterclockwise direction. Note that the schematic drawing of notched laminates corresponds to x'-y' coordinate.

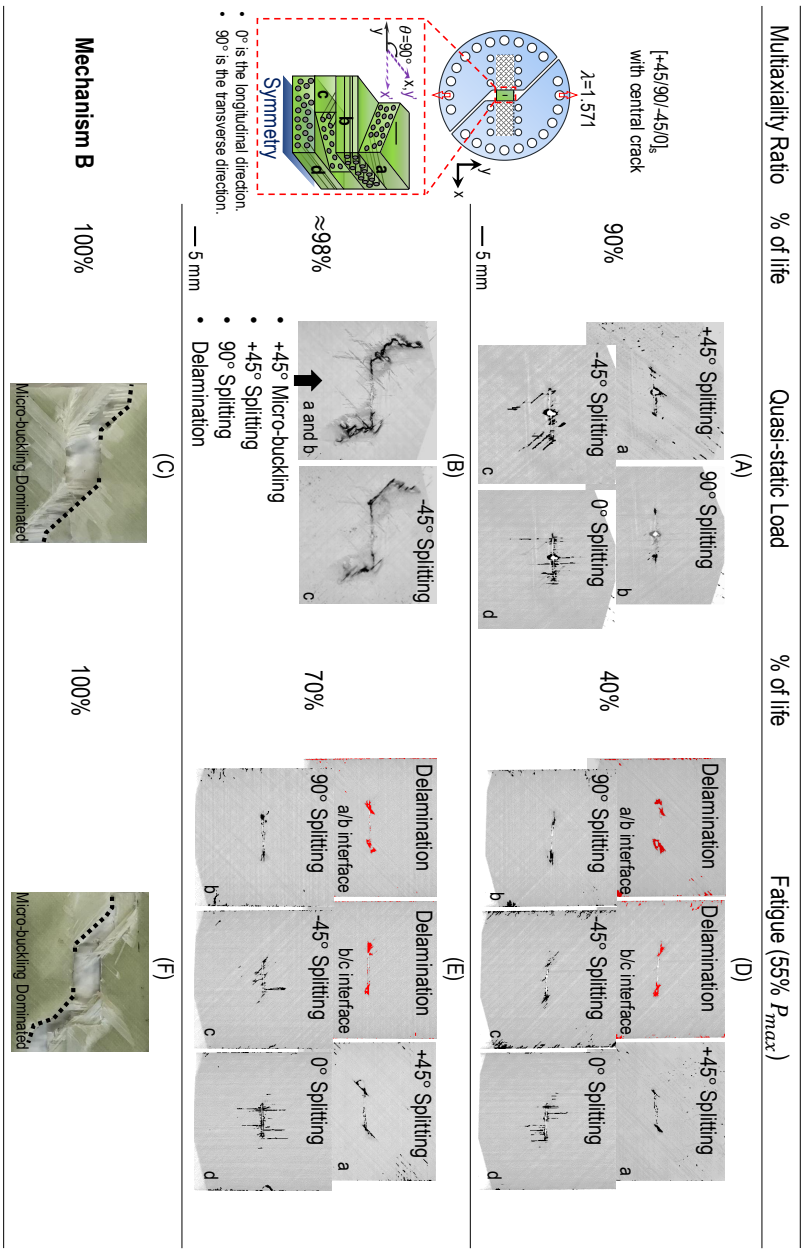

Figure 10.16: Analysis of quasi-static and fatigue damage mechanisms by micro-computed tomography. Comparison between quasi-static and fatigue damage in $[+45/90/-45/0]_s$ specimens weakened by a 10 mm central crack for a multiaxiality ratio $\lambda = 1.571$ in the $+45°$, $90°$, $-45°$, $0°$ layers and at the interfaces. Note that the original colors of the images were inverted for a better visualization on the damage and the figure should be viewed by rotating $90°$ in a counterclockwise direction. Note that the schematic drawing of notched laminates corresponds to x'-y' coordinate.

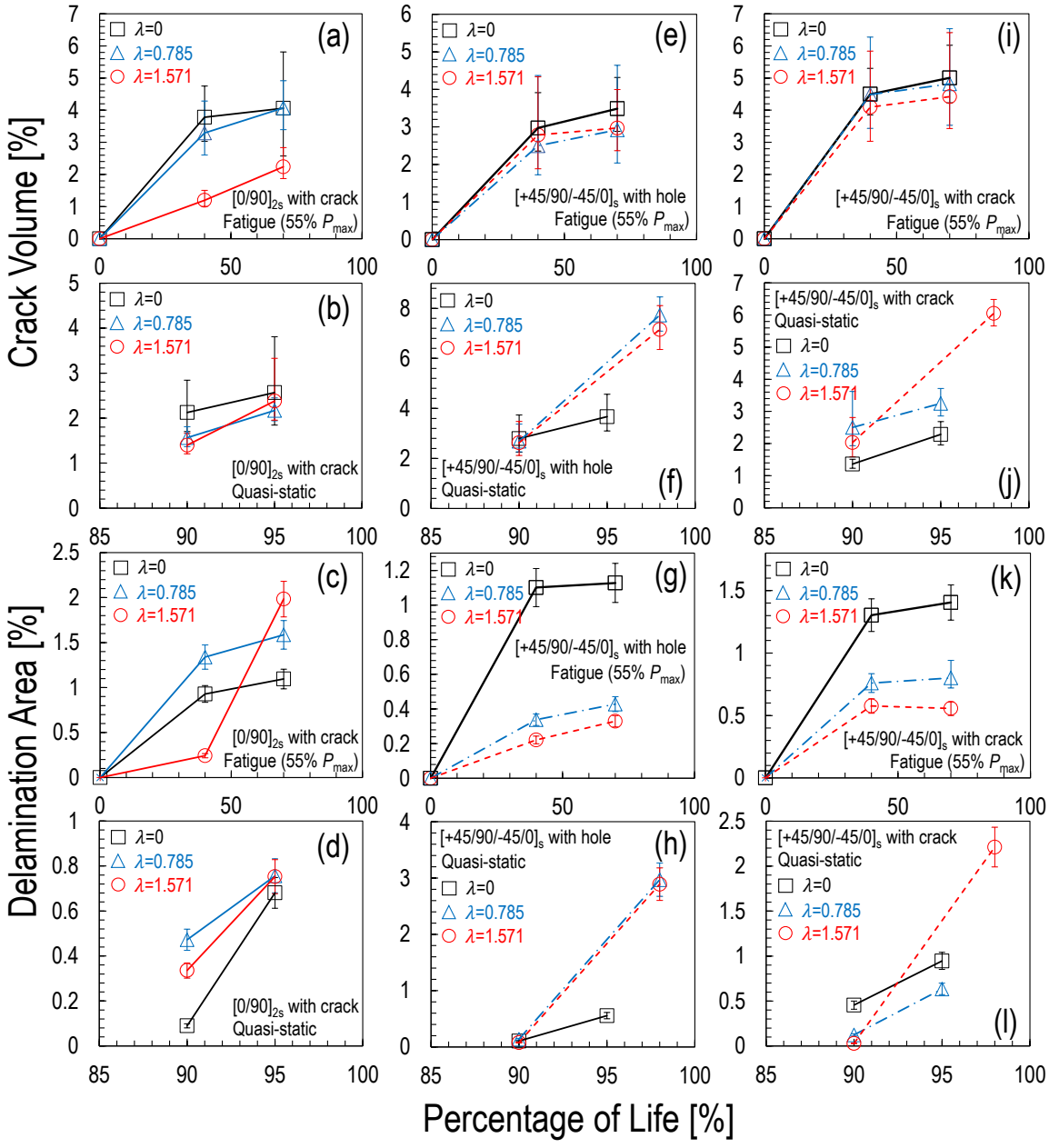

Figure 10.17: The evolution of the total crack volume and delamination area for all the investigated specimens weakened by a central crack or hole as a function of the percentage of life for three multiaxiality ratios. The graphs compare quasi-static and fatigue results.

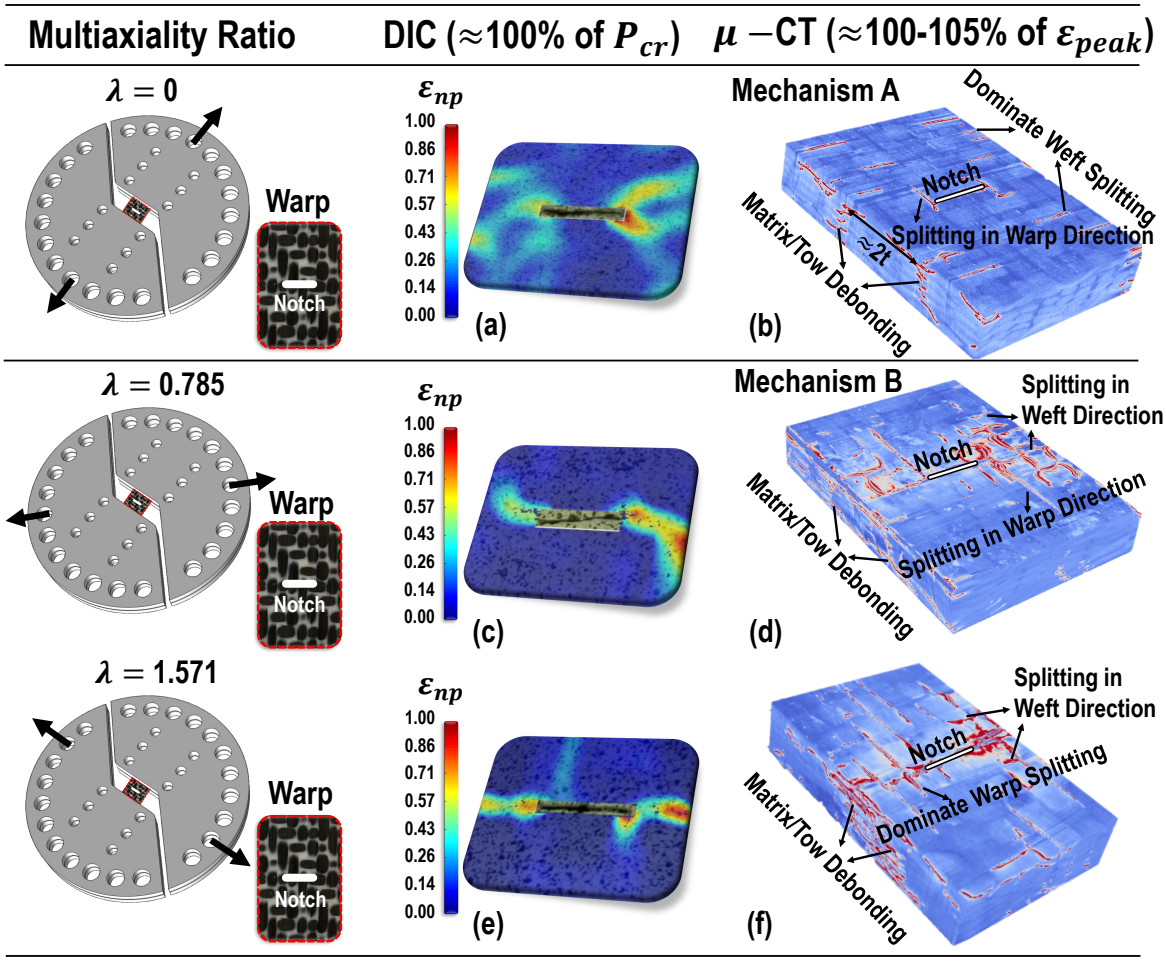

Figure 10.18: Analyses of quasi-static damage mechanisms of notched three-dimensional woven composites with the warp tows oriented toward the longitudinal direction of the specimens under multi-axial load by Digital Imaging Correlation (DIC) and micro-computed tomography (μ−CT). These figures illustrate the detailed damage characteristics almost at the peak load for the forgoing composites weakened by a 8mm central notch under the multiaxiality ratio $\lambda = 0$, 0.78 and 1.571. Note that the symbol ε_{np} in the DIC analysis represents the normalized maximum principle strain. Also note that the warp direction is the longitudinal direction whereas the weft direction is the transverse direction in this case.

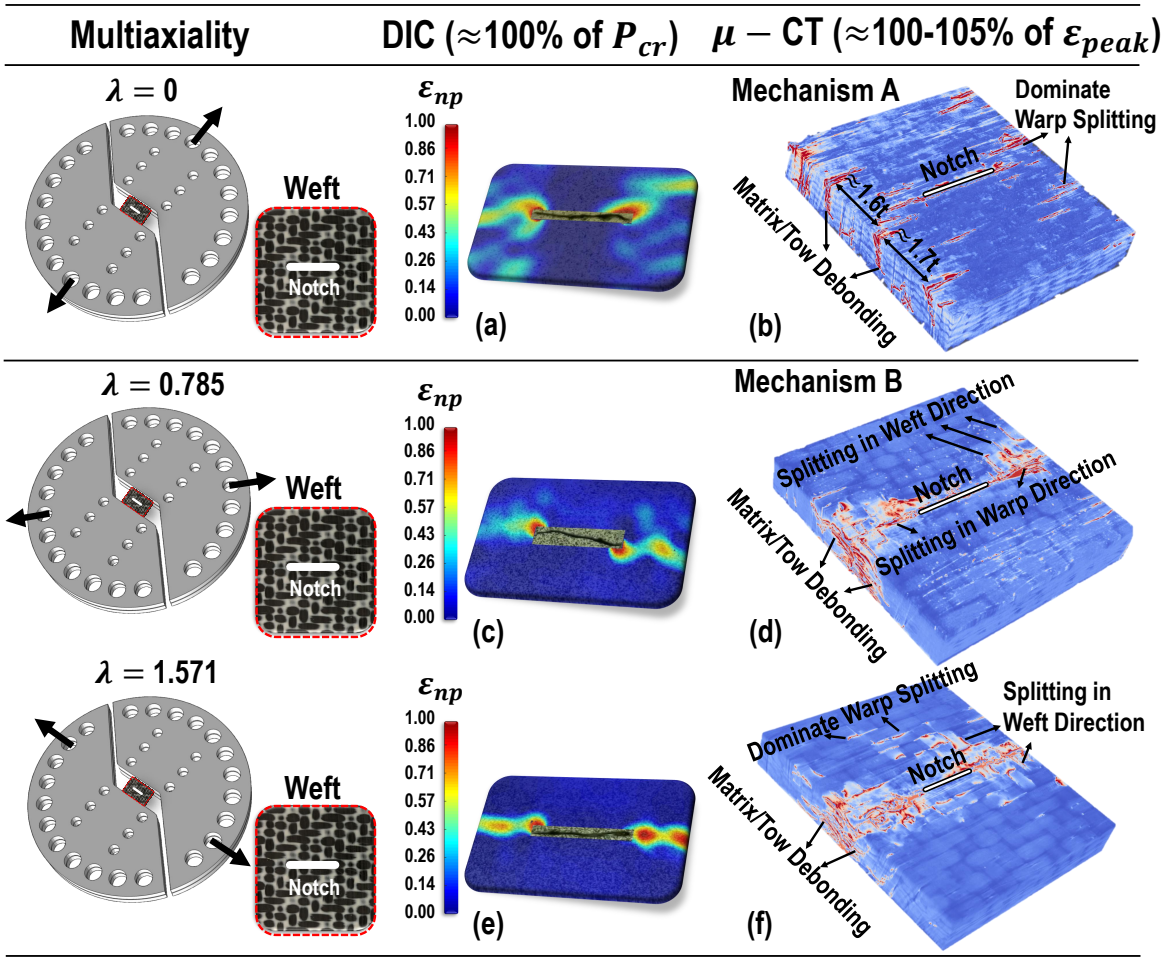

Figure 10.19: Analyses of quasi-static damage mechanisms of notched three-dimensional woven composites with the weft tows oriented toward the longitudinal direction of the specimens under multi-axial load by Digital Imaging Correlation (DIC) and micro-computed tomography (μ−CT). These figures illustrate the detailed damage characteristics almost at the peak load for the forgoing composites weakened by a 8mm central notch under the multiaxiality ratio $\lambda = 0$, 0.78 and 1.571. Note that the symbol ε_{np} in the DIC analysis represents the normalized maximum principle strain. Also note that the weft direction is the longitudinal direction whereas the warp direction is the transverse direction in this case.

10.5 Conclusions

1. For the composite layups and specimen configurations investigated in this work, the sub-critical damage mechanisms under multi-axial fatigue were similar to the ones identified under quasi-static loading. However, it is worth mentioning that in notched quasi-isotropic laminates under shear-dominated loading a more pronounced straight micro-buckling paths ahead of the notch or hole was reported in the quasi-static case compared to the fatigue loading;

2. Leveraging the μ-CT results, it is shown that the damage mechanisms of the notched cross-ply laminates are dominated by splitting in 0° plies under tension-dominated loading whereas a mix of delamination and fiber kinking in 0° plies occurs with increasing shear load;

3. In the case of notched quasi-isotropic laminates, significant delamination and the splitting in $\pm$ 45° plies characterizes the tension-dominated fatigue behavior whereas the main damage mechanism for the shear-dominated case is the micro-buckling in +45° plies in combination with splitting in the same plies;

4. Regarding the damage mechanisms of three-dimensional woven composites under multi-axial scenario, a distributed damage with the formation of splitting in the transverse direction mainly characterizes the material under tension-dominated loading whereas a localized damage region features the material under shear-dominated loading. This region is typically formed by various damage morphologies including matrix/fiber debonding, matrix cracking, and splitting in both longitudinal and transverse directions. The foregoing damage characteristics were observed for the material with either weft or warp tows oriented towards the longitudinal direction of the specimen;

5. The quantitative analysis of the crack volume via μ-CT and the maximum principal strain distribution by means of DIC reveals a substantial difference in the damage

evolution between the quasi-static and fatigue loading conditions. In fatigue, the sub-critical damage is distributed across a larger volume compared to the quasi-static case, leading to a significant strain redistribution. Further, the rate of crack volume increase throughout the life of the specimen is substantially different. While in the quasi-static case the crack volume increases quickly at almost a constant rate, in fatigue it exhibits a slow change followed by an abrupt increase towards final failure;

6. The foregoing results are of utmost importance for the structural design of polymer matrix composites under multi-axial loading condition but so far rarely investigated. The lack of experimental data on this topic in the literature hindered the development of more accurate models which can guarantee a safe design in particular when composite structural components subject to multi-axial fatigue loading. As a first step towards filling the forgoing knowledge gap, this study provides a comprehensive experimental data and damage evaluation on the fracturing behavior of notched laminates which can be used to validate the existing models for the design of composite structures under multi-axial stress states.

Chapter 11

FUTURE WORK

11.1 Molecular dynamics simulation of polymeric materials

The effects of stress state and size scaling on the plastic deformation and fracture behavior of thermoset polymers and associated particulate- or fiber-reinforced composites were investigated and discussed in the foregoing chapters. However, there is no unified model which can provide an accurate description for these effects on the polymeric materials in the literature especially for the determination of the critical strain with respect to the damage initiation in the materials. The method for describing the effects of stress state on the conventional metals by using stress tri-axiality and Lode angle [272–275] was found to not successfully characterize the foregoing effects on the polymeric materials.

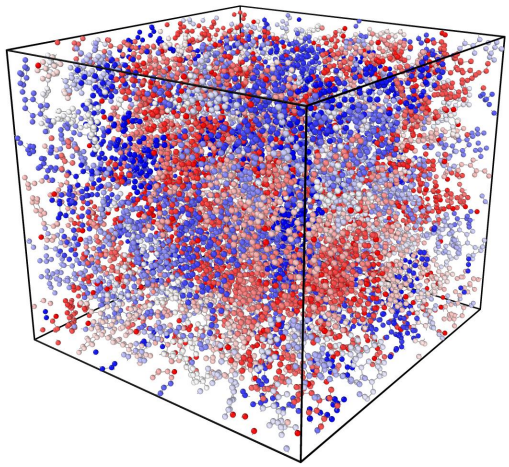

Figure 11.1: A representative thermoset polymer with the size of 50 x 50 x 50 Å generated through the software Winmostar [276]. Note that different colors represent different atoms.

In this consideration, a physical-based model must be formulated by leveraging molecular dynamics simulation to bridge the versatile mechanical behavior of polymeric materials at various length and time scales and investigate the corresponding damage mechanisms. To proceed these simulations, the molecular structures of epoxy resin and hardener can be generated by leveraging the software Winmostar as exemplified in Figure 11.1. The cross-linking process and the computational tests can be performed through the LAMMPS molecular dynamics simulator. It is worth mentioning here that the detailed information about the potential fields for the molecules and atoms can be referred to the ones recently proposed by the authors [277]. The investigation related to this direction is considered as one of the long-term future works and may have a significant impact on the multi-scale modeling of polymeric materials and their composites with any geometries under complex loading conditions.

11.2 Computational characterization of fiber/matrix interfacial properties

The fracturing behavior of fiber-reinforced composites in the transverse direction exhibits great differences compared to the one of pure thermoset polymers as experimentally shown in the previous chapters. Moreover, the micro-scale computational modeling was also conducted to further understand the transverse matrix cracking and its evolution in fiber-reinforced composites. A further step towards improving the fidelity of the micro-scale computational modeling can be the investigation on the fiber/matrix interfacial behavior which is still elusive in the open literature. In this consideration, the following computational strategy can be used to explore the fiber/matrix interfacial behavior.

As illustrated in Figure 11.2, the distribution of the fibers can be observed by means of microscopic techniques (e.g. Optical Microscopy, Scanning Electron Microscopy, etc). Accordingly, the location of the center of a single fiber tow and its diameter can be exactly determined through the Matlab script. To have an accurate simulation considering the same distribution of the fibers as observed in the experiment, the forgoing geometrical information on the fibers can be used to generate the partition on the specimens in ABAQUS by leveraging the Python script. Eventually, the interfacial behavior between the fiber and the matrix can

be explored by matching the load-displacement curves for the fiber-reinforced specimens with different sizes since the multi-scale plastic and cohesive behavior of the pure matrix were already determined as shown in the previous chapters.

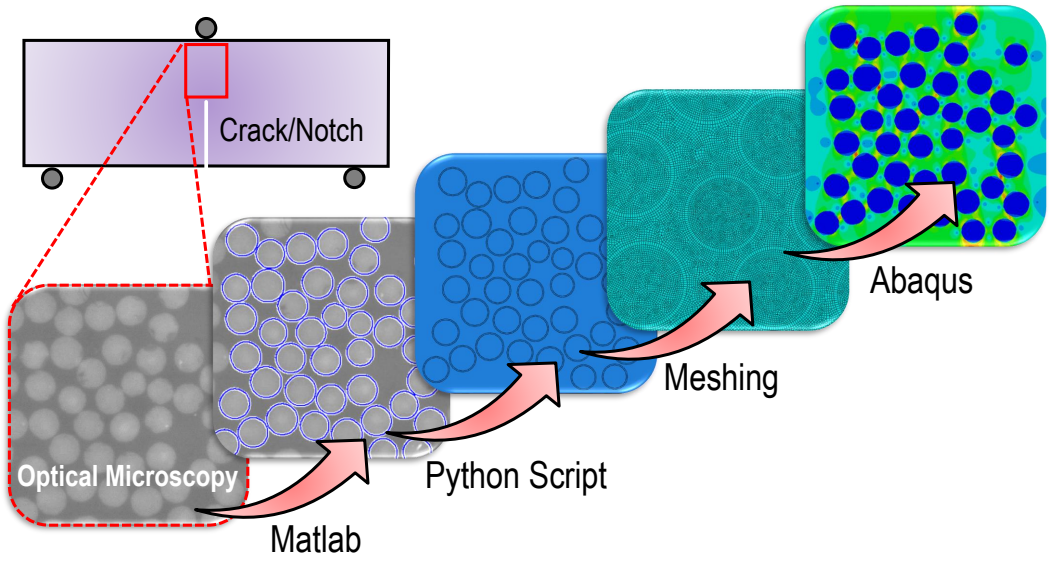

Figure 11.2: Computational modeling strategy for the investigation on the mechanical properties of fiber/matrix interface in polymer matrix composites.

11.3 Modeling of fiber-reinforced composites under multi-axial loading

The previous chapters investigated the effects of stacking sequence, multiaxiality ratio, and the loading condition on the local damage characteristics and the global mechanical behavior of fiber-reinforced composites. These useful results are important for the model calibration and validation since future efforts can be the formulation of efficient discrete or continuum model to account for all the aforementioned aspects and the structural size and geometry. The potential models can be the micro-plane model [102,278–280] and lattice discrete particle model [281,282] which were extensively used in other quasi-brittle materials and these models can be further extended to also take other aspects (e.g. strain rate, temperature, fatigue and impact loading, etc) into the consideration.

BIBLIOGRAPHY

[1] Rana S, Fangueiro R. *Advanced Composite Materials for Aerospace Engineering: Processing, Properties and Applications*. Woodhead Publishing, 2016.

[2] Baker A, Dutton S, Kelly D. *Composite Materials for Aircraft Structures*. American Institute of Aeronautics and Astronautics, 2004.

[3] Kaiser R. *Automotive Applications of Composite Materials*. National Technical Information Service, 1978.

[4] Elmarakbi A. *Advanced Composite Materials for Automotive Applications: Structural Integrity and Crashworthiness*. Wiley, 2013.

[5] Karbhari VM, Chin J, Hunston D, Benmokrane B, Juska T, Morgan R, Lesko JJ, Sorathia U, Reynaud AD. Durability gap analysis for fiber-reinforced polymer composites in civil infrastructure. *J Compos Constr*, 7(3):238–47, 2003.

[6] Brandt AM. Fibre reinforced cement-based (frc) composites after over 40 years of development in building and civil engineering. *Compos Struct*, 86:3–9, 2008.

[7] Ceccato C, Salviato M, Pellegrino C, Cusatis G. Simulation of concrete failure and fiber reinforced polymer fracture in confined columns with different cross sectional shape. *Int J Solids Struct*, 108:216–29, 2017.

[8] Carloni C, Focacci F. Frp-masonry interfacial debonding: An energy balance approach to determine the influence of the mortar joints. *Eue J Mech A-Solid*, 55:122–33, 2016.

[9] D'Ambrisi A, Feo L, Focacci F. Masonry arches strengthened with composite unbonded tendons. *Compos Struct*, 98:323–29, 2013.

[10] Mishnaevsky L, Branner K, Petersen HN, Beauson J, McGugan M, Sørensen BF. Materials for wind turbine blades: An overview. materials. *Compos Struct*, 10(11):1285, 2017.

[11] Chortis DI. *Structural Analysis of Composite Wind Turbine Blades*. Springer, 2013.

[12] D'Mello RJ, Maiarù M, Waas AM. Effect of the curing process on the transverse tensile strength of fiber-reinforced polymer matrix lamina using micromechanics computations. *IMMI*, 4(1):119–36, 2015.

[13] D'Mello RJ, Waas AM. Influence of unit cell size and fiber packing on the transverse tensile response of fiber reinforced composites. *Materials*, 12(16):2565, 2019.

[14] Zhang X, Brandyberry DR, Geubelle PH. Igfem-based shape sensitivity analysis of the transverse failure of a composite laminate. *Comput Mech*, 64(5):1455–72, 2019.

[15] Herráez M, Mora D, Naya F, Lopes CS, González C, Llorca J. Transverse cracking of cross-ply laminates: A computational micromechanics perspective. *Compos Sci Technol*, 110:196–204, 2015.

[16] Higuchi R, Aoki R, Yokozeki T, Okabe T. Evaluation of the in-situ damage and strength properties of thin-ply cfrp laminates by micro-scale finite element analysis. *Advanced Composite Materials*, 29(5):475–93, 2020.

[17] Hobbiebrunken T, Fiedler B, Hojo M, Tanaka M. Experimental determination of the true epoxy resin strength using micro-scaled specimens. *Compos Part A-Appl S*, 38:814–18, 2007.

[18] Kaneko R, Kaneko E, Sumigawa T, Kitamura T. Development of experimental methodology on the fracture toughness of microscale polymer resins under in situ observation. *Mat Design Process Comm*, page e102, 2019.

[19] Asp LE, Berglund LA, Gudmundson P. Effects of a composite-like stress state on the fracture of epoxies. *Compos Sci Technol*, 53(1):27–37, 1995.

[20] Asp LE, Berglund LA, Talreja R. A criterion for crack initiation in glassy polymers subjected to a composite-like stress state. *Compos Sci Technol*, 56(11):1291–301, 1996.

[21] Asp LE, Berglund LA, Talreja R. Prediction of matrix-initiated transverse failure in polymer composites. *Compos Sci Technol*, 56(9):1089–97, 1996.

[22] Qiao Y, Zhang Q, Salviato M. Effects of *in-situ* stress state and size scaling on the plastic deformation and fracture behavior of thermoset polymers and related fiber-reinforced composites. *In: Proceedings to 35th Annual Technical Conference on Composite Materials*, 2020.

[23] Talreja R. Physical modelling of failure in composites. *Phil Trans Royal Society A*, 374, 2016.

[24] Elnekhaily S, Talreja R. Effect of axial shear and transverse tension early failure events in unidirectional polymer matrix composites. *Compos Part A-Appl S*, 119:275–82, 2019.

[25] Sahputra IH, Echtermeyer AT. Molecular dynamics simulations of strain-controlled fatigue behaviour of amorphous polyethylene. *J Polym Res*, 21, 2014.

[26] Sahputra IH, Echtermeyer AT. Creep–fatigue relationship in polymer: Molecular dynamics simulations approach. *Macromol Theory Simul*, 24:65–73, 2015.

[27] Quaresimin M. 50th anniversary article: Multiaxial fatigue testing of composites: From the pioneers to future directions. *Macromol Theory Simul*, 51:16–29, 2015.

[28] Owen MJ, Found MS. Static and fatigue failure of glass fibre reinforced polyester resins under complex stress conditions. *Faraday Discuss Chem Soc*, 2:77–89, 1972.

[29] Owen MJ, Griffiths JR. Evaluation of biaxial stress failure surfaces for a glass fabric reinforced polyester resin under static and fatigue loading. *J Mater Sci*, 13:1521–37, 1978.

[30] Owen MJ, Rice DJ. Biaxial strength behaviour of glass reinforced polyester resins. Composite Materials: Testing and Design, ASTM STP 787 EB 1982.

[31] Owen MJ, Rice DJ. Biaxial strength behaviour of glass fabric-reinforced polyester resins. *Composites*, 12(1):13–25, 1981.

[32] Owen MJ, Rice DJ, Griffiths JR, Found MS. Biaxial static and fatigue strength of glass mat and fabric reinforced polyester resins. *In: Proceedings of 35th Annual Technical Conference, Reinforced Plastics/Composite Institute, The Society of the Plastics Industry*, 23(E):1–8, 1980.

[33] Owen MJ. Biaxial fatigue of composites with short and long fibres. *In: Proceeding of 3rd Risø International Symposium on Metallurgy and Materials Science*, pages 101–12, 1982.

[34] Amijima S, Fujii T, Hamaguchi M. Static and fatigue tests of woven glass fabric composite under biaxial tension-torsion loading. *Composites*, 22:281–89, 1991.

[35] Fujii T, Amijima S, Lin F, Sagami T. Study on strength and nonlinear stress-strain response of plain woven glass fiber laminates under biaxial loading. *J Compos Mater*, 26:2493–510, 1992.

[36] Amijima S, Fujii T, Sagami T. Nonlinear behavior of plain woven gfrp under repeated biaxial tension/torsion loading. *J Energ Resour-ASME*, 113(4):235–40, 1991.

[37] Fujii T, Lin F. Fatigue behavior of a plain-woven glass fabric laminate under tension/torsion biaxial loading. *J Compos Mater*, 29:573–90, 1995.

[38] Fujii T, Shina T, Okubo K. Fatigue notch sensitivity of glass woven fabric composite having a circular hole under tension/torsion biaxial loading. *J Compos Mater*, 28(3):234–51, 1994.

[39] Takemura K, Fujii T. Fatigue strength and damage progression in a circular-hole-notched grp composite under combined tension/torsion loading. *Compos Sci Technol*, 52:519–26, 1994.

[40] Takemura K, Fujii T. Fracture mechanics evaluation of progressive fatigue damage in a circular-hole-notched grp composite under combined tension/torsion loading. *Compos Sci Technol*, 52:527–34, 1994.

[41] Talreja R, Singh CV. *Damage and Failure of Composite Materials*. Cambridge University Press, 2012.

[42] Wang SS, Chim ES-M, Socie DF. Biaxial fatigue of fiber-reinforced composites at cryogenic temperature. part i: Fatigue fracture life and damage mechanisms. *J Eng Mater Technol*, 104:128–36, 1982.

[43] Wang SS, Chim ES-M, Socie DF. Stiffness degradation of fiber-reinforced composites under uniaxial tensile, pure torsional, and biaxial fatigue at cryogenic temperature. Composite Materials: Testing and Design, ASTM STP 787 EB, 1982.

[44] Smith EW, Pascoe KJ. Biaxial fatigue of glass-fibre reinforced composite. part 1: fatigue and fracture. *In: Brwon M, Miller KJ, editors. Biaxial and multi-axial fatigue EFG 3. Mechanical Engineering Publications*, pages 396–412, 1989.

[45] Chen AS, Matthews FL. Static and cyclic biaxial bending of cfrp panels. *Compos Sci Technol*, 52:267–73, 1994.

[46] Adden S, Horst P. Damage propagation in non-crimp fabrics under bi-axial static and fatigue loading. *Compos Sci Technol*, 66(5):626–33, 2006.

[47] Quaresimin M, Carraro PA. On the investigation of the biaxial fatigue behaviour of unidirectional composites. *Compos Part B*, 54:200–8, 2013.

[48] Quaresimin M, Carraro PA, Mikkelsen LP, Lucato N, Vivian L, Brondsted P, Sørensen BF, Varna J, Talreja R. Damage evolution under cyclic multi-axial stress state: A comparative analysis between glass/epoxy laminates and tubes. *Compos Part B*, 61:282–90, 2014.

[49] Quaresimin M, Carraro PA. Damage initiation and evolution in glass/epoxy tubes subjected to combined tension–torsion fatigue loading. *Int J Fatigue*, 63:26–35, 2014.

[50] Maragoni L, Carraro PA. Quaresimin m. fatigue behaviour of glass/epoxy laminates in the presence of voids. *Int J Fatigue*, 95:18–28, 2017.

[51] Quaresimin M, Carraro PA, Maragoni L. Quaresimin m. early stage damage in off-axis plies under fatigue loading. *Compos Sci Technol*, 128:147–54, 2016.

[52] Maragoni L, Carraro PA, Quaresimin M. Quaresimin m. effect of voids on the crack formation in a $[+45/\text{-}45/0]_s$ laminate under cyclic axial tension. *Compos Part A-Appl S*, 91:493–500, 2016.

[53] Quaresimin M, Susmel L, Talreja R. Fatigue behaviour and life assessment of composite laminates under multiaxial loadings. *Int J Fatigue*, 32(1):2–16, 2010.

[54] Papageorgiou DG, Kinloch IA, Young RJ. Mechanical properties of graphene and graphene-based nanocomposites. *Prog Mater Sci*, 90:75–127, 2017.

[55] Bažant ZP, Kim KT, Yu Q. Non-uniqueness of cohesive-crack stress-separation law of human and bovine bones and remedy by size effect tests. *Int J Fract*, 181:67–81, 2013.

[56] Morel G, Dourado N, Valentin G. Wood: a quasibrittle material r-curve behavior and peak load evaluation. *Int J Fract*, 131:385–400, 2005.

[57] Bažant ZP, Kazemi MT. Size effect in fracture of ceramics and its use to determine fracture energy and effective process zone length. *J Am Ceram Soc*, 73:1841–53, 1990.

[58] Wen L, Bažant ZP. General fishnet statistics of strength: Nacreous, biomimetic, concrete, octet-truss, and other architected or quasibrittle materials. *J Appl Mech*, 87(3):031015, 2020.

[59] Bažant ZP. Scaling of sea ice fracture—part i: Vertical penetration. *J Appl Mech*, 69(1):11–8, 2002.

[60] Bažant ZP. Scaling of sea ice fracture—part ii: Horizontal load from moving ice. *J Appl Mech*, 69(1):19–24, 2002.

[61] Hexion. Bellevue, Washington, USA http://hexion.com.

[62] Vacmobiles. Auckland, New Zealand https://www.vacmobiles.com.

[63] TAP Plastics. Seattle, Washington, USA http://www.tapplastics.com.

[64] ASTM D638-02a. Standard Test Method for Tensile Properties of Plastics 2003.

[65] ASTM D5045-99. Standard Test Methods for Plane-Strain Fracture Toughness and Stain Energy Release Rate of Plastic Materials 1999.

[66] Rinne H. *The Weibull distribution: a handbook*. CRC Press, 2008.

[67] Barsoum R. A degenerate solid element for linear fracture analysis of plate bending and general shells. *Int J Numer Meth Eng*, 10(3):551–64, 1976.

[68] Rice J. A path independent integral and the approximate analysis of strain concentration by notches and cracks. *J Appl Mech*, 35(2):379–86, 1968.

[69] Martínez-López M, Martínez-Barrera G, Nunes LCS, Reis JML, da Costa Mattos HS. Mixed mode fracture analysis in a polymer mortar using the brazilian disk test. *Eng Fract Mech*, 154:140–51, 2016.

[70] Zeinedini A. A novel fixture for mixed mode i/ii/iii fracture testing of brittle materials. *Fatigue Fract Eng Mater Struct*, 42:838–53, 2018.

[71] Bahmani A, Aliha MRM, Sarbijan MJ, Mousavi SS. An extended edge-notched dis bend (endb) specimen for mixed-mode i+ii fracture assessments. *Int J Solids Struct*, 193:239–50, 2020.

[72] Zappalorto M, Salviato M, Quaresimin M. Mixed mode (i+ii) fracture toughness of polymer nanoclay nanocomposite. *Eng Fract Mech*, 111:50–64, 2013.

[73] Kumar A, Roy S. Characterization of mixed mode fracture properties of nanographene reinforced epoxy and mode i delamination of its carbon fiber composite. *Compos Part B*, 134:98–105, 2018.

[74] Popelar CF, Liechti KM. Multiaxial nonlinear viscoelastic characterization and modeling of a structural adhesive. *J Eng Mater Technol*, 119(3):205–10, 1997.

[75] Chowdhury SC, Elder RM, Sirk TW, Gillespie Jr JW. Epoxy resin thermo-mechanics and failure modes: Effects of cure and cross-linker length. *Compos Part B*, 186:107814, 2020.

[76] Unified nano-mechanics based probabilistic theory of quasibrittle and brittle structures: I. strength, static crack growth, lifetime and scaling. *J Mech Phys Solids*, 59:1291–321, 2011.

[77] Bažant ZP, Le JL, Bazant MZ. Scaling of strength and lifetime probability distributions of quasibrittle structures based on atomistic fracture mechanics. *Proceedings of the National Academy of Sciences*, 106(28):11484–89, 2009.

[78] Xu Z, Le JL. A first passage based model for probabilistic fracture of polycrystalline silicon mems structures. *J Mech Phys Solids*, 99:225–41, 2017.

[79] Salviato M, Bažant ZP. The asymptotic stochastic strength of bundles of elements exhibiting general stress–strain laws. *Probabilist Eng Mech*, 36:1–7, 2014.

[80] Salviato M, Kirane K, Bažant ZP. Statistical distribution and size effect of residual strength of quasibrittle materials after a period of constant load. *J Mech Phys Solids*, 64:440–54, 2014.

[81] Zike S, Sørensen BF, Mikkelsen LP. Experimental determination of the micro-scale strength and stress-strain relation of an epoxy resin. *Mater Design*, 98:47–60, 2016.

[82] Cusatis G, Schauffert EA. Cohesive crack analysis of size effect. *Eng Fract Mech*, 76:2163–73, 2009.

[83] Xiao K, Ye L, Kwok YS. Effects of precracking methods on fracture behaviour of an araldite-f epoxy and its rubber-modified systems. *J Mater Sci*, 33:2831–36, 1998.

[84] Cayard MS, Bradley WL. The effect of various precracking techniques on the fracture toughness of plastics. *International Conference of Fracture ICF7 (Houston. USA)*, pages 2713–23, 1980.

[85] Salazar A, Patel Y, Williams JG. Influence of crack sharpness on the fracture toughness of epoxy resin. *13th International Conference on Fracture*, 2013.

[86] Souza JM, Yoshimura HN, Peres FM, Schön CG. Effect of sample pre-cracking method and notch geometry in plane strain fracture toughness tests as applied to a pmma resin. *Polym Test*, 31:834–40, 2012.

[87] Kuppusamy N, Tomlinson RA. Repeatable pre-cracking preparation for fracture testing of polymeric materials. *Eng Fract Mech*, 152:81–7, 2016.

[88] Di Luzio G, Cusatis G. Cohesive crack analysis of size effect for samples with blunt notches and generalized size effect curve for quasi-brittle materials. *Eng Fract Mech*, 204:15–28, 2018.

[89] Kinloch AJ, Williams JG. Crack blunting mechanisms in polymers. *J Mater Sci*, 15:987–96, 1980.

[90] Gómez FJ, Elices M, Berto F, Lazzarin P. A generalized notch stress intensity factor of u-notched components loaded under mixed mode. *Eng Fract Mech*, 75(16):4819–33, 2008.

[91] Gómez FJ, Guinea GV, Elices M. Failure criteria for linear elastic materials with u-notches. *Int J Fract*, 143:99–113, 2006.

[92] Atrzori B, Lazzarin P, Meneghetti G. Fracture mechanics and notch sensitivity. *Fatigue Fract Eng M*, 26:257–67, 2003.

[93] Atrzori B, Lazzarin P. Notch sensitivity and defect sensitivity under fatigue loading: two sides of the same medal. *Int J Fracture*, 107:1–8, 2001.

[94] Mefford CH, Qiao Y, Salviato M. Failure and scaling of graphene nanocomposites. *Compos Struct*, 176:961–72, 2017.

[95] Qiao Y, Salviato M. A cohesive zone modeling study on the fracturing behavior of thermoset polymer nanocomposites. *In: Proceedings to 33rd Annual Technical Conference, 18th US-Japan Conference on Composite Materials ASTM D30*, 2018.

[96] Qiao Y, Salviato M. Study of the fracturing behavior of thermoset polymer nanocomposites via cohesive zone modeling. *Compos Struct*, 220:127–47, 2019.

[97] Ko S, Tuttle ME, Yang J, Salviato M. Characterization and computational modeling of the fracturing behavior in discontinuous fiber composite structures. *In: Proceedings to 33rd Annual Technical Conference, 18th US-Japan Conference on Composite Materials ASTM D30*, 2018.

[98] Ko S, Yang J, Tuttle ME, Salviato M. Effect of the platelet size on the fracturing behavior and size effect of discontinuous fiber composite structures. *Compos Struct*, 227:111345, 2019.

[99] Ko S, Davey J, Douglass S, Yang J, Tuttle ME, Salviato M. Effect of the thickness on the fracturing behavior of discontinuous fiber composite structures. *Composites Part A*, 125:105520, 2019.

[100] Deleo AA, Salviato M. Computational study for size effect in composites and nanocomposites. *In: Proceedings to 33rd Annual Technical Conference, 18th US-Japan Conference on Composite Materials ASTM D30*, 2018.

[101] Bažant ZP, Daniel IM, Li Z. Size effect and fracture characteristics of composite laminates. *J Eng Mater-T ASME*, 118:317–24, 1996.

[102] Bažant ZP, Planas J. *Fracture and size effect in concrete and other quasi-brittle materials*. CRC Press, 1998.

[103] Salviato M, Kirane K, Ashari SE, Bažant ZP. Experimental and numerical investigation of intra-laminar energy dissipation and size effect in two-dimensional textile composites. *Compos Sci Technol*, 135:67–75, 2016.

[104] Tada H, Paris PC, Irwin GR. *The stress analysis of cracks handbook third edition*. American Society of Mechanical Engineers, 2000.

[105] Morgan RJ, O'Neal JE. The microscopic failure processes and their relation to the structure and their relation to the structure of amine-cured bisphenol-a-diglycidyl ether epoxies. *J Mater Sci*, 12:1966–80, 1977.

[106] Sue HJ, Garcia-Meitin EI, Yang PC, Bishop MT. Crazing in high-performance thermoset resins. *J Mater Sci Lett*, 12:1463–66, 1993.

[107] Sue HJ, Bertram JL, Garcia-Meitin EI, Puckett PM. Characterization and promotion of dilatation bands in toughenable thermosetting resins. *J Polym Sci*, 33:2003–17, 1995.

[108] Qiao Y, Salviato M. Strength and cohesive behavior of thermoset polymers at the microscale: A size-effect study. *Eng Fract Mech*, 213:100–17, 2019.

[109] Ladner LS, Cullinan MA, Saha SK. Tensile properties of polymer nanowires fabricated via two-photo lithography. *RSC Adv*, 9:28803–13, 2019.

[110] Yang SR, Qu JM. Coarse-grained molecular dynamics simulations of the tensile behavior of a thermosetting polymer. *Phys Rev E*, 90(1):012601, 2014.

[111] Bžant ZP, Gettu R. Rate effects and load relaxation in static fracture of concrete. *Aci Mater J*, 89:456–68, 1992.

[112] Di Luzio G. Numerical model for time-dependent fracturing of concrete. *J Eng Mech*, 135:632–40, 2009.

[113] Gross B. Least squares best fit method for the three parameter weibull distribution: analysis of tensile and bend specimens with volume or surface flaw failure. *NASA TM-4721*, 1996.

[114] Lohbauer U, Petchelt A, Greil P. Lifetime prediction of cad/cam dental ceramics. *J Biomed Mater Res*, 63(6):780–85, 2002.

[115] Munz D, Fett T. *Ceramics: Mechanical Properties, Failure Behavior, Materials Selection.* Springer-Verlag, 1999.

[116] Salem JA, Nemeth NN, Powers LP, Choi SR. Reliability analysis of uniaxially ground brittle materials. *J Eng Gas Turbines Power*, 118:863–71, 1996.

[117] Tinschert J, Zwez D, Marx R, Ausavice KJ. Structural reliability of alumina-, feldspar-, leucite-, mica- and zirconia-based ceramics. *J Dent*, 28:529–35, 2000.

[118] Bažant ZP, Le JL. *Probabilistic Mechanics of Quasibrittle Structures: Strength, Lifetime, and Size Effect*. Cambridge University Press, 2017.

[119] Psylotech. Evanston, Illinios, USA https://www.psylotech.com.

[120] Olympus Corporation. Tokyo, Japan, USA https://www.olympus-ims.com.

[121] Wang TJ, Kishimoto K, Notomi M. Effect of triaxial stress constraint on the deformation and fracture of polymers. *Acta Mechanica Sinica*, 18(5):480–93, 2002.

[122] Kinloch AJ. *Fracture Behaviour of Polymers*. Springer Netherlands, 1995.

[123] Neogi A, Mitra N, Ramesh T. Cavitation in epoxies under composite-like stress states. *Compos Part A-Appl S*, 106(5):52–58, 2018.

[124] Chevalier J, Morelle XP, Bailly C, Camanho PP, Pardoen T, Lani F. Micro-mechanics based pressure dependent failure model for highly crosslinked epoxy resins. *Eng Fract Mech*, 158:1–12, 2016.

[125] Nguyen HT, Pathirage M. Rezaei M, Issa M, Cusatis G, Bažant ZP. New perspective of fracture mechanics inspired by gap test with crack-parallel compression. *Proceedings of the National Academy of Sciences*, 117(25):14015–20, 2020.

[126] Nguyen HT, Pathirage M, Cusatis G, Bažant ZP. Gap test of crack-parallel stress effect on quasibrittle fracture and its consequences. *J Appl Mech*, 87(7):071012, 2020.

[127] Wang JF, Zhang XH, Jiang L, Qiao JL. Advances in toughened polymer materials by structured rubber particles. *Prog Polym Sci*, 98:101160, 2019.

[128] Argon AS, Cohen RE. Toughenability of polymers. *Polymer*, 44:6013–32, 2003.

[129] Argon AS, Cohen RE, Mower TM. Mechanisms of toughening brittle polymers. *Mater Sci Eng*, 176:79–90, 1994.

[130] Pineau A, Benzerga AA, Pardoen T. Failure of metals i: Brittle and ductile fracture. *Acta Mater*, 107:424–83, 2016.

[131] Graphene Supermarket. New York, USA https://graphene-supermarket.com.

[132] Mixer Direct. Louisville, USA http://www.mixerdirect.com.

[133] Hielscher Ultrasound Technology. Ringwood, USA https://www.hielscher.com.

[134] Quaresimin M, Salviato M, Zappalorto M. Fracture and interlaminar properties of clay-modified epoxies and their glass reinforced laminates. *Eng Fract Mech*, 81:80–93, 2012.

[135] Zappalorto M, Salviato M, Pontefisso A, Quaresimin M. Notch effect in clay-modified epoxy: a new perspective on nanocomposite properties. *Compos Interfaces*, 20(6):405–19, 2013.

[136] Jeol. Tokyo, Japan http://www.jeol.co.jp/en/.

[137] Chandrasekaran S, Seidel C, Schulte K. Preparation and characterization of graphite nano-platelet (gnp)/epoxy nano-composite: mechanical, electrical and thermal properties. *Eur Polym J*, 49(12):3878–88, 2013.

[138] Chandrasekaran S, Sato N, Tölle F, Mülhaupt R, Fiedler B, Schulte K. Fracture toughness and failure mechanism of graphene based epoxy composites. *Compos Sci Technol*, 97:90–99, 2014.

[139] Bažant ZP. Size effect in blunt fracture: concrete, rock, metal. *J Eng Mech-ASCE*, 110(4):518–35, 1984.

[140] Bažant ZP, Kazemi MT. Determination of fracture energy, process zone length and brittleness number from size effect, with application to rock and concrete. *Int J Fracture*, 44:111–31, 1990.

[141] Salviato M, Zappalorto M, Quaresimin M. The effect of surface stresses on the critical debonding stress around nanoparticles. *Int J Fracture*, 172(1):97–103, 2011.

[142] Salviato M, Zappalorto M, Quaresimin M. Plastic yielding around nanovoids. *Procedia Engineer*, 10:3316–21, 2011.

[143] Zappalorto M, Salviato M, Quaresimin M. Influence of the interphase zone on the nanoparticle debonding stress. *Compos Sci Technol*, 72(1):49–55, 2011.

[144] Zappalorto M, Salviato M, Quaresimin M. Assessment of debonding-induced toughening in nanocomposites. *Procedia Engineer*, 10:2973–78, 2011.

[145] Zappalorto M, Salviato M, Quaresimin M. A multiscale model to describe nanocomposite fracture toughness enhancement by the plastic yielding of nanovoids. *Compos Sci Technol*, 72(14):1683–91, 2012.

[146] Zappalorto M, Salviato M, Quaresimin M. Stress distributions around rigid nanoparticle. *Int J Fracture*, 176(1):105–12, 2012.

[147] Salviato M, Zappalorto M, Quaresimin M. Plastic shear bands and fracture toughness improvements of nanoparticle filled polymers: a multiscale analytical model. *Compos Part A-Appl S*, 48:144–52, 2013.

[148] Salviato M, Zappalorto M, Quaresimin M. Nanoparticle debonding strength: a comprehensive study on interfacial effects. *Int J Solids Struct*, 50(20):3225–32, 2013.

[149] Quaresimin M, Salviato M, Zappalorto M. A multi-scale and multi-mechanism approach for the fracture toughness assessment of polymer nanocomposites. *Int J Solids Struct*, 91:16–21, 2014.

[150] Mettler Toledo DSC 3+. Columbus, Ohio State, USA https://www.mt.com.

[151] Hakvoort G, Van Reijen LL, Aartsen AJ. Measurement of the thermal conductivity of solid substances by dsc. *Thermochimica Acta*, 93:317–20, 1985.

[152] Kamal MR. Thermoset characterization for moldability analysis. *Polymer Engineering and Science*, 14(3):231–239, 1974.

[153] Jiang T, Kuila T, Kim NH, Ku BC, Lee JH. Enhanced mechanical properties of silanized silica nanoparticle attached graphene oxide/epoxy composites. *Compos Sci Technol*, 79:115–25, 2013.

[154] Konnola R, Nair CPR, Joseph K. High strength toughened epoxy nanocomposite based on poly(ether sulfone)-grafted multi-walled carbon nanotube. *Polym Advan Technol*, 27:82–89, 2015.

[155] Carolan D, Ivankovic A, Kinloch AJ, Sprenger S, Taylor AC. Toughening of epoxy-based hybrid nanocomposites. *Polymer*, 97:179–90, 2016.

[156] Zamanian M, Mortezaei M, Salehnia B, Jam JE. Fracture toughness of epoxy polymer modified with nanosilica particles: particle size effect. *Eng Fract Mech*, 97:193–206, 2013.

[157] Kim BC, Park SW, Lee DG. Fracture toughness of the nano-particle reinforced epoxy composite. *Compos Struct*, 86:69–77, 2008.

[158] Vaziri HS, Abadyan M, Nouri M, Omaraei IA, Sadredini Z, Ebrahimnia M. Investigation of the fracture mechanism and mechanical properties of polystyrene/silica nanocomposite in various silica contents. *J Mater Sci*, 46:5628–38, 2011.

[159] Dittanet P, Pearson R. Effect of silica nanoparticle size on toughening mechanisms of filled epoxy. *Polymer*, 53:1890–1905, 2012.

[160] Liu HY, Wang GT, Mai YW, Zeng Y. On fracture toughness of nano-particle modified epoxy. *Compos Part B-Eng*, 42:2170–75, 2011.

[161] Suman C, Nitai CA, Pranab S, Naresh CM, Tapas K. Functionalized reduced graphene oxide/epoxy composites with enhanced mechanical properties and thermal stability. *Polym Test*, 61:1–11, 2017.

[162] Mirjalili V, Ramachandramoorthy R, Hubert P. Fenhancement of fracture toughness of carbon fiber laminated composites using multi wall carbon nanotubes. *Carbon*, 79:413–23, 2014.

[163] Paris PC, Erdogan F. A critical analysis of crack propagation law. *J Basic Eng*, 85:528–34, 1963.

[164] Kirane K, Bažant ZP. Size effect in paris law and fatigue lifetimes for quasibrittle materials: Modified theory, experiments and micro-modeling. *Int J Fatigue*, 83:209–20, 2016.

[165] Xu KM, Baănt ZP. Size effect in fatigue fracture of concrete. *ACI Mater J*, 88(4):390–99, 1991.

[166] L JL, Manning J, Labuz JF. Scaling of fatigue crack growth in rock. *Int J Rock Mech Min*, 72:71–9, 2014.

[167] L JL, Bažant ZP. Unified nano-mechanics based probabilistic theory of quasibrittle and brittle structures: Ii. fatigue crack growth, lifetime and scaling. *J Mech Phys Solids*, 59(7):1322–37, 2011.

[168] Kramers HA. Brownian motion in a field of force and the diffusion model of chemical reaction. *Pysica*, 7:284–304, 1941.

[169] Harper PW, Hallett SR. A fatigue degradation law for cohesive interface elements – development and application to composite materials. *Int J Fatig*, 32:1774–87, 2010.

[170] Landry B, LaPlante G. Modeling delamination growth in composites under fatigue loadings of varying amplitudes. *Compos Part B*, 43:533–41, 2012.

[171] May M, Hallett SR. A combined model for initiation and propagation of damage under fatigue loading for cohesive interface elements. *Compos Part A-Appl S*, 41:1787–96, 2010.

[172] Turon A, Costa J, Camanho PP, Dávila CG. Simulation of delamination in composites under high-cycle fatigue. *Compos Part A-Appl S*, 38:2270–82, 2007.

[173] Khoramishad H, Crocombe AD, Katnam KB, Ashcroft IA. Fatigue damage modelling of adhesively bonded joints under variable amplitude loading using a cohesive zone model. *Eng Fract Mech*, 78:3212–25, 2011.

[174] Nguyen O, Pepetto EA, Ortiz M, Radovitzky RA. A cohesive model of fatigue crack growth. *Int J Fract*, 110:351–69, 2001.

[175] Ortiz M, Pandolfi A. Finite-deformation irreversible cohesive elements for three-dimensional crack-propagation analysis. *Int J Numer Meth Eng*, 44(9):1267–82, 1999.

[176] Robinson P, Galvanetto U, Tumino D, Bellucci G, Violeau D. Numerical simulation of fatigue-driven delamination using interface elements. *Int J Numer Meth Eng*, 63:1824–48, 2005.

[177] Roe KL, Siegmund T. An irreversible cohesive zone model for interface fatigue crack growth simulation. *Eng Fract Mech*, 70:209–32, 2003.

[178] Yang B, Mall S, Ravi-Chandar K. A cohesive zone model for fatigue crack growth in quasibrittle materials. *Int J Solids Struct*, 38:3927–44, 2001.

[179] Yang QD, Shim DJ, Spearing SM. A cohesive zone model for low-cycle fatigue life prediction of solder joints. *ASME J Microelectron Eng*, 75:85–95, 2004.

[180] Maiti S, Geubelle PH. A cohesive model for fatigue failure of polymers. *Eng Fract Mech*, 72:691–708, 2005.

[181] Brown EN. Fracture and fatigue of a self-healing polymer composite material. *PhD dissertation, University of Illinois at Urbana-Champaign*, 2003.

[182] Dávila CG. From s-n to the paris law with a new mixed-mode cohesive fatigue model for delamination in composites. *Theor Appl Fract Mech*, 106:102499, 2020.

[183] Nojavan S, Schesser D, Yang QD. An in situ fatigue-czm for unified crack initiation and propagation in composites under cyclic loading. *Compos Struct*, 146:34–49, 2016.

[184] MSC Software. Newport Beach, California, USA https://www.mscsoftware.com.

[185] Daniel IM, Ishai O. *Engineering Mechanics of Composite Materials*. Oxford University Press, 2005.

[186] Mortell DJ, Tanner DA, McCarthy CT. An experimental investigation into multi-scale damage progression in laminated composites in bending. *Compos Struct*, 149:33–40, 2016.

[187] Maragoni L, Carraro PA, Quaresimin M. Development, validation and analysis of an efficient micro-scale representative volume element for unidirectional composites. *Compos Part A-Appl S*, 110:268–83, 2018.

[188] Garapati SH. Analysis of single fiber pushout test of fiber reinforced composite with a nonhomogeneous interphase. *MS Thesis, University of South Florida*, 2009.

[189] Feih S, Wonsyld K, Minzari D, Westermann P, Lilholt H. Testing procedure for the single fiber fragmentation test. *Riso report R-1483, Riso National Laboratory*, 2004.

[190] Sockalingam S, Nilakantan G. Fiber-matrix interface characterization through the microbond test. *Int J Aeronaut Space Sci*, 13(3):282–95, 2012.

[191] Miller B, Muri P, Rebenfeld L. A microbond method for determination of the shear strength of a fiber/resin interface. *Compos Sci Technol*, 28:17–32, 1987.

[192] Nishikawa M, Okabe T, Hemmi K, Takeda N. Micromechanical modeling of the microbond test to quantify the interfacial properties of fiber-reinforced composites. *Int J Solids Struct*, 45:4098–4113, 2008.

[193] Nishikawa M, Okabe T, Hemmi K, Takeda N. Fracture analysis of carbon fiber/epoxy matrix interface through microbond and cruciform tests. *MS Thesis, University of Illinois at Urbana-Champaign*, 2016.

[194] FibreGlast. Brookville, Ohio State, USA https://www.fibreglast.com/.

[195] Arndt CM, Carvalho NV, Czabaj MW. Experimental reexamination of transverse tensile strength for im7/8552 tape-laminate composites. *J Compos Mater*, 54(3297–312), 2020.

[196] Talreja R. Fatigue of composite materials: damage mechanisms and fatigue life diagrams. *Proc Roy Soc Lond A*, 378:461–75, 1981.

[197] Sims DF, Brogdon VH. Fatigue behaviour of composites under different loading modes. Fatigue of filamentary materials. ASTM STP 636, 1977.

[198] Tsai SW. Strength theories of filamentary structures. *In: Schwartz RT, Schwartz HS, editors. Fundamental aspects of fibre reinforced plastic Composites. NewYork: Wiley Interscience*, pages 3–11, 1968.

[199] Francis PH, Walrath DE, Sims DF, Weed DN. Biaxial fatigue loading of notched composites. *J Compos Mater*, 11:488–501, 1977.

[200] Tsai SW, Wu EM. A general theory of strength for anisotropic materials. *J Compos Mater*, 5:58–80, 1971.

[201] Aboul Wafa MN, Hamdy AH, El-Midany AA. Combined bending torsional fatigue of woven rowing grp. *J Eng Mater Technol (Trans ASME)*, 119:181–5, 1997.

[202] Kawai M, Yajima S, Hachinohe A, Takano Y. Off-axis fatigue behaviour of unidirectional carbon fiber-reinforced composites at room and high temperatures. *J Compos Mater*, 35(7):545–76, 2001.

[203] Philippidis TP, Vassilopoulos AP. Fatigue strength prediction under multiaxial stress. *J Compos Mater*, 33(17):1578–99, 1999.

[204] Singh CV, Talreja R. Analysis of multiple off-axis ply cracks in composite laminates. *Int J Solids Struct*, 45(16):4574–89, 2008.

[205] McCartney LN. Mechanics of matrix cracking in brittle-matrix fibre-reinforced composites. *Proc Roy Soc Lond A*, 409(1837):329–50, 1987.

[206] McCartney LN. New theoretical model of stress transfer between fibre and matrix in a uniaxially fibre-reinforced composite. *Proc Roy Soc Lond A*, 425(1868):215–44, 1989.

[207] McCartney LN. Analytical models of stress transfer in unidirectional composites and cross-ply laminates, and their application to the prediction of matrix/transverse cracking. *In: : Reddy JN., Reifsnider K, editors. Local mechanics concepts for composite material systems*, pages 251–82, 1992.

[208] McCartney LN. Theory of stress transfer in a $0°-90°-0°$ cross-ply laminate containing a parallel array of transverse cracks. *J Mech Phys Solids*, 40(1):27–68, 1992.

[209] McCartney LN, Schoeppner GA, Becker W. Comparison of models for transverse ply cracks in composite laminates. *Compos Sci Technol*, 60(12-13):2347–59, 2000.

[210] McCartney LN. Physically based damage models for laminated composites. *In: Proceedings of the Institution of Mechanical Engineers, Part L: Journal of Materials: Design and Applications*, 217(3):163–99, 2003.

[211] Lundmark P, Varna J. Constitutive relationships for laminates with ply cracks in in-plane loading. *Int J Damage Mech*, 14(3):235–59, 2005.

[212] Lundmark P, Varna J. Crack face sliding effect on stiffness of laminates with ply cracks. *Compos Sci Technol*, 66(10):1444–54, 2006.

[213] Carraro PA, Quaresimin M. A stiffness degradation model for cracked multidirectional laminates with cracks in multiple layers. *Int J Solids Struct*, 58:34–51, 2015.

[214] Carraro PA, Maragoni L, Quaresimin M. Prediction of the crack density evolution in multidirectional laminates under fatigue loadings. *Compos Sci Technol*, 145:24–39, 2017.

[215] Mitsubishi Chemical Carbon Fiber and Composites, Sacramento, California, USA http://www.mccfc.com/.

[216] ASTM D3039/D3039M-17 - Standard Test Method for Tensile Properties of Polymer Matrix Composite Materials.

[217] Tan JLY, Deshpande VS, Fleck NA. Failure mechanisms of a notched cfrp laminate under multi-axial loading. *Compos Part A-Appl S*, 77:56–66, 2015.

[218] Harilal R, Ramji M. Adaptation of open source 2d dic software ncorr for solid mechanics applications. *In: Proceedings of 9th International Symposium on Advanced Science and Technology in Experimental Mechanics, New Delhi, November*, 2014.

[219] Blaber J, Adair B, Antoniou A. Ncorr: open-source 2d digital image correlation matlab software. *Exp Mech*, 55(6):1106–22, 2015.

[220] Ng WH, Salvi AG, Waas AM. Characterization of the in-situ non-linear shear response of laminated fiber-reinforced composites. *Compos Sci Technol*, 70:1126–34, 2010.

[221] Salviato M, Ashari SE, Cusatis G. Spectral stiffness microplane model for damage and fracture of textile composites. *Compos Struct*, 137:170–84, 2016.

[222] Kirane K, Salviato M, Bažant ZP. Microplane triad model for simple and accurate prediction of orthotropic elastic constants of woven fabric composites. *J Compos Mater*, 50(9):1247–60, 2015.

[223] Bažant ZP, Cedolin L. *Stability of Structures: Elastic, Inelastic, Fracture and Damage Theories*. New York: Dover Publications, 2003.

[224] Salviato M, Chau VT, Li W, Bažant ZP, Cusatis G. Direct testing of gradual postpeak of fracture specimens of fiber composites stabilized by enhanced grip stiffness and mass. *J Appl Mech*, 83(11):111003, 2016.

[225] Salviato M, Chau VT, Li W, Bažant ZP, Cusatis G. Patent NO.US20180259431A1, Grips For A Linear Fracture Testing Machine And Method of Designing Same.

[226] Xu X, Wisnom MR, Mahadik Y, Hallett SR. An experimental investigation in size effects in quasi-isotropic carbon epoxy laminates with sharp and blunt notches. *Compos Sci Technol*, 100:220–7, 2014.

[227] Salviato M, Kirane K, Bažant ZP, Cusatis G. Mode i and ii interlaminar fracture in laminated composites: a size effect study. *J Appl Mech*, 86(9):091008, 2019.

[228] Kirane K, Salviato M, Bažant ZP. Microplane-triad model for elastic and fracturing behavior of woven composites. *J Appl Mech*, 83(4):041006, 2016.

[229] Qiao Y, Deleo AA, Salviato M. A study on the multi-axial fatigue failure behavior of notched composite laminates. *Compos Part A-Appl S*, 127:105640, 2019.

[230] Pearce GM, Tao C, Quek YHE, Chowdhury NT. A modified arcan test for mixed-mode loading of bolted joints in composite structures. *Composite Structures*, 187(1):203–11, 2018.

[231] Laux T, Gan KW, Dulieu-Barton JM, Thomsen OT. A simple nonlinear constitutive model based on non-associative plasticity for ud composites: Development and calibration using a modified arcan fixture. *Int J Solids Struct*, 162(1):135–47, 2019.

[232] Mirza MS, Barton DC, Church P. The effect of stress triaxiality and strain-rate on the fracture characteristics of ductile metals. *J Mater Sci*, 31:453–61, 1996.

[233] Li W, Qiao Y, Cusatis G, Salviato M. Experimental characterization of the comprehensive mechanical properties of three-dimensional woven composites (to be submitted). 2020.

[234] Carraro PA, Maragoni L, Quaresimin M. Influence of load ratio on the biaxial fatigue behavior of glass/epoxy tubes under combined tension-tension loading. *Compos Part A-Appl S*, 78:294–302, 2014.

[235] Jones DL, Poulose PK, Liebowitz H. Effect of biaxial loads on the static and fatigue properties of composite materials. Multi-axial fatigue. ASTM STP 853, 1985.

[236] Kortschot MT, Beaumont PWR. Damage mechanics of composite materials: I-measurements of damage and strength. *Compos Sci Technol*, 39:289–301, 1990.

[237] Spearing SM, Beaumont PWR. Fatigue damage mechanics of composite materials. i: experimental measurement of damage and post-fatigue properties. *Compos Sci Technol*, 44:159–68, 1992.

[238] De Morais AB. Open-hole tensile strength of quasi-isotropic laminates. *Compos Sci Technol*, 60:1997–2004, 2000.

[239] Bourchak M, Farrow IR, Bond IP, Rowland CW, Menan F. Acoustic emission energy as a fatigue damage parameter for cfrp composites. *Int J Fatigue*, 29:457–70, 2007.

[240] Silversides L, Maslouhi A, Laplante G. Acoustic emission monitoring of interlaminar delamination onset in carbon fibre composites. *Struct Health Monit*, 12(2):126–40, 2013.

[241] Lomov SV, Ivanov DS, Truong TC, Verpoest I, Baudry F, Bosche KV, Xie H. Experimental methodology of study of damage initiation and development in textile composites in uniaxial tensile test. *Compos Sci Technol*, 68(12):2340–9, 2008.

[242] Barile C, Casavola C, Pappalettera G, Vimalathithan PK. Damage characterization in composite materials using acoustic emission signal-based and parameter-based data. *Compos Part B-Eng*, 178:107468, 2019.

[243] Azadi M, Sayar H, Ghasemi-Ghalebahman A, Jafari SM. Tensile loading rate effect on mechanical properties and failure mechanisms in open-hole carbon fiber reinforced polymer composites by acoustic emission approach. *Compos Part B-Eng*, 158:448–58, 2019.

[244] Meola C, Boccardi S, Carlomagno GM. *Infrared Thermography in the Evaluation of Aerospace Composite Materials*. Woodhead Publishing, 2016.

[245] Meola C, Carlomagno GM. Infrared thermography to evaulate impact damage in glass/epoxy with manufacturing defects. *Int J Impact Eng*, 67:1–11, 2014.

[246] Meola C, Boccardi S, Carlomagno GM, Boffa ND, Monaco E, Ricci F. Nondestructive evaluation of carbon fibre reinforced composites with infrared thermography and ultrasonics. *Compos Struct*, 134:845–53, 2015.

[247] Goidescu C, Welemane H, Garnier C, Fazzini M, Brault R, Péronnet E, Mistou S. Damage investigation in cfrp composites using full-field measurement techniques: Combination of digital image stereo-correlation, infrared thermography and x-ray tomography. *Compos Part B-Eng*, 48:95–105, 2013.

[248] Umar MZ, Vavilov V, Abdullah H, Ariffin AK. Quantitative study of local heat sources by ultrasonic infrared thermography: An approach for estimating total energy released by low energy impact damage in c/c composite. *Compos Part B-Eng*, 165:167–73, 2019.

[249] Scarponi C, Briotti G. Ultrasonic technique for the evaluation of delaminations on cfrp, gfrp, kfrp composite materials. *Compos Part B-Eng*, 31:237–43, 2000.

[250] Ivanov D, Ivanov S, Lomov S, Verpoest I. Strain mapping analysis of textile composites. *Opt Laser Eng*, 47:360–70, 2009.

[251] Quek SC, Waas AM, Shahwan KW, Agaram V. Compressive response and failure of braided textile composite: part i-experiments. *Int J Non-linear Mech*, 39:635–48, 2004.

[252] Mehdikhani M, Steensels E, Standaert A, Vallons KAM, Gorbatikh L, Lomov SV. Multi-scale digital image correlation for detection and quantification of matrix cracks in carbon fiber composite laminates in the absence and presence of voids controlled by the cure cycle. *Compos Part B-Eng*, 154:138–47, 2018.

[253] Garcea SC, Wang Y, Withers PJ. X-ray computed tomography of polymer composites. *Compos Sci Technol*, 156:305–19, 2018.

[254] Yu B, Blanc R, Soutis C, Withers PJ. Evolution of damage during the fatigue of 3d woven glass-fibre reinforced composites subjected to tension–tension loading observed by time-lapse x-ray tomography. *Compos Part A-Appl S*, 82:279–90, 2016.

[255] McCombe GP, Rouse J, Trask RS, Withers PJ, Bond IP. X-ray damage characterisation in self-healing fibre reinforced polymers. *Compos Part A-Appl S*, 43:613–20, 2012.

[256] Zhou YW, Zheng YW, Pan J, Sui LL, Xing F, Sun HF, Li PD. Experimental investigations on corrosion resistance of innovative steel-frp composite bars using x-ray microcomputed tomography. *Compos Part B-Eng*, 161:272–84, 2019.

[257] Rolland H, Saintier N, Wilson P, Merzeau J, Robert G. In situ x-ray tomography investigation on damage mechanisms in short glass fibre reinforced thermoplastics: Effects of fibre orientation and relative humidity. *Compos Part B-Eng*, 109:170–86, 2017.

[258] Wright P, Fu X, Sinclair I, Spearing SM. Ultra high resolution computed tomography of damage in notched carbon fiber—epoxy composites. *J Compos Mater*, 42(19):1993–2002, 2008.

[259] Vieira PR, Carvalho EML, Vieira JD, Toledo Filho RD. Experimental fatigue behavior of pultruded glass fibre reinforced polymer composite materials. *Compos Part B*, 146:69–75, 2018.

[260] Carraro PA, Maragoni L, Quaresimin M. Characterisation and analysis of transverse crack-induced delamination in cross-ply composite laminates under fatigue loadings. *Int J Fatigue*, 129:105217, 2019.

[261] Nguyen MH, Davidson P, Waas AM. Particle-toughened interlayers enhance mechanical response of composite laminates. *Compos Sci Technol*, 182:107761, 2019.

[262] North Star Imaging. California, USA https://4nsi.com.

[263] Yu B, Bradley BS, Soutis C, Hogg PJ, Withers PJ. 2d and 3d imaging of fatigue failure mechanisms of 3d woven composites. *Compos Part A-Appl S*, 77:37–49, 2015.

[264] Nexon-Pearson OJ, Hallet SR. An experimental investigation into quasi-static and fatigue damage development into bolted hole specimen. *Compos Part B*, 77:462–73, 2015.

[265] Lin SH, Thorsson SI, Waas AM. Predicting the low velocity impact damage of a quasi-isotropic laminateusing est. *Compos Struct*, 251:112530, 2020.

[266] ImageJ. Usa https://imagej.nih.gov/ij/.

[267] Ahrens J, Geveci B, Law C. *ParaView: An End-User Tool for Large Data Visualization, Visualization Handbook*. Elsevier, 2005.

[268] Suresh S. *Fatigue of Materials*. Cambridge University Press, 2012.

[269] Guo K, Qiao Y, Salviato M. Scaling of fatigue crack growth in pristine epoxy. *In: Proceedings to 33rd Annual Technical Conference, 18th US-Japan Conference on Composite Materials ASTM D30*.

[270] Tan JLY, Deshpande VS, Fleck NA. The effect of laminate lay-up on the multi-axial notched cfrp panels: Simulation versus experiment. *Eur J Mech A-Solid*, 66:309–21, 2017.

[271] Hallett SR, Green BG, Jiang WG, Wisnom MR. An experimental and numerical investigation into the damage mechanisms in notched composites. *Eur J Mech A-Solid*, 40:613–24, 2009.

[272] Mohr D, Marcadet SJ. Micromechanically-motivated phenomenological hosford–coulomb model for predicting ductile fracture initiation at low stress triaxialities. *Int J Solids Struct*, 67-68:40–55, 2015.

[273] Xue L. Damage accumulation and fracture initiation in uncracked ductile solids subject to triaxial loading. *Int J Solids Struct*, 44:5163–81, 2007.

[274] Xue L. Constitutive modeling of void shearing effect in ductile fracture of porous materials. *Eng Fract Mech*, 75(11):3343–66, 2008.

[275] Li W, Liao F, Zhou T, Askes H. Ductile fracture of q460 steel: Effects of stress triaxiality and lode angle. *J Constr Steel Res*, 123:1–17, 2016.

[276] Winmostar. Tokyo, Japan https://winmostar.com.

[277] Oya Y, Hino Y, Inuyama K, Kikugawa G, Li J, Kuwahara R, Kishimoto N, Waizumi H, Nishikawa M, Waas A, Odagiri N, Koyanagi A, Salviato M, Okabe T. Molecular dynamics simulation with reaction model based on accurate quantum chemical calculation for cross-linking process of epoxy resins and its comparison to experimental measurement. *arXiv:1907.06829*, 2019.

[278] Caner FC, Bažant ZP. Microplane model m7 for plain concrete. i: Formulation. *Journal of Engineering Mechanics*, 139(12), 2013.

[279] Oh BH, Bažant ZP. Microplane model for progressive fracture of concrete and rock. *Journal of Engineering Mechanics*, 111(4):559–582, 1985.

[280] Ozbolt J, Bažant ZP. Nonlocal microplane model for fracture, damage, and size effect in structures. *Journal of Engineering Mechanics*, 116(11):2485–505, 1990.

[281] Cusatis G, Pelessone D, Mencarelli A. Lattice discrete particle model (ldpm) for failure behavior of concrete. i: Theory. *Cement and Concrete Composites*, 33(9):881–90, 2011.

[282] Cusatis G, Mencarelli A, Pelessone D, Baylot J. Lattice discrete particle model (ldpm) for failure behavior of concrete. ii: Calibration and validation. *Cement and Concrete Composites*, 33(9):891–905, 2011.